

DIGITAL ACCESS TO SCHOLARSHIP AT HARVARD
DASH.HARVARD.EDU

HARVARD LIBRARY


Wide Tunability of Magnetron Sputtered Titanium Nitride and Titanium Oxynitride for Plasmonic Applications

Citation

Zgrabik, Christine Michelle. 2016. Wide Tunability of Magnetron Sputtered Titanium Nitride and Titanium Oxynitride for Plasmonic Applications. Doctoral dissertation, Harvard University, Graduate School of Arts & Sciences.

Link

http://nrs.harvard.edu/urn-3:HUL.InstRepos:33493259

Terms of use

This article was downloaded from Harvard University's DASH repository, and is made available under the terms and conditions applicable to Other Posted Material (LAA), as set forth at

https://harvardwiki.atlassian.net/wiki/external/NGY5NDE4ZjgzNTc5NDQzMGIzZWZhMGFlOWI2M2EwYTg

Accessibility

https://accessibility.huit.harvard.edu/digital-accessibility-policy

Share Your Story

The Harvard community has made this article openly available.
Please share how this access benefits you. Submit a story

Wide Tunability of Magnetron Sputtered Titanium Nitride and Titanium Oxynitride for Plasmonic Applications

A DISSERTATION PRESENTED
BY
CHRISTINE MICHELLE ZGRABIK
TO
THE HARVARD JOHN A. PAULSON SCHOOL OF ENGINEERING AND APPLIED SCIENCES

IN PARTIAL FULFILLMENT OF THE REQUIREMENTS
FOR THE DEGREE OF
DOCTOR OF PHILOSOPHY
IN THE SUBJECT OF
APPLIED PHYSICS

HARVARD UNIVERSITY
CAMBRIDGE, MASSACHUSETTS
MAY 2016

©2016 – Christine Michelle Zgrabik
all rights reserved.

Dissertation Advisor: Professor Evelyn L. Hu Christine Michelle Zgrabik

Wide Tunability of Magnetron Sputtered Titanium Nitride and Titanium Oxynitride for Plasmonic Applications

Abstract

Transition metal nitrides have recently garnered much interest as alternative materials for robust plasmonic device architecture including potential applications in solar absorbers, photothermal medical therapy, and heat-assisted magnetic recording. Titanium nitride (TiN) is one such potential candidate. One advantage of the transition metal nitrides is that their optical properties are tunable according to the deposition conditions. The controlled achievement of tunability, however, is also a challenge. Although the formation of TiN has been the subject of numerous previous studies, a thorough analysis of the deposition parameters necessary to form metallic TiN films optimized for plasmonic applications had not been demonstrated. Similarly, such TiN films had not been subjected to detailed optical measurements which could be used in FDTD device simulations to optimize plasmonic device designs.

To be able to design, simulate and build robust and optimal device structures, in this work a systematic and thorough examination of the effect of varied substrates, temperatures, and reactive gas compositions on magnetron sputtered TiN was conducted. In addition, the effects of application of an additional substrate bias were studied. The resulting optical properties at visible to near-infrared frequencies were the focus of this thesis. The optical properties of each film were measured via spectroscopic ellipsometry with more "metallic" films demonstrating a larger negative value of the real part of the permittivity. These optical measurements were correlated with both the films' deposition conditions and microstructural measurements including x-ray photoelectron spectroscopy (XPS), x-ray

diffraction (XRD), and transmission electron microscopy (TEM) measurements; the different deposition conditions resulted in TiN and TiO_xN_y films with widely tunable optical responses. By sputtering under different conditions, the value of the real part of the permittivity was tuned from small positive values, through small and moderate negative values, and finally all of the way to large negative values which are comparable to those measured in gold.

It was determined that both the chemical composition as well as the film crystallinity had a significant effect on the resulting properties with the most metallic films in general exhibiting a Ti:N ratio close to 1:1, low oxygen incorporation, more N bound as TiN rather than in oxynitride form, and better crystallinity. Increased substrate temperature in general increased the metallic character while application of a substrate bias reduced crystalline order, however also reduced oxygen incorporation and allowed for deposition of metallic TiN at room temperature. The close lattice match of TiN and MgO allowed for heteroepitaxial growth on this substrate under carefully controlled conditions.

Finally, to demonstrate the viability of the optimized TiN thin films for plasmonic applications, three benchmark plasmonic structures were simulated using the measured, optimized optical properties including a plasmonic grating coupler, infrared nanoantennas, and a nanopyramidal array. The devices were successfully fabricated and preliminary measurements show promise for plasmonic applications for example in solar conversion and photothermal medical therapy.

Contents

0 Introduction 1

1 Background 4
1.1 Fundamentals of Plasmonics . . . 5
1.1.1 Bulk Plasmons . . . 5
1.1.2 Surface Plasmons . . . 7
1.2 Plasmonic Materials . . . 10
1.2.1 Material Optical Constants . . . 10
1.2.2 Plasmonic Material Property Needs . . . 11
1.2.3 Alternative Plasmonic Materials . . . 14
1.3 Basic Properties of Titanium Nitride . . . 15

2 Magnetron Sputtering of Titanium Nitride Thin Films 20
2.1 Thin Film Nucleation and Growth . . . 22
2.2 Magnetron Sputtering . . . 26
2.3 Reactive sputtering . . . 28
2.4 Control Parameters . . . 29
2.4.1 Target Parameters . . . 29
2.4.2 Chamber Parameters . . . 30
2.4.3 Gas Flow Parameters . . . 32
2.4.4 Substrate Parameters . . . 33
2.5 Structure Zone Models . . . 33
2.6 Experimental Setup . . . 36

3 Modeling Thin Film Optical Properties 39
3.1 Properties of Light . . . 40
3.1.1 Polarization . . . 41
3.1.2 Fresnel Reflection Coefficients . . . 44
3.2 Spectroscopic Ellipsometry Overview . . . 46
3.3 Experimental Setup . . . 48
3.4 Ellipsometric Data Analysis and Modeling Process . . . 49
3.5 Drude-Lorentz Model for Modeling TiN Thin Films . . . 50

3.6 Evaluation of an SE Model 56

4 Correlation of Deposition Conditions with Optical and Electrical Properties of Sputtered ITO, TiO_xN_y, and TiN Films 59
4.1 Indium Tin Oxide (ITO) 60
4.2 Overview of Optical Behavior of Titanium Nitride (TiN) and Titanium Oxynitrides (TiO_xN_y) 65
4.3 Titanium Oxynitrides (TiO_xN_y) 67
4.4 Metallic Titanium Nitride 75
4.4.1 Non-reactive Sputtering at Elevated Deposition Temperature 76
4.4.2 Reactive Sputtering at Elevated Temperature on Varied Substrates 77
4.4.3 Sputtering with Varied Reactive Gas Ratios 81
4.4.4 Ar-Bias Sputter Cleaning of Substrates prior to Deposition 84
4.4.5 Applied Substrate Bias during Deposition 86

5 Atomic Composition and Chemical Bonding of TiN Thin Films via X-ray Photoelectron Spectroscopy (XPS) 89
5.1 X-ray Photoelectron Spectroscopy (XPS) Introduction 90
5.1.1 Basic Theory 90
5.1.2 Experimental Setup 93
5.1.3 Depth Profile Sputtering Rate Determination 94
5.2 Correlation of Deposition Conditions with Chemical Composition and Bonding . . 94
5.2.1 Dependence of Metallic Character on Oxygen Content 95
5.2.2 Effect of Chemical Bonding on Metallic Character 100
5.2.3 Effect of Substrate Bias on Oxygen Content and Nitrogen Bonding 110
5.3 Oxidation of TiN thin films 114
5.4 Using Si_3N_4 as Oxidation Resistant Capping Layer 116

6 Micro- and Nanostructural Properties of TiN Thin Films 120
6.1 X-ray Diffraction Studies (XRD) 122
6.1.1 Dependence of TiN Film Orientation on Substrate 124
6.1.2 XRD Peak Shifts due to Variations in Lattice Constant and Crystallite Size . 130
6.2 Scanning Electron & Transmission Electron Microscopy (SEM/STEM) 136
6.2.1 High-temperature reactively sputtered TiN 138
6.2.2 Room-temperature non-reactively sputtered Metallic TiN 141
6.2.3 Room-temperature reactively sputtered Metallic TiN 143
6.2.4 Discussion of Structural Data (STEM/XRD) in Combination with Chemical Data (XPS) in Determining Optical Behavior 145

7 Simulated and Fabricated TiN Benchmark Plasmonic Structures 150
7.1 Surface Plasmon Grating Couplers . . . 151
7.1.1 Introduction and Motivation . . . 151
7.1.2 Finite-Difference Time Domain (FDTD) Simulations . . . 153
7.1.3 Experimental Results . . . 159
7.2 Mid-infrared (Mid-IR) Nanoantennas (collaboration with University of Stuttgart) . . . 166
7.2.1 Fabrication Methods . . . 166
7.2.2 Simulations & Experimental Results . . . 168
7.3 Photothermal Drug Therapy using TiN Pyramidal Arrays (collaboration with Eric Mazur Research Group) . . . 172
7.3.1 Introduction and Motivation . . . 173
7.3.2 Fabrication Methods . . . 174
7.3.3 Preliminary Experimental Results . . . 176

8 Conclusions 179

Appendix A Extended list of TiN samples and deposition conditions 182

Appendix B Detailed Standard Operating Procedure for AJA International ATC-2200-V Sputtering Chamber for Metallic TiN 187
B.1 Recommended starting parameters for highly metallic TiN films . . . 188
B.1.1 High-temperature, highly crystalline on MgO . . . 188
B.1.2 Room temperature plus substrate bias, highly metallic on varied substrates . 189
B.2 Loading the substrate holder into the chamber . . . 190
B.3 Target pre-sputtering and deposition . . . 193
B.3.1 Target pre-sputtering and substrate cleaning . . . 194
B.3.2 Deposition . . . 196

Appendix C Standard Operating Procedure for Measuring TiN Spectroscopic Ellipsometry Data 198
C.1 General Spectroscopic Ellipsometry Procedure . . . 199
C.2 Set-up Measurement Parameters . . . 199

References 214

Listing of figures

1.1 Drude model illustration of metals and bulk plasmons 5
1.2 Localized surface plasmons 7
1.3 Propagating surface plasmons 8
1.4 Surface plasmon dispersion curve 9
1.5 Typical permittivity values 12
1.6 Plasma wavelength vs. carrier concentration - Drude model 13
1.7 Wide permittivity range of sputtered TiN thin films 16
1.8 TiN crystal structure 17
1.9 TiN electronic band diagram 19

2.1 Basic sputtering schematic 21
2.2 Atomistic picture of film growth 23
2.3 Atomistic picture of heterogeneous nucleation wetting model 25
2.4 Film growth models 26
2.5 Magnetron sputtering source schematic 27
2.6 Titanium sputtering targets 28
2.7 Sputtering parameters 29
2.8 Thornton's Structure Zone Model 34
2.9 Anders' Revised Structure Zone Model 35
2.10 6-target Magnetron Sputtering Chamber 37

3.1 Transverse electromagnetic plane wave 42
3.2 Electric field polarization states 42
3.3 Circular, linear, and unpolarized light 43
3.4 Snell's law 44
3.5 Fresnel coefficients for multi-layered films 45
3.6 Ellipsometry general schematic 47
3.7 Experimental setup: J.A. Woollam WVASE Spectroscopic Ellipsometer 49
3.8 Ellipsometry process flow 51
3.9 Lorentz oscillators with fit parameters labeled 53
3.10 Lorentz oscillator example with varied amplitude 53

3.11 Lorentz oscillators with different center energies 54
3.12 Drude vs. Lorentz oscillator 55
3.13 TiN reference for ε_2 fit by one Drude and two Lorentzians 55
3.14 TiN reference for ε_1 fit by one Drude and two Lorentzians 56
3.15 Ellipsometry model quality analysis 57

4.1 Tunability of optical properties of sputtered ITO 60
4.2 Comparison of Drude vs. Drude-Lorentz model for ITO 62
4.3 ITO crossover wavelength and carrier concentration versus resistivity 64
4.4 Indium Tin Oxide (ITO) Plasma wavelength vs. carrier concentration - Drude model 64
4.5 Significant range of colors of TiO_xN_y thin films 66
4.6 Wide permittivity range of sputtered TiN thin films 67
4.7 Dielectric titanium oxynitride thin film optical properties 68
4.8 TiO_xN_y example of SE fitting parameters 70
4.9 Dielectric titanium oxynitride thin film optical properties 72
4.10 Resistivity compared to unscreened plasma frequency to calculate relaxation time . . 74
4.11 Elevated temperature effects during *non-reactive* sputtering 77
4.12 Reactive sputtering highlights substrate dependence 78
4.13 Resistivity compared to unscreened plasma frequency to calculate relaxation time . . 81
4.14 Reactive sputtering highlights substrate dependence - SPP Figure of Merit 82
4.15 Reactive gas variation on silicon, sapphire, and MgO substrates at 600°C 83
4.16 Effect of substrate pre-sputtering prior to deposition 85
4.17 Reactive gas variation on silicon, sapphire, and MgO substrates at 200°C plus substrate bias 87

5.1 X-ray photoelectron spectroscopy (XPS) Process Schematic 91
5.2 XPS Ti_{2p} reference data for TiO_2, and TiN films 92
5.3 XPS survey reference spectra for TiN reference film 94
5.4 Atomic % Depth Profile via XPS 95
5.5 Real permittivity of TiN films reactively sputtered onto different substrates at 600°C and corresponding Ti:N and atomic% oxygen as measured by XPS 96
5.6 Atomic % via XPS at surface and after Ar^+ sputter etch of surface 97
5.7 Permittivity of TiN sputtered on MgO over wide range of gas compositions 98
5.8 Atomic % via XPS after 40s Ar^+ sputter etch of surface on TiN sputtered on MgO over wide range of gas compositions 99
5.9 XPS high resolution reference scans of TiN thin films 101
5.10 XPS high resolution reference Ti2p scans of TiN films deposited at 600°C with varied $Ar:N_2$ ratios 103

5.11 XPS high resolution reference O1s scans of TiN films deposited at 600°C with varied Ar:N_2 ratios . . . 105
5.12 XPS high resolution reference N1s scans of TiN films deposited at 600°C with varied Ar:N_2 ratios . . . 106
5.13 Example of Peak Fit Models for XPS high resolution reference N1s scans of TiN films 107
5.14 XPS high resolution reference N1s scans of TiN films including peak fits to describe N-bonding after Ar^+ sputter-etch . . . 108
5.15 Permittivity reference data corresponding to XP spectra in Figure 5.16 . . . 110
5.16 XPS N_{1s} data for "moderately metallic" film vs. highly metalllic films deposited at high temperature and at room temperature with bias . . . 112
5.17 Ellipsometry reference data for TiN films deposited at 20°C plus 100V substrate bias with varied Ar:N_2 ratios . . . 113
5.18 Atomic % Depth Profile via XPS . . . 114
5.19 Schematic of TiN film sputtered with onto Si_3N_4 with Si_3N_4 cap . . . 116
5.20 Depth profile of TiN film sputtered with bias and Si_3N_4 cap . . . 117
5.21 Depth profile of TiN film sputtered with bias and Si_3N_4 cap with oxidation shown . 118

6.1 Scanning electron micrograph of several TiN and TiO_xN_y thin films with deposition conditions and substrate labeled . . . 121
6.2 Schematic of Bragg's Law Diffraction off of a Crystal Lattice . . . 122
6.3 Crystal structure of cubic TiN highlighting (100), (110), and (111) planes . . . 124
6.4 Comparison of XRD data for reactively sputtered TiN films on MgO, Si and Sapphire substrates . . . 126
6.5 Crystal structure TiN and MgO interface . . . 127
6.6 Crystal structure (100) TiN on (100) Si . . . 128
6.7 Crystal structure (222) TiN and (0001) Sapphire . . . 129
6.8 Comparison of XRD data for TiN films sputtered under different conditions onto sapphire substrates . . . 130
6.9 Comparison of XRD data for TiN films sputtered under different conditions onto sapphire substrates, (111) and (222) peaks highlighed . . . 131
6.10 SEM top-down images of TiN film sputtered reactively at high temperature vs. non-reactively at low temp. plus bias onto sapphire substrates . . . 133
6.11 Comparison of ellipsometry data for TiN films sputtered under different conditions onto sapphire substrates . . . 134
6.12 Scanning Transmission Electron Microscopy (STEM) cross-section and top-down SEM of Metallic TiN grown reactively at 600°C on MgO . . . 138
6.13 TEM FFT overlay from Metallic TiN grown reactively at 600°C and MgO substrate 140

6.14 High-Resolution Transmission Electron Microscopy (HRTEM) of Metallic TiN grown reactively at 600°C on MgO and FFT . . . 140
6.15 Scanning Transmission Electron Microscopy (STEM) cross-section and top-down SEM of TiN grown non-reactively at 20°C plus 100V substrate bias on MgO . . . 141
6.16 High-Resolution Transmission Electron Microscopy (HRTEM) of TiN grown non-reactively at 20°C + 100V bias on MgO and FFT . . . 142
6.17 Scanning Transmission Electron Microscopy (STEM) cross-section and top-down SEM of TiN grown non-reactively at 20°C plus 100V substrate bias on MgO . . . 143
6.18 High-Resolution Transmission Electron Microscopy (HRTEM) of Metallic TiN grown reactively at 20°C + bias on MgO and FFT . . . 144
6.19 Comparison of ellipsometry data for TiN films sputtered under different conditions onto MgO substrates . . . 145
6.20 Comparison of x-ray diffraction data for TiN films sputtered under different conditions onto MgO substrates . . . 146
6.21 Peak by peak inspection of XRD data . . . 147

7.1 Surface plasmon grating coupler theory schematic . . . 151
7.2 Vector diagram describing surface plasmon phase-matching condition . . . 152
7.3 Setup of 2D FDTD simulations of TiN metallic surface plasmon grating coupler . . . 154
7.4 FDTD simulated reflectance dip for varied etched grove depths on a TiN metallic grating on sapphire . . . 155
7.5 FDTD simulated reflectance dip for varied duty cycle on a TiN metallic grating on sapphire . . . 156
7.6 FDTD simulated reflectance dip for varied incident wavelengths on a TiN metallic grating on sapphire . . . 157
7.7 FDTD simulated reflectance dip for varied thickness dielectric grating on top of a thin TiN film on sapphire substrate . . . 158
7.8 FDTD simulated reflectance dip for TiN films of varied metallic character . . . 159
7.9 Schematic of fabricated plasmon grating coupler design including fabrication steps . . . 160
7.10 Grating coupler reflectance measurement geometry . . . 161
7.11 Measured experimental reflectance off of SiO_2 grating on TiN as a function of angle at 880, 900, 920nm compared to simulations . . . 162
7.12 SEMs of fabricated plasmonic grating coupler . . . 163
7.13 FDTD simulations showing effect of slight grating geometry variations on expected reflectance dips . . . 164
7.14 Measured experimental reflectance off of SiO_2 grating on TiN as a function of angle at 880, 900, 920nm compared to modified simulations . . . 165

7.15 Fabrication steps for mid-infrared nanoantennas 167
7.16 Optical properties of TiN thin films extrapolated into mid-infrared 168
7.17 Simulated and experimental results of TiN nanoantenna relative transmittance on sapphire substrate 169
7.18 Experimental results of tunable TiN nanoantennas fabricated by direct laser writing (DLW) on Si substrate 170
7.19 Experimental results of large-area TiN nanoantennas fabricated by laser interference lithography (LIL) 171
7.20 Overview of drug delivery process 172
7.21 Overview of experimental photothermal drug delivery setup 174
7.22 SEM of biological cells on TiN plasmonic nanopyramid array and zoom in of pyramids prior to irradiation 175
7.23 Optical image of different colored dyes showing successful cell poration and viability 176
7.24 SEM of TiN plasmonic pyramid array sputtered at room temperature onto flexible polymer epoxy substrate 178

B.1 Empty sample holder and empty transfer arm 190
B.2 Sample holder in load lock 190
B.3 Transfer height adjustment 191
B.4 Gate valve and transfer arm 191
B.5 Confocal 6-target sputtering chamber setup with inverted rotating substrate holder and sample holder on transfer arm in load loack 192
B.6 Thumbwheel and substrate rotation control 193

Listing of tables

1.1 TiN density as a function of composition 18
1.2 TiN material properties 19

3.1 TiN Reference Example: Ellipsometry Fit Parameters 56

4.1 ITO Drude-Lorentz Ellipsometry Model Parameters according to Equation 4.1 . . . 61
4.2 ITO calculated plasma wavelength and measured Van der Pauw resistivity, Hall carrier density and mobility values 63
4.3 TiO_xN_y Drude-Lorentz Ellipsometry Model Parameters 71
4.4 TiO_xN_y calculated unscreened plasma frequency/wavelength and measured Van der Pauw resistivity 73
4.5 Drude-Lorentz model parameters for TiN reactively sputtered onto various substrates at 600°C 79
4.6 Unscreened, screened and surface plasmon frequency and resistivity for TiN reactively sputtered onto various substrates at 600°C 80

5.1 XPS Ti:N ratio and atomic % oxygen for Metallic TiN 99
5.2 XPS high resolution reference N1s scans of TiN films deposited at 600°C with varied $Ar:N_2$ ratios 109
5.3 XPS Ti:N ratio and atomic % Oxygen for Metallic TiN 111
5.4 XPS atomic %N1s bonding 112
5.5 XPS high resolution reference N1s scans of TiN films deposited at 20°C plus 100V substrate bias with varied $Ar:N_2$ ratios 113
5.6 Atomic % via XPS Depth Profile for TiN sputtered with Si_3N_4 cap 117

6.1 Calculation of XRD 2θ diffraction peak angles for TiN 125
6.2 Calculated XRD 2θ diffraction peak angles for TiN with different lattice constants . 131
6.3 FWHM for XRD 2θ diffraction peaks for TiN sputtered onto sapphire under different deposition conditions 132
6.4 XPS Ti:N ratio and Atomic % oxygen for TiN 135
6.5 Summary of deposition conditions for TEM samples 137

6.6 Metallic character, microstructure, and XPS Ti:N ratio and atomic % oxygen for TiN films studied in TEM 148

A.1 List of Extended TiN & TiO_xN_y Deposition Conditions (No Bias, TiN1 - 34) 184
A.2 List of Extended TiN Deposition Conditions (With Bias, TiN35 - 63) 185
A.3 List of Extended ITO Deposition Conditions 186

Dedicated to my family (past, present, and future, both near and far):
for your love, care and unending support,
for teaching me many life-long lessons, and
for instilling in me the desire for life-long learning.

Acknowledgments

When I first started graduate school, I knew that I wanted to do interdisciplinary research in materials and devices but was not set on one particular research area or advisor. The one thing I knew was that I did not want to work in an optics lab. By the end of my first year however, I made the easy decision to join the Evelyn Hu Lab, a mainly nanophotonics or "tiny optics" lab. My interest had been piqued by two closely related fields: metamaterials and plasmonics, and I had found an amazing advisor to work with. Therefore, first and foremost I would like to thank my Ph.D. advisor, Professor Evelyn Hu for introducing me to these exciting new fields. Evelyn allowed me freedom to explore and to set my own path, but whenever I reached out and asked for help, she was always available. She is also an amazing teacher with a special talent for explaining concepts which can be hard to grasp in simple terms and was an aspirational mentor in this regard throughout my Ph.D. career. I cannot thank her enough for her compassionate guidance.

Evelyn also managed to bring together a wonderful group of people to work in her lab and my graduate career would not have been the same without them, so thank you to all Hu group members, past and present. There are a few of you whom I would like to especially thank. During my third year, I decided to pursue a new direction and there were two postdocs in our lab: Kasey Russell and Igor Aharonovich who were especially helpful to me during that transitional time. Thank you both for looking out for us younger students and acting in a way as additional advisors for me. In addition, I would like to thank Shanying Cui who always brought laughter into the lab and who inspired me to keep going even when things got tough as well as Katie Pooley. Katie, those first couple of years especially it was wonderful to have a friend I could count on to work through problem sets with me and to create countdowns of the number of classes remaining with me. Thank you for listening and being a great friend. I must also thank current Hu group member David Bracher. Thank you for helping me build the IR photoluminescence setup so that I didn't have to work in the optics lab in the dark alone all day. Your positive attitude and seemingly unending knowledge of various fun facts always brightened my day and led to great conversation.

Outside of the official Hu group members, this journey would not have been possible without several collaborators whom I would also like to thank. I was lucky enough to meet Prof. Dr. Harald Giessen from the University of Stuttgart after I had just begun my work on TiN. I would like to thank

him as well as his student, Shahin Bagheri for their interest in my work and for a fruitful collaboration. Thank you also to all members of the 4th Physics Institute for hosting me in Stuttgart. You were incredibly kind and generous during my visit and our hard work during those couple of weeks led to many promising results which re-energized my work once I returned home. In addition, I would like to thank Nabiha Saklayen and Alexander Raun, members of the Eric Mazur Group for their interest in TiN for biomedical applications. Nabiha, you have been a pleasure to work with - always on-top of things in addition to being a wonderfully positive person to work with. Alex, I have enjoyed watching you decide on the next steps in your career and am excited to see where you end up next. Thank you both for teaching me a bit of biophysics.

During the last year of my graduate work, I also had the opportunity to mentor several aspiring researchers: Mena Gadalla, Mono Livingston, and Jordan Docter. I would like to thank all of you for being so eager to learn and for all of your hard work in the lab. You all made your own technical impacts on my thesis work and it was energizing for me to work with each and every one of you. Thank you for your inspiration every day.

Finally, I must thank the Harvard CNS staff, especially Ed Macomber who has been instrumental in keeping the sputtering chambers up and running, Jiangdong Deng for his help with the ellipsometer, Greg Lin for keeping the XPS system in working order and Andrew Magyar for his mentorship as a postdoc in our lab and also for his work on the STEM measurements of my samples. Much of this work was done in CNS and this thesis would not have been possible if not for the facility and the help of the amazing staff. In addition, I was allowed much more freedom to explore due to the National Science Foundation Graduate Research Fellowship program and the Harvard University GSAS Merit Fellowship - John Parker Bequest fund. I acknowledge both funding sources and thank them for their generous support of my studies.

While my thesis work clearly was a large component of my life over the past several years, my work would not have been nearly as satisfying if not for those who supported me outside of the lab. I would like to thank the group of amazing professors and students whom I taught alongside and learned so much from including: Eric Mazur and the AP50 staff; Chris Lombardo and the ES173 staff including the undergraduate teaching labs staff; Hamed Majedi; and John Girash as well as everyone at the Bok Center and all of the Departmental Teaching Fellows with whom I was lucky enough to interact. I would also like to thank the entire GSAS Residence Halls Staff and all of the RAs and residents for limitless memories during my 3 years in the residence halls. Graduate school can be an isolating experience but living in the halls connected me with many new friends both within the sciences and across all of Harvard and I could not be more grateful for this experience. I would like to thank several of you specifically including: Emily - for endless smiles and laughter when we are together - thank you

for becoming a new life-long friend, Kelly - for encouraging me to start rowing with Dudley House which turned out to be one of the best decisions I made in graduate school and to all of the members of my Dudley crews, especially coxswain Orad, for somehow making it fun to wakeup at 5am and go outside in the freezing cold in March, to Anna - for being so kind and thoughtful and always up for an adventure including early morning figure skating lessons, and Mike - for bringing so many people and new friends together and for many great memories.

And finally, I would not be here today without the support of my amazing family. I am so lucky to have so many supportive, loving, and inspiring people who have surrounded me throughout my life. It has been incredibly difficult to be away from you over the past several years, but I have felt your support even from afar and cannot thank you enough for shaping me into the person who I have become today. Special thanks are due to my parents who have always encouraged me to 'never give up' and to pursue my dreams. There is one person in particular however, who may have endured just as much of the suffering which accompanies the excitement of pursuing a career in research as I have, and who I cannot thank enough, my husband, Jeremy. There are no words to capture the amount of love and support he has shown for me throughout this process. He is better than the best husband I could have ever asked for and I thank him from the bottom of my heart.

0

Introduction

Careful design and structuring of metals on the nanoscale allows scientists to create and observe new optical behavior that is not observable using traditional large-scale optics. To observe these behaviors, we carefully sculpt tiny patterns into thin metal films. The starting films are typically on the order of tens to hundreds of nanometers thick. As a frame of reference, a typical human hair is about 50 microns, or 50,000 nm, in diameter. Therefore, these films are 1,000 times smaller than a strand of hair to start with, and then we pattern them laterally to create even smaller nanostructures.

The resulting extraordinary optical behavior is due to a phenomenon called plasmonics in which electromagnetic energy, typically in the form of visible or infrared light, is coupled into a wave of electrons at a metallic interface. New geometries taking advantage of this effect promise novel optical responses including perfect absorption [1, 2] and negative refraction [3, 4]. Potential applications of

these nanoscale metallic plasmonic structures include: compact optical components [5, 6], increased efficiency photovoltaics and thermophotovoltaics [5, 7, 8], improved memory technologies [5, 8, 9], photothermal biomedical therapies [5, 10–12], potential advances in information processing [13–15], and improved sensor technologies[16, 17].

Plasmonics is a relatively new field that is just beginning to come into its prime. Right now, most devices that we use daily are electronic devices. More and more common however, are photonic devices which use packets of light called photons instead of electrons to transmit information. Since photons travel much faster than electrons, photonic devices are much faster than electronic devices. They also can have a higher bandwidth because multiple wavelengths can be used to simultaneously transmit information over the same spatial extent. In addition, a significant amount of energy is lost in electronic devices due to resistive heating. As electrons flow through wires they dissipate heat, leading to an energy loss. Photons do not have the same magnitude of losses, leading to an additional potential increase in energy efficiency.

Plasmonic devices are a sort of blend of electronic and photonic devices. They couple visible or infrared wavelengths of light (photons) into waves of oscillating electrons at metallic interfaces. Noble metals, usually silver and gold, have been used to design conventional plasmonic devices because they have lower optical losses than other metals. Both materials, however, have challenges which may be easier to overcome by exploring alternate materials. Silver and gold are ductile metals and can be difficult to fabricate into robust plasmonic device structures since they often bend, peel, and can be scratched off. They also have relatively low melting temperatures, near 1000°C, which can easily be exceeded locally since plasmonic devices confine energy into tiny volumes, causing a degradation of plasmonic performance and device stability.

My thesis work has included studying a new class of alternative plasmonic materials called conducting oxides and nitrides, with a focus on titanium nitride (TiN). Conducting oxides and nitrides have only recently been identified as potential replacements for the conventional silver and gold metal-

lic components currently in many plasmonic device designs [9]. Titanium nitride is a particularly promising candidate. As a refractory metal it is hard and durable, with a melting point of almost 3000°C and is often used as a coating for drill bits. It is also bio-compatible and chemically stable so given its durability could conceivably be used as a plasmonic bio-sensor without significant degradation expected even in harsh body environments, for example high acidity [8]. An additional potential advantage of TiN over silver and gold is the tunability of its optical properties, yet this is also a challenging materials problem which has not yet been fully explored in the literature. The focus of this research was to better understand the tunability of these optical properties and optimize them for plasmonic applications.

In Chapter 1 of this dissertation, I will provide background information on the fundamentals of plasmonics, the need for alternative plasmonic materials and will introduce the material of my focus, titanium nitride (TiN). Chapter 2 discusses the deposition of thin films of titanium nitride via a method known as magnetron sputtering. Chapters 3 and 4 describe the optical properties of the sputtered films, focusing on the methods used to model the thin film properties and the dependence of the film properties on the sputtering deposition conditions, respectively. Next, Chapters 5 and 6 describe structural studies used to better understand the optical behavior of these films including: x-ray photoelectron spectroscopy (XPS), scanning transmission electron microscopy (STEM), and x-ray diffraction (XRD) measurements. Finally, several benchmark structures which were fabricated to confirm the high quality of the optimized TiN for plasmonic applications and the preliminary results are shown in Chapter 7 followed by conclusions and a discussion of potential future work.

1

Background

Plasmonics, as mentioned in the introduction, involves the coupling of incoming light waves into waves of free electrons in a metallic material. A brief background including the theory out of which this phenomenon arises will be included in this section followed by the a discussion of the ideal properties of a plasmonic material. Finally, this chapter will conclude with some further background information on the properties of TiN, the alternative plasmonic material focused on throughout this work.

1.1 Fundamentals of Plasmonics

The basic theory of plasmonics will be briefly described here. For a more in depth treatment, the textbook "Plasmonics: Fundamentals and Applications" by Stefan Maier provides a thorough and comprehensive review of the field and is highly recommended for any student new to plasmonics or as a reference book for those more familiar with the field [18]. Plasmons are defined as the collective oscillations of electrons and therefore, generally occur only in metals or semiconductors which have large numbers of free electrons ($10^{18} - 10^{23}/cm^3$). There are two main types of plasmons: bulk (or volume) plasmons and surface plasmons [19].

1.1.1 Bulk Plasmons

According to the Drude model, metallic materials consist of a core of positive ions which are fixed in location and a sea of negative free electrons which in general move randomly throughout the material. A depiction of this model is shown in Figure 3.12(a) with the small black dots representing electrons. As shown in (b), if an external electric field pointing down were applied to a bulk piece of metal, the

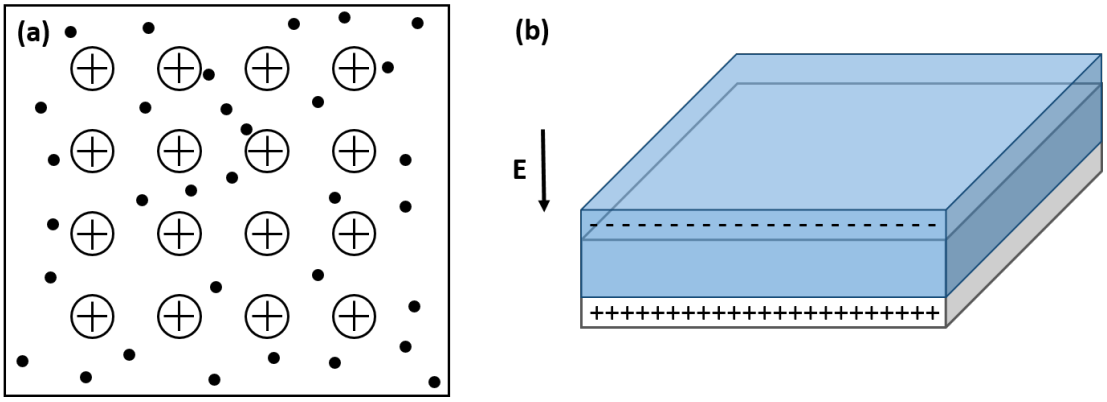


Figure 1.1: (a) Graphic illustration of Drude metal with positive ion cores and a sea of negative free electrons (small black dots), (b) Bulk metal with applied static electric field showing collective shift of free electron cloud (blue) away from positive cores. Adapted from [18].

electrons would move in the direction opposite to the field leading to a net negative charge at the top of

the sample and leaving a net positive charge near the bottom of the sample due to the positive ion cores. If the field were removed, the charge difference would cause the electrons to accelerate back towards the cores. Bulk plasmons can be visualized as this sea of free electrons oscillating back and forth in unison. The frequency at which these oscillations occur is called the unscreened plasma frequency, ω_{pu}. According to the Drude free electron model [20, 21], this plasma frequency depends only on the number density of electrons, n, the electron charge, e = 1.6 x 10^{-19}C, the vacuum permittivity, ε_0 = 8.85 x 10^{-12} F/m, and m^*, the electron effective mass.

$$\omega_{pu}{}^2 = \frac{ne^2}{\varepsilon_0 m^*} \tag{1.1}$$

This plasma frequency has a significant impact on the optical properties of materials, perhaps already suggesting why nanostructuring of metallic materials leads to novel optical behavior. In terms of macroscopic behavior, the plasma frequency defines the cutoff point at which for frequencies which are larger than than the plasma frequency, or $\omega >> \omega_{pu}$, metals become transparent (and also explains why they are so shiny, reflecting a majority of light at slower frequencies). At these higher frequencies, the electrons cannot react quickly enough to the changing field and thus, the energy is transmitted through the material [22]. Since energy can be written in terms of frequency, plasma frequencies are also often referred to as occurring at a specific stated energy rather than frequency. Converting between the two is easy, requiring only a multiplication by Planck's constant, $\hbar$ = 1.05 x 10^{-34} m^2kg/s.

$$E_p = \hbar\omega_{pu}$$

For typical metals, ω_{pu} is usually in the ultraviolet, therefore within the visible range (shorter frequencies) most metals appear reflective or shiny [19, 21]. Metals which have specific coloration often exhibit a particular hue due to interband transitions which cause absorption of particular wavelengths of light. The most common example is gold which appears yellow-ish in color due to interband ab-

sorption near 2.3eV [23], though the same is true for TiN which looks similar in appearance to gold. Silver which does not have a well-defined color, does not have significant absorption bands within the visible regime [24].

1.1.2 Surface Plasmons

The second type of plasmons are surface plasmons which exist at the surface of a material rather than within the bulk, often at the interface between a metallic and dielectric (or non-metallic) material. They are two commonly studied types of surface plasmons: localized surface plasmons and surface plasmon polaritons. Localized surface plasmons (LSP) are excited in metallic nanostructures which have dimensions smaller than the wavelength of the incident radiation used to excite them. The resonances (often called LSPRs) are strongly dependent upon the nanostructure geometry (e.g. diameter for spherical nanoparticles, or length for nanoantennas) [19] as well as the medium surrounding the nanostructure and they are thus commonly used for sensing applications.

A diagram depicting how LSPs are excited at the surface of a metallic nanoparticle is shown in Figure 1.2. The nanoparticle in the figure is excited with an oscillating electric field (such as visible

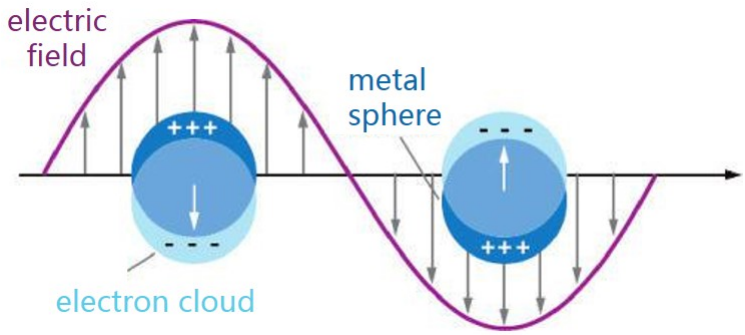


Figure 1.2: Schematic depicting localized surface plasmons. Adapted from Willets and Van Duyne [16]

light). When the electric field points up, the cloud of electrons on the surface of the nanoparticle is repelled in the opposite direction of the field. As the field passes in time, it will then reverse and

point down, causing the electrons to oscillate to the other side of the particle. This oscillation causes a resonance at a particular frequency, dependent upon the incident radiation and the particle geometry.

The second type of surface plasmon is the propagating surface plasmon wave, also often referred to as a surface plasmon polariton (SPP) due to the strong coupling of incident light with an electron plasmon wave. SPPs are confined to the interface between a metal and a dielectric with the direction of propagation, or the surface plasmon wavevector, k_{SP}, parallel to the interface. A schematic depicting incoming light coupling to an SPP mode between a metal film with permittivity, ε_m (shown here as TiN), and a dielectric substrate with permittivity, ε_d, is shown in Figure 1.3. In this example, the SPP propagation is in the x-direction. The white lines depict the propagation of the electron density wave along the interface with the negative charges highlighting the locations of dense electron density and the positive charges depicting the electron-deficient regions. The effective wavelength of the surface wave, λ_{SPP} as labeled in the diagram is shorter than the wavelength of the incoming photon (photon not to scale).

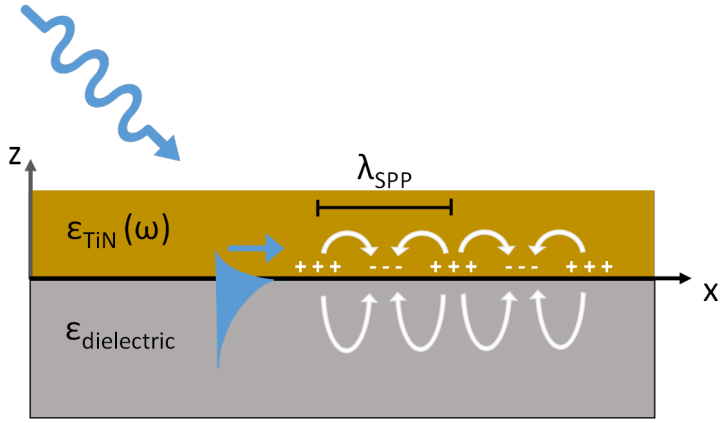


Figure 1.3: Incident energy can be confined and propagate along the interface between a metal and dielectric. These electron density waves have effective wavelengths which are shorter than the wavelength of the incident radiation and are called propagating surface plasmons.

SPPs are evanescently confined to the interface meaning that the electric fields are strongest at the interface and decay exponentially a perpendicular distance, z, from the interface. This exponential

decay happens faster in the metal than in the dielectric as depicted in the schematic. How far an SPP can travel along an interface, also known as the propagation length depends on how confined the mode is to the interface. SPPs which are less confined have smaller frequencies (longer wavelengths) and longer propagation lengths and SPPs which are more confined have more intense fields and larger frequencies (up to the surface plasmon frequency $\omega_{sp} = \omega_{pu}/\sqrt{2}$).

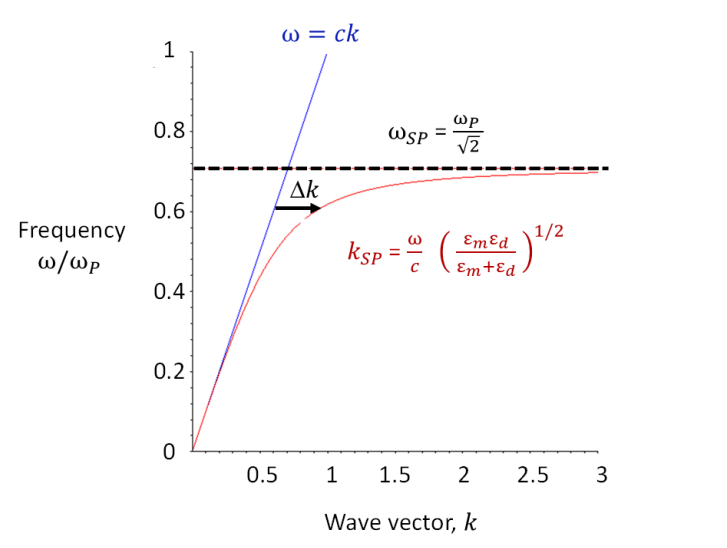


Figure 1.4: Blue line shows the light line with a linear relationship between wavevector and frequency. Red line shows surface plasmon dispersion curve according in Equation (1.2). Black dashed line denotes maximum surface plasmon frequency where the curve plateaus. Adapted from [25]

The trade-off between confinement and propagation length can be more easily seen by examining the sample SPP dispersion curve shown in Figure 1.4 which looks at the relationship between the SPP wavevector and frequency. The shape of the curve is governed by the SPP dispersion relation:

$$k_{SP} = k\sqrt{\frac{\varepsilon_m \varepsilon_d}{\varepsilon_m + \varepsilon_d}} \tag{1.2}$$

While LSPs can be directly excited optically, SPPs a large wavevector which lies to the right of the light line in the dispersion curve (outside of the dielectric light cone) and therefore require special

techniques to excite the surface plasmons (by adding extra Δk). Two of the most commonly used methods are prism and grating coupling [18]. Grating coupling is used to excite surface plasmons on our sputtered TiN films and will be discussed further in Chapter 7.

1.2 Plasmonic Materials

The plasmonic effect depends on the collective oscillation of large numbers electrons, so it is clear that to be "good" for plasmonics, a material must have a large number of free electrons, or a high carrier concentration, but this requirement leads to several additional questions: How many electrons is enough electrons? Can there be too many electrons? Are there other needs which are also important in choosing a "good" plasmonic material?

1.2.1 Material Optical Constants

The main technique used throughout this work to characterize the optical behavior of materials is spectroscopic ellipsometry (SE), which measures the optical response of a material as a function of wavelength. This technique and results will be discussed in detail in Chapters 3 and 4. But first, here we state explicitly what we mean by optical behavior of a material.

The most commonly used terms when speaking about how light interacts with a material are the refractive index, n, and the absorption coefficient, k where the complex refractive index, $\tilde{n}$:

$$\tilde{n} = n + ik$$

For plasmonics, it can be helpful to write the optical constants in a different but equivalent form, called the permittivity, ε. This term appeared in the previous section in the Drude free electron model as well as in the SPP dispersion equation. It is defined in terms of the refractive index as:

$$\varepsilon_1 = n^2 - k^2$$

$$\varepsilon_2 = 2nk$$

where,

$$\varepsilon(\lambda) = \varepsilon_1 + i\varepsilon_2.$$

In the SPP dispersion equation, the permittivity was defined as ε_m for the metallic material and ε_d for the dielectric material, but how can we tell if a material is metallic or dielectric based on its optical properties? An example is plotted in Figure 1.5 which compares the known optical constants of a common metal, gold, with those of a well-known dielectric material, SiO_2, which glass is made of. The real part of the permittivity, ε_1, remains positive and relatively small, signifying that the applied electromagnetic field (or light) does not have much effect on electrons within the material. The imaginary part of the permittivity is close to zero signifying that the optical losses are also close to zero or that the material is transparent at that particular wavelength. Examining the properties of the metal, on the other hand, gives quite different behavior. The real part of the permittivity, ε_1, starts out positive but varies significantly with wavelength showing the frequency dependence of the optical response. As the negative magnitude increases, this means more electrons can be polarized by the applied electromagnetic field. The imaginary part of the permittivity, ε_2, in the case of the metal has a much larger value, signifying absorption or optical losses.

1.2.2 Plasmonic Material Property Needs

It is known that a plasmonic material requires a large carrier concentration to support the free electron oscillations. As we have seen, metals which have large numbers of free electrons can generally be modeled by the Drude free electron model at visible wavelengths [18, 26].

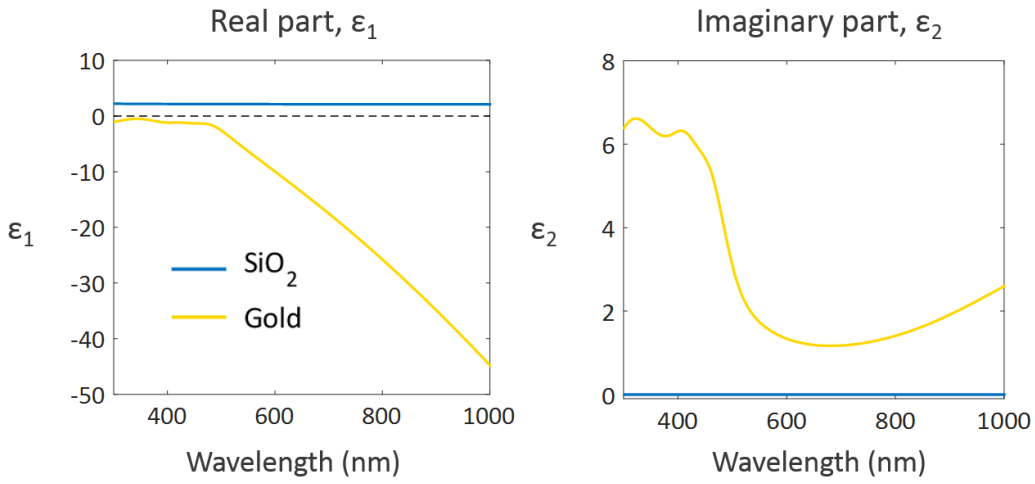


Figure 1.5: Metals typically have ε_1 which very quickly become negative simultaneous with increasing losses (correlated with larger ε_2). Dielectrics such as SiO_2 more generally have ε_1 values which are positive and small magnitude and little to no losses.

$$\omega_{pu}{}^2 = \frac{ne^2}{\varepsilon_o m^*} \tag{1.3}$$

As the number of carriers, n, increases therefore, the plasma frequency tends to shift to larger energies (shorter wavelengths). If we plot the expected plasma wavelength as a function of the carrier concentration using Equation (1.3), we see as shown in Figure 1.6 that to reach plasma wavelengths within the visible and near-IR range, according to the Drude model, the free carrier concentrations must be quite large ($> 10^{20} cm^{-3}$) and ideally closer to ($> 10^{21} - 10^{22} cm^{-3}$).

Therefore, the first requirement is that the material have a large carrier concentration and the second is that the concentration is large (or small) enough that the plasma wavelength falls within the wavelength regime of interest. Carrier concentrations this large (up to $10^{22} cm^{-3}$) are common in metals, but are there other materials which also can have carrier concentrations within this range? Can a material have too many electrons? The short answers are yes, there are a wide range of potential mate-

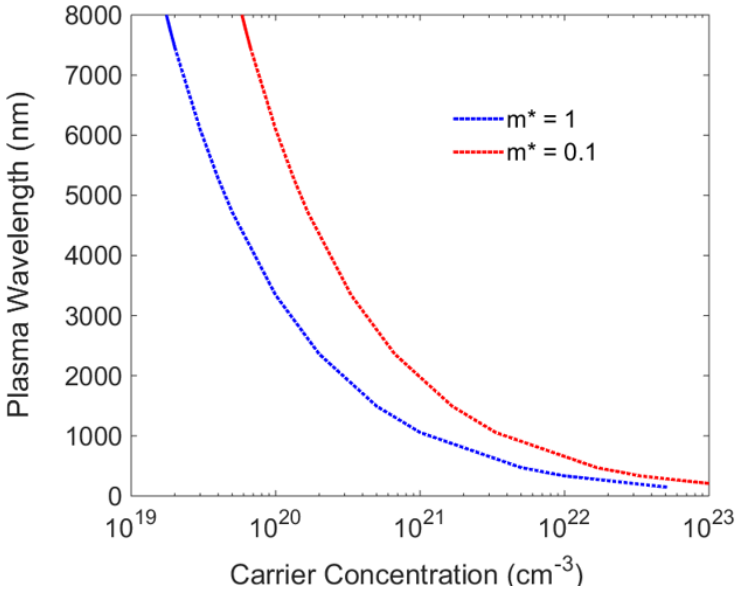


Figure 1.6: Plasma wavelength approximated via Drude free electron model for different carrier concentrations. Electron effective masses calculated for m* = 0.1 and m* = 1 to show the range.

rials to choose from, and yes, in particular applications there can be such a thing as too many electrons. This will be discussed further in the next section. A very high carrier concentration can also lead to increased optical losses within the material which can be detrimental to the plasmonic effects.

In terms of the permittivity which was just discussed, a high carrier concentration translates to a large negative real part of the permittivity, ε_1 and low optical losses translate to a small value of the imaginary part of the permittivity, ε_2. Several figures of merit (FOM) have been defined depending on the plasmonic application [23, 27–29]. Even though I just mentioned that it is indeed possible for a material to have too many carriers, the most basic FOM which compares the magnitude of the real part of the permittivity, ε_1, to the magnitude of the imaginary part of the permittivity, ε_2 has been focused on in this case for simplicity, making the overall goal to maximize the metallic character (or negative ε_1) of the TiN films while also minimizing the losses (ε_2). As will be seen shortly, the optical properties of sputtered TiN can vary widely and this is thus a great starting point.

$$\text{FOM} = \frac{|\varepsilon_1|}{|\varepsilon_2|}$$

1.2.3 Alternative Plasmonic Materials

The requirements for a 'good' plasmonic material discussed above include: a high carrier concentration and low optical losses. As shown in Figure 1.5, gold seems to satisfy these conditions quite well. One might ask therefore, why do we need to explore alternative plasmonic materials if traditionally used materials such as gold and silver already satisfy these requirements?

For one, I mentioned a caveat earlier that, depending on the wavelength regime of interest and the desired application, the highest carrier concentration might not necessarily be the best. One example of when this is true is epsilon-near-zero (ENZ) applications [30–32]. ENZ materials are interesting because they show potential for lossless waveguiding around sharp corners and pinning of emitter frequencies, for example, both characteristics which could be quite useful in photonic architectures. While this is not technically a plasmonic application, it is often considered part of the same field as by definition metallic materials have a zero-crossing of ε_1 and dielectric materials do not and therefore, designs typically use metals and metallic nanostructures. In this case, the desirable optical properties would be to simultaneously have ε_1 and ε_2 as close to zero as possible and to have the frequency at which this occurred be tunable.

Second, as was briefly mentioned in the introduction, there are several reasons why traditionally used plasmonic materials such as gold and silver, while still 'good' may not be the 'best' materials in all situations. If we were to create a plasmonic material properties 'wish list' of sorts, outside of having enough carriers and low enough losses to make it plasmonically active, the list might include a material which: has variable optical properties that are dynamically tunable, perhaps even optically tunable and may also include environmental considerations based on the application. For example desirable attributes might be for a material that is robust and durable; is compatible with CMOS manufactur-

ing; and is bio-compatible.

Originally silver and gold were the only commonly used plasmonic materials [19]. They were later joined by aluminum, a good plasmonic material in the ultraviolet, but with a high tendency to oxidize[33–35]. Over the past few years the range of materials explored has expanded to included not only a wider range of metals, but also many intermetallic compounds including nitrides, borides, and carbides, oxides, and even heavily doped semiconductors such as silicides, germanides, and arsenides [23, 36–41]. Heavily doped semiconductors do not have a large enough carrier concentration to exhibit plasmonic behavior in the visible or near-IR wavelength regime. Within this range, several transition metal nitrides including TiN, TaN, VN, and HfN have been suggested as potential candidates [29, 42–50] due to their high carrier concentrations and also robustness.

TiN is robust, bio-compatible, CMOS-compatible and the optical properties can be deliberately chosen as required for the device design by sputtering over a wide range of deposition conditions. Figure 1.7 shows a sample of the wide range of optical properties which I was able to achieve by controlling the deposition conditions. How to control these optical properties and what causes these variations will be discussed throughout the remainder of this dissertation. In addition, in the following section, the basic properties of TiN will be discussed, showing that as compared to gold and silver, TiN has the potential to satisfy many of the conditions on this wish list.

1.3 Basic Properties of Titanium Nitride

TiN will be the main material focused on throughout this thesis; therefore, some basic information on its crystal structure, as well as electrical, optical and other basic properties will be discussed here. TiN is a particularly promising alternative plasmonic material. While it can be tuned to have optical properties similar to gold which has served as a plasmonic material successfully for many years, TiN also can be used to create much more robust, bio- and CMOS-compatible plasmonic devices due to its higher melting point and increased hardness compared to gold as well as its chemical stability.

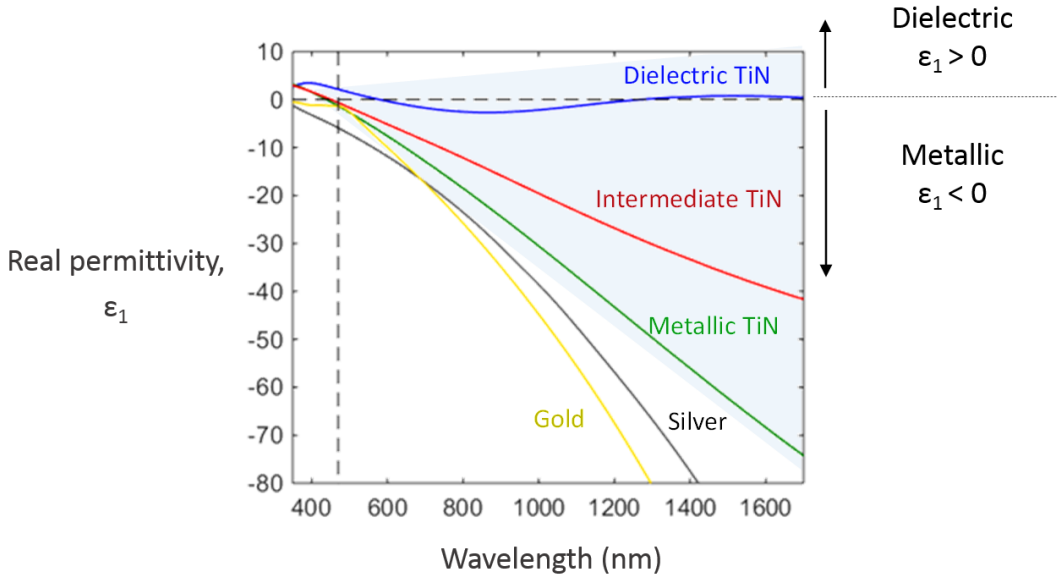


Figure 1.7: The optical properties of TiN and TiO_xN_y films vary widely dependent upon sputtering chamber conditions prior to and during deposition.

TiN in its most common form has a cubic (NaCl) crystal structure with geometry specified by space group $Fm\bar{3}m$, No. 225 as shown in Figure 1.8. The most commonly cited lattice constant, a, of stoichiometric TiN is 4.24 Å though variations down to 4.21Å have been measured in N-deficient TiN_x[51]. The NaCl-type lattice can be though of as two separate face-centered cubic lattices, one of all the metal Ti atoms and a second of all of the N atoms offset by distance, a/2.

TiN is a transition metal nitride and a refractory metal, named as such due to its high melting temperature. The melting point has been measured to be >2900°C [53, 54] significantly higher than typically used plasmonic metals silver and gold, both near 1000°C and aluminum near 660°C [53]. In terms of its structural properties, TiN has a high hardness near 9 on the Mohs hardness scale as compared to gold, silver, and aluminum near 2.5-3 [53]. Due to this high hardness and insensitivity to heat, TiN is quite robust, even commonly used as a protective coating on drill bits and gears [54–57].

TiN_x is also chemically stable, existing in a thermodynamically stable state over a wide range of stoi-

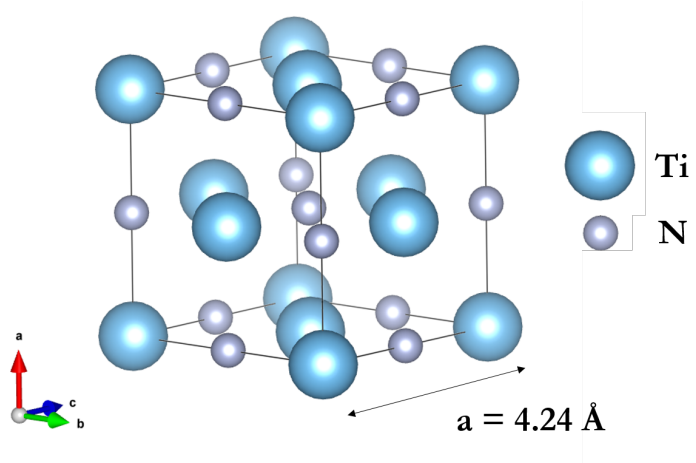


Figure 1.8: Schematic of TiN crystal structure. Lattice parameter a = 4.24Å. Schematic produced using VESTA software [52]

chiometries, where 0.6 < x < 1.1 [58], with Ehrlich [51] reporting TiN being stable in this phase further still until $TiN_{0.42}$ and switching to hexagonal phase only for lower N-content. For this reason, many of the measured properties of TiN vary quite significantly. For example, the density of TiN has been shown to vary with the N-content as measured by Ehrlich [51] and reported in [59]. Stoichiometric films with Ti:N ratio of 1:1 are more dense than N-deficient films as shown in Table 1.1. It has also been reported that films with higher porosity exhibit higher electrical DC resistivities [60]. The resistivity has in turn also been shown to depend significantly on the chemical composition and crystallinity. It been measured as low as 18$\mu\Omega$-cm [61] and 21.7$\mu\Omega$-cm [62] at room temperature but values within the range of 50-500$\mu\Omega$-cm seem to be most common for polycrystalline TiN films [63–67] though much higher resistivity films have also been measured, even up to 12 x 10^{-4} Ω-cm [68].

Since TiN is chemically stable, it is not etched by hydrochloric acid, sulfuric acid, or nitric acid [59]. It is soluble in aqua regia [59] and has also been wet-etched via basic Piranha solution [69, 70]. Using a 1NH_4OH : 2H_2O_2 : 5H_2O at 75°C, the etch rate of TiN was found to be approximately 0.5nm/sec [71]. For nanostructuring purposes, TiN can also successfully be dry etched using both F-based [72, 73] and Cl-based etch recipes [72–77]. Chromium is a commonly used etch mask since

Composition	Density (g/cm^3), 25°C
$TiN_{1.00}$	5.21
$TiN_{0.70}$	5.10
$TiN_{0.44}$	4.87
$TiN_{0.30}$	4.74
$TiN_{0.10}$	4.57
Ti	4.45

Table 1.1: TiN density as a function of composition. From [59]

TiN is not etched by Cr etchant, so after etching the Cr mask can be easily removed [70].

The metallic behavior of TiN is due to the intersection of the valence band of the Ti 3d electrons with the Fermi level as can be seen in band diagram in Figure 1.9 calculated by Patsalas and Logothetidis [26] based on [78]. As will be discussed in Chapter 3.5, a Drude free electron model can be used to model the behavior of these Ti 3d electrons but this does not tell the whole story. As is common in typical rather than idealized metals, there is also some intraband absorption. Patsalas and Logothetidis predicted two such bands near the L and X points with energy gaps of approximately 5-6eV and 3-4eV respectively. As we will see later, these absorptions are well-modeled by adding two Lorentzian oscillators to the Drude free electron term. The optical and electrical behavior correlate closely.

For reference, a summary of several characteristic TiN material properties is shown in Table 1.2 [79, 80].

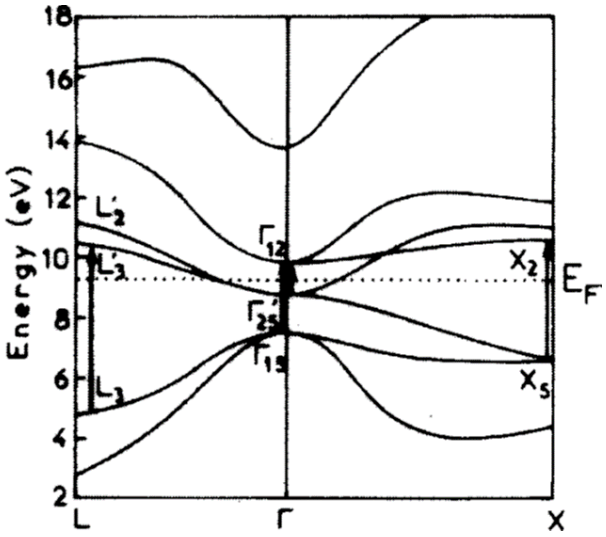


Figure 1.9: TiN electronic band diagram. Reprinted from [26] with the permission of AIP Publishing.

TiN Material Properties	
Crystal Structure	Cubic (NaCl)
Lattice constant, a	4.24 Å
Thermodynamic Stability	TiN_x 0.6 < x < 1.1
Density	5.22 g/cm^3
Hardness (Mohs)	9
Thermal conductivity	19.2W/mK
Melting point	>2900°C
DC Resistivity	30 - 70 μ m-cm
Unscreened plasma frequency	near 3.8-4eV
Plasma frequency	near 2.5eV
Surface plasmon frequency	near 1.1-1.5eV

Table 1.2: TiN material properties

2

Magnetron Sputtering of Titanium Nitride Thin Films

Titanium nitride (TiN) has been around for quite some time so it is not a new material, but rather a well-established material being considered for new applications. Interest in the material began to increase as early as the 1940s. Therefore, there are many known methods for depositing TiN thin films. The two main types of deposition are chemical vapor deposition (CVD) and physical vapor deposition (PVD). Among the CVD methods, $TiCl_4$, N_2 and H_2 compounds [81, 82] as well as $TiCl_4$ and NH_3 [82, 83] have been reacted to create TiN. In

addition, Ti powder can be turned into TiN crystallites by high temperature annealing in a nitrogen environment. The most common PVD methods used are sputtering, arc deposition, or electron beam evaporation. A disadvantage of traditional CVD and PVD methods is that under most conditions, the films need to be formed at high temperatures (850 - 1200°C+). More recently, however it has been shown that plasma and ion-assisted processes allow for the possibility of depositing TiN at lower temperatures. Examples of these deposition methods include plasma assisted chemical vapor deposition (PACVD) [84] and high-power impulse magnetron sputtering (HiPIMS) [85]. This chapter discusses the method which I used to produce TiN and TiO_xN_y films in my thesis work: a physical method called magnetron sputtering. To produce high plasmonic quality TiN thin films, the sputtering was performed either at high temperature, or at low temperature with the assistance of an additional substrate bias as will be discussed in the following chapters. An initial optimization of the *optical* properties of these films for plasmonic applications was performed. This focus on the optical properties contrasts with previous work which has historically focused on the optimization of the structural and mechanical properties.

Sputtering is a type of physical deposition method often used to deposit thin films. The basics of the sputtering deposition process are outlined in Figure 2.1. There is a 'target' which is the source

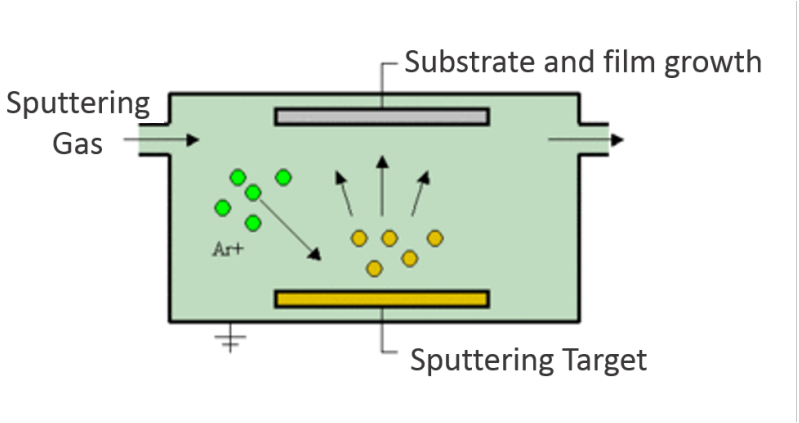


Figure 2.1: Schematic showing basics of sputtering process to deposit thin films. Adapted from [86]

material which will be sputtered to deposit the film. The target is connected to an RF or DC power supply. DC sputtering is sometimes referred to as cathodic or diode sputtering. RF sputtering is most commonly used to sputter insulating targets which cannot be sputtered using traditional DC sputtering which requires conductive targets. The substrate is positioned opposite the target and if desired, can be heated or cooled, or biased with an additional power supply, or neither or both of these options, depending on the desired properties of the resulting film. The process is performed in a vacuum chamber with a maximum base pressure of approx. 10^{-6} Torr, and ideally significantly lower ($\approx 10^{-8}$ Torr) for the best quality films with the least incorporated impurities. During deposition, the chamber pressure is raised to the 10^{-3} Torr range by backfilling with a working gas such as Argon. This gas should be inert and is typically one of the noble gases. The most common sputtering gas is Ar, but Ne, Kr, and Xe are also used. After backfilling the chamber, power is applied to the target which acts as a cathode (negative source) with the substrate acting as the anode. This initiates a glow discharge (quite similar to a plasma) within the chamber by ionizing a portion of the inert, working gas. The inert ions in this discharge are accelerated toward the target. They energetically bombard the target and eject atoms from its surface into the vacuum chamber. A portion of these atoms are then deposited onto the substrate (for example, a silicon wafer) and the film growth process begins. Clearly, this is a complex environment and only the basics are discussed here. Further details, especially those which carry elevated importance when sputtering TiN, will be discussed later in this chapter. However, before discussing the details of sputtering TiN using our experimental setup, I will first give a brief overview of the steps involved in thin film nucleation and growth in general.

2.1 Thin Film Nucleation and Growth

From an atomistic viewpoint, many processes occur on the wafer substrate surface as a film begins to grow as shown in Figure 2.2. An atom which impinges upon a substrate can first either be reflected or absorbed onto the surface. If an atom 'sticks' to the substrate, the process is called physisorption.

If the atom does not have enough energy to create a chemical bond, it can desorb. Physisorbed atoms will have some inherent energy and mobility on the surface. Mobility in this sense can be defined as the ability of an atom to diffuse across a surface with higher mobilities suggesting greater ease of movement. These 'adatoms', or new atoms being added to the new film, are not yet in equilibrium with the substrate and can move along the surface and either bind to the surface, or to other atoms or clusters of atoms. If a chemical bond is formed either between the atom and substrate or between two atoms, this process is called chemisorption. The formation of clusters of atoms is called nucleation and can proceed in several ways.

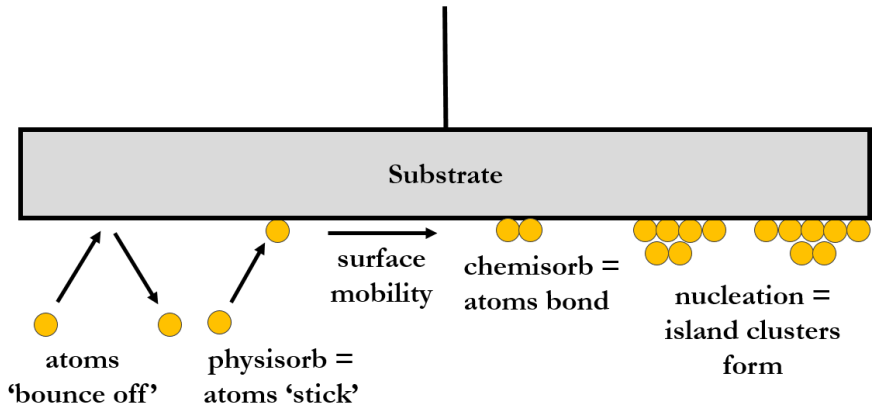


Figure 2.2: Atomistic picture of film growth on the wafer substrate. The substrate has been drawn inverted to correspond to the sputtering geometry used.

The simplest model used to represent the nucleation process is called *homogeneous nucleation*. This is an oversimplification of the gas-to-solid nucleation process which occurs in thin film deposition however is a good starting pointing for understanding the thermodynamics involved [87, 88]. During this process there is a change in Gibbs' free energy, ΔG_{homo}, due to the surfaces created and destroyed when an atom is added. This is a combination of the reduction or release of chemical free energy by the system per unit volume, ΔG_v, as well as an increase in surface free energy (or an additional energy cost) due to the new surfaces being created per unit area, γ:

$$\Delta G_{homo} = \frac{4}{3}\pi r^3 \Delta G_v + 4\pi r^2 \gamma. \tag{2.1}$$

As can be seen in Equation (2.1), homogeneous nucleation assumes the formation of spherical shaped solid-phase islands of radius r, with volume = $4/3\pi r^3$ and surface area $4\pi r^2$. ΔG_v must be negative to satisfy the thermodynamic equations. Another way of thinking about this is the energy 'costs' and 'benefits' associated with the formation of islands. Since ΔG_v is negative it corresponds to the energy benefit which happens as islands form, reducing the energy of the system overall. γ on the other hand is positive and therefore can be thought of as the 'cost' required to create an additional interface either between the film and substrate or air. By the setting $d\Delta G/dr = 0$, the critical radius $r^* = -2\gamma/\Delta G_v$ can be determined. When nuclei have radii $< r^*$, they will therefore be unstable. Larger, stable islands will increase in size at the expense of these smaller, unstable islands since this will lower the energy of the system overall. Thus, as time progresses it is expected that the average island size will increase. Exceptions include when the deposition rate is fast and when adatoms have limited surface mobility. In either case, the adatoms cannot diffuse along the surface to rearrange quickly enough before the next layer is formed.

In reality, the film nucleation and growth process is significantly more complex than the homogeneous nucleation model predicts since nucleation occurs not homogeneously, but preferentially (e.g. on ledges, dislocations and at any imperfections on the substrate surface.) A more complex model representing this *heterogeneous nucleation* process is discussed next. This model acknowledges that there must still be a volumetric energy change due to the vapor to solid phase transformation; however, instead of a single surface energy term, the surface energy between the vapor and film, γ_{vf}; the vapor and substrate, γ_{vs}; and finally the film and substrate, γ_{fs} are now all considered leading to a change in the Gibbs' free energy [88]:

$$\Delta G_{\text{hetero}} = a_3 r^3 \Delta G_v + a_1 r^2 \gamma_{vf} + a_2 r^2 \gamma_{fs} - a_2 r^2 \gamma_{sv}.$$

In this case, the nucleation is not limited to spherical islands, but rather is based on the 'wetting' of a droplet-shaped island on the surface specified by geometric parameters, a_1, a_2 and a_3, dependent only on the wetting angle, θ, as shown in Figure 2.3. Here, $a_1 r^2$ corresponds to the curved surface area of the droplet (surface area between the vapor and film), $a_2 r^2$ corresponds to the projected circular area of the droplet on the substrate (surface area between the film and the substrate), and $a_3 r^3$ corresponds to the volume of the film nucleus.

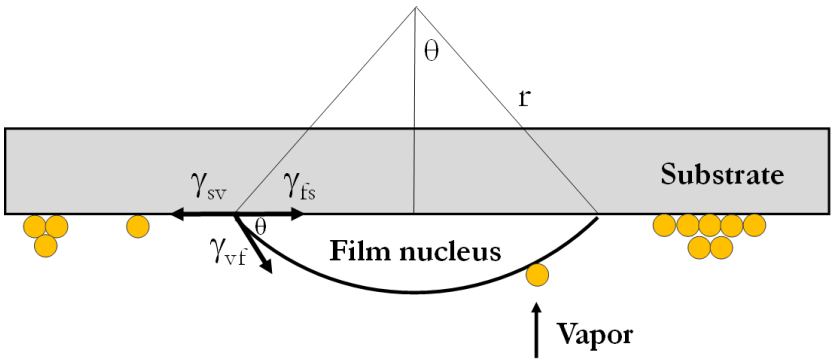


Figure 2.3: Atomistic picture of heterogeneous nucleation wetting model showing wetting angle θ. Geometric parameters a_1, a_2 and a_3 calculated using θ and droplet radius, r. Adapted from[88]

There are three main types of thin film growth which have been experimentally observed and which correspond to varied wetting angles and surface energies. These are commonly referred to as island growth (Volmer-Weber), layer growth (Frank van der Merwe), and mixed growth (Stranski-Krastanov). In terms of the surface energy, island-like growth is seen when the surface energy between the substrate and the vapor outweighs that of the film with both the substrate and vapor combined. This occurs at angles θ >0° (the growing film wants to curl up into little droplets or 'islands'). For layer growth, the substrate must be fully 'wetted', with θ = 0°. In the case of mixed or Stranski-Krastanov

growth, the surface energy between the substrate and the vapor is larger than the total between the film and either substrate or vapor which allows new nuclei to form atop the layers. Grain boundaries are formed at the interfaces between the growing islands in the film. A diagram depicting these different growth methods is shown in Figure 2.4.

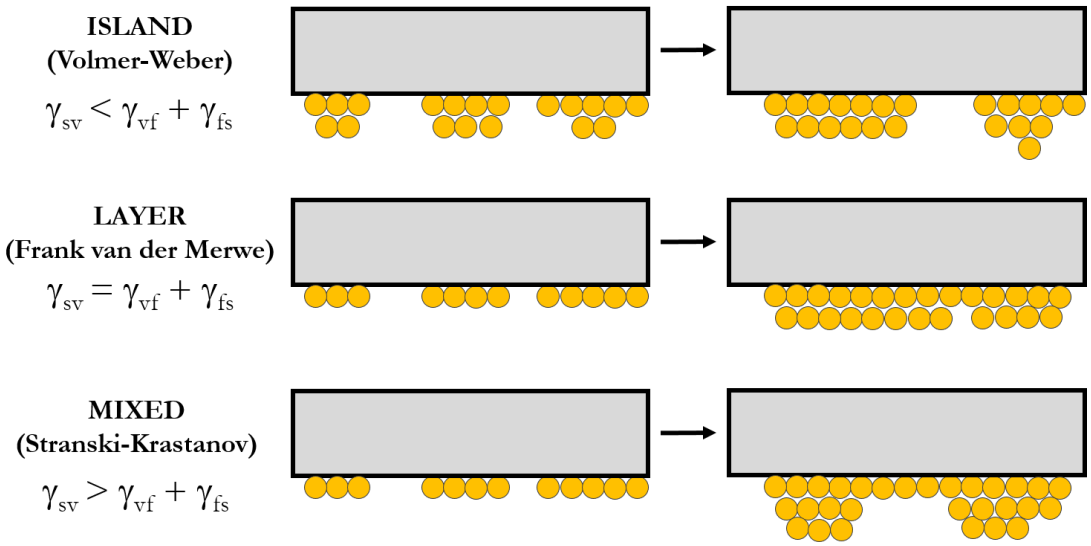


Figure 2.4: Film growth models, dependent upon surface energies between film, substrate, and vapor. Adapted from[88]

2.2 Magnetron Sputtering

My titanium nitride films are sputtered using a particular method called magnetron sputtering. Magnetron sputtering allows for faster sputtering of the target material. In this arrangement, a magnetron sputtering source is positioned beneath the sputtering target as in Figure 2.5. The magnetron sputtering source contains a magnet array which is embedded in the cathode and rests beneath the target holder.

As discussed earlier, during the sputtering process a voltage is introduced into the gas-filled chamber which creates a plasma. Some of the free electrons from the plasma ionize the neutral working gas

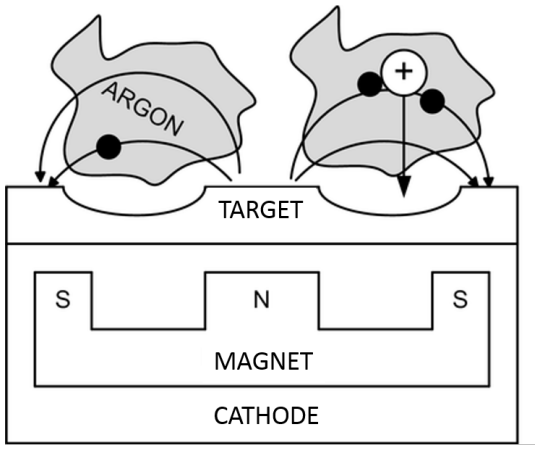


Figure 2.5: Magnetron sputtering source schematic. Adapted from [89]

atoms, in this case, Argon. The negatively charged cathode shown in the diagram attracts ionized Ar^+ atoms from the plasma towards the target. These ions which have a positive charge are accelerated towards the target/cathode and eject off material from the sputtering source target. When magnets are added beneath the sputtering target, they concentrate free electrons from the plasma close to the sputtering target. This high electron density causes an increase in the Ar ionization near the target surface and accordingly an increase in the sputtering rate.

Two examples of used 2" diameter Ti sputtering targets are shown in Figure 2.6. The circular magnet arrangement used in the magnetron guns in our sputtering chamber is very popular and causes the common "racetrack" target erosion pattern seen in the figures. This erosion pattern does not affect film quality however does decrease the overall usable area of each sputtering target. In general, the film uniformity depends mainly on the size of the target. Therefore, for a given target size there will be a given maximum area over which a uniform film can be sputtered. As a typical guideline, a high quality film can be uniformly deposited over a substrate with approximately twice the diameter of the sputtering target diameter. For example, to deposit a uniform film over a 4" wafer would require a geometry with an approx. 2" diameter target. Targets can however be fabricated in many shapes and

sizes. Industrial sputtering targets can be made incredibly large, often in more elliptical shapes with lengths up to 8 feet or more [90].



Figure 2.6: Titanium sputtering targets, diameter = 2". Both exhibit the classic "racetrack" erosion pattern due to the magnetron sources. The target on the right exhibits a golden color due to the formation of TiN on the surface during "reactive" sputtering in a mixed Ar and N_2 gas environment.

2.3 Reactive sputtering

Figure 2.6 also shows the effect that reactive sputtering can have on a sputtering target. Reactive sputtering is the process whereby instead of only inert noble gases (e.g. Ar, Ne, Xe) being backfilled into the vacuum chamber, additional reactive gases are also added. The "reactive" gases most commonly used in general are N_2 and O_2 however other gases such as CO_2, C_2H_2, CH_4 can also be used depending on the desired film material. Reactive sputtering allows multiple different films to be grown from a single target. For example, a pure Ti target could be used to sputter not only Ti films but also TiN with the addition of N_2 gas, TiO_2 with the addition of O_2 gas, or even TiO_xN_y. During reactive sputtering of TiN using pure Ti targets, the target can be passivated as shown by the golden color of the Ti target on the right-hand side of the figure. This happens when N atoms bind to the surface of the Ti target faster than they are being sputtered off. With careful control, reactive sputtering allows for complete control over the film composition and stoichiometry.

2.4 Control Parameters

Sputtering and in particular reactive sputtering allows for significant control over the stoichiometry, microstructure, and overall macroscopic film properties as compared to other thin film deposition methods. The variation of these properties depends on a wide range of parameters which I will separate into three main categories relating to the: target, chamber, and substrate.

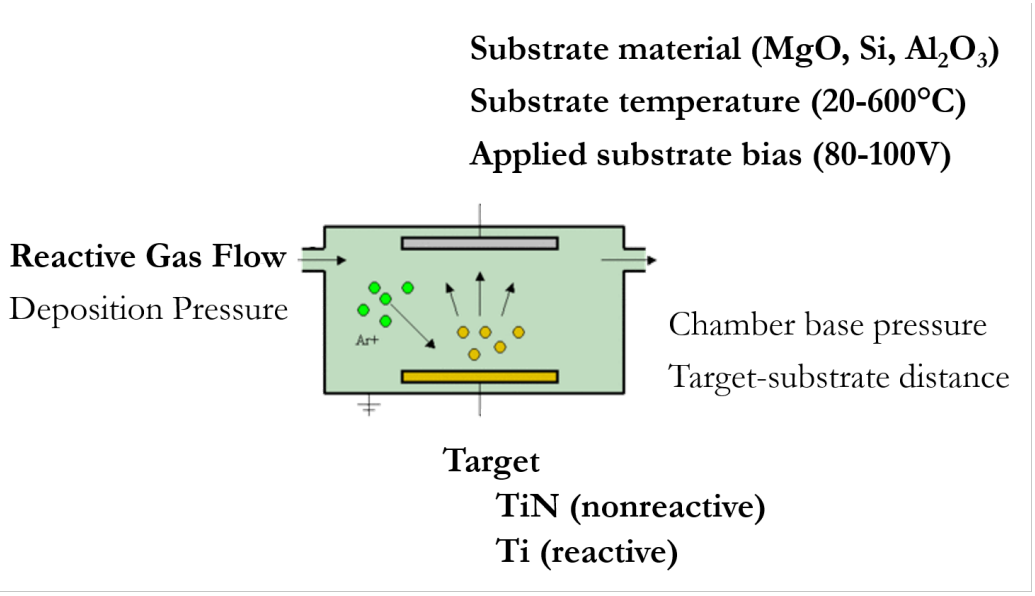


Figure 2.7: Schematic showing various sputtering parameters. The parameters studied most significantly in this thesis are highlighted in bold font with the particular ranges specified. Adapted from [86]

2.4.1 Target Parameters

In sputtering, the first choice is which sputtering target to use, mainly whether to sputter reactively or non-reactively. Non-reactive sputtering is in general easier since the target is made of the same material and stoichiometry as the desired film and only requires a single inert working gas species. Micro-structural control can still be achieved using non-reactive sputtering by adjusting the deposition pressure, substrate temperature or applied substrate bias. Reactive sputtering requires finer calibration

of the deposition conditions, but allows for significant control over not only the film microstructure but also the chemical composition and stoichiometry of the film.

Once a target is chosen, another important parameter which can affect the properties of the initial layers and subsequently the continued growth of a sputtered film is pre-sputtering of the target. Pre-sputtering the target involves sputtering the target prior to deposition to remove any surface contamination. For example, one reason to pre-sputter a target would be to remove surface oxide from a Ti or Si target. Pre-sputtering can either be done with a shutter covering the target or the substrate, or prior to loading the substrates into the chamber, dependent upon the chamber geometry.

In addition, whether a target is brand new or has been previously used can affect the deposition. This is important especially for targets which are compounds such as TiN, ITO, Si_3N_4, etc. as the stoichiometry of the target can change slightly as the target is used. For example, ITO is known to often have higher metallic content when the target has been used for some time as compared to new. In addition, if a single element target has been used under reactive sputtering conditions with different gases , longer lengths of pre-sputtering may be required to remove any contamination. Noting the color of the plasma in the chamber (or measuring the wavelength if your setup allows) is one way to ensure consistency since this is an indication of the consistency of the plasma.

2.4.2 Chamber Parameters

The second set of important parameters are those related to the chamber setup and geometry, many of which are fixed before sputtering. They are however important to consider as they may define limitations of a particular system for particular materials. These parameters include the base pressure, deposition pressure,and target-substrate distance.

The first factor is the base pressure of the chamber before deposition. Sputtering chambers can be used in the 10^{-6} Torr range though at these pressures, there are still about $10^{10} - 10^{11}$molecules per cm^3 (as compared to 10^{19} at atmospheric pressure). By using this pressure we can calculate the monolayer

time, or the time needed for a monolayer to deposit on a clean, gas-free substrate assuming that each molecule is able to find a binding site and successfully bind. At 10^{-6} Torr, the monolayer time is on the order of 10 seconds compared to about 10 milliseconds when the pressure is in the mTorr range [91]. At 10^{-9} Torr, which is a more highly recommended base pressure for sputtering highly reactive materials such as Ti, there are still about 10^7 molecules per cm^3, however this is 1000x less and mainly H_2 with only small amounts of CO, H_2O, CH_4 and CO_2, so a significant improvement would be seen in film quality [90]. In addition, the monolayer time at this ultra-high vacuum pressure is significantly extended to the order of a couple hours. Some ways to improve the base pressure of a system include using a load lock, using ion or cryogenic pumps in addition to the more common turbomolecular and roughing pumps, baking out the chamber, or long pre-sputtering using "getter" materials such as Ti.

While the base pressure of the chamber prior to backfilling with the inert working gas is critical to sputtering a high quality film with the minimum number of impurities, the deposition pressure also has a significant impact. To ignite and sustain a a plasma, generally requires pressures in the mTorr range (100mTorr for normal sputtering and about 10x lower or 1-10mTorr for magnetron sputtering). These relatively high pressures in comparison to the base pressures or pressures during other physical deposition techniques such as evaporation indicate that the mean free path (MFP) during sputtering can be quite short. The MFP can be calculated by [91]:

$$\mathrm{MFP} = \frac{1}{\sqrt{2}\pi d^2 n} = \frac{kT}{\sqrt{2}\pi d^2 p} = \frac{3.107x10^{-24}T}{d^2 p}$$

where, d = the molecular diameter (meters), n = the number of molecules per m^3, T = temperature (Kelvin), and p = pressure (Pascal). Assuming characteristic vacuum parameters, the MFP in the 10^{-6} Torr range would be approximately 10^4cm or 100m compared to about 100km for a pressure of 10^{-9} Torr. Interestingly, at deposition pressures in the mTorr range, the MFP drops significantly to the order of 10cm. Thus, dependent upon the exact deposition pressure used, the molecules being sputtered,

the temperature, and the target-substrate distance, the deposition may be dominated by either sputtered molecules which have more or less ballistically traveled from target to substrate or by molecules which have bounced off of other molecules/ions/chamber walls, etc. These interactions change the energy of the incident adatoms upon the substrate and thus changing the deposition pressure and/or the distance between the target and the substrate can have substantial impacts on the resulting sputtered film. In general, decreasing the deposition pressure decreases the number of ions and therefore the number of collisions, which increases the mean free path as can be seen in the equation.

2.4.3 Gas Flow Parameters

It is well-understood that the reactive gas purity, flow rates and injection location can also affect the sputtered film quality. The highest purity gases (e.g 99.9999% vs. 99.9% Ar) should be used to prevent impurities from being back-filled into the chamber. The base pressure may not be the limiting factor for impurity incorporation if the gas purity is an issue. In addition, as will be discussed in the following chapters, varying the flow rates of the working as compared to reactive gases can have a significant effect on the film microstructure during reactive sputtering as this varies the comparative flux of ions which physically interact with and atoms which react chemically with the target and substrate. For example, too much of a reactive gas can"poison" the target by depositing a layer on its surface and affect the sputtering conditions. The location at which reactive gases are injected into the plasma is also important. The working gas atoms can be ionized and de-ionized repetitively but the atoms that react chemically are only "used" once. Gas rings with small holes can be inserted around the cathode and in this way the gas can be evenly distributed into the plasma. In general, it is not advisable to have reactive gas inputs very close to the target since this leads to target passivation and can cause problems with arcing, etc. This is called target "passivation" or sometimes "poisoning." However, since "passivated" Ti in this case forms, TiN, a conductive material, this is not an issue. In the case of reactive sputtering of TiN in fact, injection close to the sputtering target is desired. Even if the Ti

target is poisioned with N_2 atoms, the TiN layer is still conductive, so DC sputtering can continue. In research chambers however, where insulating oxide surface contamination could cause problems, the gas is often not injected right at the target.

2.4.4 Substrate Parameters

In addition to the target, chamber and reactive gas parameters which have already been discussed, the substrates and several factors surrounding them also have significant influence over the resulting film properties and microstructure as will be shown in Chapters 4, 5, and 6. In general, the substrate material, including its crystal orientation can significantly affect the resulting properties of the sputtered film due to lattice match or mismatch, as may be expected. In addition, cooling or heating of the substrate, or application of a bias can have a large impact on the resulting film. In general, films sputtered at higher temperature will have larger, less porous grains than those sputtered at cooler temperatures. Application of a substrate bias (positive or negative, DC or RF) while sputtering is one of the easiest ways to significantly alter a wide range of film properties including resistivity, hardness, optical properties, etch rate, morphology, density, and adhesion. For metallic films, application of a bias has often shown decreased resistivity as well as increased metallic luster/reflectivity [88]. In addition, bias sputtering of the substrate *prior* to sputtering can remove surface oxides or contamination to expose a pristine surface layer for film growth and can also have significant effects on the initial layers of film growth.

2.5 Structure Zone Models

Sputter deposition involves many complex reactions and it is quite difficult to fully understand all of the details of these processes; however, structure zone diagrams (SZD) help us to qualitatively organize the expected microstructures of deposited films from porous to columnar to granular dependent upon several factors which can be controlled. The diagrams also offer suggestions for process adjustments

such as increasing temperature or adding a substrate bias, when we deposit films which have undesired properties. One of the most commonly used diagrams by Thornton [92], which refers specifically to the microstructure of sputtered films, includes two main axes affecting the film microstructure outcome: the deposition pressure and the fraction $\frac{T}{T_m}$. of the deposition temperature, T, relative to the melting temperature, T_m of the deposited film. His diagram posits that as $\frac{T}{T_m}$ increases, films tend to have lower porosity and larger grain sizes. See Figure 2.8. Thornton's model acknowledges that at the temperatures that we work with in our studies which are significantly lower than the melting temperature of TiN, there are several parameters which influence the surface morphology.

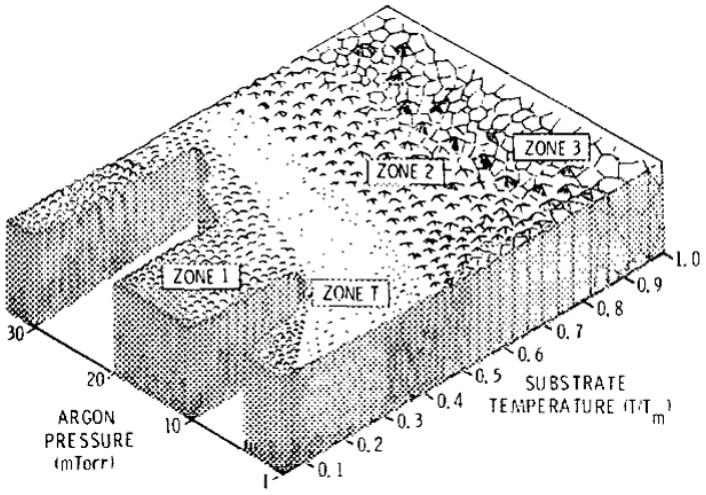


Figure 2.8: Thornton's Structure Zone Model. Reprinted with permission from [92]. Copyright 1986, American Vacuum Society.

A more recent structure zone diagram proposes that the Thornton axes be replaced by generalized temperature T* and normalized energy E* axes as shown in Figure 2.9 [93]. Anders' model suggests that the new E* axis include all parameters which contribute to the kinetic energy of ions arriving at the substrate, for example: deposition pressure, applied plasma voltage, and substrate bias. Due to the added bias, the adatoms have enough energy upon arrival at the substrate (which increases their mo-

bility) to rearrange on the surface. It is also interesting to note that Anders' generalized zone structure diagram suggests a small deposition parameter space where "low-temperature low-energy ion-assisted epitaxial growth" is possible. This correlates well with the recent advances in room-temperature ion-assisted sputtering of metallic TiN which were discussed at the beginning of this chapter.

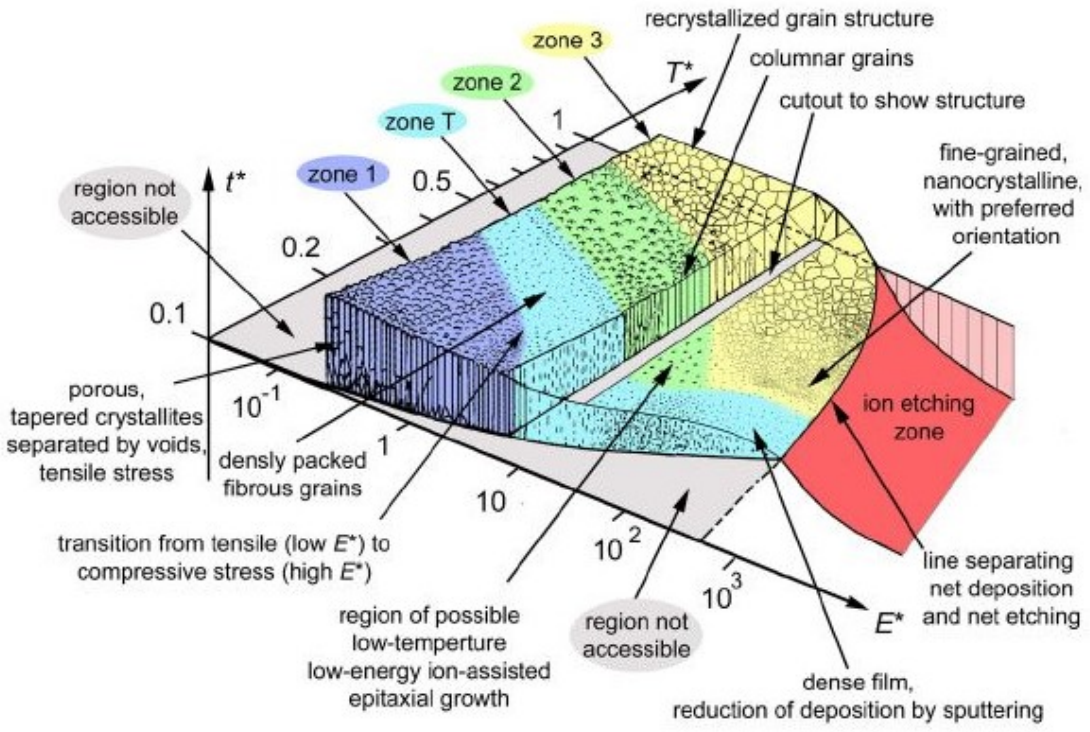


Figure 2.9: Anders' Revised Structure Zone Model. Reprinted from [93] with permission from Elsevier.

The TiO_xN_y films sputtered within our studies span across zone 1, zone T, and zone 2. To summarize the results which will be discussed in more detail in the coming chapters, TiO_xN_y films which we deposited at low temperature had low reflectivity, high resistivity and high oxygen incorporation. This high oxygen incorporation is potentially due to "zone 1 sputtering microstructure", meaning high film porosity. This porosity leads to less dense films and encourages oxidation not only during sputtering but also upon removal from vacuum to ambient. Our films sputtered at low temperature (less than

several hundred °C are always non-metallic unless additional energy is added during the deposition, such as a substrate bias. Our TiN films deposited at 600°C have small crystallites (< 50nm), high reflectivity, and low oxygen incorporation. These results are also supported by additional experiments from the literature [45, 61]. Upon examining the microstructure, we see that these films more closely correspond to the transition zone with tiny crystallites and zone 2 with columnar grain structure. The microstructure and chemical composition will be examined further in Chapters 5 and 6.

2.6 Experimental Setup

An AJA International, Inc. ATC 2200-V Confocal Sputtering System was used to deposit our TiN thin films in the Center for Nanoscale Systems (CNS), a member of the National Nanotechnology Coordinated Infrustructure Network (NNCI) and a part of Harvard University. The turbo-pumped sputtering chamber has a 22" diameter, 3 RF and 3 DC 2" magnetron sputter sources as well as the option to apply an additional substrate bias. In this system, the 6 magnetron guns are arranged in a circular pattern around the circumference of the chamber and are tilted towards the substrate holder which hangs inverted in the center of the chamber. This is often called a confocal sputtering setup. See Appendix B for more photos and details of the chamber setup. The system has a separate turbo-pumped loadlock which allows the main chamber to generally be kept in the 10^{-8} Torr pressure range.

Films were DC reactively magnetron sputtered using 2" diameter Ti targets in an AJA International ATC 2200-V load-locked turbo pumped sputtering system. To remove any residual surface oxide or contaminants from the Ti target, the target was pre-sputtered with the shutter closed until the voltage stabilized. A substrate heater controlled the temperature up to 600°C. The base pressure was less than 5×10^{-7} Torr after heating the substrate to 600°C and was in the 10^{-8} Torr range at room temperature. The deposition pressure was held constant at 4mT. The Ar: N_2 gas flow ratio was systematically varied from nitrogen-deficient 12:4 sccm to nitrogen-dense 8:12 sccm for the reactivelyf sputtered samples, monitored through mass flow controllers. For some films, as noted, a substrate bias of -80 to -100V

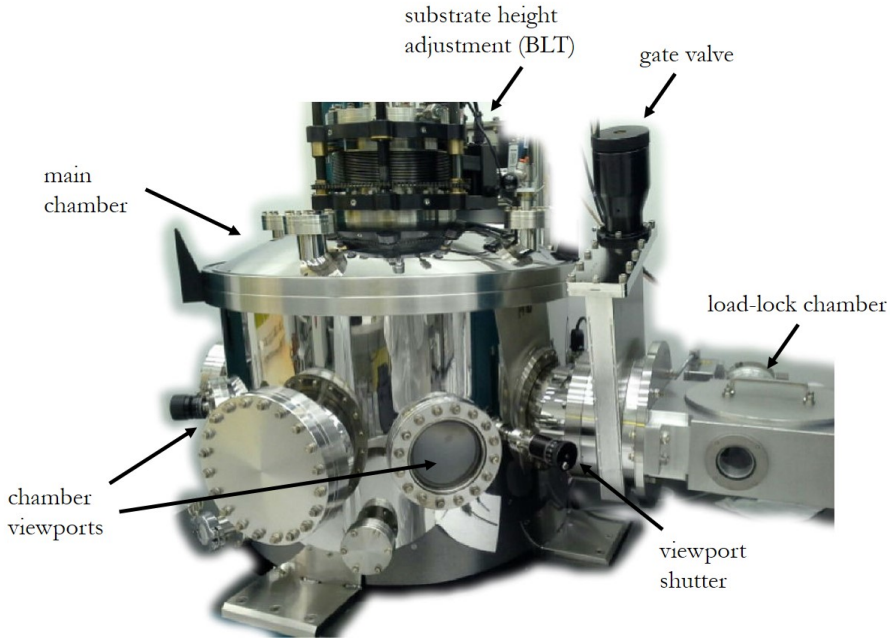


Figure 2.10: Labeled photograph of 6 target load locked magnetron sputtering chamber used to deposit TiN films. Substrate hangs inverted in the center of the chamber with height adjustable using BLT. Additional features (not shown): Turbo-molecular pump attached to back of main chamber. Second turbo pump for load-lock chamber. Magnetron sputtering guns mounted in circular confocal arrangement around the base of the main chamber.

was applied.

Additional films were non-reactively RF sputtered using a TiN target in a 40sccm Ar environment, with no N_2 gas flow. The optical properties of these non-reactively formed films were directly compared with those of the reactively sputtered films. The substrates included (100) MgO, c-plane sapphire, and (100) p-silicon. Before being loaded into the chamber, all substrates were sonicated in acetone followed by isopropyl alcohol and N_2 dried. Prior to this, Si substrates were additionally cleaned in a 49% HF dip with DI H_2O rinse and N_2 dry. The full set of standard operating procedures (SOP) has been included in Appendix B.

To limit oxidation, both Ti and TiN sputtering targets are stored in nitrogen boxes while not installed in the chamber. Upon insertion into the sputtering chamber and prior to sputter deposition,

the targets are pre-sputtered until the voltage stabilizes, for at least a minimum of 15 minutes. This serves the additional purpose of lowering the main chamber pressure due to the strong "gettering" properties of titanium.

In this arrangement, extremely slow growth rates were recorded of 0.65-0.75nm/minute or about 39-45nm/hour. Growth rates could be increased by choosing reactive sputtering over non-reactive sputtering, optimizing the target-substrate distance, or potentially increasing the sputtering voltage or adding a second sputtering target. As will be shown in the Chapter 5, significant oxygen incorporation is noted in the studied films. Increasing the sputtering rate should reduce the probability of oxygen contaminating the films. However, care must also be taken to make sure films sputtered more quickly are not too porous as denser films tend to exhibit lower resistivity and less oxygen incorporation. Initial sputtered films exhibited slightly faster deposition rates of about 50-60nm/hour. It was determined however that even though these films were deposited slightly faster, they had very significant (>30at%) oxygen content. Therefore, it is assumed that these films as-sputtered were porous and that upon removal from vacuum were oxidized from amorphous TiN to TiO_xN_y.

In summary, sputtering is a very useful but also complex process which allows for fine tuning of a deposited film's stoichiometry and microstructure due to the many knobs available to control. In this chapter, I have made an attempt to give a brief introduction to the method and describe some of these control knobs, as well as introduce some of the subtleties which I have discovered to have significant influence on the formation of TiN and TiO_xN_y thin films. For further details on sputtering, as well as on thin film growth and deposition techniques in general, I suggest "The Materials Science of Thin Films" by Ohring as an in-depth reference [88].

3

Modeling Thin Film Optical Properties

In Chapter 1.2 we discussed the properties of an ideal plasmonic material, namely high carrier concentration and low losses. We interpreted "high carrier concentration" as a significant free electron concentration, or $\varepsilon_1 < 0$, and "low losses" as $|\varepsilon_2| < |\varepsilon_1|$. We also noted that the "best" material will depend on the desired application and the wavelength regime of interest; therefore to assess whether a material qualifies as an acceptable plasmonic material, it is desirable to determine the optical constants as a function of wavelength over the regime of interest. This can be done using a technique called spectroscopic ellipsometry.

Spectroscopic ellipsometry is a relatively quick and sensitive method of assessing the optical properties of a material. However, the data provided via this method is through a modeling process which

is not always straightforward. The goal here is to strategically determine the main optical features within a film which contribute to the phase changes affecting the observed optical data. By using the ellipsometric data, together with strategic guesses concerning the material composition we can carry out a sensitive analysis of the material optical response (e.g. the real and imaginary components of ε). We can even fit non-homogeneous materials via this method which may have partial dielectric, partial metallic responses, an ideal tool and method for these kinds of unconventional plasmonic materials.

In this chapter, I will provide an overview of the spectroscopic ellipsometry (SE) method for non-invasively measuring the optical properties of thin films. A highly detailed discussion of this topic can be found in the "Guide to Using WVASE Spectroscopic Ellipsometry Data Acquisition and Analysis Software" by the J.A. Woollam Co., Inc. [94]. An additional recommended reference is Tompkins and McGahan [95]. At the end of this chapter, I will focus on the Drude-Lorentz model which is useful for modeling the optical constants of titanium nitride thin films specifically. Chapter 4 will discuss using SE to measure and compare the optical constants of TiN thin films deposited under many different sputtering conditions.

3.1 Properties of Light

Prior to describing the SE technique, I will describe the interaction of light with a multi-layered surface. Light is a form of electromagnetic energy and thus we begin with Maxwell's equations.

$$\overrightarrow{\nabla} \cdot \overrightarrow{E} = 0$$
$$\overrightarrow{\nabla} \cdot \overrightarrow{B} = 0$$
$$\overrightarrow{\nabla} \times \overrightarrow{E} + \frac{1}{c}\frac{\partial \overrightarrow{B}}{\partial t} = 0$$
$$\overrightarrow{\nabla} \times \overrightarrow{B} - \frac{\mu\varepsilon}{c}\frac{\partial \overrightarrow{E}}{\partial t} = 0$$

By combining these equations, one can arrive at the wave equation:

$$\overrightarrow{\bigtriangledown}^2 \overrightarrow{E} - \frac{\mu\varepsilon}{c^2}\frac{\partial^2 \overrightarrow{E}}{\partial t^2} = 0$$

Electromagnetic plane waves are one solution to the wave equation. In general form:

$$\overrightarrow{E}(\overrightarrow{r}, t) = \overrightarrow{E}_0 \exp(i\overrightarrow{q} \cdot \overrightarrow{r}))\exp(-i\omega t)$$

where $\overrightarrow{q} = 2\pi\widetilde{n}/\lambda$ is the wavevector along the direction of propagation, $\overrightarrow{r}$ is the position vector, $\widetilde{n} = n + ik$ is the complex refractive index as discussed in Chapter 1.2, λ is the wavelength of light, and ω is the frequency of light. Therefore, we can imagine light as a wave of oscillating electric and magnetic field components which satisfy Maxwell's equations. See Figure 3.1 for a snapshot in time depicting these components for a wave traveling along the z-direction. For a wave propagating along the z-direction, the wave equation simplifies to:

$$\overrightarrow{E}(z, t) = \begin{bmatrix} E_x \\ E_y \\ 0 \end{bmatrix} \exp(i(qz - \omega t))$$

3.1.1 Polarization

A characteristic of light waves which is extremely important in ellipsometric measurements is their polarization. The polarization state is defined by the direction along which the electric field points. For example, in Figure 3.1, the E-field oscillates back and forth between the +y and -y directions (up and down). Since the field remains within one plane, this would be considered a linear polarization state. In the typical Cartesian coordinate system, an electric field which oscillates along +x to -x will

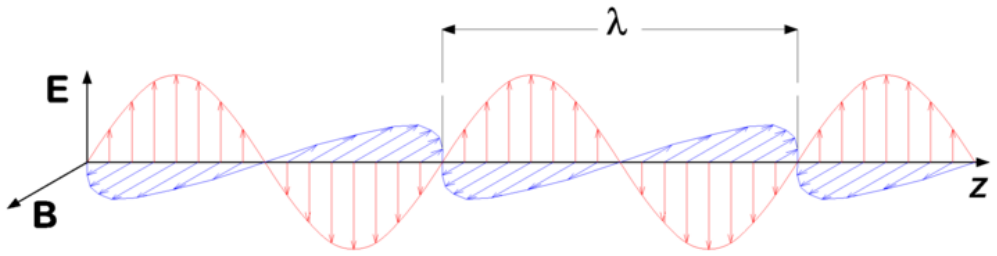


Figure 3.1: Representation of linearly polarized light as an electromagnetic plane wave traveling along the z-direction split into electric and magnetic field components depicted by the red and blue curves respectively. From [96]

generally be considered horizontally polarized and for an electric field oscillating between the +y and -y directions, the light will be considered vertically polarized. If there are both x and y-components but the E-field oscillations remain within one plane, the light is still linearly polarized.

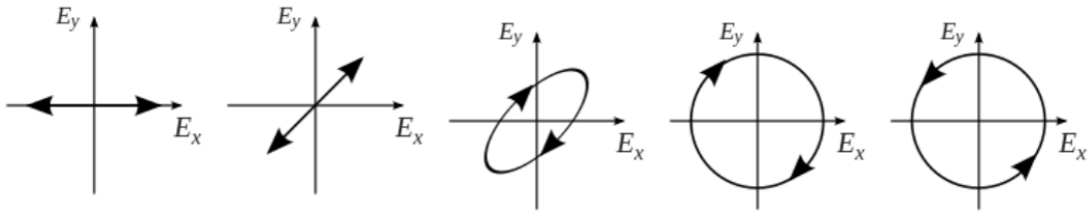


Figure 3.2: Representation of different electric field polarization states. From left to right: horizontal linear polarization, 45 ° linear polarization, elliptical polarization, left-hand circular polarization, right-hand circular polarization From [97]

Rather than oscillating within a single plane, the E-field can also oscillate along a curved path leading to either elliptical or circular polarization. Examples comparing how the electric fields look for circular as compared to linear and unpolarized states are depicted in Figures 3.2 and 3.3.

Rather than using the Cartesian (x,y,z) coordinate system, the polarization state can also be described using the s-p basis system. In this case, the p-direction is assumed to be the direction within the plane of incidence (the plane highlighted in Figure 3.6) and also perpendicular to the direction of propagation. The s-direction is also perpendicular to the plane of incidence however is parallel to the

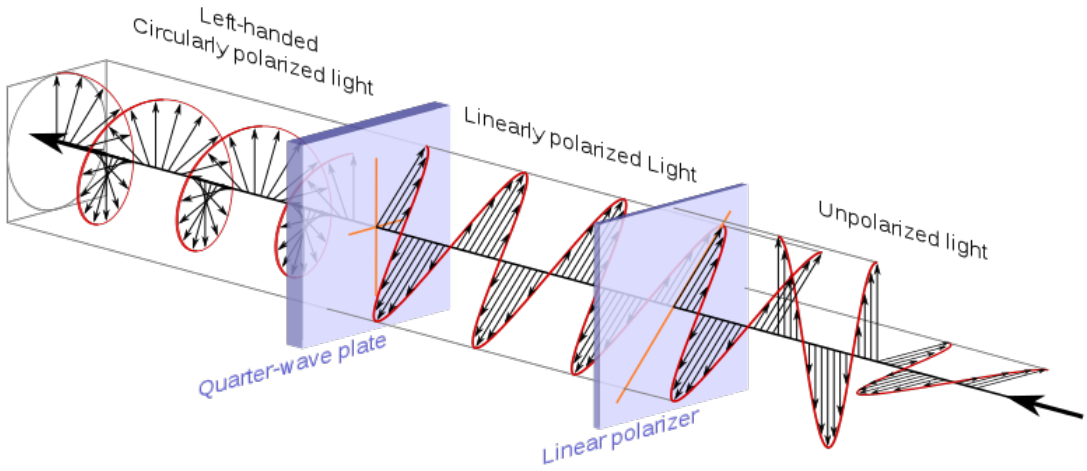


Figure 3.3: 3D representation of different electric field polarization states as an incident beam begins unpolarized, passes through a linear polarizer and then through a quarter-wave plate to become circularly polarized. From [98]

surface of the sample. Again, these directions refer to the direction in which the electric field points. Thus, you will often hear light referred to as having"p-plane" or "s-plane" polarization. Two examples are shown in Figure 3.6 with arrows denoting the s and p-directions at two particular points.

The basics of polarization are important to understand in ellipsometry because the reflection of a beam of light at an interface depends upon both the polarization as well as the angle of incidence, with the angle of incidence defined as the angle between the sample normal and the direction of the incident beam. For this reason, you will often see reflectance noted in terms of these two polarizations, R_p and R_s which will be further discussed in the next section.

3.1.2 Fresnel Reflection Coefficients

The Fresnel reflection coefficients compare the relative ratios of polarized reflected and transmitted light compared to the incident waves.

$$\widetilde{r_p} = \frac{\widetilde{E_p}^{reflected}}{\widetilde{E_p}^{incident}}$$
$$\widetilde{r_s} = \frac{\widetilde{E_s}^{reflected}}{\widetilde{E_s}^{incident}}$$
$$\widetilde{t_p} = \frac{\widetilde{E_p}^{transmitted}}{\widetilde{E_p}^{incident}}$$
$$\widetilde{t_s} = \frac{\widetilde{E_s}^{transmitted}}{\widetilde{E_s}^{incident}}$$

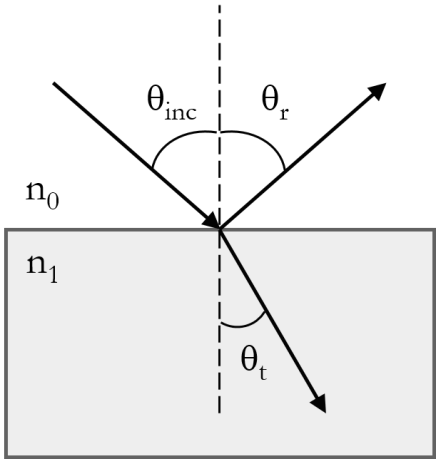


Figure 3.4: Representation of Snell's law showing an incident light beam and reflected and transmitted beams at an interface between two materials with refractive indices, n_0 and n_1

By combining these equations with Maxwell's equations, the correct boundary conditions, and Snell's law (as depicted in Figure 3.4), we can re-write them in the following form:

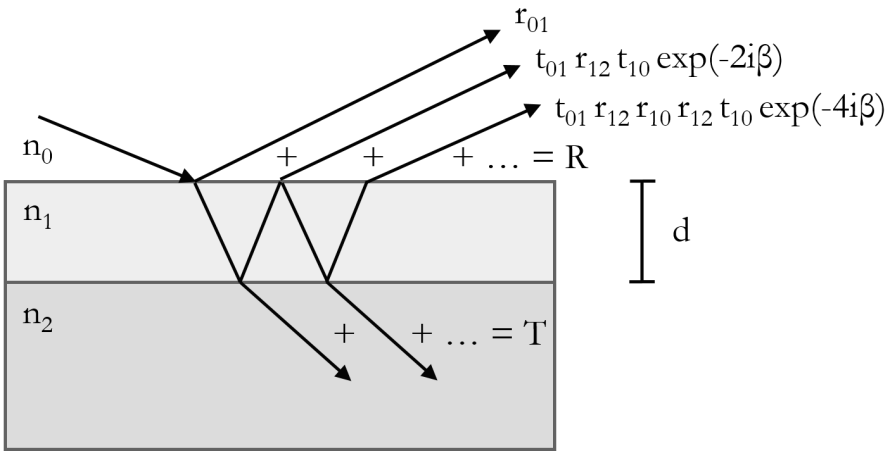


Figure 3.5: Representation of Fresnel reflection and transmission coefficients for multiple layers of films.

$$\widetilde{r_p} = \frac{\widetilde{n_1}\cos(\theta_{inc}) - \widetilde{n_0}\cos(\theta_t)}{\widetilde{n_1}\cos(\theta_{inc}) + \widetilde{n_0}\cos(\theta_t)}$$
$$\widetilde{r_s} = \frac{\widetilde{n_0}\cos(\theta_{inc}) - \widetilde{n_1}\cos(\theta_t)}{\widetilde{n_0}\cos(\theta_{inc}) + \widetilde{n_1}\cos(\theta_t)}$$
$$\widetilde{t_p} = \frac{2\widetilde{n_0}\cos(\theta_{inc})}{\widetilde{n_1}\cos(\theta_{inc}) + \widetilde{n_0}\cos(\theta_t)}$$
$$\widetilde{t_s} = \frac{2\widetilde{n_0}\cos(\theta_{inc})}{\widetilde{n_0}\cos(\theta_{inc}) + \widetilde{n_1}\cos(\theta_t)}$$

These Fresnel reflection and transmission coefficients describe what happens to the light at one interface. If multiple interfaces and multiple reflections occur such as seen in Figure 3.5, the coefficients hold for each interface but must be multiplied along with an additional phase factor due to accumulated phase along the added path lengths. In this figure, t_{12} for example, refers to the transmission coefficient for light with incidence from medium 1 through the interface at medium 2 and r_{12} refers to the reflection coefficient for light with incidence from medium 1 upon reaching the interface at medium 2. The overall reflectance and transmittance include contributions from all possible paths with the intensity decaying exponentially, dependent upon the absorption as the path lengths increase. The β phase factor is determined by the film thickness d and can be written as $\beta = 2\pi d n_1/\lambda\cos(\theta_t)$.

Reflectance is measured in terms of an intensity and is therefore calculated using the square of the field intensity. The s and p-reflectances can therefore be calculated from the Fresnel coefficients in the following way:

$$R_p = \left|\widetilde{r}_p\right|^2$$

$$R_s = \left|\widetilde{r}_s\right|^2$$

Ellipsometry measures the ratio of these components as discussed in the following section. For more detail on Snell's law and Fresnel reflection, see section 2.10 of the WVASE guide [94], Yariv & Yeh [99] or other introductory electricity and magnetism books.

3.2 Spectroscopic Ellipsometry Overview

Ellipsometry is an optical characterization technique which can be used to determine the thickness and/or optical constants of a thin film or layers of thin films. During ellipsometry measurements, a beam of polarized light is reflected off of or transmitted through a sample and the relative amplitude and phase change ratios in the beam of reflected light are measured. A diagram depicting this process is shown in Figure 3.6. The technique used in this work, spectroscopic ellipsometry, is a particular type of ellipsometry in which the wavelength of the incident beam is varied and the response measured to determine the optical properties of a material over a range of frequencies.

The strength of ellipsometry measurements over intensity reflectance measurements is the measurement of both the relative change in amplitude and also the relative change in phase. We define Δ as the difference in phase before and after reflection which can vary from -180° to +180°. There will also be a difference in phase in different polarizations. For example, assuming an s-p basis, let δ_1 be the phase difference in the s-polarized light and let δ_2 be the phase difference in the p-polarized light. Then,

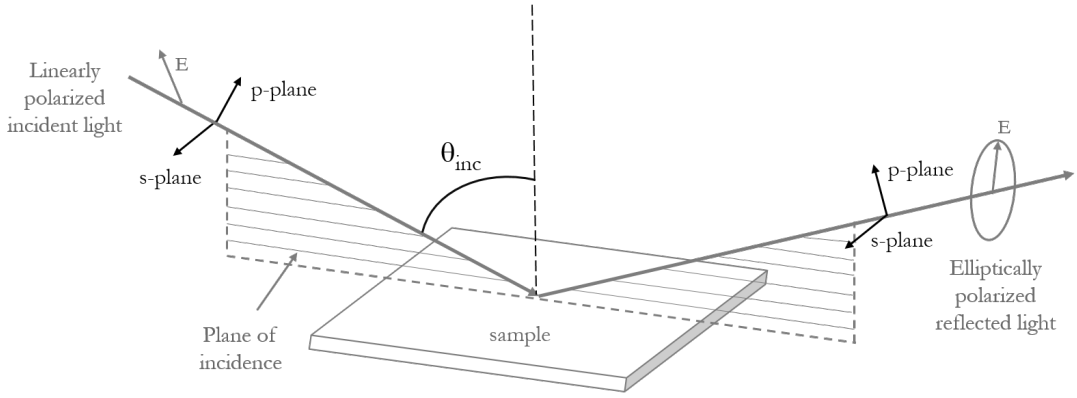


Figure 3.6: General ellipsometry schematic. Linearly polarized light is incident upon a reflective thin film sample. Both the phase and intensity of the reflected, ellipsometrically polarized light are measured.

$$\Delta = \delta_1 - \delta_2$$

As discussed in the previous section, the different polarizations of light will also have different reflectances. The ratio of their amplitudes can be measured by the system. We define a parameter ψ such that

$$\tan(\psi) = \frac{\left|\widetilde{R}_p\right|}{\left|\widetilde{R}_s\right|}$$

where $\widetilde{R_p}$ and $\widetilde{R_p}$ are the Fresnel reflection coefficients. In this case ψ is an angle which can range from zero to 90°. When the amplitudes are close in amplitude $\tan(\psi) \approx 1$ which means $\psi \approx 45°$. Thus, for a material such as TiN which becomes highly reflective for wavelengths longer than ≈ 600nm, we expect ψ to approach 45°.

Adding together the phase and amplitude information, gives the fundamental equation of ellipsometry (ρ, a complex-valued parameter). In this equation, $\tan(\psi)$ corresponds to the real part and $\exp(i\Delta)$ to the phase.

$$\widetilde{\rho} = \frac{\widetilde{R}_p}{\widetilde{R}_s} = \tan(\psi)e^{i\Delta}$$

It is important to note that the values which are measured in ellipsometry are ψ and Δ. Since these values are measured, they are therefore "correct" within experimental error. These values however are not the final desired results, e.g. film thickness, optical constants, roughness, etc. The validity of the final results depends upon the quality of the data analysis following the measurement. The modeling process and how to determine whether a model has given "good" results will be discussed in the remainder of this chapter.

3.3 Experimental Setup

A Woollam WVASE32 vertical angle spectroscopic ellipsometer by the J.A. Woollam Company, Inc. was used to optically characterize our TiN thin films in the Center for Nanoscale Systems (CNS), a member of the National Nanotechnology Coordinated Infrastructure Network (NNCI) and a part of Harvard University. The tool is a rotating analyzer ellipsometer with a spectral range from deep UV to near-IR (193 - 1700nm) wavelengths, achieved via a Xenon arc lamp. The system has known fixed input polarization and the analyzer continuously rotates to measure output polarization. Multi-mode fibers are used to send light from the HS-190 75 W light source and high speed monochromator system to the sample. The light spot is collimated and approximately 2-3mm in diameter. Focusing attachments are available for the system which can decrease the spot size to 200 microns but were not used in this work. Stacked solid state detectors collect the light, a Si detector from 185-1100nm and an InGaAs detector from 800-1700nm. A goniometer base is present for automatic and precise control of the angle from 20° to grazing angles of incidence. A double monochromator is present to reduce stray light and allow measurements to be made under ambient lighting. A rotating analyzer with AutoRetarder® can be used for measurement of depolarization or anisotropic samples with high

accuracy, however it was found that for TiN thin films there is very little depolarization or anisotropy so this measurement was not needed. The experimental process for taking SE data for TiN thin films can be found in Appendix C.

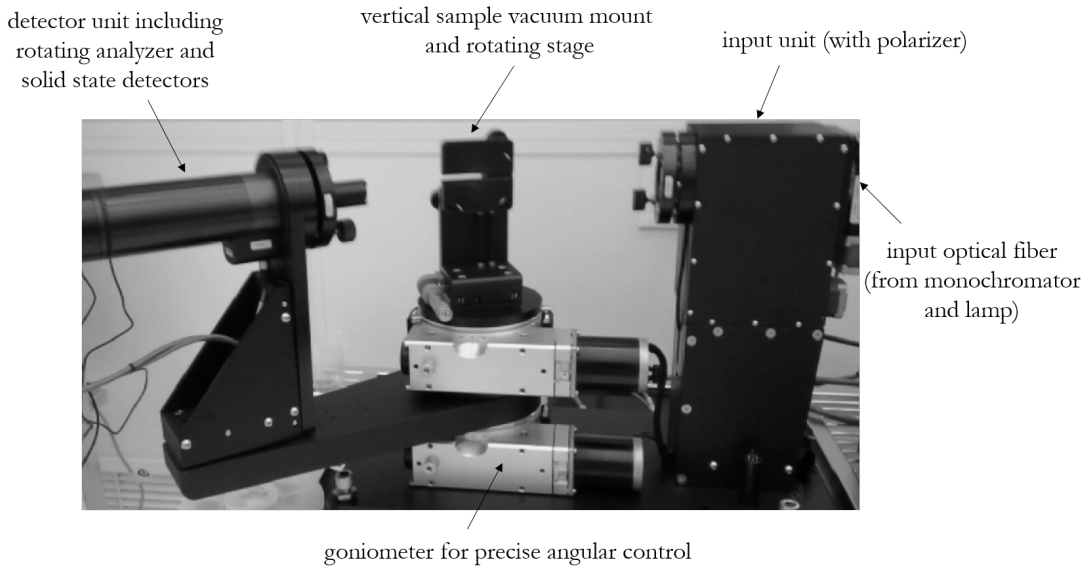


Figure 3.7: Experimental setup: J.A. Woollam WVASE Spectroscopic Ellipsometer

3.4 Ellipsometric Data Analysis and Modeling Process

The first step in measuring the optical constants and thickness of a film using ellipsometry is to collect ellipsometry data over the desired frequency range. This will provide the raw data ψ and Δ as a function of wavelength and incident angle. After data collection, an initial physical model describing the sample must be created in the analysis software. This first model should include the substrate, any native oxides or interface layers which are known or can be assumed, and any thin film layers. It is important to have good starting guesses of the values for both the thicknesses and optical constants of each of these layers. Therefore, any information which can be determined via other measurement techniques (e.g. profilometry, XRD, AFM, etc.) will be useful to have at this point to choose which

parameters to fix and which to fit and also to understand the ranges which are acceptable for various parameters. Generally, this initial model will give a good starting point but will not correctly model all of the complexities of the measured sample.

After the model has been created, the data analysis software can be used to generate expected ψ and Δ based on the thicknesses and optical constants of the layers in the model using the Fresnel coefficients and multi-layer reflection and transmission theory discussed earlier. If the generated results from the model look relatively close to the measured data, regression fitting algorithms can be used to adjust the fit parameters and minimize the error. At this point, initial results such as layer thicknesses and optical constants will be available. It is important to note however, that the process is not yet finished. It is very important to first analyze the quality of the results found and whether they make sense. After analyzing the results and fit quality, the model will generally be adjusted and the data re-fit as necessary to provide new results until the agreement is reached between the physical model and measured data. This iterative process is shown graphically in Figure 3.8. The process of assessing the quality of a model is discussed further in Section 3.6.

3.5 Drude-Lorentz Model for Modeling TiN Thin Films

As described in Chapter 1, the dielectric constant or permittivity is a material property that describes how light interacts with the electrons within a material. The way in which these electrons are bound in the material depends on the type of material. Common categories of materials are metals, dielectrics, and semiconductors. There are several common parameterized models which can be used to represent the optical properties of these materials. Parameterizing measured data by using these models allows for adjustment of only a few fit parameters rather than fitting the data at each frequency point by point. For absorbing materials, using these models also assures that the resulting optical constants are Kramers-Kronig consistent (meaning ε_1 is dependent upon ε_2 as defined by Equation (3.1) where P is the Cauchy principal value and E is the frequency or energy in eV [94]. There are many models which

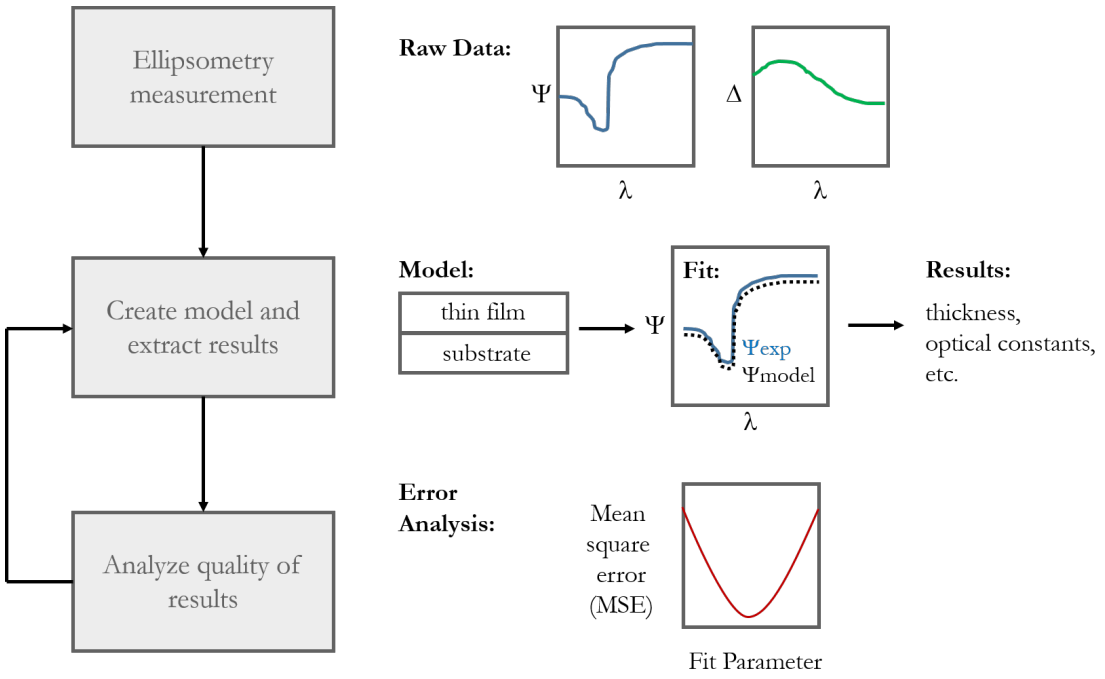


Figure 3.8: Process flow for spectroscopic ellipsometry data measurement and analysis to extract results. The analysis and modeling process should be repeated as necessary until a high quality model is attained.

aim to mathematically describe the nature of these bonds. The most commonly used models will be discussed here.

$$\varepsilon_1(E) - 1 = \frac{2}{\pi} P \int_0^\infty \frac{E' \varepsilon_2(E')}{E'^2 - E^2} dE' \tag{3.1}$$

Dielectric materials such as SiO_2 generally have a real part of the permittivity ε_1 which is positive and relatively constant over a wide range of wavelengths and an imaginary part ε_2 which is close to zero, an indication that the optical losses are small as seen in Figure 1.5. This type of behavior can be modeled by the Cauchy equation where A, B, and C are fit parameters. This is one of the most commonly used ellipsometric models for non-absorbing materials. This model can also be used to determine the thickness of an absorbing material if there is a frequency regime over which that material is not

absorbing.

$$n(\lambda) = A + \frac{B}{\lambda^2} + \frac{C}{\lambda^4} + ...$$

For absorbing materials, a standard Lorentzian (mass on a spring) damped oscillator model can be used. The form of the Lorentz equation used in our models:

$$\varepsilon_{n,\text{Lorentz}} = \varepsilon_{\text{offset}} + \frac{A_n B_n E_c}{E_c^2 - E^2 - iB_n E}$$

exhibits three main fit parameters for each oscillator, n. These are the amplitude (A_n, dimensionless), broadening (B_n, eV), and the center energy (E_c, eV). In addition, the residual dielectric constant ($\varepsilon_{\text{offset}}$, eV) can add a constant value to the ε_1 curve. In the mass-on-a-spring model, the damping constant, γ has a similar effect as the broadening constant, B, in this version of he equation. The typical shape of this curve is plotted in Figure 3.9 with the fit parameters specified. The typical Lorentzian bell-type curve models the absorption (thus ε_2, the imaginary part of the equation shown) and the real part of the equation models the corresponding Kramers-Kronig consistent ε_1. Figures 3.10 and 3.11 demonstrate examples of how these fit parameters can be manipulated strategically to shift and stretch to fit a given optical function.

The Drude model is typically used to represent ideal metals. It is a simplification of the Lorentz model. Because the electrons in a metal are free rather than bound, the restoring force disappears. In terms of our model, this means the peak center energy E_c is close to zero eV and thus drops out of the equation. This can also be seen in Figure 3.12 which compares the shape of the Drude and Lorentzian models in terms of the optical constants.

$$\varepsilon_{n,\text{Drude}} = -\frac{A_n B_n}{E^2 + iB_n E}$$

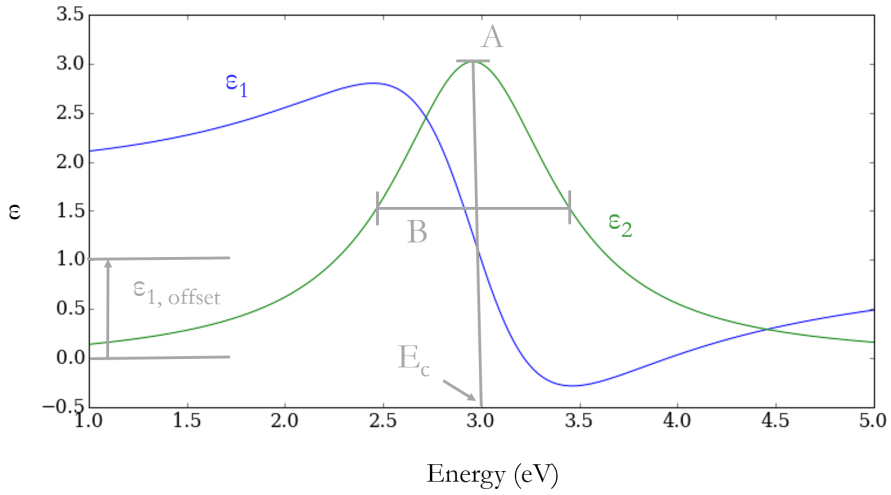


Figure 3.9: Lorentz oscillators with fit parameters labeled

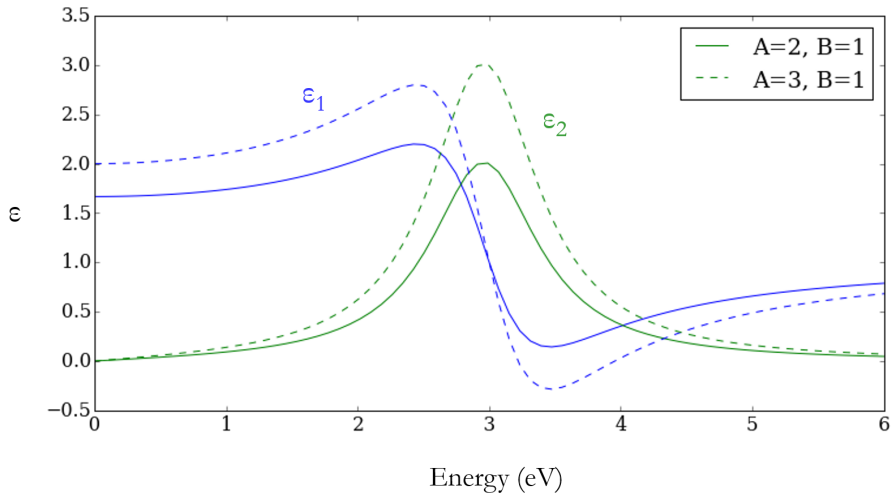


Figure 3.10: Two Lorentz oscillator examples showing fit parameters for amplitude (A), broadening (B), center energy (E_c) and the residual dielectric constant offset, ε_{offset}. Both oscillators have B=1,E_c=3eV, and ε_{offset}=1 however differing amplitudes A=2 and A=3 show how increasing the amplitude of the resonator increases the absorption ε_2.

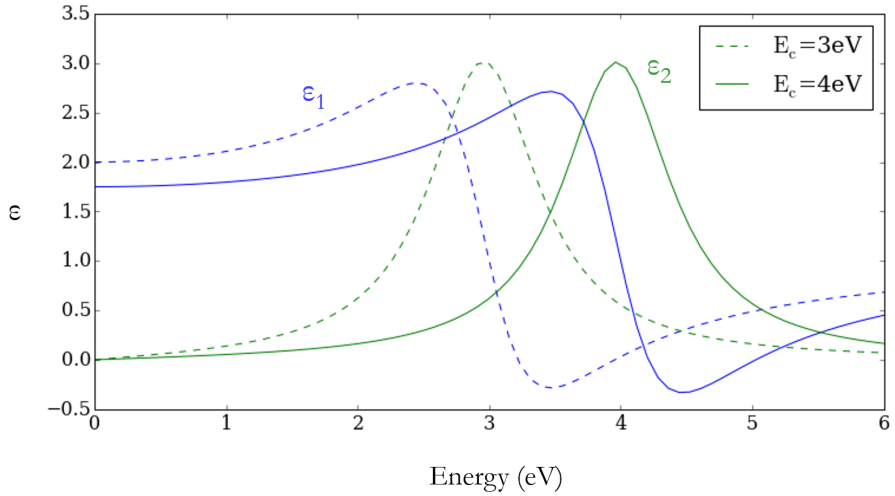


Figure 3.11: Comparison of two Lorentz oscillators with the same fit parameters A=3, B=1, and ε_{offset}=1 but different center energies E_c =3eV and 4eV

The Drude model exhibits therefore only two fit parameters (A_n and B_n), as a function of E (units = eV.) The fit parameter A_n is related to the plasma energy by $A_n = \varepsilon_\infty E_p^2$ where E_p is the energy of the plasma frequency as defined in Chapter 1 and ε_∞ is ε_{offset} far from the region of interest. In addition to ideal metals, some transparent conducting oxides (TCOs) can potentially be well-modeled using a Drude term, for example metallic indium-tin-oxide (ITO) in the visible to near-IR regime.

In many materials however, a single Drude term is not enough to fully describe the optical behavior. Highly metallic and conductive TiN behaves as one would expect for a more typical metal. Throughout the visible and into the near-infrared frequency range, the optical behavior can be modeled by a combination of a single Drude component representing the free d-band electrons and two Lorentzians at higher energies within the short visible to ultra-violet range which are thought to represent inter-band transitions similar to those exhibited by gold [48, 100–102]. An example of a moderately metallic TiN film which can be modeled via these three components is shown in Figure 3.13. Table 3.1 shows the sample fit parameters used in this reference example. Note that only the imaginary part of the permittivity, ε_2 is shown in Figure 3.13 for clarity with the three individual components in green and

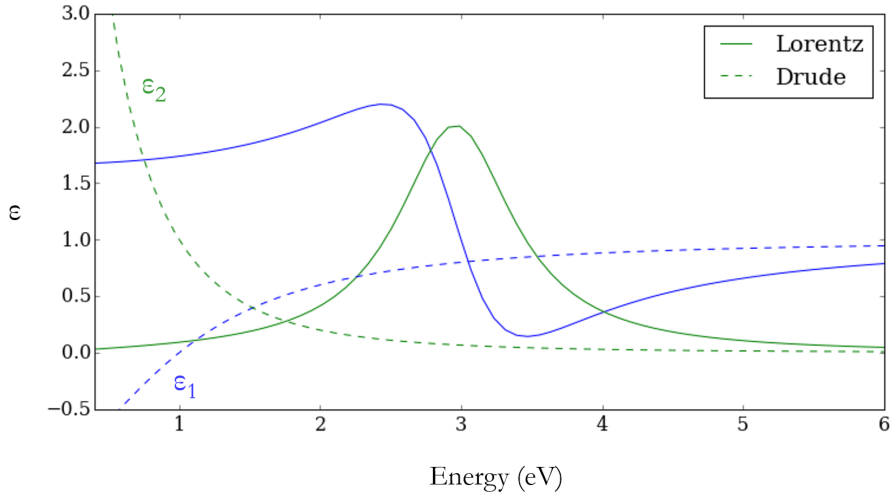


Figure 3.12: Comparison of Lorentz oscillator with fit parameters A=2, B=1, E_c=3eV and ε_{offset}=1 and Drude component with fit parameters A=2, B=1, and ε_{offset}=1

the sum of all components in black. Figure 3.14 shows the corresponding real components.

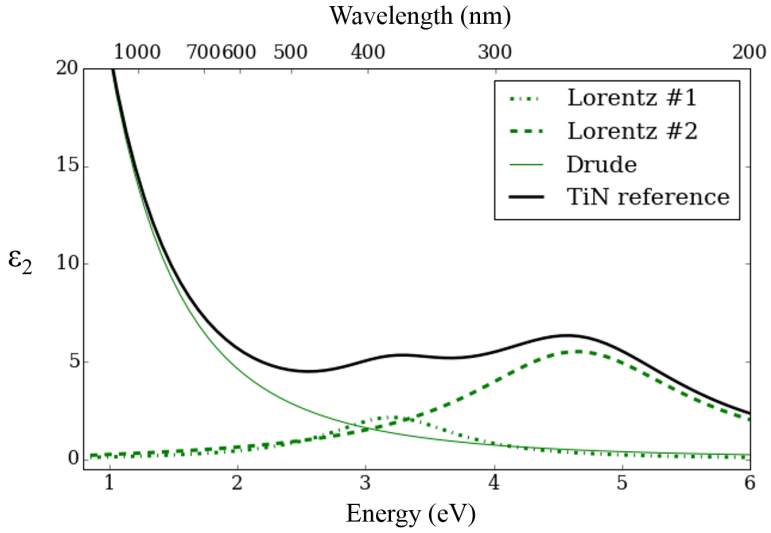


Figure 3.13: TiN reference (black) for ε_2 fit by one Drude (green solid) and two Lorentzians (green dashed)

This type of parameterized modeling of WVASE SE data can be accomplished in the WVASE software by building a "General oscillator model" with one Drude and two Lorentzian oscillators from a

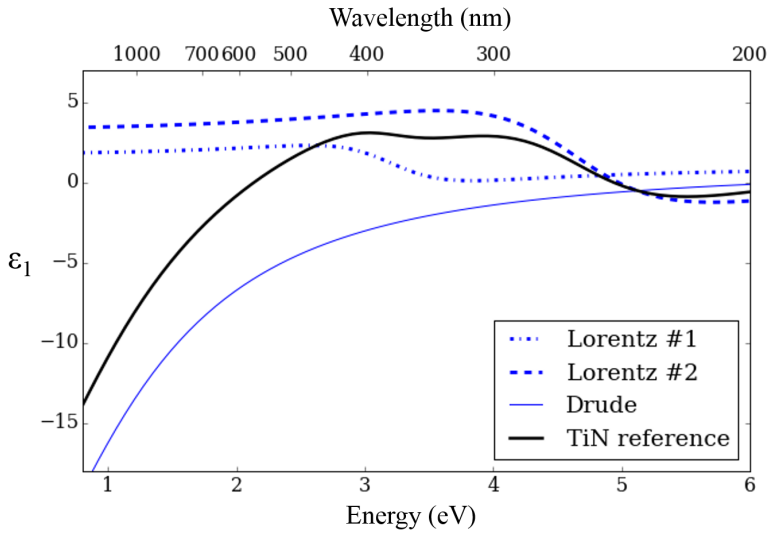


Figure 3.14: TiN reference (black) for ε_1 fit by one Drude (blue solid) and two Lorentzians (blue dashed)

Fit Parameter	Drude	Lorentz #1	Lorentz #2
A	35.0	2.12	5.4391
B (eV)	1.2	1.2472	2.0849
E_c(eV)	-	3.2636	4.761

Table 3.1: TiN Reference Example: Ellipsometry Fit Parameters

reference TiN spectra and then adjusting the fit parameters as necessary to get high quality results as discussed theoretically in this chapter. The details of how to create this type of model in the WVASE software are explained well in Chapter 8 of the Woollam manual [94].

3.6 Evaluation of an SE Model

Finally, it has been mentioned several times that the optical constants and thickness derived from ellipsometric measurements are not measured directly, but rather are the product of creating a model of the measured sample and deriving results from that model. Therefore, it is important to not hastily trust results derived from the first model used without first verifying that the model is indeed "cor-

rect". The first step in this process is to check the fit. Compare the data generated from the model with the experimental data. Do they look similar "by eye"? Quantitatively, the goodness of the fit can be checked by looking at the mean squared error (MSE). In the data fitting process, regression analysis is used to fit the data and the Levenberg-Marquardt algorithm [103] is used to find the minimum MSE. It is important to check if the MSE is low enough at this point. The minimization algorithm may have ended up in a local rather than global minimum due to not having the best starting value or the model may need additional complexity added to fully capture the most important features (e.g. surface roughness, grading, anistropy, etc).

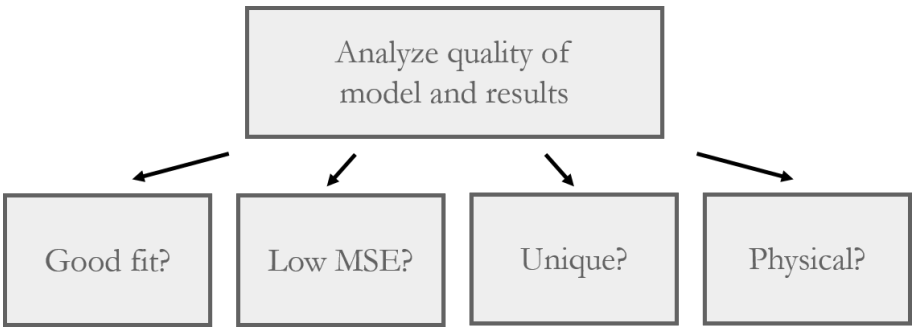


Figure 3.15: Main parameters to consider when analyzing the quality of a fit to SE data

In addition, a more subtle modeling challenge is the determination of whether a model is unique. Unique in this sense refers to the idea that multiple models could have a similar "goodness of fit" by eye and similar MSE values. This is often due to correlation between multiple parameters or overfitting of data. Therefore a uniqueness test should be done to find the minimum number of parameters needed to achieve the same quality of fit. For example, a standard uniqueness test to run for a thin, absorbing film such as TiN would be to vary the thickness of the film while allowing the optical model to be freely fit and plot the MSE values of each fit as a function of the film thickness. There should be a minimum to the curve corresponding to the actual film thickness as shown in the example in Figure 3.8. If the curve is flat rather than parabolic in shape, this means there are many 'equally good'

models and therefore, the model is not unique. Finally, once a model is determined to be a good fit, it should also be confirmed that the results are indeed physical. For example, is the model Kramers-Kronig consistent? Is there normal dispersion? As a specific example, for transparent materials, as λ increases, the index of refraction should always decrease. If it increases, the model is not physical and cannot be correct.

An ellipsometric model is just that, a model. The MSE will never be exactly zero and the model will never be perfect. The goal is to create a model which correctly captures the main optical features of the film which contribute to phase changes and thus affect the ellipsometric data. As described earlier, this is an iterative process so the best ways to get the correct data are practice and patience. For more details see Chapter 9 of Tompkins and McGahan [95] or Chapter 13 of the WVASE Guide [94].

Acknowledgements

I would like to specifically thank Nina Hong, Ph.D. from J.A. Woollam Co., Inc. for many helpful discussions, web conferences, and emails on the subtleties of both ellipsometric measurement and modeling. Her suggestions were instrumental in my understanding of the SE technique.

4

Correlation of Deposition Conditions with Optical and Electrical Properties of Sputtered ITO, TiO_xN_y, and TiN Films

The general method of characterizing the optical properties of a sputtered thin film via spectroscopic ellipsometry (SE) was well-described in the previous chapter. In this chapter, the deposition conditions are correlated with these optical models. In addition, the optical models are compared to electrical measurements to further verify their validity.

This chapter is split into three main sections. First, indium tin oxide (ITO) will be discussed due to both the vast collection of previous work on this material and also due to the comparative simplicity of the optical models [104–109]. Next, titanium oxynitrides (TiO_xN_y) will be discussed as interest in them has recently begun to be piqued within the optical realm [110] for applications where absorption can be beneficial (e.g. solar cells [111, 112] and glazed coatings [113].) Finally, more metallic TiN will be discussed in detail in the remainder of the chapter with the focus on describing the critical deposition conditions necessary to maximize the 'metallic character' of these films for plasmonic applications.

4.1 Indium Tin Oxide (ITO)

Sputtered indium tin oxide (ITO) is an example of a doped transparent conducting oxide (TCO). As the carrier concentration (doping) of the film changes, the electrical and optical properties of the film change [105, 109, 114]. We have confirmed that by varying the sputtering conditions, we can control the carrier concentration. This renders the optical properties of ITO as widely tunable as shown in Figure 4.1. As can be seen in the figure, increased substrate temperature during sputter deposition

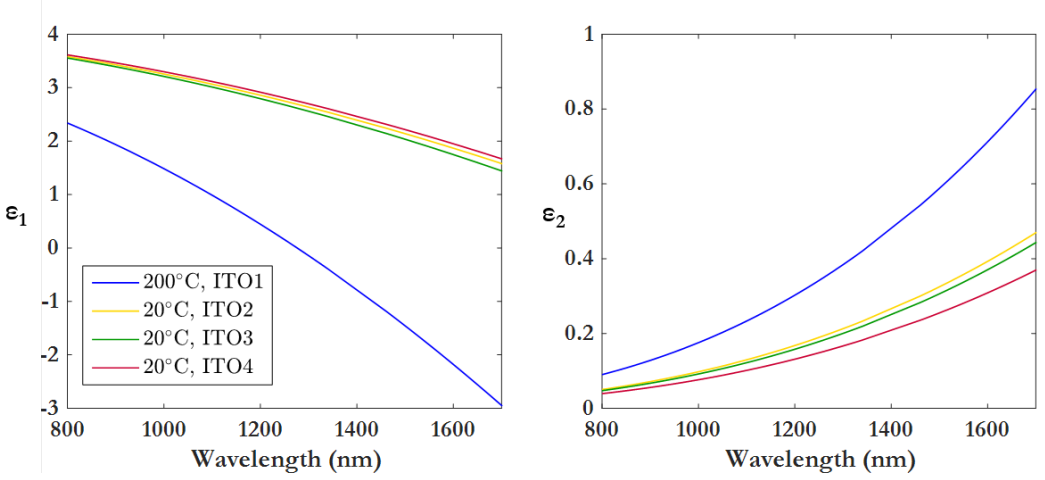


Figure 4.1: By changing the sputtering conditions, the conductivity and optical properties of ITO are tunable. Increasing the substrate temperature during deposition shifts the plasma frequency to shorter near-IR wavelengths.

results in increased metallic character of the films but with increased losses. In more comprehensive studies, the plasma frequency has been tuned throughout the near-IR wavelength regime mainly by controlling the substrate deposition temperature or by post-deposition annealing [107, 109]. Similar results were seen in this study. All films in this study were sputtered non-reactively at 3mT deposition pressure and with 60W RF power. The detailed deposition conditions for these films can be found in Appendix A.

Table 4.1 shows the Drude-Lorentz ellipsometric model parameters using the format as specified in Equation (4.1) for the data plotted in Figure 4.1. The parameters are compared for 4 different sputtered films (labeled ITO1-4). For each film, several ellipsometric models consisting of either a Drude term plus Lorentz term as shown in the equation or only a Drude term were compared.

Sample	Range	ε_{offset}	Drude		Lorentz			Thickness	MSE
			A_D	B_D	A_L	B_L	E_c	(nm)	
ITO1 model2	800-1700	3.87	3.68	0.09	-	-	-	134.6	44.6
ITO2 model4	400-1700	3.45	1.38	0.13	2.61	0.14	4.14	86.5	5.5
ITO2 model5	400-1700	4.42	1.63	0.12	-	-	-	87.2	71.7
ITO2 model6	800-1700	4.17	1.42	0.13	-	-	-	86.6	2.9
ITO3 model5	800-1700	3.43	1.41	0.12	1.95	0.22	3.43	87.5	0.4
ITO3 model6	800-1700	4.17	1.49	0.12	-	-	-	87.0	0.9
ITO4 model2	800-1700	3.34	1.29	0.11	2.54	0.21	3.73	86.4	0.4
ITO4 model3	800-1700	4.18	1.36	0.11	-	-	-	86.0	0.9

Table 4.1: ITO Drude-Lorentz Ellipsometry Model Parameters according to Equation 4.1

$$\begin{aligned} \varepsilon_{ITO} &= \varepsilon_1 + i\varepsilon_2 = \varepsilon_{offset} + \varepsilon_{Drude} + \varepsilon_{Lorentz} \\ \varepsilon_{ITO} &= \varepsilon_{offset} - \frac{A_D}{E^2 + iB_D E} + \frac{A_L B_L E_c}{E_c^2 - E^2 - iB_L E} \end{aligned} \tag{4.1}$$

As can be seen by comparing the mean squared error (MSE) values in Table 4.1, ITO can in general be roughly approximated using a single Drude oscillator for near-IR wavelengths greater than

about 800nm. If we focus on ITO2 model4, we see that a model with a Drude plus single Lorentzian approximates the data well with a mean square error (MSE) of only 5.5. When the Lorentzian is removed and the data modeled using only a single Drude term the MSE increases significantly to 71.1 (ITO2 model5). However, if the range is restricted to include only wavelengths longer than 800nm, the model again improves within an acceptable range (ITO2 model6). The results for this particular film are compared directly in Figure 4.2. The figure shows almost complete overlap between the red curve (Drude + Lorentz oscillator, 400-1700nm) and the black curve (Drude only, restricted to >800nm). When modeled using only a Drude oscillator over the full range of wavelengths however (blue curve), there is a significant increase in the error (MSE) and in the visual agreement of the modeled optical properties of the film. This is due to the significant absorption peak in the ultraviolet which must be modeled by a Lorentzian, the tail of which extends into the visible range.

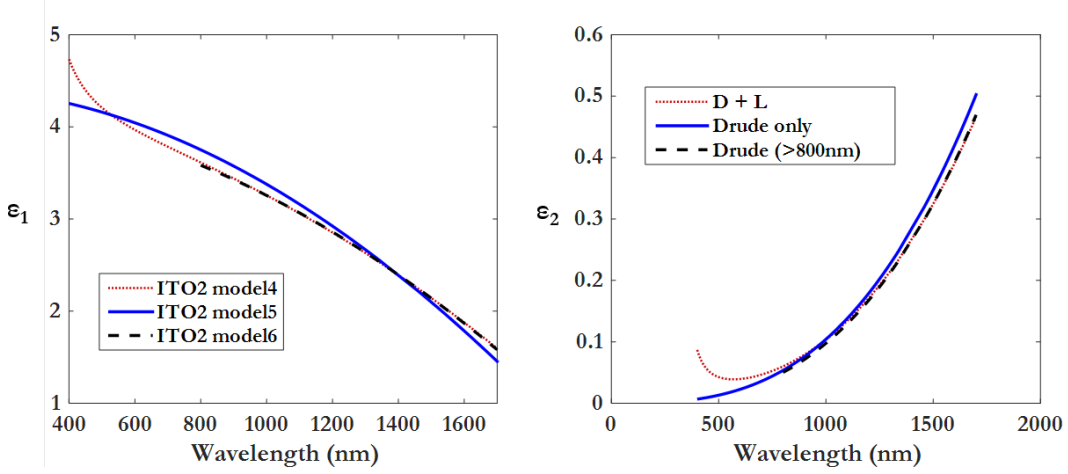


Figure 4.2: Comparison of Drude vs. Drude-Lorentz model for ITO

Note that while these models in general do accurately model the rough average optical constants of these films, ITO films are known to exhibit gradation in optical properties throughout the thickness of the film which should be included to improve the accuracy of the results[115]. In addition, a surface roughness layer has not been added here since the results were studied mainly in the near-IR; how-

ever, if visible or ultraviolet data is required, then the addition of both the Lorentzian and a surface roughness layer would likely be necessary.

In addition to determining the best optical models, basic electrical measurements of these films have been taken and the results compared to the SE optical models. The crossover wavelength λ_c where ε_1 is nearly zero was calculated from the Drude model for each of the ITO films shown and compared to the measured Hall resistivity in Table 4.2 and Figure 4.3(a). For a model which consists of only a single Drude term, the crossover frequency is also known as the unscreened plasma frequency, ω_{pu}. The more conductive ITO (sample: ITO1) sputtered at elevated substrate temperature exhibited both lower resistivity and a shorter crossover wavelength (higher plasma frequency) as expected based on the Drude model. In addition, as shown in Figure 4.3(b), the more conductive sample also had a significantly higher carrier concentration than the samples deposited at room temperature. Therefore, it can be inferred that increasing the substrate temperature during deposition increases the carrier concentration which in turn leads to a shorter crossover wavelength.

Sample	Temp (°C)	ω_{pu} (eV)	λ_c (nm)	Resistivity (Ω-cm)	Carrier Density (cm^{-3})	Hall Mobility ($\frac{cm^2}{Vs}$)
ITO1	200	0.97	1280	2.2×10^{-4}	-1.1×10^{21}	-26.7
ITO2	20	0.57	2180	7.4×10^{-4}	-3.1×10^{20}	-27.0
ITO3	20	0.59	2120	7.6×10^{-4}	-3.2×10^{20}	-25.5
ITO4	20	0.56	2220	8.5×10^{-4}	-2.8×10^{20}	-26.6

Table 4.2: ITO Plasma Frequency/Crossover wavelength as calculated using Drude model spectroscopy ellipsometry parameters from Table 4.1 compared to measured Van der Pauw resistivity and Hall mobility and carrier concentration

It has been shown that within the longer visible to near-IR wavelength range, ITO is well-modeled by the Drude model signifying that within this range, the material essentially has metallic-like behavior with free electrons distributed throughout. Therefore the electrical properties of the film can also be well approximated by spectroscopic ellipsometry measurements and modeling and vice-versa. A

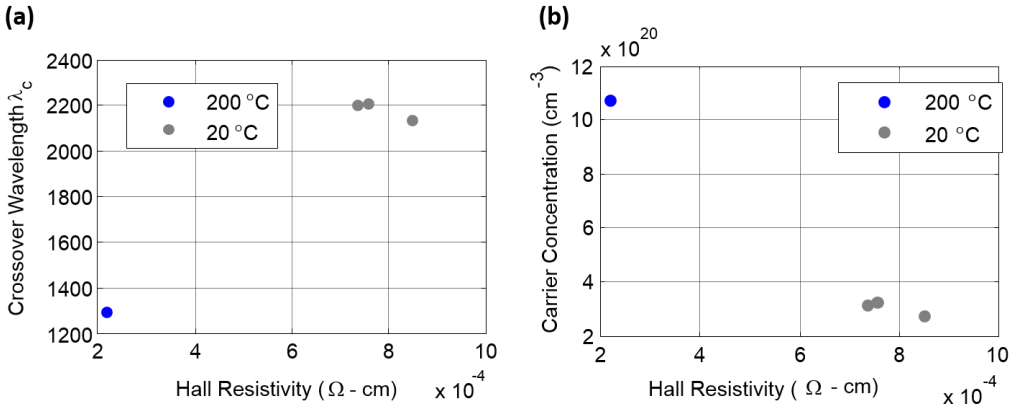


Figure 4.3: ITO crossover wavelength and carrier concentration versus resistivity

simple Drude free electron model curve predicting plasma wavelength as a function of carrier concentration is shown in Figure 4.4. The calculated λ_c values from the optical SE models correlate well with the Drude model predictions per Equation (1.3) with $m^* = 1.1m_e$. Therefore, for ITO films a Drude model can be used to accurately predict the approximate crossover wavelength λ_c using only quick Hall measurements.

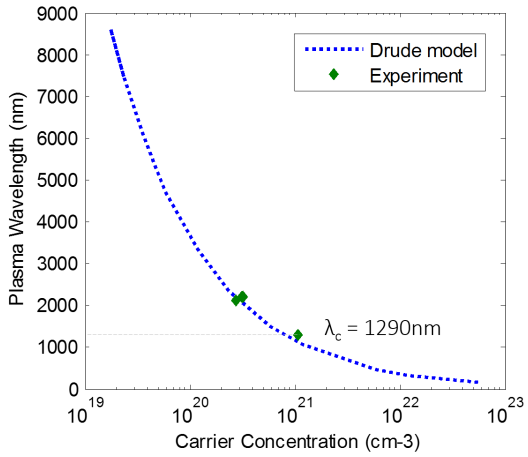


Figure 4.4: Plasma wavelength is approximated via Drude free electron model for different carrier concentrations and compared to experimental data points for sputtered ITO thin films with carrier concentration measured via Hall measurements and plasma wavelength via spectroscopic ellipsometry

ITO is a well-developed material which has been thoroughly characterized previously both electrically and optically, widely used for applications in which a transparent conductive layer is desired. ITO and other transparent conducting oxides such as doped zinc oxide (AZO/GZO) have recently garnered renewed interest within the plasmonics community with potential uses as electrically and optically tunable epsilon-near-zero (ENZ) materials. [116–118]

In this thesis, after my experimental and data analysis techniques were established using ITO, I focused therefore on a "new" and less-studied material optically and plasmonically, titanium nitride (TiN). As discussed earlier, previous characterization of this material has focused heavily on structural and mechanical properties. Using the same techniques as shown in this short case study of conductive ITO, next I focus on the optical and electrical properties of sputtered TiOxN$_y$ and TiN, with a specific focus in this chapter on how to control and optimize the optical properties in sputtered thin films for plasmonic applications.

4.2 Overview of Optical Behavior of Titanium Nitride (TiN) and Titanium Oxynitrides (TiO_xN_y)

Similar to ITO, the deposition of thin films of TiO_xN_y and TiN can be controlled by changing the deposition conditions to produce films with varied optical, electrical, and structural properties. Even small changes in the stoichiometry and chemical bonding can have profound changes in the electronic band structure and optical properties. While stoichiometric TiN exhibits a gold-like hue, the color of films with oxygen impurities added can vary from gold-like to brown and purple as shown in Figure 4.5. It is important to note that this is not an interference effect. All thin films shown in Figure 4.5, are of similar thickness and have been sputtered onto transparent substrates. The variations in color are due to the varying optical properties of the films. The most conductive films exhibit a reflective yellow color similar to that of gold and the most resistive, a range of darker shades from purple to brown. Previous studies have quantified this effect in further detail and suggest that films with lower values of

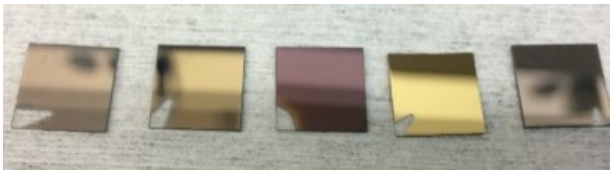


Figure 4.5: TiO_xN_y films of similar thickness deposited under varying conditions onto transparent substrates exhibit widely varying colors.

brightness have lower resistivity and higher carbon or oxygen content, with Ti:N values further from stoichiometric [119–122].

The optical properties of TiN thin films have a sensitive dependence on the deposition conditions and thus exhibit wide tunability as shown in Figure 4.1. As a general trend, those TiN films identified by SE to have a larger magnitude of negative real permittivity (i.e. were "more metallic") also exhibited lower values of Hall resistivity, had a lower concentration of oxygen impurities, and exhibited better crystallinity. As discussed in Chapter 3, the optical properties of metallic TiN can be modeled by one Drude and two Lorentzian oscillators. Films determined to be 'dielectric' through ellipsometric measurements were actually oxynitrides exhibiting high oxygen impurity concentrations and no discernible long-term crystalline order. Modeling SE data for these films required the addition of an extra Lorentz term to model the NIR absorption.

We found that the substrate temperature, substrate choice, amount of N_2 gas flow, and any additional applied bias all had significant effects on the optical properties of the final films. Varying the composition of gases during reactive sputtering of TiN in general gave a greater degree of control to the thin film formation as compared to nonreactive sputtering; however, by varying the substrate temperature during deposition, a significant range of properties can also be achieved via nonreactive sputtering. In addition, by applying a bias while sputtering we were able to deposit metallic TiN films at room temperature.

In the next section of this chapter, I will first focus on the more 'dielectric' oxynitride films followed by a discussion of the critical factors required to sputter the most metallic TiN films for plasmonic

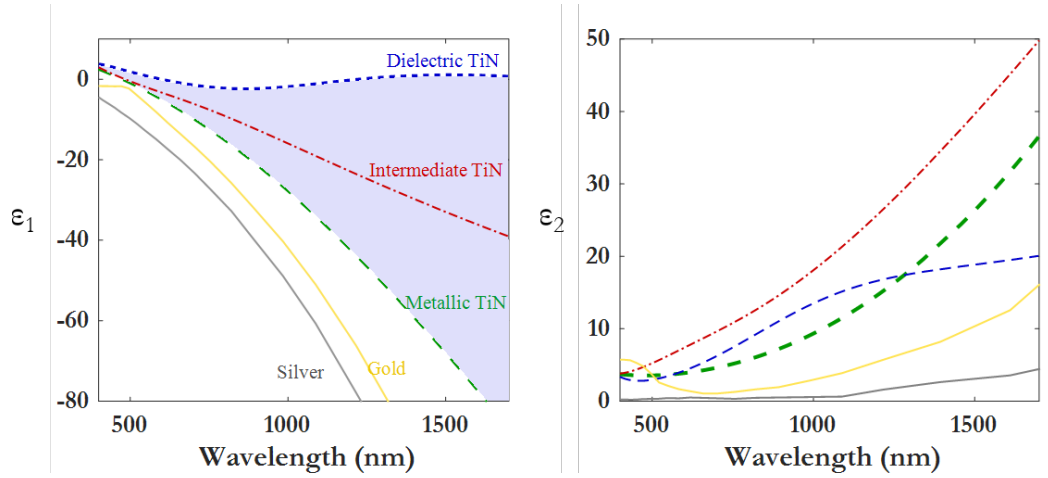


Figure 4.6: The optical properties of TiN and TiO_xN_y films vary widely dependent upon sputtering chamber conditions prior to and during deposition.

applications. In Chapters 5 and 6 , I will add correlations of this optical behavior with structural and compositional measurements to provide initial suggestions as to the underlying structural cause of the variation in optical properties.

4.3 Titanium Oxynitrides (TiO_xN_y)

Preliminary sputtering trials showed that reactively sputtering thin films from a Ti sputtering target with no or little elevation of the substrate temperature during deposition (tested 20 to 50°C) created titanium oxynitride (TiO_xN_y) thin films which exhibited entirely dielectric behavior, far from the expected metallic behavior of titanium nitride. This was true both at reactive gas ratios of 4:6 and 10:5 sccm Ar : N_2. The results are shown in Figure 4.7. Upon elevation of the substrate deposition temperature (400 to 600°C) the metallic character gradually increased, however was still far from the metallic-like behavior expected of TiN.

All films shown in this figure were reactively sputtered at 250W (or 200W denoted by *) direct current at either 4:6 sccm or 10:5 sccm (Ar: N2) onto Si wafers with a thick PECVD SiO_2 layer (400-

3500nm). The thick SiO_2 layer beneath the sputtered oxynitride was used to enhance the optical signal for improved SE data modeling. The base pressure was in the 10^{-7} Torr range for all films prior to substrate heating; however, for the films deposited at $> 400^{\circ}C$ were in the 10^{-6} Torr range after heating. The deposition time was 25 – 30 minutes (exception: TiN10, sputtered for 60 minutes, 110nm). The resulting sputtered films ranged in thickness from approximately 30-70nm thick giving deposition rates near 2nm/min. (exceptions: TiN15 1.1nm/min, TiN16 2.8nm/min). X-ray photoelectron spectroscopy (XPS) studies which will be further detailed in Chapter 5 revealed that these film were high in oxygen content and thus oxynitrides rather than the TiN that was originally desired.

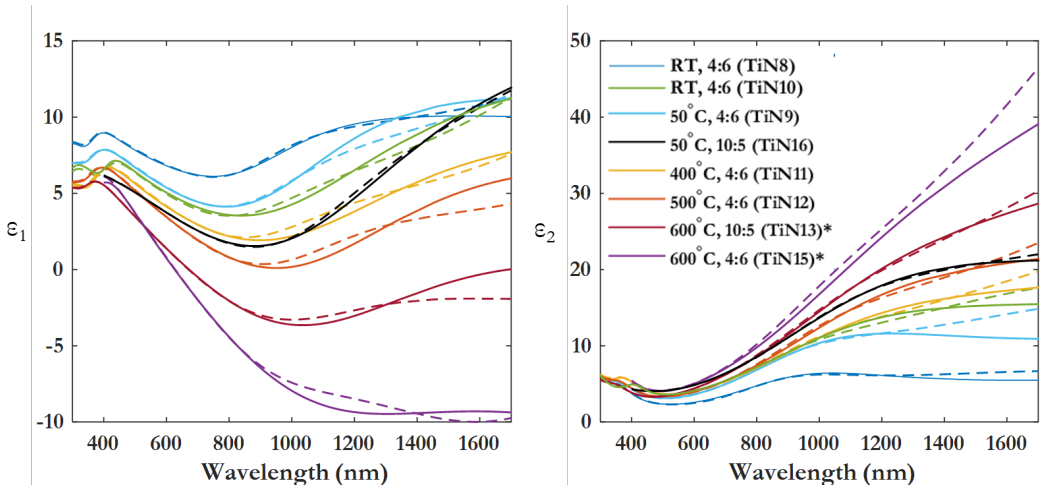


Figure 4.7: Thin TiO_xN_y films on thick SiO_2(400-3500nm) layers on Si substrates can be tuned to exhibit varied dielectric character by changing the substrate deposition temperature and other deposition conditions. (Solid and dashed lines denoted two different types of SE models: (- - -) 4 Lorentz oscillators , (—) 1 Drude + 3 Lorentz oscillators)

It is difficult to create high quality and unique ellipsometry models for dielectric films like these because they do not conform to the known optical properties of either metallic TiN or dielectric TiO_2 but are rather somewhere intermediate so there is not good reference data from which to make good starting parameter guesses. Unlike ITO films which we showed can be modeled well over a significant wavelength range by a single Drude term, TiO_xN_y films require several oscillators within the visible

to near-IR range to produce an acceptable model. The TiO_xN_y films deposited at the lowest temperatures (RT, 50°C) are predicted to be porous as sputtered [123] and then oxidize both at the surface and along grain boundaries and throughout the porous areas upon being removed from vacuum. For this reason, the best initial ellipsometric models for these films were derived from an effective medium approximation (EMA) layer which was fit to a % TiN and the remaining % TiO_2 to form a starting model.

$$\varepsilon_{EMA} = x * \varepsilon_{TiN} + (1 - x) * \varepsilon_{TiO_xN_y}$$

The best fit attainable from that model was then converted into a general oscillator model. Two types of models were tested. The first consisted of 4 Lorentz terms and is denoted by the dashed lines in Figure 4.7. The second set of models consisted of one Drude term and three Lorentzians to parameterize the model (denoted by solid lines in figure). While the behavior varies slightly between the two sets of models the results are in general quite close. Therefore, to improve the consistency of the optical data fits as compared to the metallic films the second set of models including the Drude term was used for the remainder of the analysis. The parametric equation for the TiO_xN_y model used in this section is shown below. Therefore, as compared to the TiN SE example model discussed in Chapter 3, rather than 1 Drude and 2 Lorentzians, modeling oxynitride films requires the addition of a third Lorentzian term to capture the lower energy/longer wavelength absorption centered near 1eV.

$$\varepsilon_{TiO_xN_y} = \varepsilon_1 + i\varepsilon_2 = \varepsilon_{offset} + \varepsilon_{Drude} + \varepsilon_{Lorentz\#1} + \varepsilon_{Lorentz\#2} + \varepsilon_{Lorentz\#3}$$

$$\varepsilon_{TiO_xN_y} = \varepsilon_{offset} - \frac{A_D B_D}{E^2 + iB_D E} + \frac{A_1 B_1 E_{c_1}}{E_{c_1}^2 - E^2 - iB_1 E} + \frac{A_2 B_2 E_{c_2}}{E_{c_2}^2 - E^2 - iB_2 E} + \frac{A_3 B_3 E_{c_3}}{E_{c_3}^2 - E^2 - iB_3 E}$$

An example of an oxynitride film whose SE data is fit using this model to retrieve the optical properties ε_1 and ε_2 as a function of wavelength is shown in Figure 4.8. The film chosen is TiN9, a dielectric

film for which the full deposition properties are shown in the Appendix. As can be seen in the figure, the Drude component trends negative in ε_1 as wavelength increases. The *unscreened* plasma frequency shown where the Drude component only is nearly equal to zero, in this case at just over 1600nm. The fit parameters for this film and all oxynitrides shown in Figure 4.7 are listed in Table 4.3. The Drude component is seen to increase in amplitude as the metallic character increases. The Lorentz oscillators are centered within 3 energy ranges: 1-1.3eV, 3-3.6eV and near 5eV.

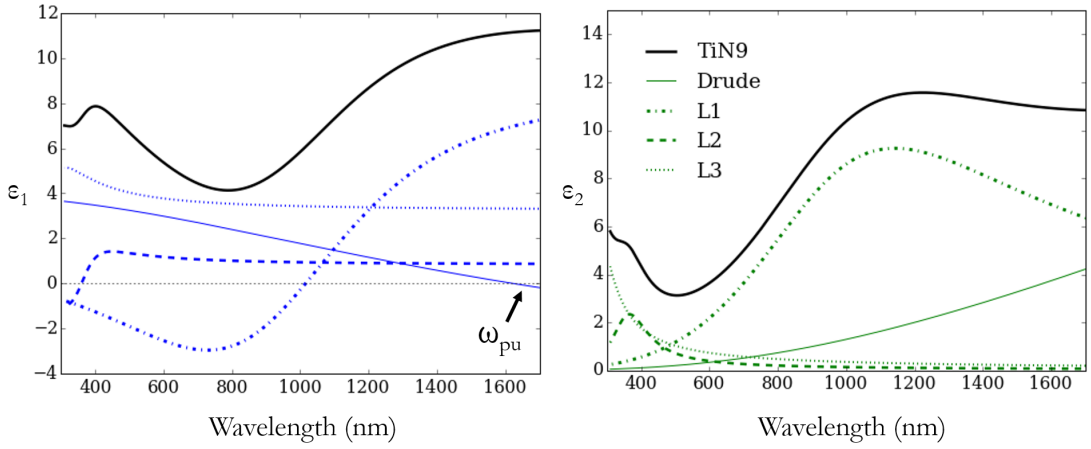


Figure 4.8: TiO_xN_y example of SE fitting parameters for optical properties using one Drude term and three Lorentz terms to model the additional absorption in these films. The unscreened plasma frequency ω_{pu} is designated by the frequency where the Drude component is nearly zero.

As shown in Chapter 1 the unscreened plasma frequency depends on two parameters, the carrier concentration, N, and the effective mass, m^*. This dependence is shown again in Equation 4.3. Since there is a direct dependence of ω_{pu} on the carrier concentration, how "metallic" a film is can be determined by directly comparing ω_{pu} from different films as determined by optical SE data. As will be discussed further in the next chapter, this metallic character can be controlled by varying the stoichiometry and chemical composition of the film. While not explored in this work, the mass density has also been shown to have an effect on ω_{pu} [26].

Sample	ε_{offset}	Drude		Lorentz			Thickness	MSE
		A	B	A	B	$E_c(eV)$	(nm)	
TiN8 model15 (RT,4:6)	4.05	3.01	1.20	4.60 2.10 9.33	1.03 1.01 1.82	1.33 3.43 5.00	53.0/9.8	24.7
TiN9 model11 (50°C,4:6)	3.91	5.99	0.75	8.74 2.32 8.24	1.15 1.23 1.99	1.22 3.44 5.04	51.4/9.2	14.1
TiN10 model11 (RT,4:6)	4.09	6.47	0.81	10.31 1.77 7.24	1.32 0.74 2.44	1.11 3.06 4.96	110.7/6.0	33.7
TiN11 model4 (400°C,4:6)	3.04	9.67	0.82	9.86 2.72 7.69	1.28 1.12 2.25	1.08 3.33 5.09	48.7/5.6	57.8
TiN12 model2 (500°C,4:6)	3.81	14.01	0.69	12.09 2.44 7.15	1.17 1.26 2.02	1.04 3.48 4.99	58.9/5.1	42.1
TiN13 model4 (600°C,10:5)	3.64	22.3	0.67	13.64 2.14 7.29	1.21 1.28 1.88	1.01 3.60 5.08	48.4/4.9	29.2
TiN15 model4 (600°C,4:6)	3.05	35.95	0.70	14.05 2.77 22.53	1.18 1.08 0.88	0.97 3.20 5.02	28.6/3.3	31.6
TiN16 model9 (50°C,10:5)	4.44	7.62	0.97	13.81 1.57 7.55	1.22 2.50 1.35	1.04 3.28 4.38	70.6/13.5	24.2

Table 4.3: TiO_xN_y Drude-Lorentz Ellipsometry Model Parameters

$$\omega_{pu} = \sqrt{\frac{Ne^2}{\varepsilon_o m^*}}$$

The substrate temperature during film deposition is known to affect the structure and properties of sputtered TiN films [45, 61, 124]. The general trend in Figure 4.7 showed that by increasing the

substrate deposition temperature, we were similarly able to increase and control the metallic character of our TiO_xN_y films. We now focus on a subset of these films to quantify this trend further (TiN8, 9, 11, 12, 15 - all sputtered at 4:6 sccm Ar:N_2). This subset is plotted in Figure 4.9. The "metallic character" in this case can be thought of simply as how negative ε_1 becomes, or more carefully, by tracking the value of the unscreened plasma frequency, ω_{pu}. "More metallic" films have larger ω_{pu}, or a greater number of conduction electrons and ε_1 becomes more negative as compared to more dielectric film. The unscreened plasma frequency is calculated using only the Drude term as shown in Figure 4.8;

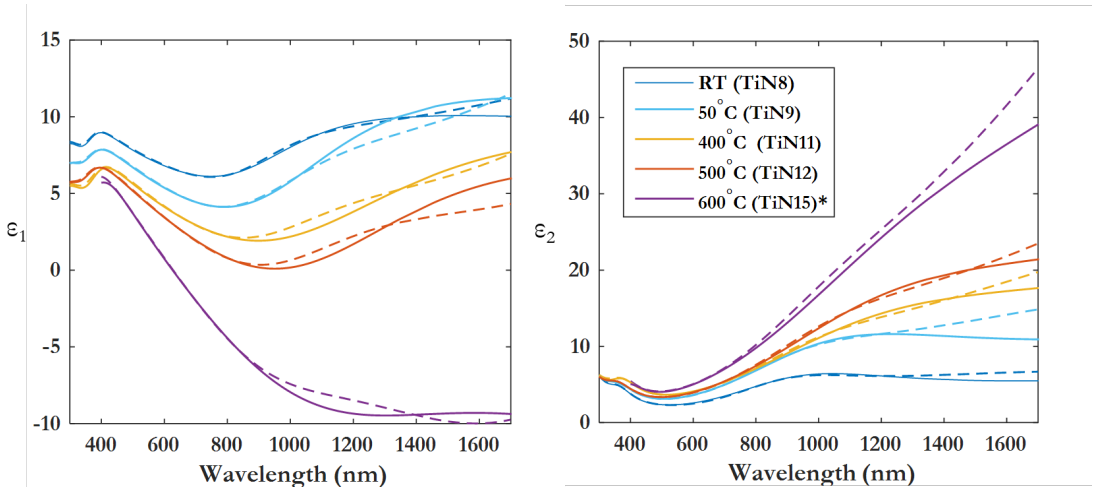


Figure 4.9: Thin TiOxNy films on thick SiO2 (400-3500nm) layers on Si substrates can be tuned to exhibit varied dielectric character by changing the substrate deposition temperature.

however, as shown in that figure, in oxynitrides there are significant contributions from three additional Lorentzian terms which reduce the overall metallic character. One may therefore ask whether this method of classifying the metallic character, focused solely on the Drude component, makes sense for titanium oxynitrides. To confirm the validity of these comparisons between the metallic character of TiO_xN_y films using only optical SE data, the electrical resistivity was also measured and the results compared.

The resistivity of these oxynitride films was measured using Van der Pauw and Hall geometries.

The results are plotted versus the unscreened plasma frequency as calculated using only the Drude and offset components from SE data with the corresponding data shown in Table 4.4. The thicknesses of each film were determined by a combination of the expected sputtering rate as well as the SE models. The electrical measurements were made directly on the film surface with gold probes without additional electrical contacts. The measured resistivities were comparable between the Hall and Van der Pauw geometries and were highly repeatable even without additional contacts. Hall mobility and carrier concentration measurements however were more variable and would require more careful measurements. This is likely due to the fact that the mobilities measured in these films were quite low ($0.04 - 0.14 cm^2/Vs$). Carrier concentrations were on the order of $10^{22} cm^{-3}$.

Sample	Temp (°C)	ω_{pu} (eV)	λ_{pu} (nm)	Resistivity (Ω-cm)
TiN8	RT	-	-	2.85×10^{-2}
TiN9	50	0.766	1620	6.4×10^{-3}
TiN10	RT	0.791	1570	6.8×10^{-3}
TiN11	400	1.392	890	2.5×10^{-3}
TiN12	500	1.436	860	2.1×10^{-3}
TiN13	600	1.912	650	1.3×10^{-3}
TiN15	600	2.786	445	-
TiN16	50	0.851	1460	-

Table 4.4: TiO_xN_y calculated unscreened plasma frequency/wavelength as calculated using only Drude model term from spectroscopy ellipsometry parameters from Table 4.3 compared to measured Van der Pauw resistivity

Electrical resistivity also has a direct relationship with the unscreened plasma frequency as defined by [21, 26]

$$\tau_D = \frac{m^*}{\rho N e^2}$$

$$\rho = \left(\frac{1}{\varepsilon_0 \tau_D}\right) \cdot \frac{1}{\omega_{pu}^2}$$

By plotting the measured electrical resistivities (ρ) of these films against the inverse square of the plasma frequency ($1/\omega_{pu}^2$), it is therefore expected that the relationship should be linear with the slope equal to $1/(\varepsilon_0 \tau_D)$ where ε_0 is the permittivity of free space in SI units and τ_D is the mean relaxation time of free conduction electrons in the film. Oxynitride films TiN9-13 do indeed satisfy this linear relationship as shown in Figure 4.10. The mean relaxation time τ_D calculated is 5.1×10^{-14}s. That these diverse films satisfy this relationship is perhaps surprising due to their wide range of resistivities (and stoichiometries/chemical compositions. See next chapter.) However, it suggests that the optical SE models used are valid and are indeed able to successfully predict the DC resistivity of TiO_xN_y films and vice versa, even for these highly varied oxynitride films.

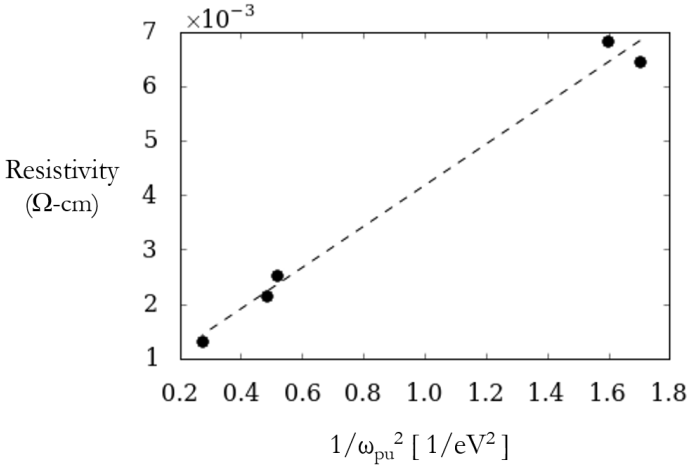


Figure 4.10: Resistivity compared to inverse of unscreened plasma frequency squared ($1/\omega_{pu}^2$). Slope of line allows calculation of relaxation time.

4.4 Metallic Titanium Nitride

In the prior sections, the variation in optical properties of ITO and TiO_xN_y was described. While there has been some discussion of the effect of deposition conditions on these optical properties, a significant amount of the focus thus far has been on the resulting optical models and fit parameters. In this section, I will focus not only on the optical models, but also more deeply on the correlation of the optical properties of the metallic TiN films with the deposition conditions, pointing out the critical parameters to control the resulting optical properties. The main goal of this work was to optimize the deposition conditions to sputter TiN films with the greatest metallic character and lowest optical losses.

We showed previously that the substrate temperature during deposition had a strong influence on the metallic character of TiO_xN_y films with conductivity increasing as temperature increased. This trend also holds for even more metallic TiN films which exhibit smaller oxygen content so I will begin this section by discussing this parameter. Note that here our "metallic" TiN films do still have some oxygen defects. In general, here films with $< 15-20$ atomic % oxygen are the main focus of discussion. Besides the temperature during deposition, the choice as well as the preparation of the substrate prior to deposition also have a large effect on the final properties and will be the next topics of discussion. We will then evaluate the changes due to gas composition in reactive sputtering as compared to non-reactive sputtering for a particular substrate, since these effects are more interactive.

In all of my initial work, it was found that high temperature was required to sputter plasmonic quality TiN films. One of the advantages of TiN as compared to gold for plasmonics is potential CMOS-compatibility, but if material deposition needs to be done at high temperature, then the process is not fully CMOS-compatible. By applying an additional substrate bias while sputtering however, I was able to reduce the oxygen content in my films and increase the metallic character. Therefore, I will finish this chapter by examining the metallic TiN films produced at room temperature with the addition

of a substrate bias.

4.4.1 Non-reactive Sputtering at Elevated Deposition Temperature

In the previous section, the initial focus was on TiO_xN_y films reactively sputtered onto SiO_2 on Si substrates. By starting directly with a TiN target and non-reactive sputtering, one may expect that the resulting film properties may vary less as compared to sputtering from a Ti target using reactive sputtering. Therefore, in an attempt to increase the metallic character of my oxynitride films further, TiN films were next *non-reactively* sputtered. A range of different substrates (e.g. (100) Silicon, (100) MgO, (0001) Al_2O_3) were used based on the literature [45, 49, 124–126].

Figure 4.11 provides a summary of the results of increased substrate temperature on non-reactively sputtered TiN films. We observed the same effect of increased deposition temperature producing more metallic films which we saw in the TiO_xN_y films on SiO_2/Si. This was true for various substrates, namely silicon, c-plane sapphire, and (100) MgO. ε_1 of the sputtered TiN shows little dependence on the particular choice of substrate, but there is a pronounced change on all substrates as the substrate deposition temperature is increased. TiN films non-reactively sputtered onto c-Sapphire, Si, and MgO at room temperature all exhibited 'minimal metallic character' including: low reflectivity, high resistivity, and relatively small ε_1 just as was seen with reactive sputtering at room temperature on SiO_2/Si. This is again due to high oxygen incorporation even though a TiN target is being used. This will be discussed further in the next chapter. At elevated substrate temperatures of 600°C, ε_1 of the films reaches negative values for longer wavelengths. The behavior for all substrates tried is similar. We can therefore achieve significant control over the properties of non-reactively sputtered TiN solely by depositing at different temperatures and on a variety of different substrates. This is likely due to an increase in adatom mobility on the surface of the developing film as discussed in Chapter 2. As temperature increases, more energy is available to incoming adatoms leading to higher mobility and more metallic films.

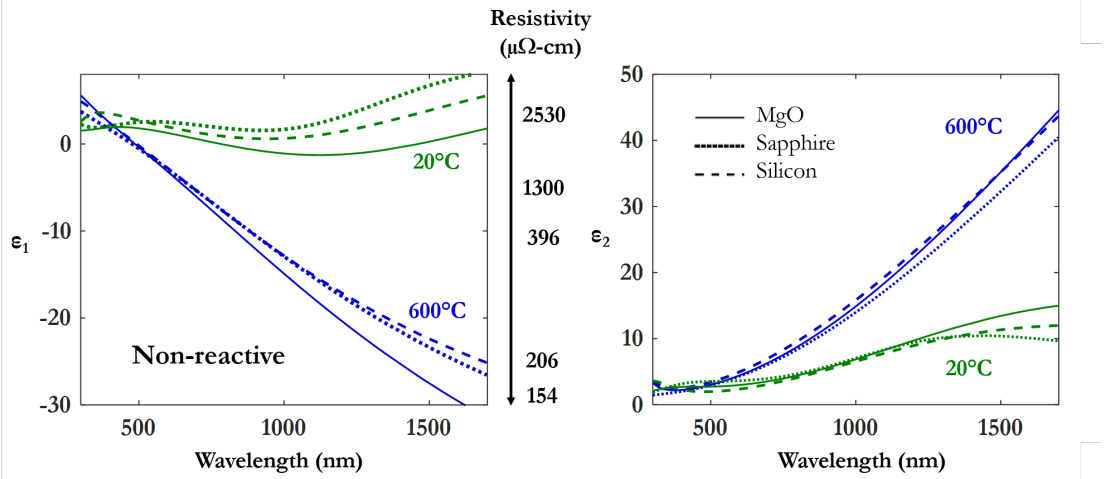


Figure 4.11: Increased substrate temperature while *non-reactively* sputtering gives adatoms more mobility and indiscriminately increases the metallic behavior of the TiN films [127]

In addition, it was shown in the last section that the measured DC resistivities of several TiO_xN_y films correlated well with the unscreened plasma frequencies, ω_{pu}, as calculated from the Drude term only of the Drude-Lorentz optical models. As a general guideline, the oxynitride films discussed in the previous section had resistivity ρ on the order of $10^{-3}\Omega$-cm. The more metallic films discussed in this section have ρ ranging from $\approx 10^{-4} - 10^{-5}\Omega$-cm or $\approx$ 40-200 $\mu\Omega$-cm. A rough diagram depicting this range of ρ as associated with the optical models of a few films is included in Figure 4.11.

4.4.2 Reactive Sputtering at Elevated Temperature on Varied Substrates

Given the more metallic behavior of non-reactively sputtered TiN films deposited at 600°C substrate temperature, our next experiments adopted this value of temperature, and in addition explored the behavior of the thin films under conditions of reactive sputtering on the new MgO, Si, and c-Sapphire substrates. This deposition procedure utilized nitrogen as the reactive gas and argon as the chemically inert sputtering gas. Figure 4.12 shows the results of one such experiment, carried out at 12:8 sccm $Ar : N_2$ reactive gas flow at 4mTorr overall deposition pressure and subjected to 200W DC power.

The films were deposited onto all substrates simultaneously to ensure consistent chamber conditions for direct comparison of the results. Unlike the situation with non-reactive sputtering, the resulting ε_1 versus λ of the reactively sputtered TiN films showed a very distinctive dependence on the choice of substrate even though all were sputtered simultaneously and at an elevated substrate temperature of 600°C. The film sputtered onto sapphire has similar behavior to the oxynitride films on SiO_2/Si while the TiN film on Si is a bit more conductive. There is a significant improvement in metallic character of the TiN film sputtered onto MgO in comparison to all previously sputtered films.

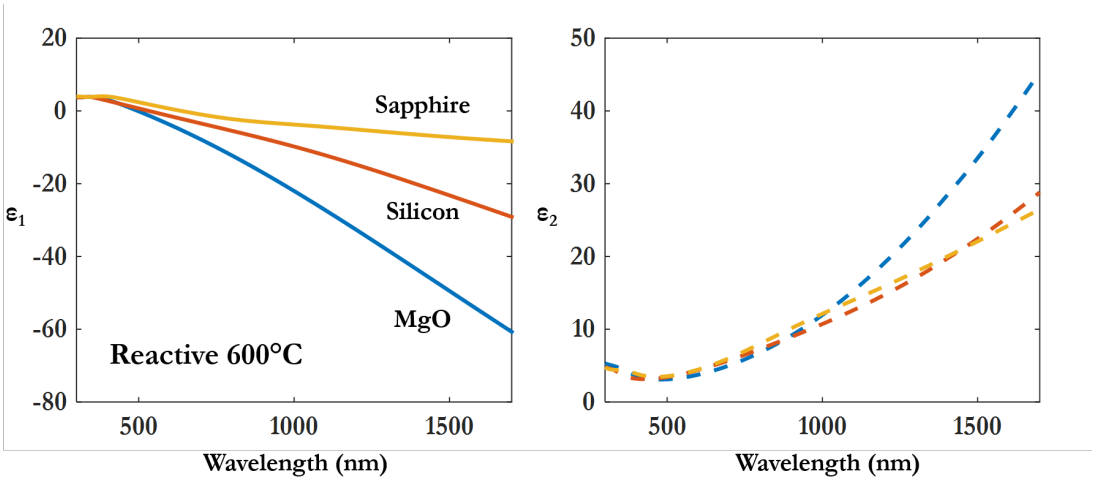


Figure 4.12: Reactive sputtering highlights substrate dependence and the potential impact of the underlying crystal lattice as a growth template, Sample: TiN23

Two main considerations come to mind in trying to better understand this dramatic change in behavior as compared to previous experiments. First, one may hypothesize that differences in thermal conductivity between the different substrates leads to different adatom mobilities on the surface. However, if this were the deciding factor, we would have also expected to see a larger difference between substrates in the non-reactively sputtered samples shown in Figure 4.11 and this was not the case. The second and more likely reason is the lattice match/mismatch between the growing film and underlying substrate. As will be discussed further in Chapter 6, MgO and TiN have the same cubic

NaCl lattice structure and very close lattice constants which allows MgO to act as an excellent growth template for sputtered TiN films.

Using the methods discussed previously, the SE models for the three films plotted in Figure 4.12 are included in Table 4.5. In the less conductive films (on sapphire and silicon), just as with the oxynitrides discussed previously, one Drude and three Lorentzian oscillators (near 1.4, 3.6, and 5.3 eV) are needed to fit the data well. However, in the more conductive sample on MgO substrate, only one Drude plus two Lorentzians are needed rather than three. In this case, trying to add the third Lorentzian near 1eV decreases the validity of the SE model. This agrees well with the metallic TiN band diagram predicted by Patsalas[26], shown in Figure 1.9 which predicts interband absorption peaks near 3-4eV and 5eV near the X and L-points respectively.

Sample	ε_{offset}	Drude		Lorentz			Thickness	MSE
		A	B	A	B	$E_c(eV)$	(nm)	
TiN23 MgO model5	3.48	107.6	0.48	1.75	1.53	3.71	29.1	5.0
				6.16	2.59	5.34		
TiN23 Si1 model5	2.19	60.20	0.49	3.32	1.99	1.47	41.0	3.8
				0.51	0.58	3.78		
				6.10	3.02	5.38		
TiN23 Saph model4	2.68	25.75	1.17	1.82	0.97	1.35	38.8	3.7
				1.42	1.21	3.44		
				5.76	2.57	5.26		

Table 4.5: Drude-Lorentz model parameters for TiN reactively sputtered on various substrates at 600°C. These models correspond to those plotted in Figure 4.14.

When studying the SE models of the higher oxygen content films discussed earlier, it was found that as a film exhibits more metallic character, the amplitude, A, of the Drude term also increases. This trend is seen to still hold valid for these more metallic films as can also be seen in Table 4.5. As before, this term is used to calculate the ω_{pu} for each film. The plasma frequencies are again compared to the measured electrical DC resistivities as shown in Table 4.6. The new results for sample TiN23

reactively sputtered at 600°C are added to Figure 4.13. Note that this figure includes the same data (in black) from previous Figure 4.10 but includes in addition the new more metallic TiN23 films with lower resistivity $\approx 10^{-4} - 10^{-5}\Omega$-cm and shorter plasma frequencies (in red).

Sample	ω_{pu} (eV/nm)	ω_p/λ_c (eV/nm)	ω_{sp} (eV/nm)	Resisitivity (Ω-cm)
TiN23 MgO	3.82/320	2.51/495	2.36/525	6.5 x 10^{-5}
TiN23 Si	3.64/340	2.34/530	2.14/580	-
TiN23 Saph	3.14/395	1.95/635	1.77/700	2.9 x 10^{-4}

Table 4.6: Unscreened, screened, and surface plasmon frequency and resistivity for TiN reactively sputtered on various substrates at 600°C.

The more metallic samples also follow the linear trend demonstrated previously according to Equation 4.3 with a slightly modified slope corresponding to a 4.8 x 10^{-14}s mean relaxation time, agreeing well with the previous data. Therefore, we conclude that the free electrons within both these TiO_xN_y and TiN films can be well-described by this Drude term over a wide range of macroscopic film resistivities. In addition, Hall measurements of these "more metallic" films found increased carrier concentrations (10^{22} - 10^{23}cm^{-3}) and slightly higher mobilities (0.20 - 0.48 cm^2/Vs) as compared to the oxynitride films.

Another notable observation from Figure 4.12 is that while the TiN film sputtered onto MgO exhibits significantly more metallic character in terms of the negative value of ε_1, the relative change in ε_2 (the "losses") as compared to films formed on silicon and sapphire substrates is much smaller. This can be seen directly by comparing the ratio $|\ \varepsilon_1\ |\ /\ |\ \varepsilon_2\ |$ which is one figure of merit (FOM) used specifically for surface plasmon applications where the losses are more important. Since the losses of the TiN films in this case on silicon and sapphire substrates are similar, but the film on silicon is more metallic, the TiN film on Si has a better FOM than that on sapphire. The TiN film sputtered onto MgO overall has the highest FOM even though it has the overall largest magnitude losses. Therefore

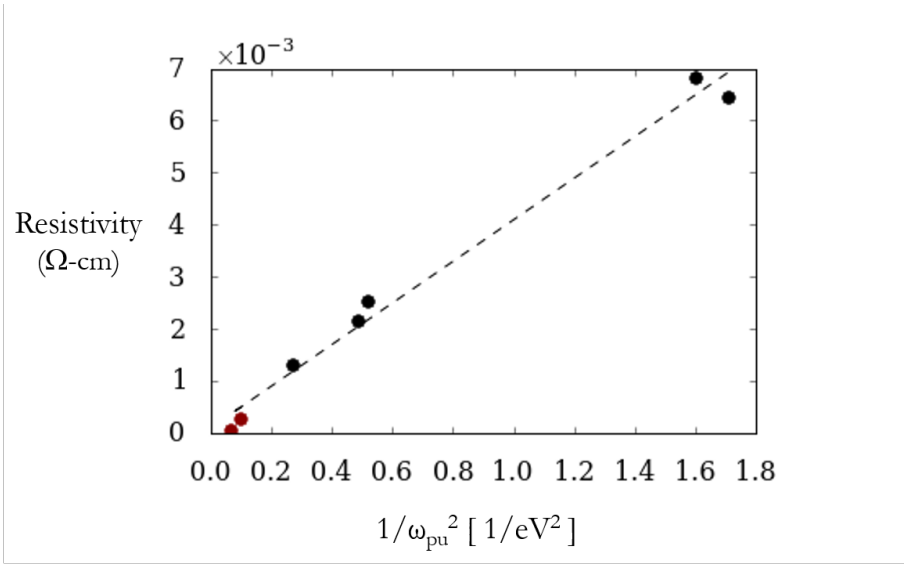


Figure 4.13: Resistivity compared to inverse of unscreened plasma frequency squared ($1/\omega_{pu}^2$). Slope of line allows calculation of relaxation time. Data from more metallic TiN23 samples on MgO and Sapphire substrates has been added (red) to the oxynitride film data from previous Figure 4.10 (black)

TiN sputtered onto MgO under these conditions would have more potential for applications requiring surface plasmons than TiN sputtered onto either Si or sapphire under the same conditions.

4.4.3 Sputtering with Varied Reactive Gas Ratios

Comparing the results of Figures 4.11 and 4.12, it can be seen that TiN films reactively sputtered onto MgO substrates at 600°C showed far better metallic behavior than films non-reactively sputtered onto the same substrates at the same temperature. However, we note that under the same stated conditions, the reactive sputtering does not produce the same improvement of metallic properties for TiN films sputtered onto either sapphire or silicon. We tried to better understand these results for deposition on the different substrates by varying the gas composition from non-reactive conditions (Ar only) to ratios of Ar:N_2 ranging from 12:4 (nitrogen-deficient) to 8:12 (nitrogen-rich) sccm, with the total pressure held constant at 4mT. We were curious to see if we could further reduce losses while maintaining

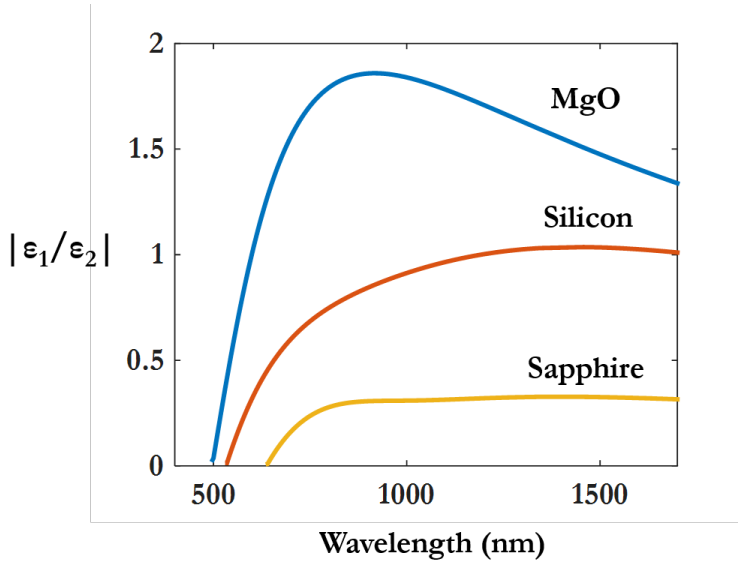


Figure 4.14: Reactive sputtering highlights substrate dependence - SPP Figure of Merit. Losses do not increase as fast as the metallic character of the film increases.

or increasing the metallic character by studying a wider range of reactive sputtering ratios. Some variation has been documented previously [45, 68]; Here, we extend the frequency range into the longer visible and near-IR wavelength regimes. In addition, we test multiple substrates simultaneously to ensure identical deposition conditions. An important sidenote here is that the particular gas ratios used in this set of experiments will hold only for this particular chamber geometry, target-substrate distance, etc. as discussed in Chapter 2. The ideal sputtering ratios should be expected to vary in different sputtering chambers.

The values of ε_1 versus λ, plotted for TiN deposited on Si, Sapphire and MgO substrates respectively, are shown in Figures 4.15(a-c), documenting a very different role of reactive sputtering for TiN deposited on the differing substrates. Note the difference in magnitude of ε_1 on MgO versus the other substrates. The reactively sputtered TiN films on MgO clearly show the best metallic performance of all films formed in these experiments. The behavior of these metallic films is clearly distinctive and superior to films that were either non-reactively sputtered (Ar:N_2 ratio = 40:0 sccm) or reactively sput-

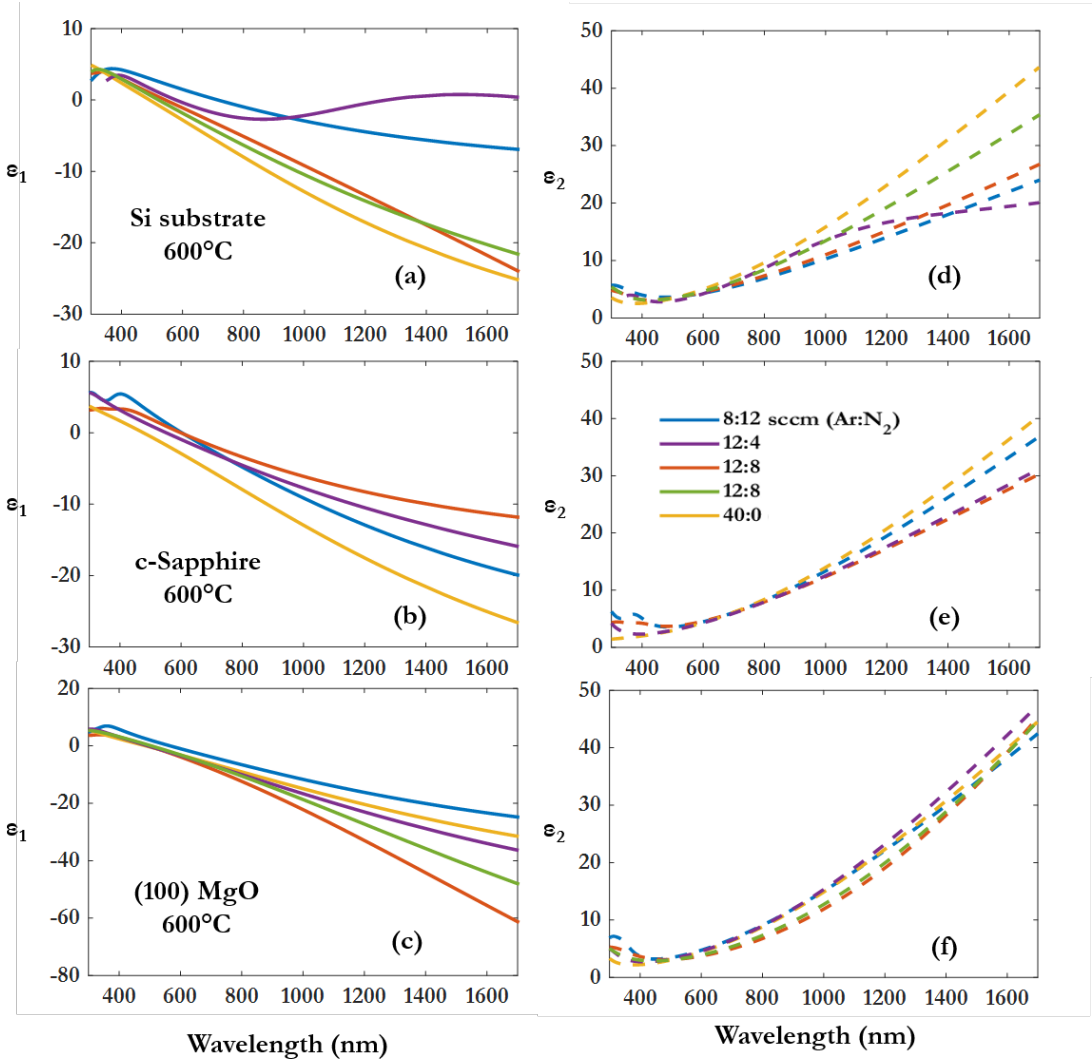


Figure 4.15: Reactive gas variation on silicon, sapphire, and MgO substrates at a substrate temperature of 600°C. Samples: — TiN22, — TiN29, — TiN23, — TiN30, — TiN27

tered with different gas compositions. As a test of reproducibility, several conditions were re-tested and exhibited similar results. An example is shown in Figures 4.15(a,c) which include a second 12:8 sccm Ar:N_2 film. For both the Si and Sapphire substrates, non-reactive sputtering produced more metallic TiN under all conditions tested in this set of experiments as compared to reactive sputtering.

This lends credence to the earlier argument that the substrate can play an important role as a lattice template for film growth.

In addition, by studying ε_2 versus λ for TiN films sputtered onto the three different substrates as shown in Figure 4.15(d-f) we notice some interesting trends. The first is that although the magnitude of ε_1 varies significantly across substrates, the magnitude of ε_2 is quite similar among the TiN deposited on all MgO, c-sapphire substrates as well as the more conductive films on silicon. This signifies that in general the FOM of the TiN films sputtered on MgO substrates under most of this conditions will in general be the highest and therefore MgO, the best substrate of the three to use for plasmonic applications requiring travel of surface plasmons. In addition, since the ε_2 curves are grouped so closely together this suggests that perhaps the optical losses in these TiN films on MgO and sapphire substrate are dominated not by simple Drude losses, but for example by scattering at grain boundaries or other optical losses. It also suggests the possibility that perhaps with further optimization of the growth conditions that these optical losses have the potential to be further reduced.

4.4.4 Ar-Bias Sputter Cleaning of Substrates prior to Deposition

We have now seen multiple instances which provide evidence of the impact of the substrate on the TiN film growth. As described in Chapter 2, the AJA sputtering chamber used has the ability to apply a bias to the substrate which can be used to sputter clean the substrates in-situ with an Ar plasma prior to sputter deposition. This sputter cleaning can remove any surface contamination or thin oxide layers prior to sputter deposition of the TiN thin film. To study the effect of an additional Ar bias clean on the different substrates in the vacuum chamber prior to sputtering, two separate sputtering runs were done with identical conditions: reactive magnetron sputtering for 60 minutes with Ti target at 600°C, 8:12 sccm Ar:N_2, 4mT deposition pressure, with 200W direct current. In the first deposition (TiN22), the sapphire and Si substrates were ultra-sonicated in acetone, followed by isopropyl alcohol, and then N_2-dried prior to entering the chamber. No bias was applied to the substrates under vacuum prior to

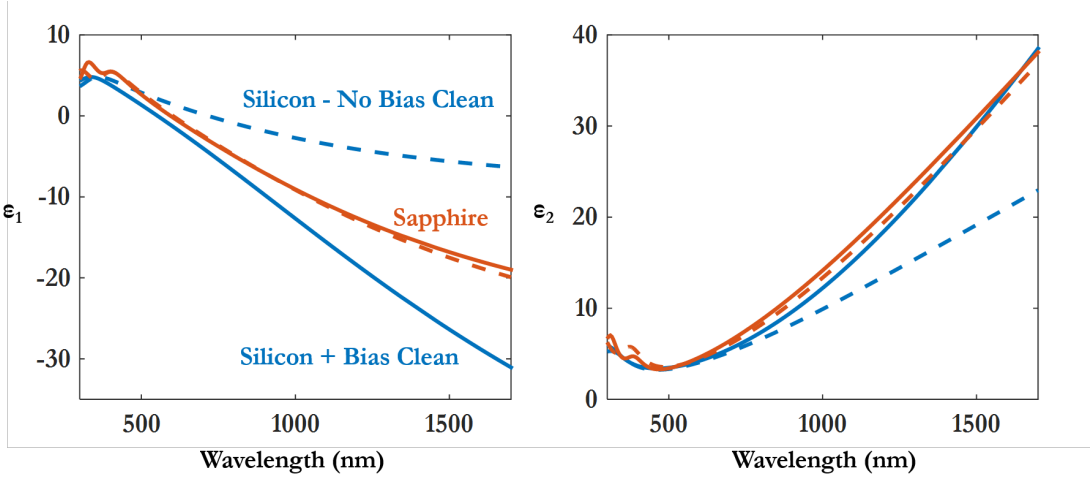


Figure 4.16: Cleaning the surface of silicon wafers using an Ar bias plasma prior to TiN thin film deposition is crucial to remove the oxide and surface contaminants and expose the Si lattice before sputtering. Using an Ar bias on sapphire wafers does not improve the film quality. Solid and dashed lines denote: (—) bias clean of substrate immediately prior to sputter deposition, (- - -) no bias sputtering pre-clean. Samples: TiN21 vs TiN22

or during sputtering. The Ti target was pre-sputtered for 11 min with the shutter closed and the film was sputtered for 60 minutes starting from a base pressure of 9.8 x 10^{-7} after heating to 600°C (7.7 x 10^{-8} prior to heating). The resulting films were 31nm thick on sapphire and 41nm on Si. The second deposition (TiN21) had the same conditions however a 5 min Ar bias sputtering clean was done of the substrates before the Ti target pre-sputter. The base pressure for this deposition was also higher, 2.5 x 10^{-6} Torr after heating to 600°C (3.2 x 10^{-7} prior to heating). The films were sputtered for 60 min resulting in 34nm films, both on sapphire and on Si.

The Ar bias clean of the substrates prior to sputtering did not significantly affect the optical behavior of the resulting TiN film when it was deposited on a sapphire substrate (Figure 4.16). Hall resistivity measurements confirmed only a small electrical difference in the films with ρ = 250 $\mu\Omega$-cm for the Ar bias cleaned film and ρ = 343 $\mu\Omega$-cm for the film without bias clean. There is however, a significant difference in metallic character of the films deposited on different silicon substrates in the two runs. The sample deposited after the 5 min applied bias clean was much more metallic (more

negative ε_1 and as expected according to Drude model, therefore also larger ε_2 than the samples which had no applied bias to remove surface oxides and contaminants prior to the sputter deposition. We hypothesize that the bias removes the native oxide from the silicon substrate exposing a fresh layer of silicon which serves as a better template for TiN film growth.

4.4.5 Applied Substrate Bias during Deposition

One of the stated advantages of TiN over other more traditional plasmonic materials is its potential for CMOS compatibility. For full compatibility, low temperature deposition of metallic TiN is necessary. The discussion so far has assumed that high temperature was necessary to sputter metallic TiN suitable for plasmonic applications; however, we discovered that films with large magnitudes of negative ε_1 can also be sputtered *even at room temperature* by applying an additional substrate bias. It was confirmed that others have also seen this effect in optical studies of sputtered TiN on silicon [26] substrates however we extend the effect to MgO and sapphire substrates and improve the metallic character. As shown in Figures 4.17(a-c), drastic improvements in metallic character of TiN films sputtered onto sapphire substrates, even at room temperature, can be achieved with the addition of an $\approx$ 100V bias. In addition, highly metallic TiN films are also sputtered onto MgO at room temperature whereas previously, elevated temperature was required. The drawback to this method is that films sputtered with the additional bias tend to be slightly rougher and have more defects than films sputtered at elevated temperatures. These initial results suggest, however, that CVD or ALD deposition of metallic TiN films, for example, is also likely possible at low temperature with proper optimization. Additionally, the ability to deposit plasmonic-quality TiN at room temperature allows for successful deposition onto a larger variety of substrates. One such example will be discussed in Chapter 7 where this method is used to create plasmonic TiN pyramids in collaboration with the Eric Mazur Research Group (Harvard University). Of final note, compared to the case of elevated substrate temperature *without bias* as shown in Figure 4.15, in this case *with bias* as shown in Figures 4.17(d-f), the losses tend

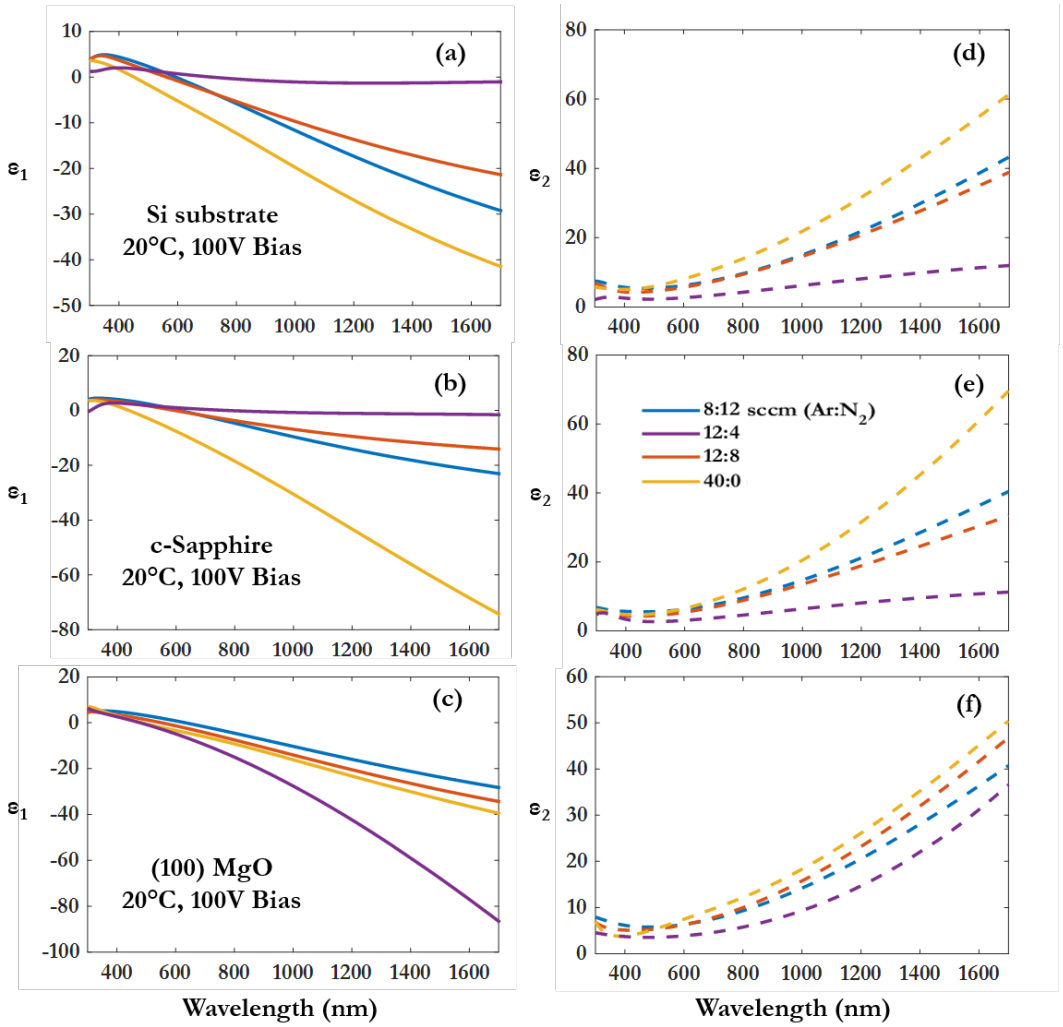


Figure 4.17: Reactive gas variation on silicon, sapphire, and MgO substrates at 20°C with addition of approx. -100V applied substrate bias. Samples: — TiN41, — TiN44, — TiN39, — TiN37

to align more closely with the metallic character of the film suggesting that they are influenced more strongly by the overall number of carriers. MgO does still seem to be the best substrate choice however based on the ratio of the losses as compared to the metallic character.

In summary, to deposit TiN films with the largest negative ε_1 which are best suited for plasmonic applications, care should be taken to reduce oxygen contamination. In addition, increasing the film

crystallinity is also helpful as will be discussed in more detail in Chapter 6. Previous studies of TiN formation have suggested addition of a substrate bias [93, 128], a closer target-substrate distance during sputtering [129], a lower deposition pressure [129], faster deposition rate [130], low energy ion bombardment [131], and higher substrate temperature [61, 130] during sputtering as potential methods of reducing the oxygen contamination and increasing the crystallinity. We have just discussed several of these factors and highlighted those which are critical to sputter metallic TiN film for plasmonic applications, describing their effects. Based on our experiments, the most important of these is to deposit the TiN films either at high substrate temperature and/or with an additional applied bias to the substrate. By using either of these methods, the result is that the oxygen content of the film is decreased and a more metallic film is formed. Additionally, the target should always be pre-sputtered before deposition to remove surface oxides and the base chamber pressure should be as low as possible.

5

Atomic Composition and Chemical Bonding of TiN Thin Films via X-ray Photoelectron Spectroscopy (XPS)

While significant time and effort during this work was concentrated on modeling the optical behavior of these materials, preliminary studies into the associated microstructure were also performed in an effort to better understand the potential underlying causes of the significant differences in optical behavior. As hinted at in the previous chapter, it was determined that both the *chemical composition*

of the film as well as the *crystallinity* had a significant impact on the optical properties.

In this chapter, x-ray photoelectron spectroscopy (XPS), a technique to measure the both the elemental composition and the chemical bonding within the films will be explored with several important results noted. Our first observation was that the overall Ti:N:O atomic ratio roughly correlated with the optical behavior. Films exhibiting a large atomic percent oxygen overall behaved more like dielectrics and films with less oxygen incorporation showed more metallic behavior, which is perhaps not surprising. We also found, however, a middle regime in which the optical behavior correlated more closely with how these oxygen impurities were bound in the film, rather than the overall impurity concentration. In this chapter, first the XPS technique will be explained and then the chemical binding and composition of our TiN films measured via XPS will be correlated with the deposition conditions and metallic character. Finally, the oxidation of these films will be briefly discussed.

5.1 X-ray Photoelectron Spectroscopy (XPS) Introduction

XPS is a surface sensitive spectroscopy technique most commonly used to determine the chemical composition as well as chemical bonding of components within a material.

5.1.1 Basic Theory

XP spectra are obtained by irradiating a sample with incident x-rays with a particular energy $\hbar\omega$ which is known depending on the type of x-ray source. The x-rays penetrate the material and eject core electrons which have binding energy ($E_B < \hbar\omega$). The electrons which escape the material are collected and their number as well as kinetic energy of outgoing electrons (E_{e^-out}) is measured.

$$\mathrm{E_{e^-out}} = \hbar\omega - \mathrm{E_{BE}} - \Phi_{\mathrm{spe}} - \mathrm{E_{charging}}$$

If a low energy electron flood gun is used to reduce charging, the energy of these electrons must be subtracted ($E_{charging}$) as well as the spectrometer work function Φ_{spe}. Both quantities are known for a particular system and can be subtracted electronically. Therefore, the equation simplifies to the following (plus a constant):

$$E_K = \hbar\omega - E_B$$

For incident radiation with known energy $\hbar\omega$, by measuring the adjusted kinetic energy E_K of the ejected electrons, the binding energy of the ejected core electrons can be easily calculated. Since each material is defined by the energies of their core electronic transitions, this allows for the determination of chemical composition. This process is represented schematically in the energy level diagram in Figure 5.1. Smaller changes in energy can denote different types of chemical bonding for a particular element.

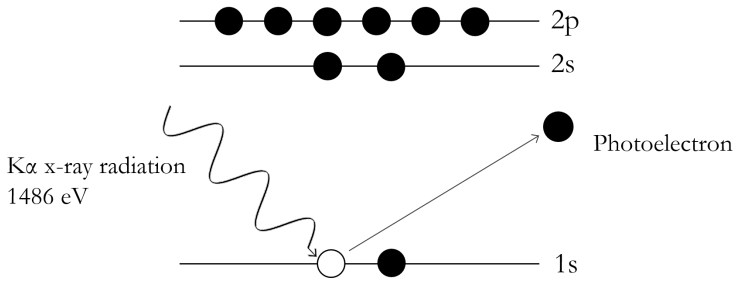


Figure 5.1: An electron energy level diagram depicting the X-ray photoelectron spectroscopy (XPS) process whereby incident monochromatic x-ray radiation ejects core electrons from the sample. The ejected electrons are collected and their kinetic energy measured.

There is a finite distance from which these electrons are able to escape from a material. For this reason, XPS is a surface technique measuring only electrons from approximately the first 10nm or less of thickness depending on the incident x-ray angle. Thinner cross sections of the surface may be examined, for example 3 or 5nm, can be accomplished by exciting from a glancing angle. Measurements can also be made deeper than 10nm into a film by sequentially etching away the surface in-situ

and remeasuring, however this is a destructive technique. The etching is typically done via Ar^{+} ion sputter-etching. The entire XPS measurement as well as etching process, if desired, is performed under vacuum, generally at pressures of 10^{-8} - 10^{-9} mBar. [132]

One subtlety which often shows up in XP spectra is the presence of spin-orbit splitting. If the photoelectrons being examined are from an s-orbital as shown in Figure 5.1, one peak will be shown for each electronic transition; however, if the electrons originate from p,d, or f orbitals, then doublets (or 2 energy peaks for each transition) will be shown due to spin-orbit coupling [132, 133]. An example of doublet peaks is seen in TiN XP data in which the Ti2p spectra splits into the $Ti2p_{1/2}$ and $Ti2p_{3/2}$ states. An example using reference TiN Ti2p data is shown in Figure 5.2.

A second subtlety which sometimes can be seen in spectra is the presence of "shake-up" lines. These peaks are a type of so-called "satellite" peak which will appear a few eV higher in binding energy than the main peak. They are due to electrons which instead of relaxing fully to their ground states, remain in excited states with energy a few eV higher than the ground state. This results in electrons which have

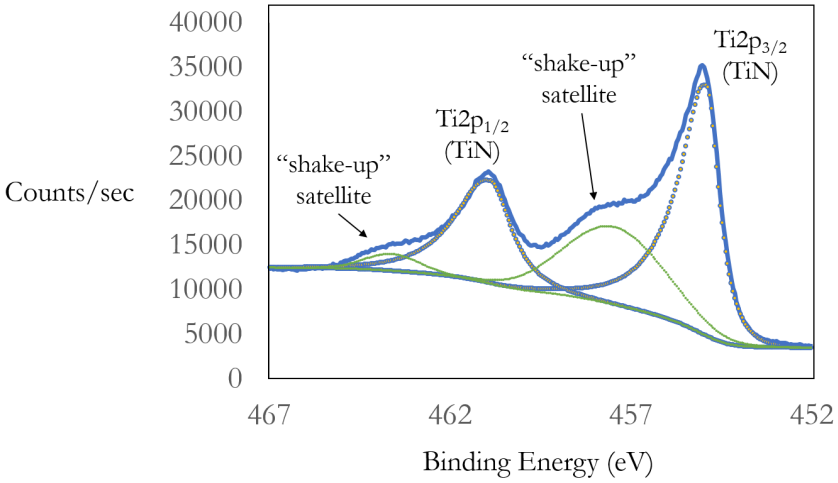


Figure 5.2: XPS Ti_{2p} reference data for TiO_2, and TiN films. Blue data points represent XP spectra. Open blue circles represent $Ti2p_{3/2}$ and $Ti2p_{1/2}$ doublet peak fits representing Ti-N bonding. Green lines represent TiN shake-up satellite doublet. Data adapted from [133]

slightly lower measured kinetic energies and therefore higher binding energies, leading to the second smaller peaks. Shake-up satellite peaks are routinely seen in TiN Ti2p XP spectra. An example of a doublet of these satellite peaks is also shown in Figure 5.2.

5.1.2 Experimental Setup

Titanium nitride (TiN_x) is known to be stable in stoichiometries ranging from $0.6 < x < 1.1$ [58] and variations in the stoichiometry have been shown to have an effect on the structural [61, 126, 134–137], electrical [63–67], and therefore, most importantly here, optical behavior [26, 100, 110, 138–141]. Therefore, XPS was one of the first measurements done to determine the relative chemical compositions of the resulting sputtered TiN and TiO_xN_Y thin films.

A Thermo Scientific K-Alpha system was used in the Center for Nanoscale Systems (CNS) at Harvard University. The x-ray source is an Al anode, producing Kα radiation which has an energy of 1486.6 eV and a line width of 0.85 eV [132]. Survey data was sampled from binding energies of -10 to 1350 eV in 1.000 eV energy steps and with a pass energy of 200eV with a dwell time of 10ms. Atomic percents were calculated from fitting the peaks of this survey data. An example of a typical survey spectra for TiN is shown in Figure 5.3. Select elemental binding data (Ti2p, N1s, O1s, C1s, Ar2p, Si2p) with higher resolution than the survey scans was taken using a 50eV pass energy, 50ms dwell time, and 0.100 eV energy steps. An example of a higher resolution Ti2p spectra was already shown for TiN in Figure 5.2. The available spot size range was 30-400μm however the largest spot size of 400μm was chosen for these studies. A low energy electron flood gun was used at all times to limit charging which causes shifts in the XP spectra. A tilt stage was available for angle-resolved measurements. A single Ar^+ ion source was used for depth profiling with sputter-etching done using ions with 1000eV energy and "high" current in steps of 20seconds unless otherwise noted.

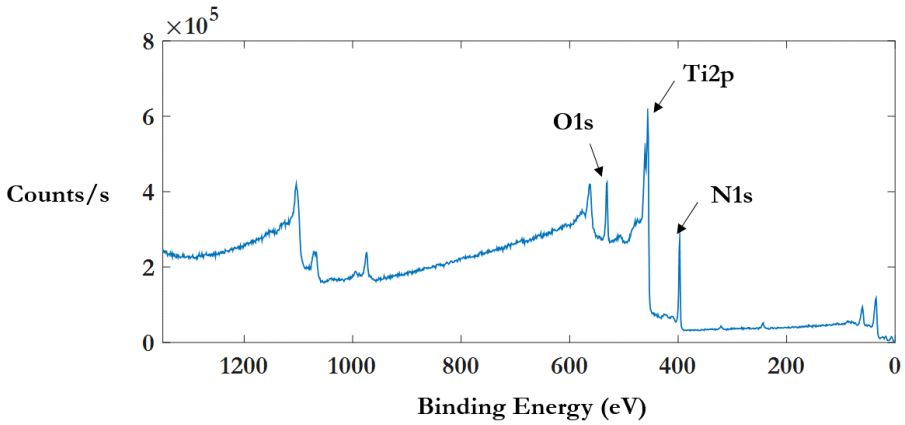


Figure 5.3: XPS survey reference spectra for TiN reference film. Peaks corresponding to O1s, Ti2p, and N1s binding energies are labeled. Sample:TiN23

5.1.3 Depth Profile Sputtering Rate Determination

Different materials are sputter-etched by Ar^+ ions at different rates. A TiO_xN_y thin film was measured at the surface then Ar^+ ion beam etched with an energy of 1000eV in 20 second steps until the Si substrate was reached to determine the approximate rate. Survey spectra were taken over a total of 42 levels (41 etch steps of 20 sec each). The atomic percent of Ti, N, O, C, Ar, and Si was calculated using the survey data after each etch step and the designated XPS peaks using the Avantage software and library sensitivity factors. The results are plotted in Figure 5.4. The film had a nominal thickness via SE models of 34nm. The etch time to reach the Si substrate ($\approx$ 700 sec) was used to calculate an etch rate of 0.04 -0.05 nm/sec and the etch time (sec) was converted to an approximate etch depth (nm).

5.2 Correlation of Deposition Conditions with Chemical Composition and Bonding

In the example plotted in Figure 5.4, the film was determined to be only "moderately metallic" by SE optical modeling and as seen via XPS measurements, this film contained $\approx$ 20-30% oxygen. We ob-

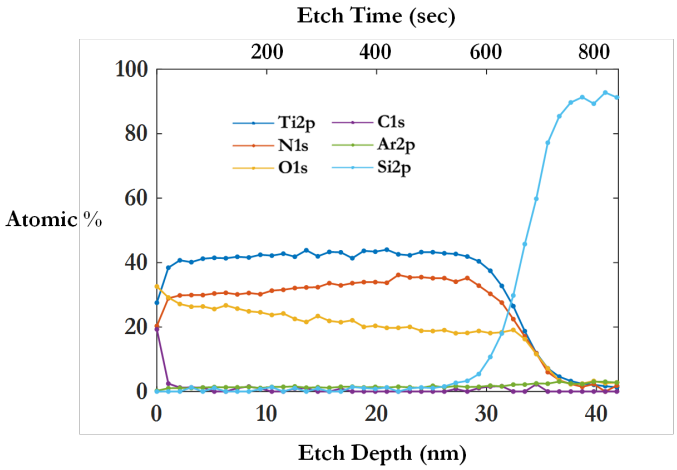
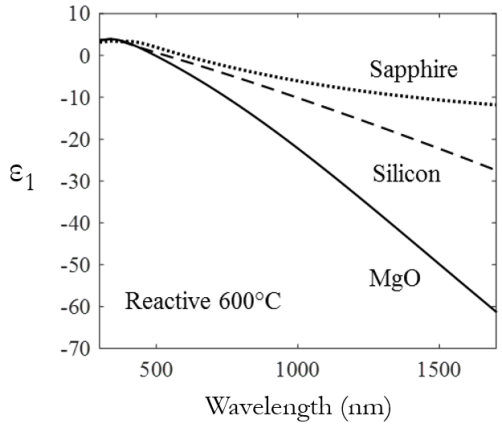


Figure 5.4: A TiO_xN_y thin film was depth profiled through to the substrate measuring the atomic makeup throughout via XPS measurements. The approximate etch rate was 0.05nm/sec. Sample: TiN21 Si4

served as a general rule that the overall Ti:N:O ratio roughly correlated with the optical behavior in a broad sense; for example, films with > 25 - 30 atomic percent oxygen overall behaved more like dielectrics and films with < 10 - 15 atomic % oxygen in general showed quite metallic behavior. In short, oxygen incorporation critically affected the films' resulting properties. In the middle regime however, when films contained near 15-20 at% oxygen, the optical behavior correlated more closely with how these oxygen impurities were bound in the film, rather than the overall impurity concentration. In this section, I will discuss these trends in further detail as well as the method for analyzing the chemical bonding within these films beyond simple elemental analysis. The discussion of the origin of this unintentionally incorporated oxygen as well as methods to reduce it will follow to conclude the chapter.

5.2.1 Dependence of Metallic Character on Oxygen Content

Recall the optical behavior of the TiN films discussed in Section 4.4.2 which were simultaneously deposited at 600°C via reactive sputtering onto three different substrates. The optical data is plotted again below for reference in Figure 5.5.



Substrate	MgO	Sapphire	Silicon
Ti:N ratio	1:0.93	1:0.78	1:0.85
Atomic % O	17.5	25.4	21.7

Figure 5.5: Real permittivity of TiN films reactively sputtered onto different substrates at 600°C and corresponding Ti:N ratio and Atomic % oxygen after removal of surface oxide as measured via XPS. This data corresponds to that plotted in Figure 5.6. Samples: TiN23 on Si, Sapphire, and MgO substrates

XP spectra were taken at the surface of each of these films and in the bulk of the film after a 20 second, 1000eV Ar^+ ion etch to remove the thin ($\approx$ 1nm) surface oxide. The measured chemical composition both at the surface and within the film after the native oxide is removed are plotted for these three TiN/TiO_xN_y films in Figure 5.6. The first thing to notice is that all films exhibit a high oxygen presence when the scan region includes the surface (top row). The surface scans measured atomic % oxygen from 26-32%. A large percentage of this is due to the thin TiO_2 surface oxide which is known to form on TiN under ambient [50, 136, 142–144]. There is also a large carbon contamination at the surface, from 12-18%. This contamination is likely higher on the sample sputtered on MgO due to additional handling and testing of this sample as compared to the others.

After removal of the surface oxide, the elemental makeup of the film remains fairly constant throughout the depth of the film and the relative percentages of elements within in each film can be easily compared. Therefore, the most important takeaway from Figure 5.6 is the difference in the relative Ti:N:O ratios of the films after removal of the oxide layer (bottom row). The film on MgO which exhibits the most metallic electrical and optical behavior has a Ti:N ratio which is close to stoichio-

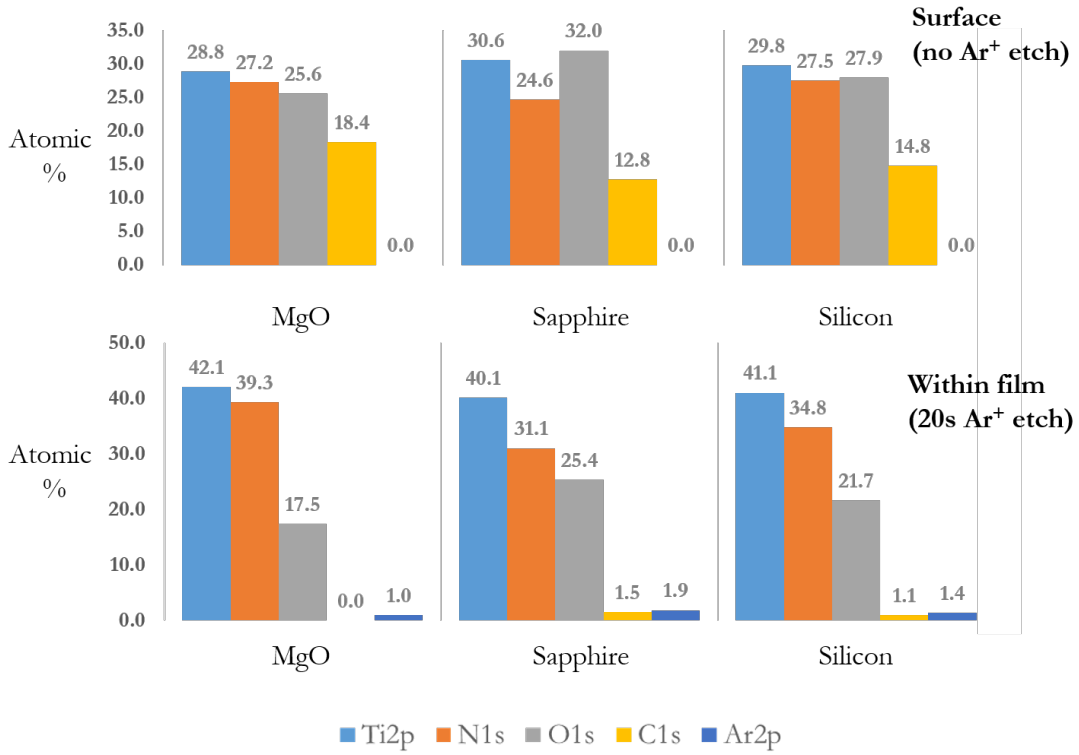


Figure 5.6: Measured chemical composition (atomic %) via XPS at surface and after Ar^+ sputter etch of surface. Samples: TiN23 on Si, Sapphire, and MgO substrates

metric within the film bulk (1 : 0.93) and has only 17.5 at% oxygen. The more "moderately metallic" film on silicon is more nitrogen-deficient with a Ti:N ratio of only 1 : 0.85 and higher oxygen content at 21.7 at%. Finally, the TiO_xN_y film on sapphire which has an ε_1 which only dips a small amount below zero and therefore may be considered only "slightly metallic" has a Ti:N ratio of 1 : 0.78 and a significant amount of oxygen still within the bulk film at 25.4at%. The TiN film sputtered onto the highly lattice-matched substrate (MgO) showed a significantly lower atomic % oxygen suggesting that the substrate may serve as a template for film growth as will be discussed further in Chapter 6.

In general this trend seemed to hold over the initial range of films deposited. Films behaved more like dielectrics or metals depending on the % oxygen incorporation in the film. Films with >30 at%

oxygen behaved as dielectrics. From about 20-30 at% oxygen the films were more moderately metallic and when the oxygen content was <15-20% films in general were conductive. However, in the metallic cases, the way in which the nitrogen was bound within the film and also the crystallinity of the film also became important.

As an example of a case when this trend is not explicitly followed, the atomic % was determined by XPS survey data for films deposited at 600°C onto MgO substrates over a range of different gas compositions (specified as a ratio of $Ar:N_2$ sccm). Since the substrate is lattice-matched well to the growing TiN films and the depositions are all done at 600°C, all films are at least moderately metallic, putting them into the range where not only the Ti:N:O ratio is important to determining the final optical constants but also the chemical bonding. The corresponding optical SE models for these samples are plotted again for reference in Figure 5.7. The elemental composition of each sample was calculated via

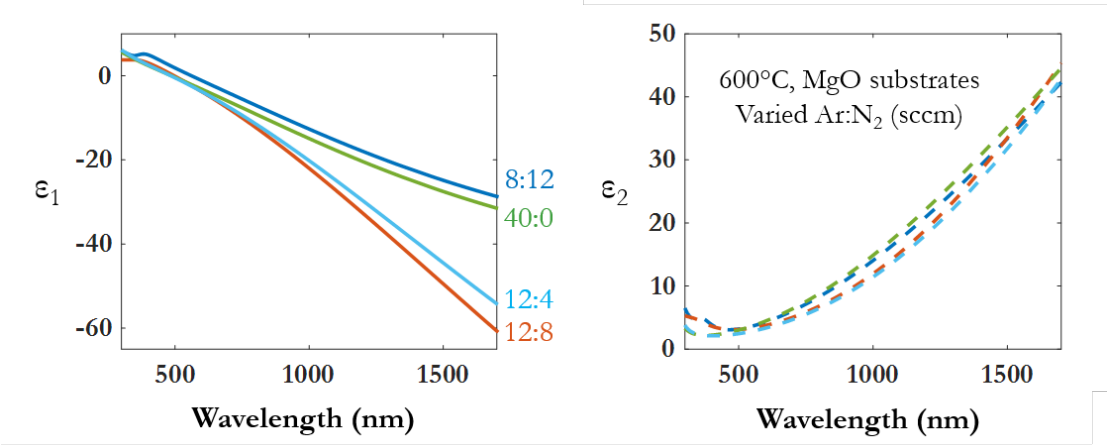


Figure 5.7: Permittivity of TiN sputtered on MgO over wide range of gas compositions determined via SE. Samples: TiN22, TiN23, TiN27, TiN29 on MgO substrates

XPS depth profile using the atomic survey measurements. The results are displayed in Figure 5.8 after removal of the surface oxide in order of increasing metallic character as determined by the SE optical models. The sputtering gas ratios are displayed on the figure in the format $Ar:N_2$ sccm.

As was done in the previous section, the atomic percent values are calculated from the Ti2p, O1s,

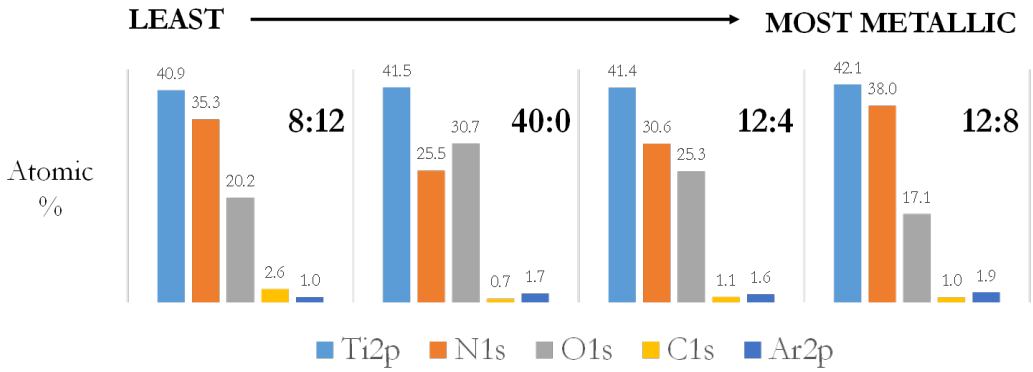


Figure 5.8: Atomic % via XPS after 40s Ar^+ sputter etch of surface on TiN sputtered on MgO over wide range of gas compositions

and N1s peaks and the Ti:N ratios are compared to see how close to stoichiometric the films are. The values for C1s and Ar2p are small away from the surface, ranging from only 0.7 - 2.6% in these scans and are thus not included. The results are shown in Table 5.1. In accordance with our previous observations, it would be expected, based on stoichiometry and oxygen %, that the film deposited at 12:8 $Ar:N_2$ sccm would be most metallic followed by the film deposited at 8:12 sccm, 12:4 sccm, and that finally the film sputtered at 40:0 sccm (or the non-reactively sputtered film) would be the least metallic. Upon examination of the SE data however, it can be clearly seen that this data does not follow that trend.

	Deposition Conditions ($Ar:N_2$ sccm)			
	Least	–>	Most Metallic	
	8:12	40:0	12:4	12:8
Ti:N ratio	1:0.86	1:0.61	1:0.74	1:0.93
Ti	40.9%	41.5%	41.4%	42.1%
N	35.3%	25.5%	30.6%	38.0%
O	20.2%	30.7%	25.3%	17.1%

Table 5.1: XPS Ti:N ratio and atomic % oxygen for Metallic TiN corresponding to the samples in Figures 5.7 and 5.8 after 40s Ar^+ ion etching to sputter away surface oxide.

While the trend did hold for all of our initial films which had relatively high oxygen content and were mainly dielectric to only slightly metallic in nature as compared to significantly more metallic films, as this example shows, *the oxygen content alone does not describe the optical behavior of all TiN and TiO_xN_y films.* Earlier in this section, the trend was described in detail for a set of films which were reactively sputtered simultaneously onto different substrates. It may be expected that something different could be happening for films which are sputtered *non-reactively* rather than reactively sputtered, so that disagreement is not as surprising, but in the case of the film sputtered at 12:4 sccm there is also disagreement, so there also seems to be something else going on. Therefore, we tried to understand what was controlling the optical behavior of these films in this intermediate range by looking at the chemical bonding in further detail.

5.2.2 Effect of Chemical Bonding on Metallic Character

As it turns out, the Ti:N:O ratio can indeed give an indicator as to whether a film is expected to be quite dielectric or somewhat metallic, however the way in which the nitrogen is bound within the film and also the crystallinity of the film become quite important within this moderately metallic to metallic range. Therefore, next I will focus on the different chemical bonding possible within a TiN or TiO_xN_Y film with a specific focus on the N-bonding and how it affects the resulting optical properties of the films.

As discussed, the XPS survey scans are quite useful in determining the overall elemental composition of a material; however, the true power of this measurement technique lies in its ability to differentiate between small shifts in electron binding energy designating different types of chemical binding within a material. To see how elements are bound within a film, higher resolution scans are needed. There are 3 main components in TiO_xN_y films and therefore the high resolution data focused on are the Ti2p, O1s, and N1s spectra. C1s spectra is also included for reference. Examples of typical scans for metallic TiN films are shown in Figure 5.9. The blue lines show measured binding energies at the

surface of an as-sputtered film. The surface is then sputter-etched with 1000eV Ar^+ ions to remove the surface native oxide and adventitious carbon contamination. The resulting measured binding energies of the film underneath are shown in orange.

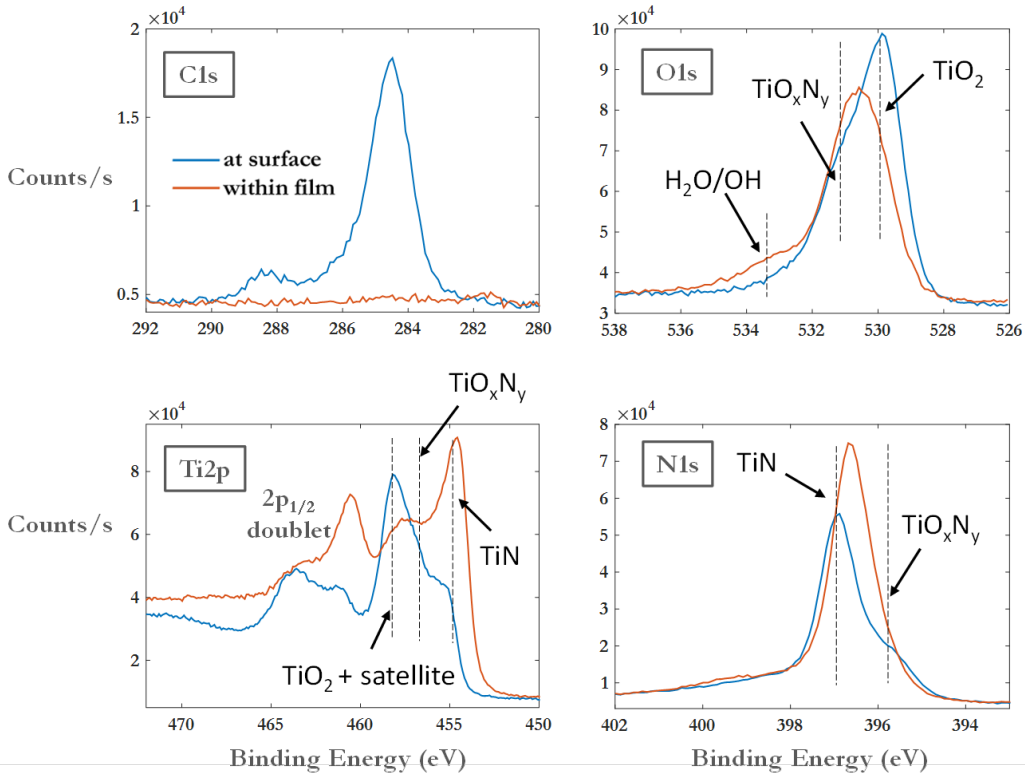


Figure 5.9: XPS high resolution reference scans of TiN thin films at the surface and after an Ar^+ etch removal of the surface oxide. — at surface vs. — within film after Ar^+ etch. Samples: TiN27 and TiN37 MgO

Several of the peaks in these high resolution scans have been roughly labeled to correspond to known chemical binding energies. There is often only a few eV or less difference between the peaks. Therefore, even at higher resolutions it can be hard to differentiate multiple overlapping peaks. As an example, examine the Ti2p scan which is a combination of at least four closely spaced $Ti2p_{3/2}$ peaks between about 454 and 459eV: TiN, TiO_xN_y, TiO_2, and shake-up satellite peaks as described in Section 5.1.1. In fact the shake-up satellite due to the TiN is so close in energy to the peak for Ti bound

as TiO_2 that it is quite difficult to separate the two. Note that these individual peaks are not shown for clarity but that vertical dashed lines delineate their approximate center energies. In addition, since this is a p-orbital, peak-splitting occurs and the same peaks will be repeated at higher energies but with reduced peak areas ($Ti2p_{1/2}$ doublet near 460-465eV). Thus, just as with SE modeling of optical data, meticulous care must be taken when fitting XPS data to model the data as best as possible.

Charging of the surface is one issue which may arise when fitting peaks to XP spectra, especially with the films that are more dielectric in behavior. Charging can shift the binding energy scale of the set of measured peaks. Therefore, it is important to have a method of calibrating the measured peaks to match standard values. A typical method is to use the adventitious C1s peak on the sample surface as a reference with a standard value at 284.8eV [145]. For TiN and TiO_xN_y films, an additional commonly used reference is to the well-known TiO_2 peak at 485.5 eV [135, 146–148]. The data can either be shifted in post-processing or if a low energy electron flood gun is present on the system, it may be possible to shift the data prior to the measurements by adjusting the flood gun beam energy. All data should be shifted by the same amount in a consistent manner. An exception is if ion sputter-etching is being used to depth profile through the material. In this case, the charge shift may need to be adjusted layer by layer.

Next, the chemical bonding is examined for the four TiN films studied in the previous section in an effort to determine why they do not seem to follow the trend of films with Ti:N stoichiometry closest to 1:1 and the lowest oxygen content being the most metallic. The permittivity was previously plotted in Figure 5.7. These films labeled in the order of least to most metallic as determined via SE data are those with sputtering gas ratio: 8:12, 40:0, 12:4 and 12:8 Ar:N_2 sccm.

Ti2p

First, the Ti2p scans (≈ 450-470eV) are compared. Titanium has many possible oxidation states from 0 to +4, ranging from titanium in Ti metal having an oxidation state of 0 with the main $Ti2p_{3/2}$ peak near 454eV [100, 133, 149] to that in TiO_2 with an oxidation state of +4 and $Ti2p_{3/2}$ peak near 458-9eV [100, 133, 135, 144]. Between these values, many additional compounds containing the elements Ti, N and O have also been measured including Ti attributed to being bound in: TiN from 454.2-456 eV [133, 144, 149], TiO at 455.3eV[135, 149],TiO_xN_y at 456.2eV[100] and Ti_2O_3 at 457.1eV[135]. Previous literature also attributed peaks in this region more generally to "intermediate" composition material after the subtraction of the expected TiO_2 and TiN peaks[144]. This wide range of available oxidation states, overlapping binding energies, and disagreement as to the exact energy of some of these transitions means that the peak fitting can be incredibly difficult in oxynitride films. Therefore to begin with, rather than fitting each peak individually, the general relatives shapes of these curves were evaluated qualitatively.

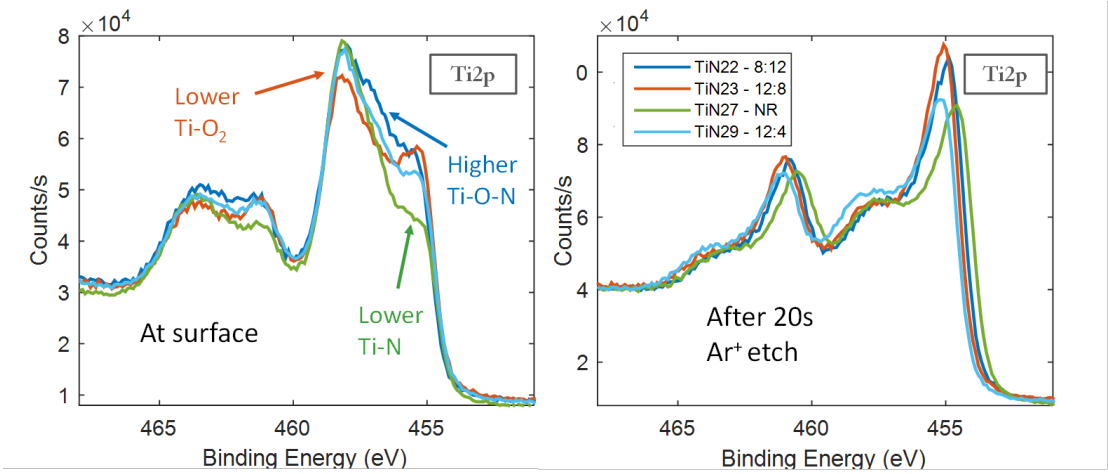


Figure 5.10: XPS high resolution reference Ti2p scans of TiN films deposited at 600°C with varied $Ar:N_2$ ratios

As shown in Figure 5.10, XPS performed at the surface of the sputtered film (left) shows a dominant

peak due to TiO_2 near 458-459eV in all four films due to the native oxide layer. There is however still a noticeable difference in the shapes of the peaks prior to sputtering. The most metallic film (12:8, orange) shows a lower intensity TiO_2 peak and higher TiN peak relative to the less metallic samples. In addition the non-reactively sputtered film (green) shows a quite significantly lower TiN peak. The least metallic film (8:12, dark blue) has a significantly increased signal in the region between the TiN and TiO_2 peaks which we attribute to a larger oxynitride content. Therefore, based only on this qualitative analysis of the Ti2p data, some suggestions begin to clearly emerge. In general, films which are more metallic seem to exhibit a higher Ti-N peak as compared to Ti-O_2 or Ti-O_xN_y binding. The differences are harder to see after sputter removal of the surface oxide in which case the spectra look quite similar, dominated by the TiN peak near 454-455eV and associated satellite near 458eV.

O1s

Next, the oxygen binding energies are analyzed qualitatively from about 525-540eV across the four same films. At the surface (Figure 5.11, left side), the data in general shows decreased intensity in both the lower energy TiO_2 peak and the higher energy oxynitride shoulder as the metallic character of the film increases. After sputter-etching to remove the surface oxide (right-side of figure), the contribution from the TiO_2 peak has decreased significantly and the spectra are dominated by the oxynitride shoulder with the most metallic film (12:8, orange) having the smallest remaining peaks. Interesting to note in this figure is that for the second most metallic film, as determined via SE (12:4, light blue) seems to still have a quite intense peak near 530-531eV. This agrees with the XPS survey data shown in Figure 5.8 which showed a higher % of oxygen within this film (25.3%) as compared to the more metallic (8:12, dark blue) film which had only 20.2% oxygen content. The binding energy of TiO which is also conductive is not documented in the literature so it is possible that part of this peak is due to oxygen bound in this way, leading to the more than expected metallic nature in this particular film based solely on the atomic composition; however, this discrepancy will next be explored further upon

examination of the N-bonding.

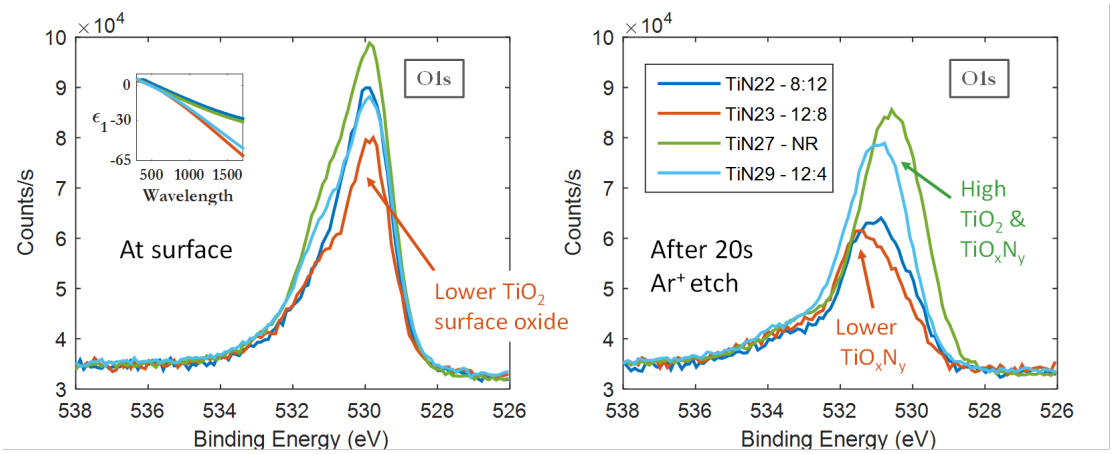


Figure 5.11: XPS high resolution reference O1s scans of TiN films deposited at 600°C with varied Ar:N_2 ratios

N1s

Finally, how the nitrogen was bound within the same four films was analyzed qualitatively from about 394-402eV. The data are plotted in Figure 5.12. In the literature, N-Ti has primarily been pinpointed near 396-397eV [100, 143, 144, 149] with metal nitrides in general being observed near 397eV as a rule of thumb [133]. We attribute the main peaks in our data near 397.3eV to N-Ti. There has commonly been a shoulder observed at lower energy compared to the N-Ti peak as is seen here, though the origin of this peak has not been determined [144]. It was however observed after oxidation was performed [144] and in another case, attributed to oxynitrides [100]. Based on the optical and electrical behavior as well as on the overall atomic make-up of these films, in our films we also attribute the low energy should to oxynitrides. Finally, there is a broad peak which appears at high energies (>398eV). High energy peaks have also been previously noted in several works with attribution to chemisorbed and adsorbed N_2 [100] but also potentially to a satellite feature [133].

Qualitative examination of the relative shapes and intensities of the N1s peaks sheds some light on a potential factor which significantly influences the optical behavior of these films. In short, it suggests

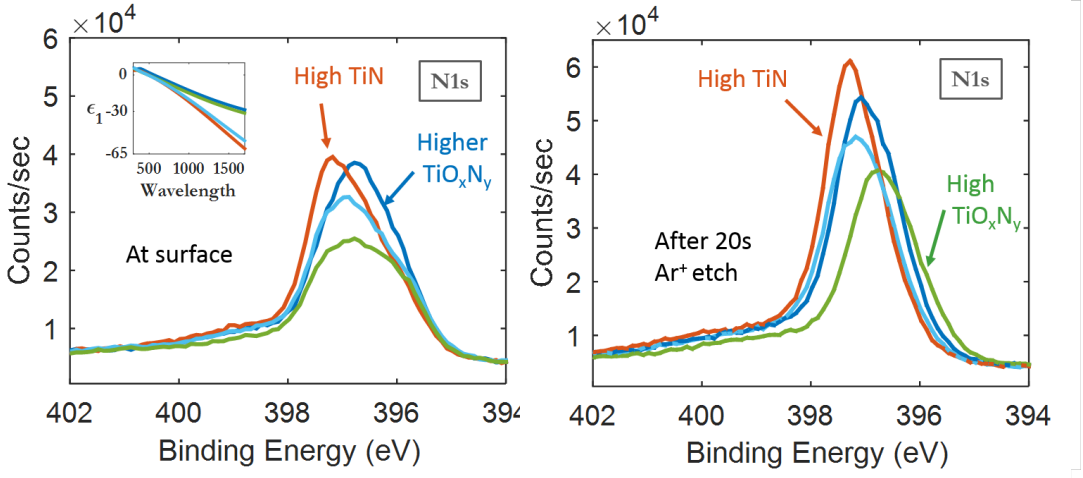


Figure 5.12: XPS high resolution reference N1s scans of TiN films deposited at 600°C with varied Ar:N_2 ratios

that films which have more N bound to TiN rather then in oxynitride form exhibit more metallic behavior. First, examining the left-hand side of the figure it can be seen that the most metallic film (orange) has an overall asymmetric shape tilted towards higher binding energy, with contributions from a large TiN peak and a smaller oxynitride shoulder at lower energies. The least metallic film on the other hand (dark blue) stands relatively upright with higher oxynitride contributions. After Ar^+ sputter-etching to remove the native oxide (right side of figure), the nonreactive film (green) is clearly dominated by oxynitride rather than TiN behavior, explaining its comparative less metallic behavior. The other less metallic film (8:12 - dark blue) is also shifted slightly to lower energies compared to the more metallic films (12:8 - orange and 12:4 - light blue) though this distinction is not as clear. The quantitative fits for these peaks reveal further detail which will be discussed next.

Just as with modeling and fitting of SE data, peak fitting of XP data is not always a straight-forward process. The most metallic (12:8 - orange) and least metallic (8:12 - dark blue) of these films were chosen as an example to demonstrate the fitting procedure while highlighting the differences clearly. The data is plotted again for these two films in Figure 5.13. The small dots signify the measured data points; the

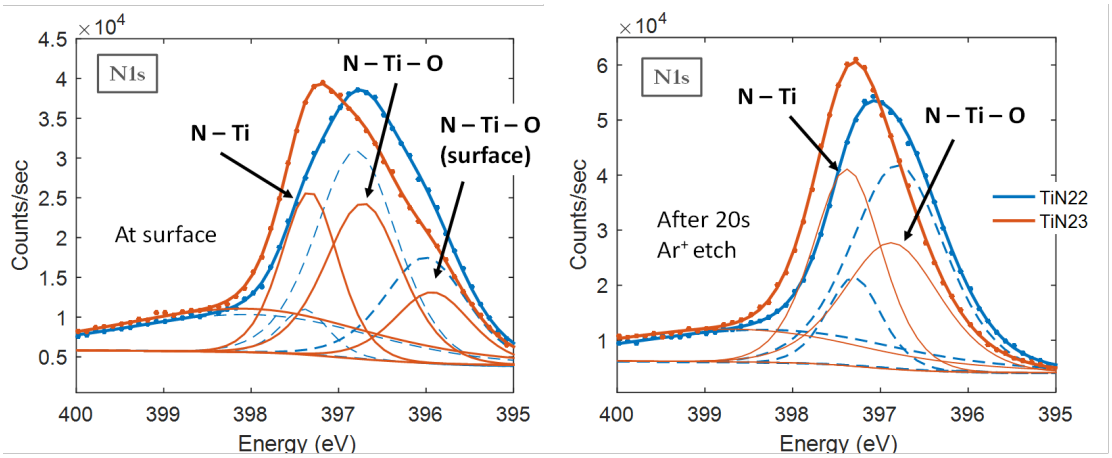


Figure 5.13: Example of Peak Fit Models for XPS high resolution reference N1s scans of TiN films. Samples: TiN22, TiN23 on MgO

thinner, lower intensity dashed lines (blue) and solid lines (orange) designate the 3-4 smaller peaks needed to fit the data; and finally, the thicker solid lines which follow along the data are the sum of the 3-4 fit lower intensity fit peaks.

Literature has reported the use of asymmetric peaks to fit N-Ti XPS data [144]; however, it was found that using symmetric peaks gave more consistent fits. In this case, symmetric peaks were therefore used to fit the N1s data. The best fits were determined by consistency across the depth profile and conformity with expected values as well as by minimization of the normalized χ^2 value and optimization of the Abbe criterion values as close to 1.0 as possible. The Powell fitting algorithm and built in "Smart" background, a modified version of the Shirley background subtraction [145] were used. The peaks were each constrained within a 0.2eV range and had a fixed Lorentzian/Gauss (L/G) product mix ratio of 50%. The fitting procedure was performed using the Thermo Avantage software v5.943. The data and associated fits for the other two films not shown in the simplified example, Figure 5.13 are now added in and all data and the corresponding peak fits are plotted together in Figure 5.14. The associated optical data is again plotted for reference.

Clearly, this figure is quite complex, but in fact it is fairly simple in comparison to the Ti2p and O1s

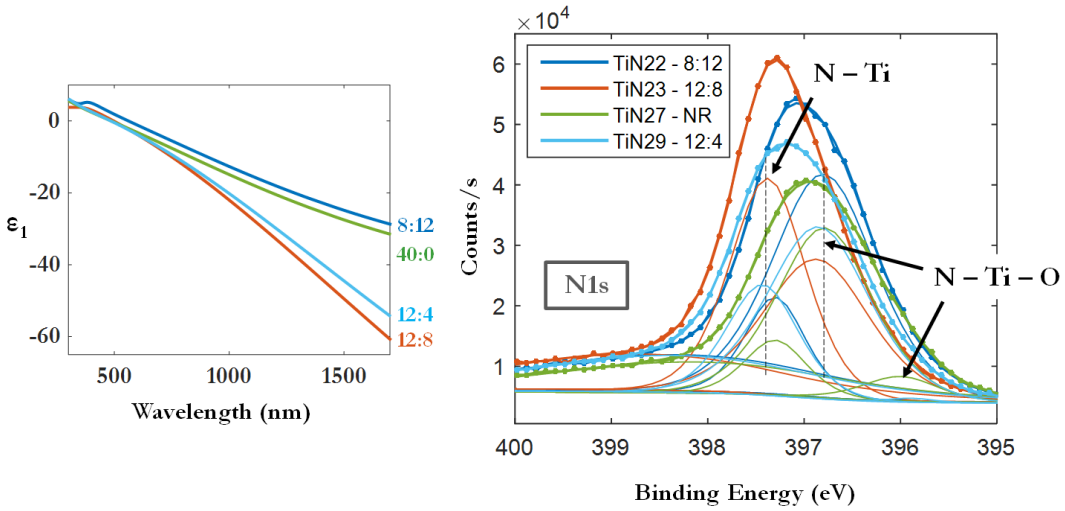


Figure 5.14: XPS high resolution reference N1s scans of TiN films including peak fits to describe N-bonding after Ar^+ sputter-etch. Corresponding data in Table 5.2

peak-fitted spectra. Even though it is complex, there are still several important things of which to take note. First, the models all include an N-Ti component close to 397.3eV. The center energy location is denoted by a vertical dashed line. This is at a slightly higher energy than the reported literature values closer to 397eV however is within an acceptable range. The intensity of this peak can be seen to vary with the more metallic films having more intense peaks. A second peak which we contribute to N-Ti-O binding is located near 396.8eV and corresponds well to the values suggested in the literature. These peaks are in general of higher intensity for less metallic films. Finally, only one of the films has a fourth peak and this is the non-reactively sputtered film with a small second oxynitride peak near 396eV. Peaks are seen at this energy on all films during the surface scan and thus, we have attributed this peak to a different form of oxynitride perhaps bound to TiO_2. Since the non-reactive film exhibits a higher TiO_2 percentage as shown in the O1s and Ti2p scans, this explanation is consistent. The basic peak fit parameters corresponding to the data plotted in this figure are shown in Table 5.2. The final column displays the atomic percent of each type of N-binding in each film as calculated using the area

under the curves. The data verifies the visual inspection, confirming that the most metallic films (12:8, orange and 12:4, light blue) have the higher amount of N-Ti as compared to N-Ti-O binding.

Depth Level	Peak	Peak BE	FWHM (eV)	Atomic %
TiN22 – 8:12 (Ar:N2) model 2 X^2 = 0.88 Abbe = 0.92	N – Ti	397.30	0.73	14.5
	N – Ti – O	396.80	1.27	58.0
	~~N – Ti – O~~	~~396.00~~	~~0.48~~	~~0.2~~
	N – ??	398.28	3.69	27.4
TiN23 – 12:8 X^2 = 0.96 Abbe = 0.80	N – Ti	397.38	0.93	39.2
	N – Ti – O	396.87	1.29	35.1
	~~N – Ti – O~~	~~395.80~~	~~1.63~~	~~0.2~~
	N – ??	398.68	3.61	25.4
TiN27 – nonreactive Model2 X^2 = 1.06 Abbe = 0.74	N – Ti	397.30	0.75	10.9
	N – Ti – O	396.79	1.17	52.5
	N – Ti – O	396.00	0.91	5.9
	N – ??	398.11	3.71	30.6
TiN29 – 12:4 X^2 = 1.08 Abbe = 0.95	N – Ti	397.43	0.87	21.6
	N – Ti – O	396.85	1.24	47.8
	~~N – Ti – O~~	~~395.89~~	~~0.55~~	~~0.5~~
	N – ??	398.33	3.65	30.1

Table 5.2: XPS high resolution reference N1s scans of TiN films deposited at 600°C with varied Ar:N_2 ratios

5.2.3 Effect of Substrate Bias on Oxygen Content and Nitrogen Bonding

If you recall from the previous chapter, by applying an additional substrate bias while sputtering, metallic TiN films were able to be sputtered onto a wide range of substrates at room temperature. Films which were sputtered with a bias were routinely measured via XPS to have oxygen contents of 10-12% and as low as 8%. This suggests that the bias either allows for preferential desorption of the oxygen incorporated during the sputtering process or that it creates more dense (less porous) films which leads to less oxidation through diffusion after the films are removed from vacuum. This observation is confirmed by previous studies [134].

The least and most metallic films studied in the previous section (at 600°C onto MgO at 8:12 and 12:8 sccm Ar:N_2 respectively) are next compared to a film sputtered at room temperature onto MgO but with an applied substrate bias of approximately 100V. The permittivity data for the three films which are compared is highlighted again for reference in Figure 5.15 and the chemical composition is compared in Table 5.3. Note that the most metallic film, deposited with the 100V bias had not only a lower percentage of oxygen at only 11.6%, but also an almost stoichiometric Ti:N composition, better than even the most metallic film sputtered onto Mgo at 600°C with 12:8 ArN_2 ratio.

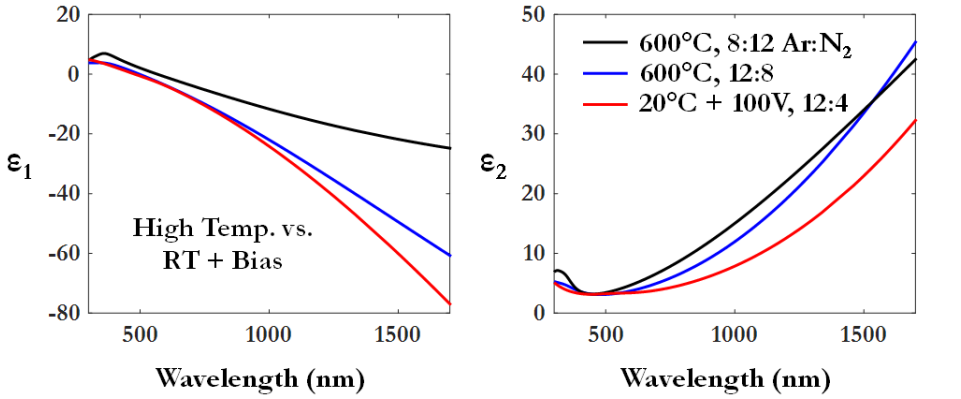


Figure 5.15: Permittivity reference data corresponding to XP spectra in Figure 5.16. Sample: — TiN22 MgO, —TiN23 MgO, — TiN44 MgO

	Deposition Conditions		
	Intermediate 600°C, 8:12	High Temp Metallic 600°C, 12:8	Low Temp + Bias Metallic 20°C, 12:4 + 100V
Ti:N ratio	1:0.86	1:0.93	1:0.98
Ti	41.4%	42.1%	43.8%
N	35.5%	39.3%	43.0%
O	21.1%	17.5%	11.6%

Table 5.3: XPS Ti:N ratio and atomic % Oxygen for Metallic TiN corresponding to the samples in Figures 5.15 and 5.16.

This relationship can be further quantified by examining the nitrogen bonding within these films as shown in Figure 5.16. The top two figures include the same data from Figure 5.13 but offset for clarity. As shown in the previous analysis, the film in which more N is bonded in oxynitride form (black curve) is less optically metallic than the film dominated by N-Ti bonding in the N1s scan (blue curve). In this figure, the difference is even more dramatic upon inspection of the film sputtered with additional substrate bias (red curve). The low binding energy shoulder due to the oxynitrides is far smaller in this case and the N-Ti peak is clearly dominant. The data corresponding to this figure is compiled in Table 5.4. Note also that the sample with applied bias exhibits lower optical losses.

To show that the hypothesis proposed in the previous section that the N-binding correlates closely with the metallic character applies over a broad range of samples, the optical properties of a set of samples sputtered again at different $Ar:N_2$ ratios, but now *at room temperature and with an applied substrate bias* were also measured. The N-binding within these films was as before compared to the relative metallic character as measured by SE. The SE models of the permittivity for these films are shown in Figure 5.17.

The peak fitting data and corresponding atomic percentages of N-binding in TiN versus in oxynitride form are displayed in Table 5.5. Just as in the previous case with the films sputtered at 600°C, the less metallic films have more N bound in oxynitride form whereas the more metallic films have more N

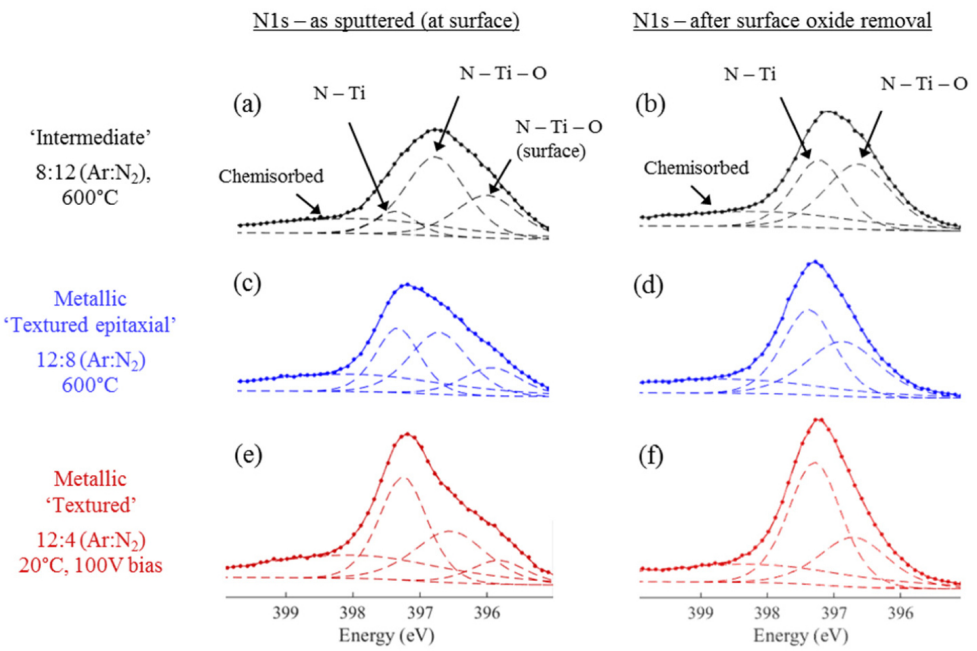


Figure 5.16: XPS N_{1s} data for "moderately metallic" film vs. highly metalllic films deposited at high temperature and at room temperature with bias. Sample: TiN23 MgO, TiN [127]

		At surface			Within film		
Peak	Energy (eV)	Intermed. 600°C	Metallic 600°C	Metallic 20°C+100V	Intermed. 600°C	Metallic 600°C	Metallic 20°C+100V
N - Ti	397.4	5.7%	24.6%	34.2%	14.5%	39.2%	46.8%
N - Ti - O	396.8	45.0%	31.3%	25.7%	58.0%	35.1%	24.7%
N - Ti - O	396.0	23.6%	14.3%	9.2%	-	-	-

Table 5.4: XPS atomic %N1s bonding data corresponding to Figure 5.16.

bound in TiN form. Also of note is the fact that the non-reactively sputtered film (green) does follow the trend but not quite as closely. This was also the case in the earlier high temperature study. The microstructure of non-reactively versus reactively sputtered films will be further compared in the next chapter to potentially explain these subtle differences using additional techniques including scanning transmission electron microscopy (STEM) and x-ray diffraction studies (XRD).

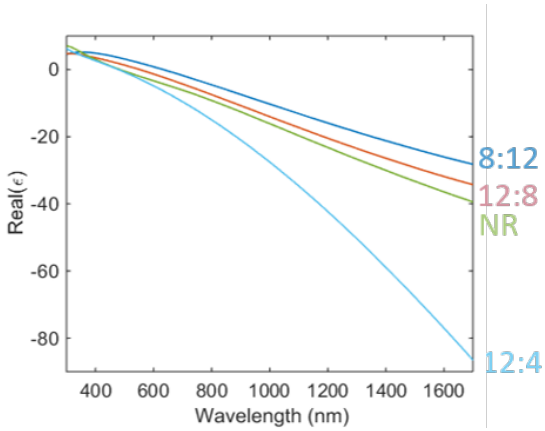


Figure 5.17: Ellipsometry reference data for TiN films deposited at 20°C plus 100V bias, varied Ar:N_2 ratio

Depth Level	Peak	Peak BE	FWHM (eV)	Atomic %
TiN41 – 8:12 (Ar:N2) model 1 X^2 = 1.03 Abbe = 0.94	N – Ti	397.27	0.85	18.3
	N – Ti – O	396.80	1.39	54.3
	~~N – Ti – O~~	~~395.89~~	~~0.48~~	~~0.3~~
	N – ??	398.30	3.60	27.1
TiN39 – 12:8 model 1 X^2 = Abbe =	N – Ti	397.22	0.75	14.6
	N – Ti – O	396.78	1.45	59.3
	~~N – Ti – O~~	~~395.92~~	~~0.59~~	~~0.8~~
	N – ??	398.30	3.53	25.3
TiN37 – nonreactive Model 5 X^2 = 1.75 Abbe = 0.59	N – Ti	397.27	0.89	48.9
	N – Ti – O	396.80	1.28	24.8
	N – Ti – O	396.00	1.47	0
	N – ??	398.53	3.74	26.4
TiN44 – 12:4 model 1 X^2 = 1.27 Abbe = 0.77	N – Ti	397.28	0.93	46.8
	N – Ti – O	396.70	1.22	24.7
	~~N – Ti – O~~	~~395.99~~	~~0.48~~	~~0.2~~
	N – ??	398.28	3.77	28.3

Table 5.5: XPS high resolution reference N1s scans of TiN films deposited at 20°C plus 100V substrate bias with varied Ar:N_2 ratios

5.3 Oxidation of TiN thin films

Throughout this chapter, we have shown that both the overall atomic % oxygen as well as the ratio of nitrogen bound as TiN versus in oxynitride form have shown significant correlation with the optical properties. The main questions which remain at this point are: why is there such a significant amount of oxygen unintentionally incorporated into these films and where does it come from? The depth profile used to determine the approximate etch rate in Section 5.1.3also shows the relative homogeneity of the film with the exception of a thin native oxide and adventitious carbon contamination at the surface. The figure is displayed here again for reference. TiN is thermodynamically stable however

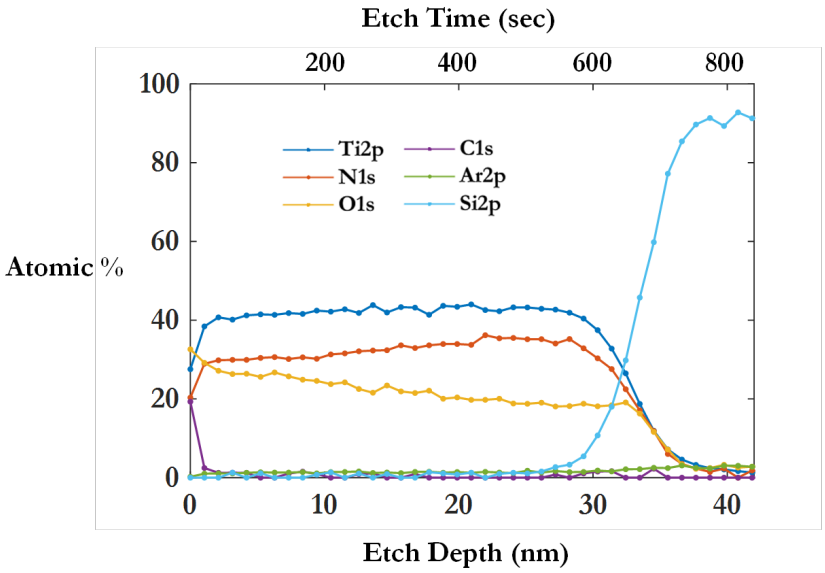


Figure 5.18: A TiO_xN_y thin film was depth profiled through to the substrate measuring the atomic makeup throughout via XPS measurements. The presence of a surface oxide is noted as well as oxygen content which is decreasing deeper into the film. Sample: TiN21 Si4

when exposed to air will oxidize since the reaction $TiN + O_2 \rightarrow TiO_2 + 1/2\, N_2$ is energetically favorable with $\Delta G° = -139$ kcal/mol [144]. Therefore, a thin native oxide layer as seen in the figure is expected at the film surface and has been confirmed in prior studies [50, 136, 142–144]. However, the thickness

of this surface oxide is less than 1nm and seems to be self-limiting and therefore does not explain the oxygen incorporated throughout the bulk of the film.

In Figure 5.18, it is also clear that the oxygen content is slowly decreasing from close to 30% at the top of the film (etch depth = 0nm) down to 18% near the silicon substrate. Over this same distance the titanium content is remaining stable near 41-43% and the nitrogen content is slowly increasing from 30 to 35%. One concern may be that the film is being significantly altered during the sputtering process, perhaps with preferential sputtering of oxygen as compared to nitrogen, increasing the N_2% and decreasing the O_2 % overall. Unfortunately, there is not agreement as to whether this is true or not. It has been shown the Ar^+ sputtering does not seriously alter the oxidation state of TiN films [149] but the possibility of preferential sputtering, chemical reduction, or atomic mixing due to the ion bombardment has also been suggested [143].

There are two main methods via which oxygen could contaminate the bulk of TiN films. First, it is possible that the oxygen is incorporated directly during film growth, either in the form of substitutional impurities for N in the Ti-N lattice, or in oxynitride form. In this case, the oxygen could come either from the introduced gases (Ar and N_2) or from remaining water vapor, CO_2, etc. in the chamber since the deposition rate is quite slow. The second possibility is that oxygen diffuses through the lattice after deposition upon removal from the sputtering chamber. There has been previous evidence that films sputtered at room temperature exhibited lower densities and higher resistivities due to a porous structure [123]. In this case, it might be expected that these porous structures allowed for easier oxygen diffusion and incorporation resulting in the large measured oxygen percentages.

In addition, epitaxially grown films have shown increased oxidation resistance as compared to polycrystalline films [150]. One possible explanation is that in nanocrystalline films, diffusion of oxygen along grain boundaries could form oxynitrides between grains. We do not have the capability to do structural measurement in-situ before removing the samples to atmosphere however, based on the measurements described throughout this chapter, we believe that both cases play some role in increas-

ing the oxygen content and modifying the optical properties of our films.

5.4 Using Si_3N_4 as Oxidation Resistant Capping Layer

In an additional effort to determine if oxygen is mainly incorporated during growth or if it diffuses through from the surface a Si_3N_4 capping layer was tested due to it also being a high melting temperature nitride [53]. Assuming that the sputter rate for Si_3N_4 is similar to that for TiO_xN_y calculated in Section 5.1.3, then approximately 1nm will be etched in 20 sec. Therefore, after 200 sec approximately 10nm has been removed. The expected thickness of the Si_3N_4 capping layer based on the sputtering rate is about 5nm (5 min deposition time). The substrate was another Si_3N_4 film which had been previously sputtered onto a Si substrate as shown in Figure 5.19.

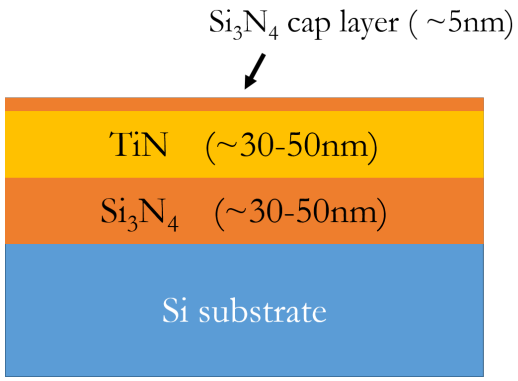


Figure 5.19: Schematic of TiN film sputtered with onto Si_3N_4 with Si_3N_4 cap. A full XPS depth profile was performed on this sample as shown in Figure 5.20. Sample:TiN35 SiNx on Si

An XPS depth profile was performed on this sample starting at the surface of the Si_3N_4 capping layer, fully through the TiN film and into the top of the Si_3N_4 substrate layer. The measured chemical composition (atomic %) throughout the film is plotted as a function of the etch time in seconds in Figure 5.20. The corresponding data is shown in Table 5.6. Since the Si_3N_4 capping layer film is expected to be about 5nm thick, if the etch rate is similar to that of the TiN at about 0.05nm/sec, it should be fully etched away after 100 seconds, but this is not the case. There is still a significant Si2p peak until

about 200sec, therefore either the Si diffuses into the top 5nm of the TiN film while sputtering or the etch rate of the Si_3N_4 is significantly slower than expected.

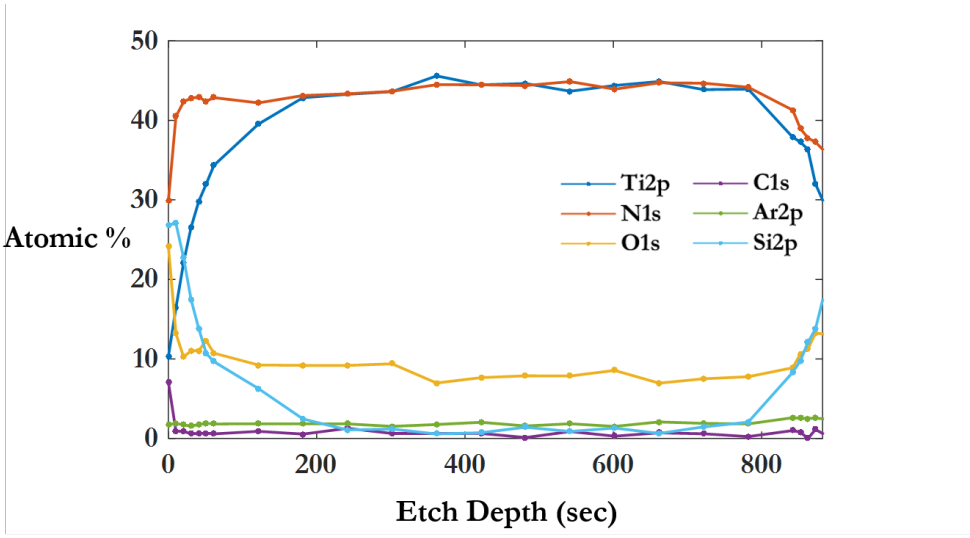


Figure 5.20: Depth profile of TiN film sputtered with bias and Si_3N_4 cap. Sample:TiN35 SiNx on Si

Etch Time (s)	0	20	40	60	120	180	240	300
Ti2p	10.3%	22.1%	29.8%	34.3%	39.5%	42.9%	43.3%	43.6%
N1s	29.9%	42.3%	42.9%	42.9%	42.2%	43.1%	43.3%	43.7%
O1s	24.1%	10.3%	11.1%	10.7%	9.2%	9.2%	9.2%	9.4%
Ar2p	1.7%	1.7%	1.8%	1.8%	1.9%	1.8%	1.8%	1.5%
C1s	7.1%	0.9%	0.6%	0.6%	0.9%	0.6%	1.3%	0.7%
Si2p	26.8%	22.8%	13.8%	9.7%	6.3%	2.5%	1.1%	1.2%

Table 5.6: Atomic % via XPS Depth Profile for TiN sputtered with Si_3N_4 cap. This data corresponds to that plotted in Figure 5.20.

More importantly however, once the capping layer is fully removed, the oxygen content seems to stabilize unlike the earlier case with the oxynitride depth-profiled film which decreased from about 30% at the surface to 18% about 30nm in. Once the silicon is gone within the bulk of the capped film (about 15-40nm etch depth and 300-800 seconds etch time) as can be seen in Figure 5.20, the oxygen

concentration is the lowest at about 7-9%. Within measurement error, the film is stoichiometric with a measured Ti:N ratio of 1:1. Therefore, based on on the first depth profile of the oxynitride film, we conclude that in dielectric films which are expected to be porous some diffusion occurs from the surface into the film bulk, but that there is also some constant level of oxygen incorporation into the films during the sputtering process itself (under these conditions, for example, approximately 7-8 at%). This experiment does also suggest the possibility of using a thin layer of Si_3N_4 to prevent oxygen diffusion into the film bulk for any application where a native titanium dioxide surface layer is undesirable.

As a sidenote, this experiment also verified that even under vacuum, the time for a monolayer of native oxide to deposit on the surface of a TiN film is very fast. The data from the previous figure was slightly modified from the raw data. In the raw data, there are vertical jumps at four specific etch times (60 ,300, 360, and 820 seconds) where the measurements were repeated. See Figure 5.21. In the actual

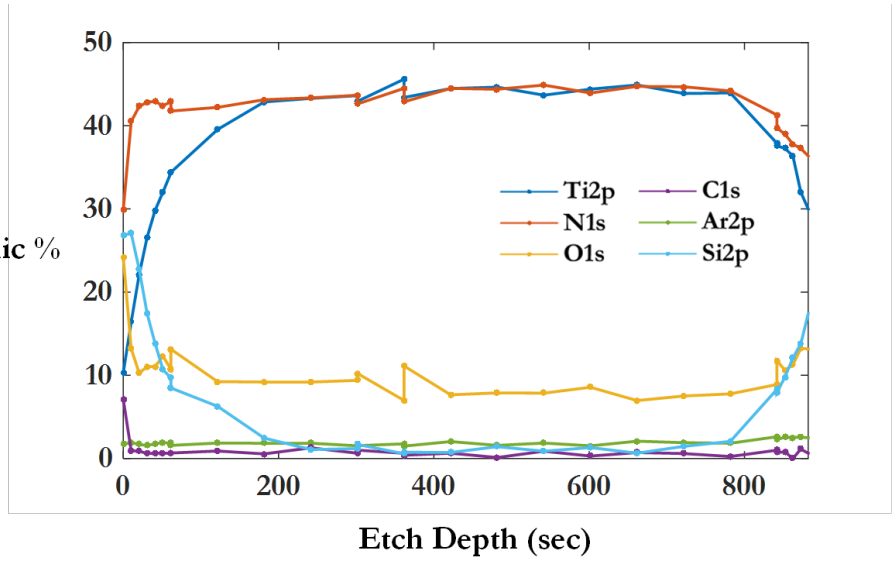


Figure 5.21: Depth profile of TiN film sputtered with bias and Si_3N_4 cap. Oxidation shown by small O1s peak increases at repeated etch depths. Sample:TiN35 SiNx on Si

experiment, high resolution measurements were taken at certain points and near the interfaces the

time steps were also shortened. Each change to the scan parameters required that a scan was repeated at the same etch depth, but after a finite amount of time (should be after only about one minute or less). The repeated scans were at the same etch depth but after a short time. In each case, they show up as sharp jumps in the depth profile data. In the previous figure (Figure 5.20) the first scan of each new section was removed. Upon closer inspection, it can be noted that in each case the atomic % oxygen increased by about 1-3% in the repeated scan. This signifies that oxidation occurred on the freshly sputtered surface during that short time, even under the high vacuum of the sputtering chamber.

6

Micro- and Nanostructural Properties of TiN Thin Films

The microstructure of a film can vary drastically as described by the Thornton and Anders models in Chapter 2. While it has been determined that a large portion of the variation of the optical behavior can indeed be described by the chemical composition and bonding within the films, preliminary studies into the micro- and nanostructure of the sputtered films were also undertaken for completeness since the microstructure is known to also have a significant impact on film properties. Films with a large variety in microstructure were sputtered during these studies, from textured epitaxial to

nanocrystalline growth. Figure 6.1 gives an idea as to the wide variety of microstructures observed. Labels including the deposition conditions ($Ar:N_2$ sccm ratio, deposition temperature (room temper-

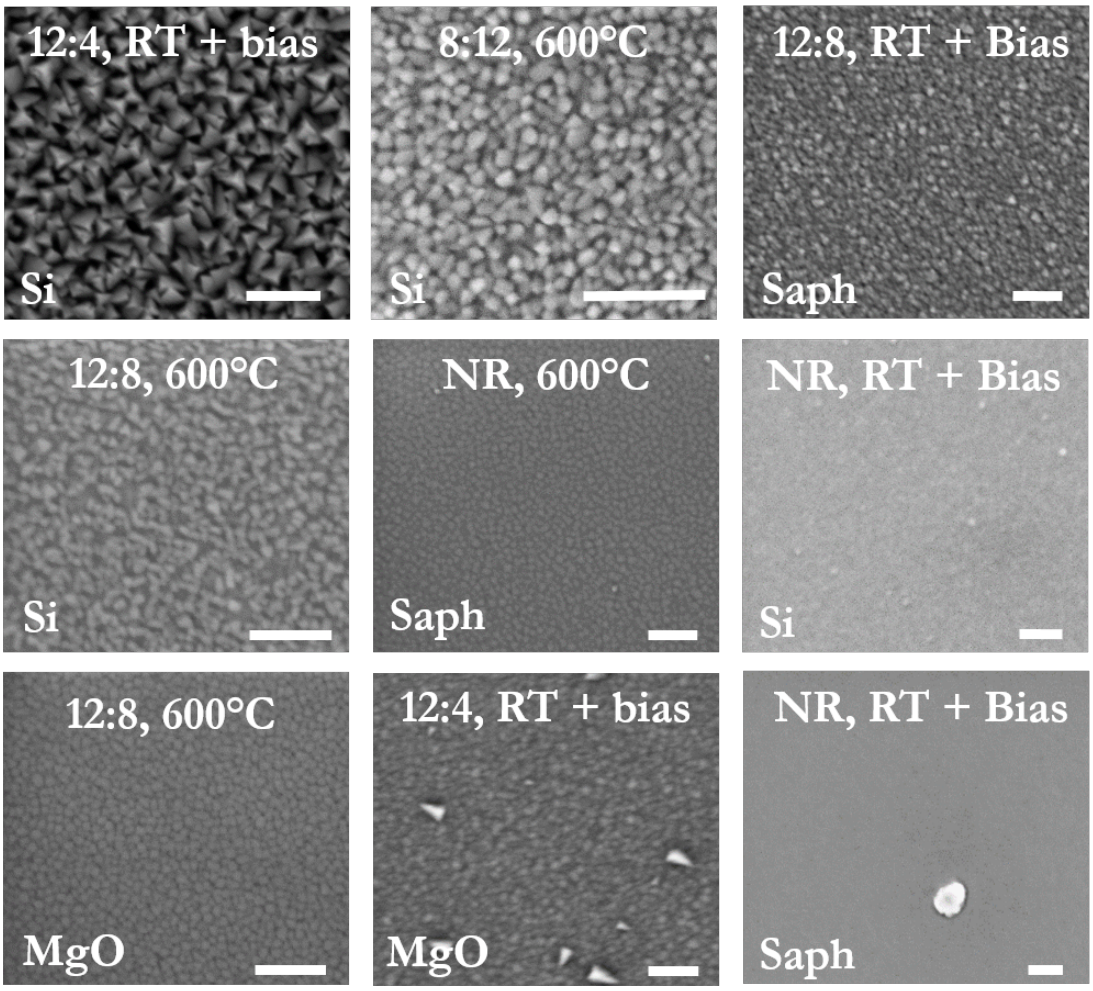


Figure 6.1: Scanning electron micrograph of several TiN and TiO_xN_y thin films with deposition conditions and substrate labeled. Films are ordered from approximately least metallic to most metallic as measured via SE. Scale bar = 100nm. Top row (left to right): TiN44Si, TiN22 Si, TiN39 Saph. Middle row: TiN23 Si, TiN27 Saph, TiN37 Si. Bottom row: TiN23 MgO, TiN44 MgO, TiN37 Saph

.

ature or 600°C), and if a bias was added ($\approx$ 100V)) as well the substrate onto which the TiN/TiO_xN_y films were deposited have been added to the micrographs. The most metallic film grown at elevated

temperature showed textured epitaxial growth with strongly preferred orientation (bottom left) while the most metallic film grown at room temperature with an additional applied bias was textured with small crystallites (bottom right). In this chapter, a variety of techniques used to examine the micro- and nano-structure of these films will be discussed including: x-ray diffraction (XRD) as well as scanning transmission electron microscopy (STEM) and standard scanning electron microscopy (SEM) studies.

6.1 X-ray Diffraction Studies (XRD)

XRD is a powerful material characterization technique which can be used to determine many structural material properties including: crystal orientation, lattice constant, interplanar spacing, crystallite sizing and potentially even distortions or imperfections in the lattice [151]. One of the most common uses is the determination of crystal orientation and lattice dimensions. A schematic is shown below. The schematic indicates the incoming x-rays, relative to the interplanar spacing or lattice constant within a crystal lattice.

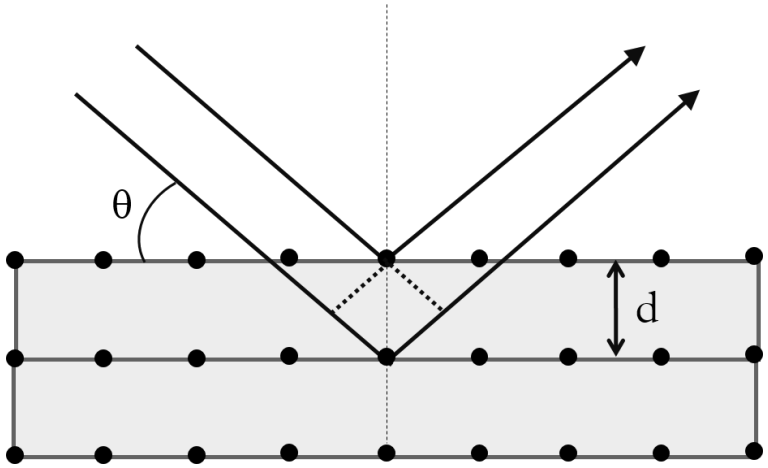


Figure 6.2: Schematic of Bragg's Law Diffraction off of a Crystal Lattice

In Figure 6.2, the two lines at the left denote incoming x-ray beams. The beam on the top hits an

atom at the surface and is scattered back towards the detector. The beam on the bottom penetrates into the material and hits an atom which is located an atomic plane deeper, or a distance d, into the film. The extra path length, x, which this beam traveled before hitting an atom as compared to the distance the top beam traveled can be calculated as:

$$x = d \sin(\theta)$$

After scattering, the beam must again pass through the same extra distance to exit the material giving the total path difference between beams as:

$$2d \sin(\theta)$$

For constructive interference of these waves to occur, the path length difference must be equal to an integer number, m, of wavelengths as shown by the Bragg equation.

$$m\lambda = 2d \sin(\theta)$$

Setting m = 1 and solving for d gives a way to calculate the expected angles at which the x-ray diffraction peaks will occur, given a known x-ray source wavelength and the spacing between atomic planes in a crystal lattice. By making XRD measurements, which commonly are expressed as intensity over a range of angles, these peaks can be detected and the data analyzed to back-out the interplanar spacings in a crystal lattice.

$$\theta = \sin^{-1}\left(\frac{\lambda}{2d}\right) \tag{6.1}$$

6.1.1 Dependence of TiN Film Orientation on Substrate

It has been suggested that films with 'better crystallinity' have greater metallic character with epitaxially grown films being more metallic than polycrystalline or amorphous films [49, 130], though as we have already shown this is not the only critical factor in determining the optical behavior of these films. Nevertheless, the influence of the substrate on the crystal growth is not unexpected and an important factor to consider. X-ray diffraction (XRD) studies have confirmed this strong influence of substrate specifically on the TiN thin film microstructure, as will be seen in Figure 6.4.

As discussed in Chapter 1, TiN has a face-centered cubic (FCC) lattice with the Ti metal atoms positioned at the FCC sites and the N atoms at the interstitial sites [59]. The (100), (110), and (111) planes in Figure 6.3 highlight the common growth planes, where (hkl) are the Miller indices describing the crystal directions.

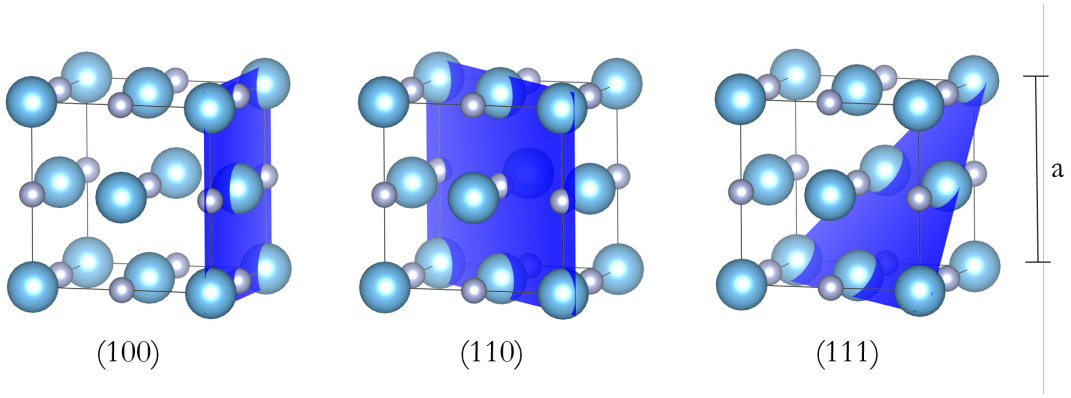


Figure 6.3: Crystal structure of cubic TiN highlighting (100), (110), and (111) planes, Produced using VESTA software [52]

The d-spacing describes the closest distance between two lattice planes along a particular direction. In a cubic lattice such as TiN, d can be easily calculated according to the following equation where a is the lattice constant as shown in Figure 6.3 and is equal to 4.24 Å for stoichiometric TiN [51, 53]. Using Equations (6.1) and (6.2), the expected 2θ XRD diffraction peak angles for a stoichiometric TiN film

can be calculated as shown in Table 6.1. By convention, according to the Bragg condition, 2θ is used rather than θ since 2θ is the difference in angle with respect to the incident beam.

$$\frac{1}{d^2} = \frac{h^2 + k^2 + l^2}{a^2} \tag{6.2}$$

h	k	l	$h^2 + k^2 + l^2$	d-spacing	2θ
1	0	0	1	4.24	21.0
1	1	0	2	3.00	29.8
1	1	1	3	2.45	36.7
2	0	0	4	2.12	42.6
2	2	0	8	1.50	61.9
3	1	1	11	1.28	74.2
2	2	2	12	1.22	78.1
4	0	0	16	1.06	93.3

Table 6.1: Calculation of XRD 2θ diffraction peak angles for TiN using lattice spacing a = 4.24Å and the x-ray Cu K-alpha wavelength, λ=1.5418 Å

A Bruker D2 PHASER x-ray diffractometer with LYNXEYE detector was used to collect 2θ data in Continuous PSD fast scan mode from 10 - 100° in increments of 0.01° with a collection time of 0.1 sec per angle. The system uses Bragg-Brentano geometry. The crystalline orientations of three TiN films which were simultaneously sputtered onto (100) MgO, (100) p-Si, and c-sapphire were studied. The sputtering was done reactively at 600°C and with a 12:8 Ar:N_2 sccm ratio with no applied substrate bias. The results of the experiment are displayed in Figure 6.4. Since there were no peaks of interest below 30°, this data was not included for clarity.

On the MgO substrates, the only significant peaks due to the TiN lattice were in the (200) and (400) directions signifying textured growth of the TiN film in the (100) direction, as expected. Without high-resolution XRD (HRXRD), it is not easy to resolve the TiN and MgO peaks in this case due to the close lattice match and spacing. On silicon substrates, single crystal epitaxial growth in the

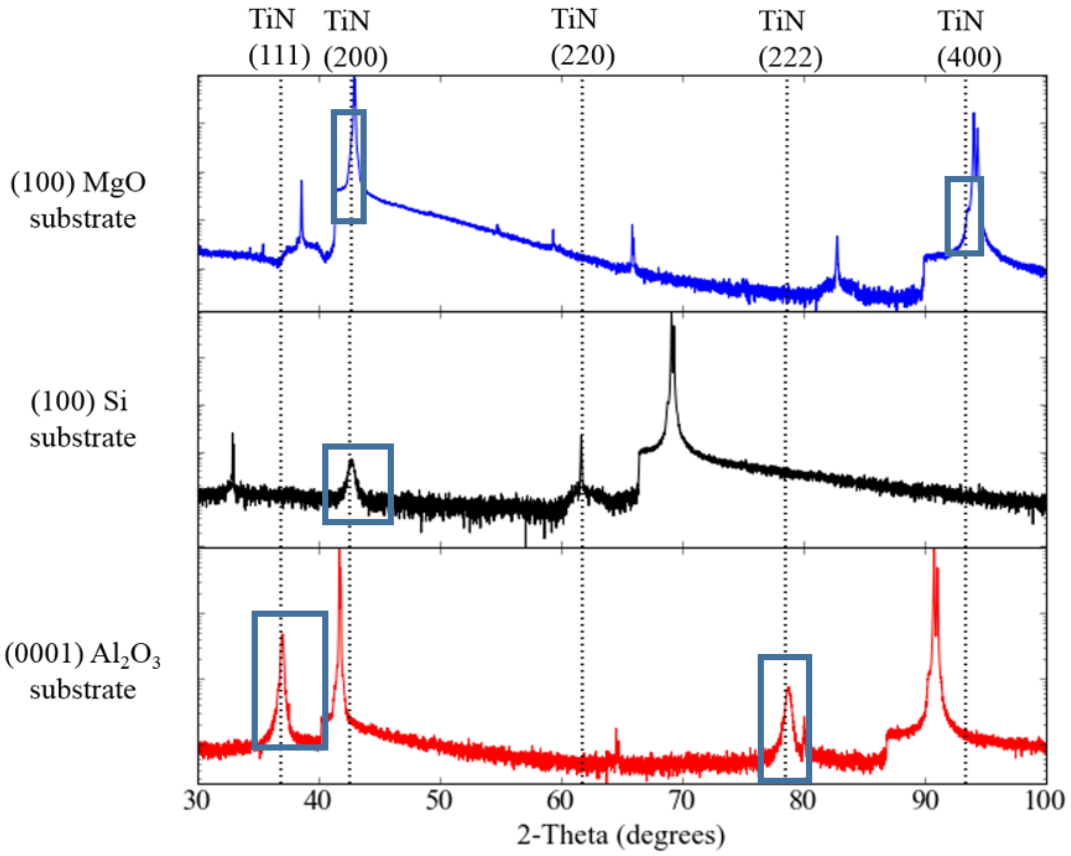


Figure 6.4: Comparison of XRD data for reactively sputtered TiN films on MgO, Si and Sapphire substrates. The optical properties of these three films are shown in Figure5.5. Samples: TiN23

.

(100) direction has been shown on (100) silicon via domain matching epitaxy (DME) [124]. In our studies, mainly TiN (200) growth was observed, however epitaxial growth was not achieved, rather, films were polycrystalline. There also seems to be a small portion of (220) TiN in the film grown on Si, however it is difficult to tell as the potential peak is overlapping a strong signal from the substrate. On c-plane sapphire, the primary XRD peaks seen were the sapphire (006) peak and the TiN (111) and (222) peaks signifying that the TiN grows primarily in the (111) direction. See Figure 6.4. The relevant 2θ diffraction angles calculated for TiN in Table 6.1 are plotted as vertical dashed lines in the figure for

reference and the main TiN growth directions observed on each type of substrate are boxed.

Clearly, since these three films were sputtered in the same chamber simultaneously and therefore experienced the same chamber deposition conditions, the strong preferences in growth direction must be dependent upon the substrate. The lattice therefore can be thought of as a template for the TiN film growth. The ideal candidate demonstrating an almost perfect lattice match with TiN is MgO. As shown in Figure 6.5, MgO also has an FCC crystal structure with the metal Mg atoms occupying the FCC lattice sites and the oxygen atoms occupying the interstitials. The lattice parameter defining the size of the unit cell is a = 4.212Å which is very close to the specified values for TiN. Therefore it is not surprising that epitaxial and even single crystalline growth have been reported for TiN on MgO substrates [49, 126]. This relationship will be examined further via transmission electron microscopy (TEM) measurements in the second half of this chapter.

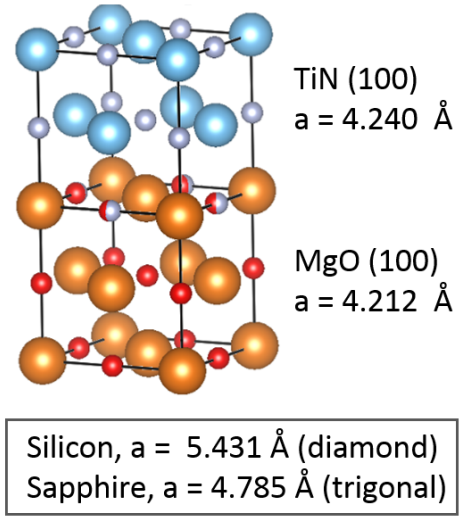


Figure 6.5: Close lattice match of TiN and MgO (100), Produced using VESTA software [52]

Silicon atoms on the other hand, are arranged in a pattern which is referred to as the diamond

crystal structure. It is a cubic lattice which can be thought of as two offset FCC lattices. The lattice parameter is significantly larger than that of the TiN lattice with a value of a = 5.431Å. This leads to a large 30% lattice mismatch. However, if the TiN lattice constant is multiplied by 4.5 and the Si lattice constant by 3.5, the new mismatch is 0.4%. For this reason, it was suggested and experimentally verified that under the correct conditions a technique called domain matching epitaxy could be used to grow TiN epitaxially on Si, including a mix of 3/4 and 4/5 length Si/TiN grains [124]. This relationship is represented schematically in Figure 6.6. While epitaxial growth of TiN on Si was not observed in our experiments, when using (100) Si as the substrate, preferential and even highly textured growth of (100) TiN was observed, in agreement with this model.

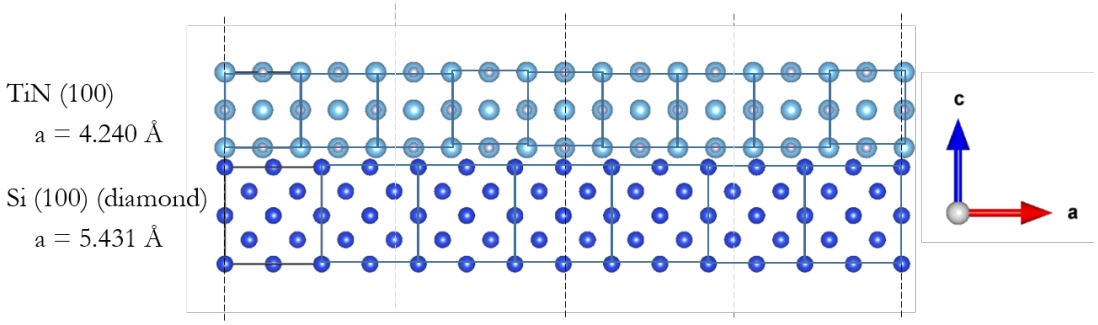


Figure 6.6: Crystal structure (100) TiN on (100) Si showing possibility of domain matching epitaxial growth, Produced using VESTA software [52]

Finally, according to the results shown in Figure 6.4, the preferred growth direction of TiN on c-plane sapphire is the (111) direction. Sapphire has a more complex trigonal crystal structure and thus is harder to visualize, however a schematic representation is again shown in Figure 6.7 showing the alignment of the preferred (111) TiN growth plane with the interface of the sapphire substrate.

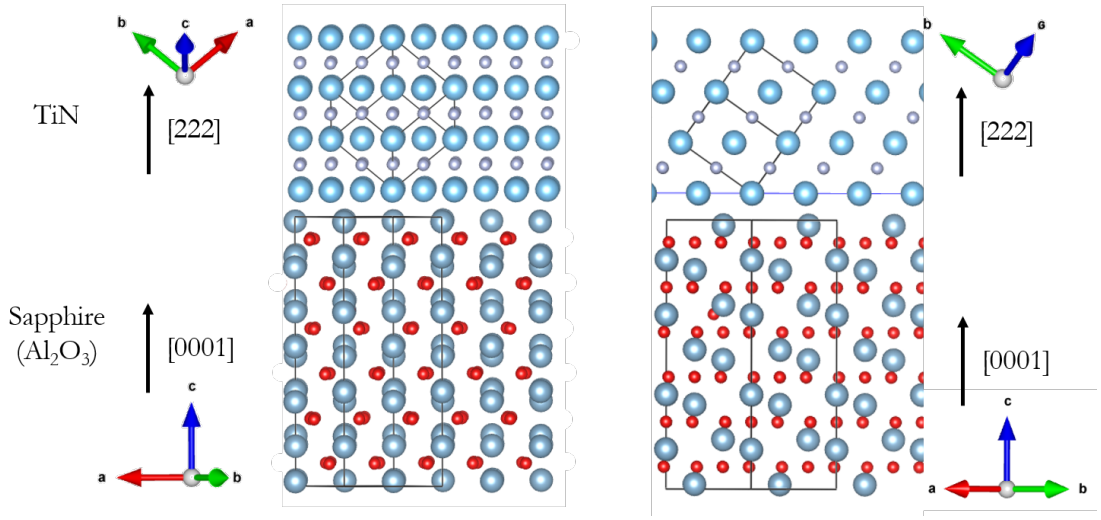


Figure 6.7: Crystal structure (222) TiN and (0001) Sapphire interface, Produced using VESTA software [52]

6.1.2 XRD Peak Shifts due to Variations in Lattice Constant and Crystallite Size

As shown in the section above, TiN films sputtered onto sapphire substrates prefer growth in the (111) direction. In a later experiment, XRD measurements were taken via the same D2 PHASER system, however this time the three films measured were all sputtered onto sapphire substrates but during different sputtering runs and different deposition conditions. It was noted that when films were sputtered under different conditions (e.g. with vs. without bias, reactively vs. non-reactively), the same growth directions still dominated as can be seen in Figure 6.8.

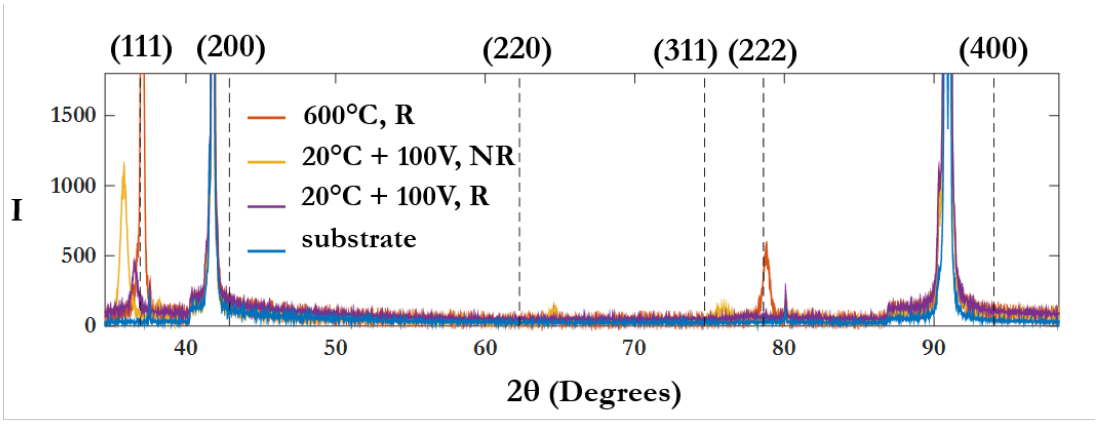


Figure 6.8: Comparison of XRD data for TiN films sputtered under different conditions onto sapphire substrates. Samples: — TiN23 Saph — TiN37 Saph — TiN44 Saph — Saph substrate. The details of the deposition conditions can be found in Appendix A.

While the crystalline structure of all three films was dominated by peaks near the expected (111) direction at 36.7° for a TiN lattice constant of a = 4.24 Å as seen in Figure 6.8, there was a shift in the data noted across the different samples. To determine the cause of the shifted peaks, the regions surrounding the dominant (111) and (222) TiN peaks were examined in further detail as seen in Figure 6.9. Note in this figure that there are peaks near 37.5° and just above 80° which are due to the substrate. These peaks show up in all datasets so the data does not seem to be shifted overall, just the TiN peaks.

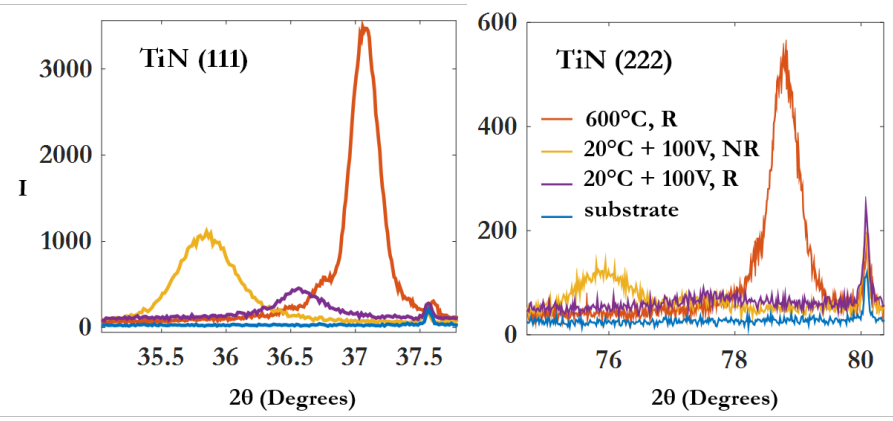


Figure 6.9: Comparison of XRD data for TiN films sputtered under different conditions onto sapphire substrates. Samples: — TiN23 Saph — TiN37 Saph — TiN44 Saph — Saph substrate

.

One reason which could cause XRD diffraction peaks to shift is a larger or smaller lattice constant. These (111) and (222) peak shifts therefore, can potentially be accounted for by assuming small variations in the lattice constant of the sputtered film. The 2θ maximum peak angles from Figure 6.9 have been used to calculate new lattice constants. First, Equation (6.1) was used to find the new d-spacing.

Deposition Conditions	$2\theta_{(111)}$	a (Å)
Reference	36.7	4.24
600°C,R	37.06	4.201
20°C + 100V,R	36.57	4.256
20°C + 100V,NR	35.85	4.338

Deposition Conditions	$2\theta_{(222)}$	a (Å)
Reference	78.1	4.24
600°C,R	78.78	4.208
20°C + 100V,R	77.53	4.265
20°C + 100V,NR	75.95	4.340

Table 6.2: Calculated XRD 2θ diffraction peak angles for TiN with different lattice constants, a, compared to stoichiometric spacing of a = 4.24Å and using the x-ray Cu K-alpha wavelength, λ=1.5418 Å. The peak angles are calculated for (hkl) = (111) - left table and (222) - right table.

Then Equation (6.2) was used to find the lattice constant corresponding to the measured 2θ values. The resulting lattice constants displayed in Table 6.2 were calculated twice for each film, using the (111) and (222) peaks individually. The results are consistent, giving similar lattice constants using either the (111) or (222) peak for each film.

In addition, the diffraction peaks are expected to broaden as the crystallite size decreases, since the peak width, B, is inversely proportional to the crystallite size, L, according to the Debye-Scherrer equation:

$$B(2\theta) = \frac{K\lambda}{L\cos(\theta)}$$

where K = a shape factor usually near 0.9 - 1.0 (dimensionless) and λ = the x-ray wavelength. [152–155]. To determine the absolute crystallite size, broadening of the peaks due to the instrument must be taken into account; however, since these measurements were not the focus of our work, the instrument broadening is unknown and only relative comparisons will be made. All XRD measurements were made using the same instrument and settings.

Deposition Conditions	$FWHM_{(111)}$	$FWHM_{(222)}$
600°C	0.26°	0.55°
20°C + 100V, R	0.48°	-
20°C + 100V, NR	0.52°	-

Table 6.3: FWHM for XRD 2θ diffraction peaks for TiN sputtered onto sapphire under different deposition conditions. The FWHM is calculated for the (hkl) = (111) and (222) peaks. Two of the peaks are too broad (several degrees) for the FWHM to be reliably measured at higher angle.

As is shown in Figure 6.9 and Table 6.3, the film exhibiting the most narrow diffraction peaks is that which was sputtered at high temperature. The peaks for each of the reactively sputtered films measured were significantly broader. Thus, according to the Debye-Scherrer equation, it is expected that the low temp. + bias sputtered films will have significantly smaller crystallites than the 600°C film due to the inverse proportionality of the crystallite size, L, with the peak broadening, B. This means that films with smaller crystallites will in general display broader XRD peaks (larger FWHM).

The surface of two of these films was briefly compared via scanning electron microscopy (SEM) as

shown in Figure 6.10. The high temperature reactively sputtered film which contains a large percent oxygen shows significant surface variation with grain sizes on the order of 10nm (left side) whereas the highly metallic sample sputtered at room temperature with an applied substrate bias shows little significant structural variation which is visible by SEM (right side). Since the grains are expected to be smaller in this film, it is possible that the nanocrystallites were too difficult to resolve at the given resolution. Therefore, this data seems to correspond well to the XRD structural measurements.

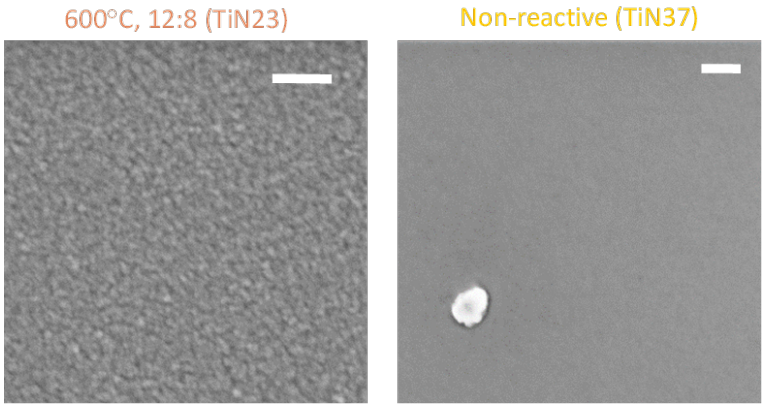


Figure 6.10: SEM top-down images of TiN film sputtered reactively at high temperature vs. non-reactively at low temp. plus bias onto sapphire substrates. Scale bars = 100nm. Films correspond to those measured via XRD in Figure 6.9. Samples: — TiN23 Saph — TiN37 Saph

.

Via SEM inspection of the granular quality of films sputtered under many different conditions, the non-reactively sputtered films and also the films sputtered at low temperature + bias have in general seemed to exhibit smaller nanocrystallites than their reactively and high-temperature sputtered counterparts. Therefore this result does not seem to be specific to this case study. Several examples of non-reactively (NR) sputtered films can be seen in the earlier Figure 6.1.

As mentioned previously, it has been suggested that films with 'better crystallinity' have greater metallic character with epitaxially grown films being more metallic than polycrystalline or amorphous films [49, 130]. One may deduce from this statement that films therefore with larger crystallites may

also be expected to have better metallic character than those with smaller nanocrystallites. If the intensity and FWHM of the XRD peaks from the study above is compared to the optical properties, interestingly, the peak which is the most intense and most narrow (orange) does not correspond to the most metallic film in this case (yellow) as might be expected if only the grain size determined the metallic character. See Figures 6.9 and 6.11.

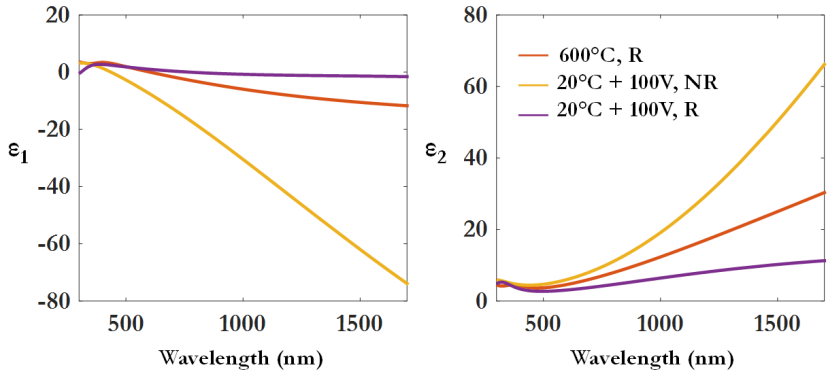


Figure 6.11: Comparison of ellipsometry data for TiN films sputtered under different conditions onto sapphire substrates. Films correspond to those measured via XRD in Figure 6.9. Samples: — TiN23 Saph — TiN37 Saph — TiN44 Saph

.

In the previous chapters, I have shown that the optical properties are influenced not only by the crystallinity but also have significant dependence on the incorporated oxygen content as well as how the N is bound within the film. Therefore, in an attempt to explain the variation in optical properties between these films, chemical composition measurements are made via XPS to examine the Ti:N:O ratio and overall atomic % oxygen in these films. As can be seen in Table 6.4, there is a significant oxygen incorporation (25.5%) in the high temperature sputtered film as compared to a low oxygen percentage (11.8%) in the low temperature non-reactively sputtered film which also has a much closer to stoichiometric Ti:N ratio and therefore likely more N bound as N-Ti then in oxynitride form leading to a more metallic film. Unfortunately, XPS data is not available for the reactively sputtered low-

temperature grown film (purple) however it is predicted that this film also contains a large percentage of incorporated oxygen based on the optical behavior. These variations easily explain the differences in optical behavior which are not explained by the differences in crystallinity.

	600°C, R (TiN23 -orange)	20°C + 100V, NR (TiN37 - yellow)
Ti:N ratio	1:0.82	1:0.92
Ti	38.4%	45.2%
N	31.6%	41.5%
O	25.5%	11.8%

Table 6.4: XPS Ti:N ratio and Atomic % oxygen for TiN corresponding to the samples in Figures 6.11 and 6.10 after 20s Ar^+ ion etching to sputter away surface oxide.

In summary, we have shown that to truly understand the origination of the optical behavior of these films, all of the data - optical, electrical and microstructural needs to be taken together. Based on the results of this chapter as well as the previous chapter, it is expected that more dielectric films will have a higher oxygen content and the more metallic films will have a lower oxygen content with more N-Ti bonding as compared to N bound in oxynitride form. It is also expected that those films deposited on Si will have a preferred orientation in the (111) direction whereas those sputtered onto MgO or Sapphire substrates will have a preferred orientation in the (100) direction and that non-reactively sputtered films will have smaller crystallites in general as compared to reactively sputtered films. While a wealth of knowledge has been learned about this films, there is still a vast amount left to learn. In an attempt to better understand some of the microstructural variation within these films beyond the limits of traditional scanning electron microscopy and at a different, but complementary scale to the XRD measurements, cross-sections of a small set of films were taken via focused ion-beam (FIB) milling and transmission electron measurements (TEM) done to study the nanostructure in further detail. The results are discussed in the remainder of this chapter.

6.2 Scanning Electron & Transmission Electron Microscopy (SEM/STEM)

So far we have studied the optical, electrical and chemical properties of these films in detail however we have just started to examine them visually in a more traditional sense to determine how they "look", for example if the growth is columnar or granular, or if the films look dense or porous, etc. Transmission electron microscopy (TEM) is a materials characterization method which can be used to visualize materials at the nanoscale level (generally on a scale of <1-100nm). A visible light microscope, or what is often called an optical microscope allows visualize of structures down to a minimize resolvable size of about 300nm. This limit is set by the Raleigh criterion which specifies that the minimum resolvable resolution for a microscope can be approximated by half of the wavelength of the light used [156]. For a visible light microscope and assuming the wavelength of the middle of the visible spectrum of 550nm, the resolution would be limited to not much below 300nm and therefore to visualize materials truly at the nanoscale, additional methods are required.

The idea of wave-particle duality discovered in the early twentieth century states that objects like electrons which we typically consider as particles can also be considered as waves. According to the deBroglie equation, they have some characteristic wavelength dependent upon their mass, m, and velocity, v.

$$\lambda = \frac{h}{mv}$$

With some manipulation and approximations, this equation can be rearranged to another common form which relates the energy (in eV) and the wavelength (in nm).

$$\lambda = \frac{1.22}{\sqrt{E}}$$

Using this equation, we can therefore approximate the "wavelength" associated with an electron mi-

croscope which corresponds to the resolution. SEMs generally use electron beams with energies of a few keV and TEMs higher energy beams closer to 100keV, giving expected resolutions on the order of 0.03 nm (or 0.3 Å) and 0.004nm (or 4pm), respectively. In reality, there are practicalities which limit the resolutions to about 1-20nm for an SEM and about an order of magnitude lower for TEM [156].

As was shown earlier, SEM images were taken of many films showing the wide range of microstructures which can develop. SEM is generally a qualitative imaging technique however, and thus it is difficult to draw significant conclusions from these images alone. In addition, the resolution is not fine enough to study materials and interfaces at the nanoscale level. Therefore, TEM measurements which allow direct visualization of the lattice structure were next undertaken in an effort to better quantify the films' microstructure in coordination with the previous XRD studies.

The samples required significant preparation prior to measurement since specimens must be on the order of 100nm for clear imaging and since cross-section views examining the film microstructure from the side were desired. In this study, focused ion-beam (FIB) etching using an FEI Helios 660 was done to cut out cross-sections of several TiN thin films on MgO substrates and thin them in preparation for TEM measurements to examine the local structure. Prior to FIB milling, a platinum layer was added to protect the TiN films and MgO substrates from damage. Several samples were carefully chosen to compare films deposited at high temperature vs. room temperature with a bias (TiN23 vs. TiN37/44) and also films sputtered non-reactively (TiN37) with those sputtered reactively (TiN23,44). The deposition conditions of the chosen films are summarized in Table 6.5.

Sample	Deposition Temp/Bias	Reactive/Non-Reactive ($Ar:N_2$) sccm
TiN23	600°C	R, 12:8
TiN37	20°C + 100V	NR, 40:0
TiN44	20°C + 100V	R, 12:4

Table 6.5: Summary of deposition conditions for samples examined via TEM

6.2.1 High-temperature reactively sputtered TiN

The first of the three films in this study was sputtered reactively at 600°C substrate temperature at 12:8 Ar:N_2 sccm gas flow during deposition onto a (100) MgO substrate. Figure 6.12 shows a cross-sectional scanning transmission electron microscope (STEM) image of a FIB-milled section of the film (left) and a top-down scanning electron microscope (SEM) image of a larger portion of the film (right).

The STEM image shows a layer of Pt at the top which was laid down prior to FIB-milling to protect the TiN film and MgO substrate underneath. It has an amorphous structure. The TiN film underneath displays heteroepitaxial growth on the (100) MgO substrate with the crystal lattice of the TiN film aligning in the same direction as the MgO substrate underneath. At the resolution shown

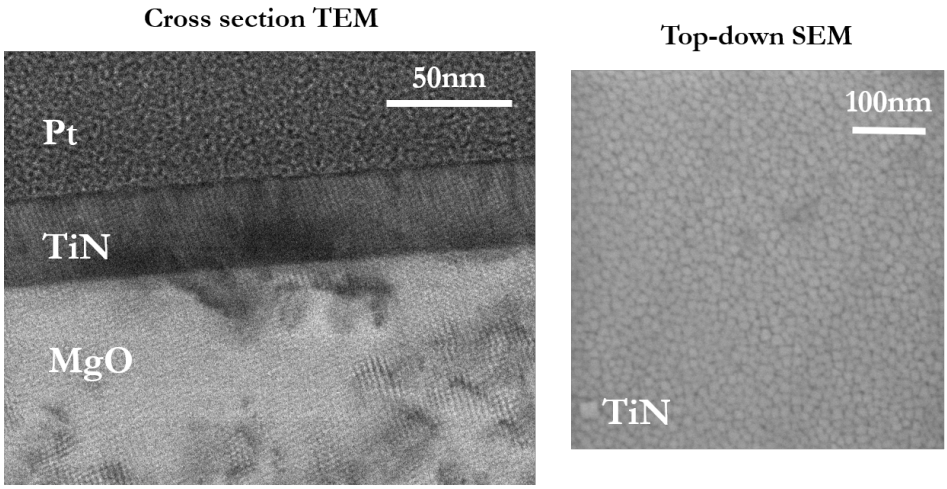


Figure 6.12: Scanning Transmission Electron Microscopy (STEM) cross-section and top-down SEM of Metallic TiN grown reactively at 600°C on MgO. Sample: TiN23 on MgO substrate

however, individual lattice planes cannot be resolved. In this image, also of note are the large defects present in the MgO substrate. The defects near the surface of the substrate (center of the image) seem to be transferred into the TiN film. This large defect concentration could be due to high temperature processing since this effect was not noticed in the other two samples studied which were deposited at room temperature. Another possible explanation is exposure of the substrate to a humid environ-

ment prior to sputtering. MgO substrates are highly sensitive to water vapor and since this was not known initially, it is possible that the substrates may have not been properly stored since this was an earlier sample. The SEM image shown in Figure 6.12 (right) is looking down at the TiN film from above. (This is prior to the Pt deposition on top for FIB-milling.) From this image, the TiN film seems to have grains on the order of 15-20nm in diameter. Combining the knowledge gained from this image with the STEM image and XRD data which showed textured (200) growth, this film can be considered highly-textured with columnar, but perhaps heteroepitaxial growth.

Fast Fourier transforms (FFT) are commonly used in image processing for filtering, to reduce noise, and to recognize patterns. In the case of TEM data, they can be used to recognize repeating patterns such as the lattice spacings exhibited in crystalline materials [155, 157]. FFTs were performed on the TiN film alone (Figure 6.13 left) and subsequently on the MgO substrate alone (middle) using the data selected within the yellow boxes. The FFTs are shown below the corresponding images. The red background corresponds to the FFT of the TiN film and the blue background to the FFT of the MgO substrate. These two images have been overlaid to produce the purple image at the far right of the figure. Four white dots can be noted within a cubic arrangement around the center spot, signifying that indeed there is likely heteroepitaxial growth with good lattice-matching. However, as mentioned earlier at this resolution individual lattice planes cannot be resolved so this analysis is still qualitative.

Therefore, high-resolution TEM (HRTEM) images were also taken of this film to confirm the crystal growth direction and quantify the lattice plane spacing. The HRTEM image shown in Figure 6.14 clearly shows highly uniform crystalline growth. Of the four films measured, only this high-temperature, reactively grown film exhibited epitaxial growth. When FFTs are performed on an HRTEM image, information similar to that obtained directly from an electron diffraction pattern can be obtained [49, 157]. An FFT was taken of this image using the ImageJ analysis software [158] which agrees with previous results for epitaxial (001) TiN [49]. The FFT diffractogram confirms a (200) orientation with interplanar spacing of 2.1 Å as predicted in Table 6.1.

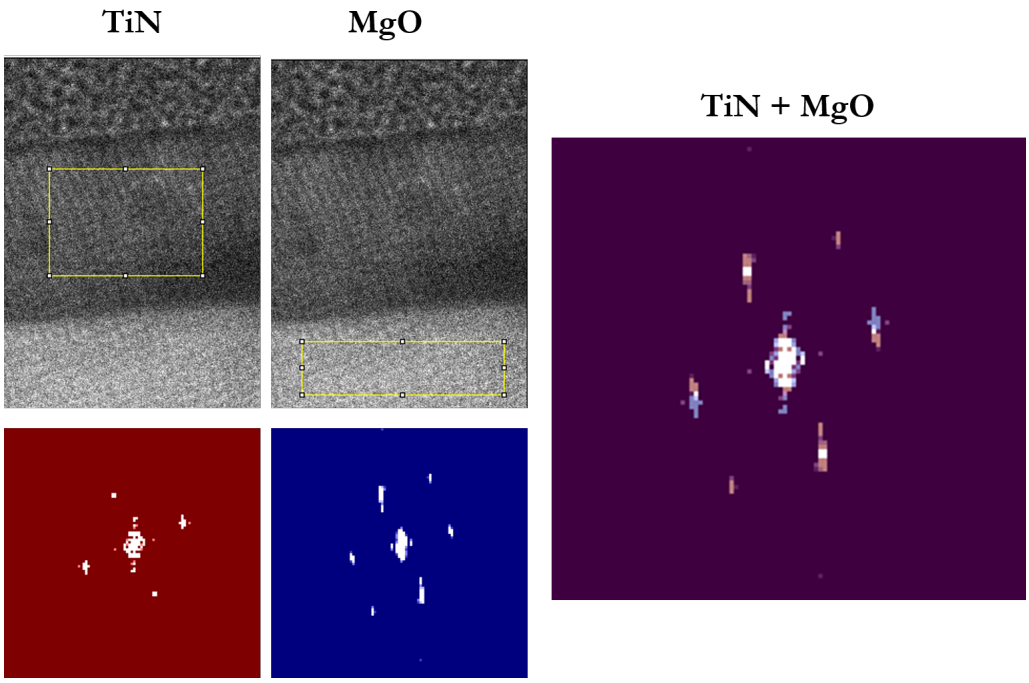


Figure 6.13: FFT of select region of TEM film (red) and of select region of MgO substrate (blue) are overlaid to compare crystalline orientation. Sample: TiN23 on MgO

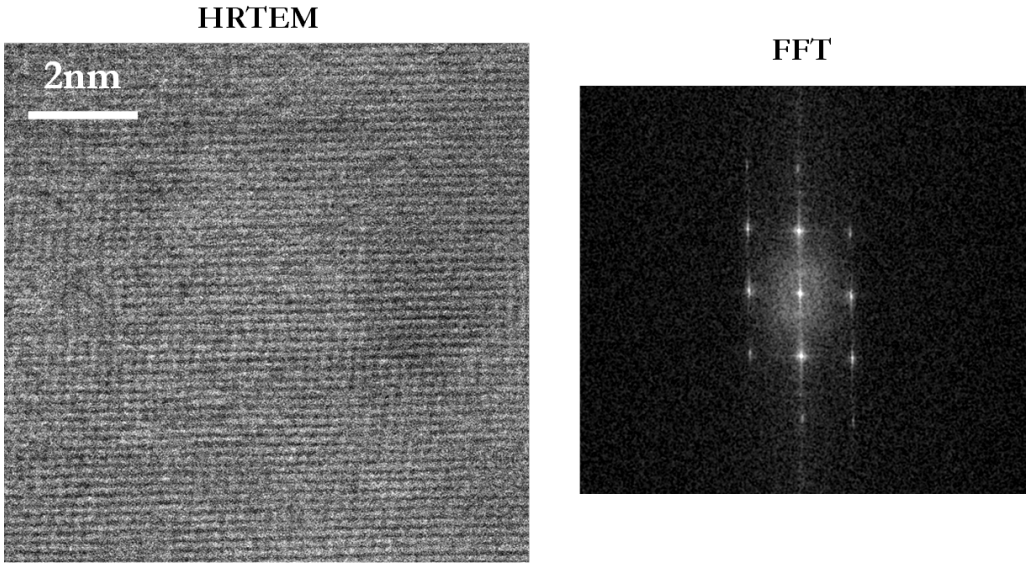


Figure 6.14: High-Resolution Transmission Electron Microscopy (HRTEM) of Metallic TiN grown reactively at 600°C on MgO and FFT. Sample: TiN23 on MgO

6.2.2 Room-temperature non-reactively sputtered Metallic TiN

The next sample analyzed via TEM was sputtered non-reactively at room temperature and with an additional applied substrate bias, also onto a (100) MgO substrate. As before, a STEM cross-section of the sample is shown in Figure 6.15 (left) along with a top-down SEM of the surface of the TiN film (right). The STEM image shows a clearly less ordered TiN film as compared to the previous high-temperature reactively sputtered film. As noted in the previous section, the MgO substrate here does not seem to exhibit the extensive damage seen in the previous example. Upon examination of the STEM and SEM images in tandem, it is hypothesized that there is a nanocrystalline nature to this film. This agrees well with the XRD analysis in Section 6.1.2 that the crystallite size was significantly smaller

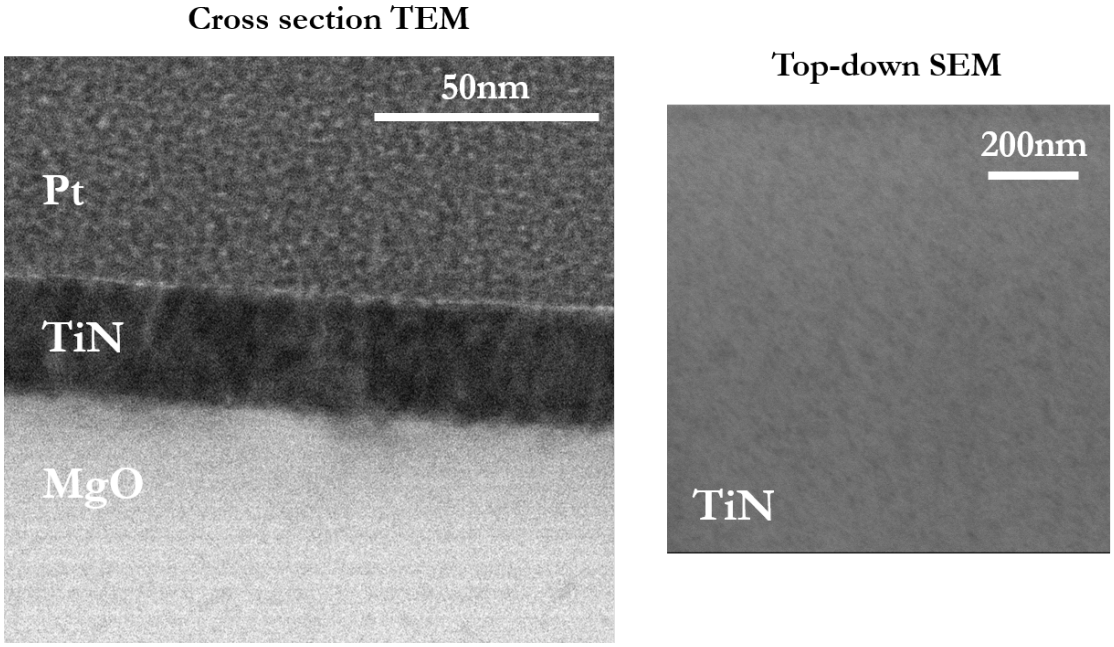


Figure 6.15: Scanning Transmission Electron Microscopy (STEM) cross-section and top-down SEM of TiN grown non-reactively at 20°C plus 100V substrate bias on MgO. Sample: TiN37 on MgO substrate

in a non-reactively sputtered film with bias than the similarly metallic high-temperature reactively sputtered film. Note here that the substrates are different (MgO rather than sapphire) but the trend

seems to hold.

As previously, HRTEM images are taken to visualize and quantitatively assess the lattice. Typically, diffraction patterns exhibit rings rather than discrete spots in nanocrystalline samples which are sampled over a number of crystals with orientations in different directions [159, 160]. This effect can begin to happen even when sampling over only 2 or 3 different crystalline grains. The HRTEM image shown in Figure 6.16 and the corresponding FFT are not quite as clear as the previous example, however seem to be exhibiting the beginning of a ring-like pattern with arcs forming from the north to east and west to south quadrants around the center point. The spacing of this potential partial ring wraps around between the expected positions of the [200] and [111] diffraction spots with lattice spacing ranging from 2.1-2.4Å.

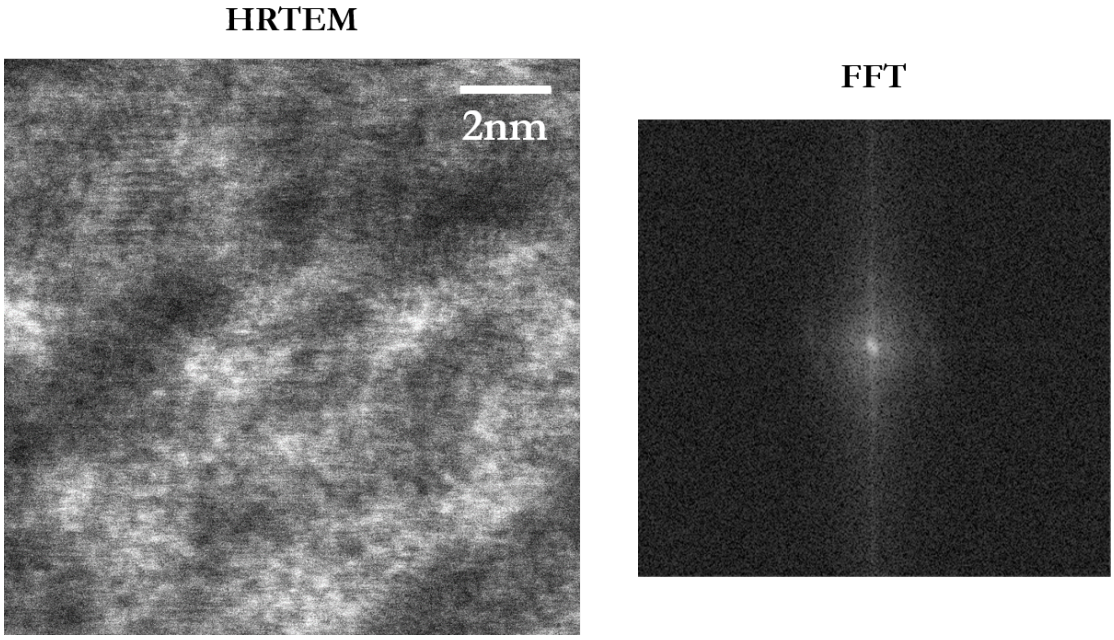


Figure 6.16: High-Resolution Transmission Electron Microscopy (HRTEM) of TiN grown non-reactively at 20°C + 100V bias on MgO and FFT.Sample: TiN37 on MgO

6.2.3 Room-temperature reactively sputtered Metallic TiN

The final sample studied via TEM was sputtered at room temperature with an additional applied substrate bias, but unlike the previous sample was sputtered *reactively* rather than non-reactively at an Ar:N_2 ratio of 12:4 sccm. The low resolution STEM images of this sample were harder to interpret, but overall the film appeared to be less homogeneous. The top-down SEM image shows what appears to be a granular or nanocrystalline film. There is more significant variation in shades of different grains in both images (some appear light and some appear darker) as compared to either of the previous samples. In addition, tetrahedral structures were observed on the surface of the film. Unfortunately, while the intention was to use the TEM to image a cross-section of one of these tetrehedral structures in addition to the film, none of the tetrahedra were successfully cross-sectioned during the FIB preparation.

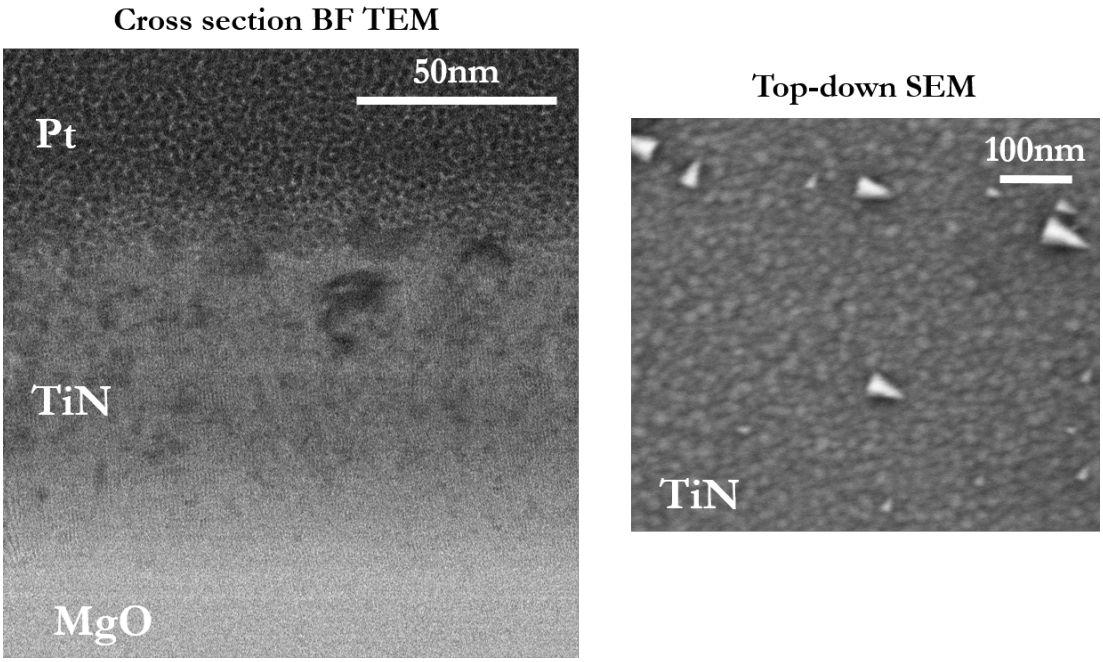


Figure 6.17: Scanning Transmission Electron Microscopy (STEM) cross-section and top-down SEM of TiN grown non-reactively at 20°C plus 100V substrate bias on MgO. Sample: TiN44 on MgO substrate

Nevertheless, HRTEM images were taken within several different regions of this film with interesting results. The low resolution TEM is shown again in Figure 6.18 (left) for reference. A small white box has been added which shows the location at which the top HRTEM image was taken. Notice that this is near the surface of the TiN film and that the darker portion of the region appears to be a different crystallite with (111) orientation rather than (200). This is confirmed by performing an FFT of this image which has been indexed successfully in accordance with the expected FCC diffraction patterns [159, 161, 162] and using the d-spacing of 2.4Å for (111) and 2.1Å for (200) TiN calculated in Table 6.1. The lower HRTEM image is taken at a different location within the film and only evidence of (200) growth is seen after an FFT is performed. This image is more representative of the film bulk.

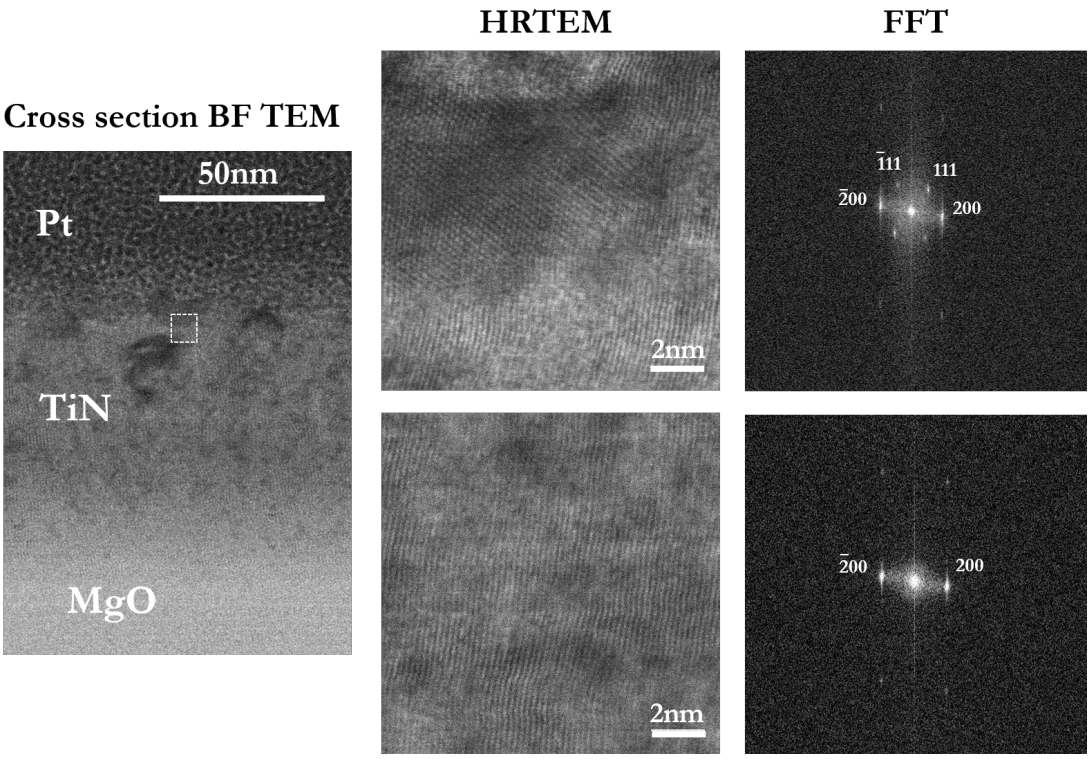


Figure 6.18: High-Resolution Transmission Electron Microscopy (HRTEM) of Metallic TiN grown reactively at 20°C + bias on MgO and FFT]. Sample: TiN44 on MgO

6.2.4 Discussion of Structural Data (STEM/XRD) in Combination with Chemical Data (XPS) in Determining Optical Behavior

The XRD and STEM micro and nano-structural data presented in this chapter, in combination with the optical data presented in Chapter 4 and the XPS data presented in Chapter 5 give a fairly comprehensive image of the main factors which contribute to the overall optical behavior of our sputtered TiN and TiO_xN_y thin films. To briefly summarize, there are several critical parameters to sputter metallic TiN which is suitable for plasmonic applications, namely, careful control of the chemical composition and bonding as well as the crystallinity of the deposited film. To give a clear example of the interactions between these factors, the optical, chemical, and structural data of the three films just examined via TEM are all considered simultaneously. The optical properties are shown in Figure 6.19.

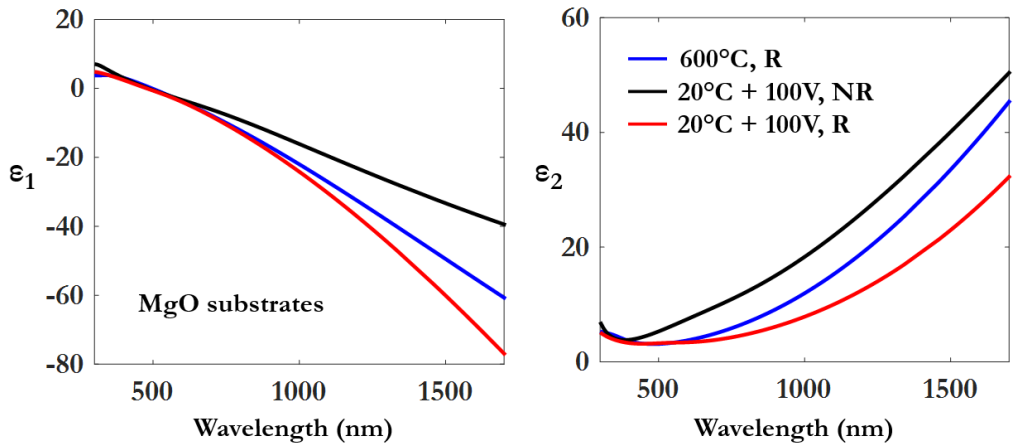


Figure 6.19: Comparison of ellipsometry data for TiN films sputtered under different conditions onto MgO substrates. Films correspond to those measured via STEM. Samples: — TiN23 MgO — TiN37 MgO — TiN44 MgO

.

First, the structural data is considered. XRD data for these samples showed that all three films were highly textured with dominant (200) TiN film growth. This is expected based on the analysis in

Section 6.1.1 which showed that the film growth direction was highly dependent upon the substrate. The XRD data for all three films is plotted in Figure 6.20. The dashed lines in the figure are drawn at the expected 2θ angles for cubic TiN with a lattice constant of a = 4.24 Å. The two largest peaks in the figure located just to the right of the (200) and (400) lines correspond to the MgO substrate. The spacing between the TiN and MgO (200) and (400) peaks is very close since the substrate and film have <1% lattice mismatch and therefore it is hard to distinguish between them. The expected location of the TiN (200) peak is drawn at 42.6° corresponding to a lattice constant of 4.24 Å. There is a shoulder located at slightly smaller angles than the main peak due to TiN (200). This can be seen more clearly in Figure 6.21 which zooms in on each set of diffraction peaks individually. A slightly larger lattice parameter of 4.30 Å would shift this peak left, closer to 42.0°. This may explain the (200) peak shift seen in the two room-temperature + bias films as compared to in the 600°C film which seems to overlap very closely with the substrate.

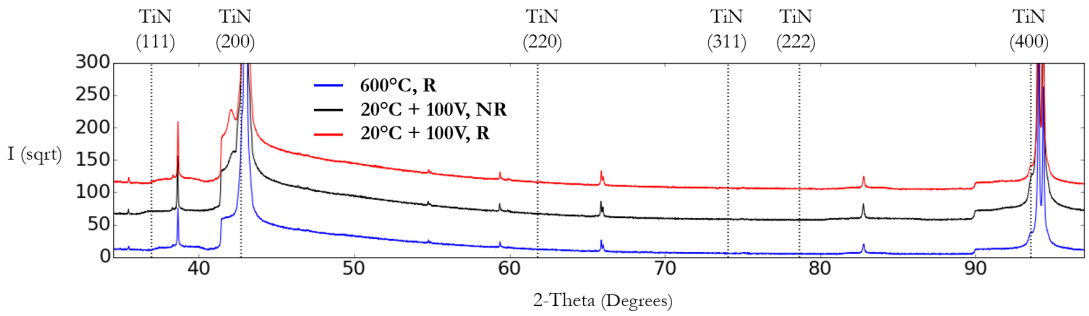


Figure 6.20: Comparison of x-ray diffraction data for TiN films sputtered under different conditions onto MgO substrates. Intensity values are arbitary and offset for clarity. Films correspond to those measured via STEM. Samples: — TiN23 MgO — TiN37 MgO — TiN44 MgO

.

Summarizing the XRD data shown in Figure 6.21, all three films are dominated by (200) growth with the room-temp + bias films showing relatively broad peaks shifted to slightly shorter angles near 42°. The 600°C reactively sputtered film (blue) shows only (200)/(400) peaks and has the 'best crystallinity' of the three with textured heteroepitaxial growth on the MgO substrate. This is consistent

with the STEM data from the previous section. The room temperature plus bias, *non-reactively* sputtered film (black) shows a small (111) peak in addition to the dominant (200) peak, however it is quite broad and the film seems to be dominated by (200) growth. The FFT of the HRTEM data taken for this film was almost ring-like signifying nanocrystalline structure and the smallest grains of the three films. This agrees well with the broadness of the peaks seen in the XRD data since smaller crystallites are known to cause XRD peak broadening based on Equation 6.1.2. The HRTEM FFT ring spacing varied from 2.1 - 2.4 Å which is also consistent with the (200) and (111) directions seen in the XRD data.

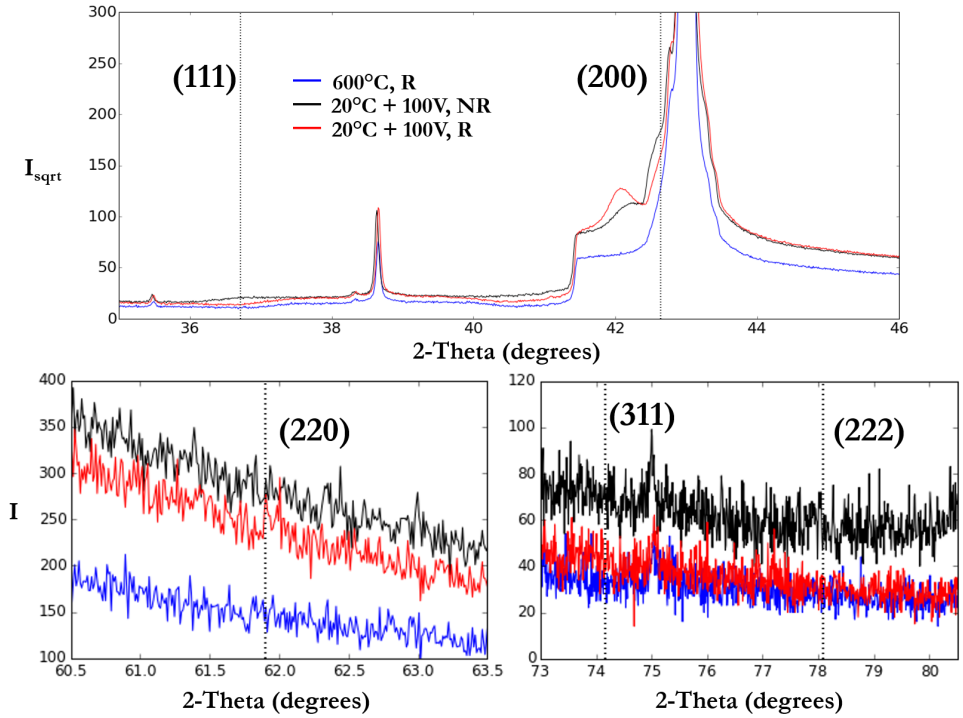


Figure 6.21: Peak by peak inspection of XRD data for TiN films sputtered under different conditions onto MgO substrates. Films correspond to those measured via STEM. Samples: — TiN23 — TiN37 — TiN44

.

Finally, the room temperature plus substrate bias *reactively* sputtered film (red) is again dominated by the (200) growth which agrees with the second HRTEM image studied. This film seems to be

highly textured with the majority of the structure consisting of (200) crystallites but perhaps with local areas of smaller growth in varied directions. One such area was seen in the first HRTEM near the film surface with (111) orientation. While the XRD data suggests the possibility of (220) or (311) crystallites also being present within the film, these XRD 'peaks' are almost level with the noise floor and hard to confirm for sure so it is not surprising that they were not seen in the HRTEM images. Characterizing these films in terms of crystallinity only, the 600°C film (blue) would be the 'best" with textured heteroepitaxial growth, followed by the low temp + bias reactively sputtered film (red) with highly textured but polycrystalline growth, and finally the low temp + bias non-reactively sputtered film (black) with textured nanocrystalline growth.

	Deposition Conditions		
	600°C, R (TiN23 -blue)	20°C + 100V, NR (TiN37 -black)	20°C + 100V, R (TiN44 - red)
Metallic Character	Middle	Least	Most
Crystallinity	Heteroepitaxial	Nanocrystalline	Polycrystalline
Ti:N ratio	1:0.94	1:0.0.93	1:0.99
Ti	42.1%	43.3%	44.1%
N	39.4%	40.3%	43.8%
O	17.5%	15.2%	10.7%

Table 6.6: Comparison of metallic character as determined via SE data, structural character as determined via XRD/STEM and chemical character as determined via XPS Ti:N ratio and atomic % oxygen for TiN corresponding to the samples studied via TEM after 20s Ar^+ ion etching to sputter away surface oxide.

Therefore, based on the crystallinity (XRD + STEM) only, we would expect the high-temperature film (blue) to be the most metallic; however, the film sputtered reactively at low-temperature (red) is in fact more metallic and in addition has lower losses than this highly crystalline film. Therefore, there must be other factors involved, as we suspected. For completeness, the chemical composition and bonding data collected via XPS is displayed in Table 6.6 along with the optical and structural results. Based on our previous analysis, we expect that this variation may be due to the Ti:N ratio or atomic %

oxygen. Checking Table 6.6, the most metallic film (red) has 10.5% oxygen as compared to the highly crystalline film (blue) which has a significantly higher amount of oxygen 17.5%. If this fully explained the optical behavior however, then the non-reactively sputtered film (black) would be in the middle in terms of metallic character, with only 15.2% oxygen. Therefore, it is clear that both the crystallinity and the chemical composition are important in determining the overall optical behavior.

Acknowledgement

I would like to thank Dr. Shao-Liang Zheng, director of the X-ray Laboratory in the Department of Chemistry & Chemical Biology at Harvard University for his help with the X-ray data collection. In addition, I would like to thank Dr. Andrew Magyar of the Center for Nanoscale Science for the FIB sample preparation and TEM measurements as well as for providing analysis suggestions for the TEM data.

7

Simulated and Fabricated TiN Benchmark Plasmonic Structures

Throughout this thesis, the optical behavior of sputtered TiN and TiO_xN_y was studied as a function of the sputtering deposition conditions. The ultimate goal was optimization of the metallic character of these films for plasmonic applications. To verify the viability of the optimized TiN as an alternative plasmonic material, several benchmark plasmonic nanostructures were next fabricated. In this final chapter, three different types of fabricated structures demonstrating the potential of TiN as a plasmonic material will be discussed: surface plasmon grating couplers, mid-infrared nanoantennas,

and micro-pyramids for photothermal drug therapy.

7.1 Surface Plasmon Grating Couplers

As discussed in Chapter 1, though surface plasmons couple light into surface electron waves, they cannot be excited solely by shining light at the interface due to the required phase-matching condition. One way of matching the phase of the incoming light is by using a grating coupler. This will be the first type of fabricated benchmark structure discussed.

7.1.1 Introduction and Motivation

Gratings can be used to couple the incoming light into the surface plasmon mode by using interference to match the wavevector of the incoming light, k, to that of the surface plasmon mode, k_{SPP}.

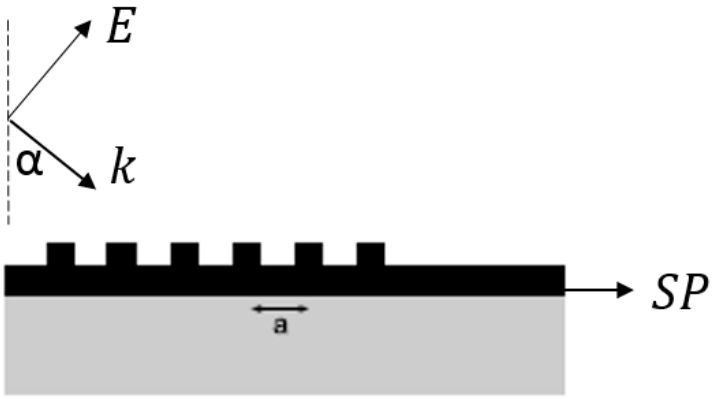


Figure 7.1: Surface plasmons at a metal air interface have a larger k-vector than attainable in air from incident radiation. One method to increase the k vector is by using a grating to couple the light into the surface plasmon mode.

Using the metallic grating geometry, incident light couples into the surface plasmon mode at the angles at which the phase-matching condition [18, 163–165]:

$$k\sin(\alpha) + k_{grating} = k_{SP}$$

is satisfied, where k =$2\pi/\lambda$ is the incident wavevector in air and α is the angle of the incident light from the normal as shown in Figure 7.1. The wavevector is defined as $2\pi/\lambda = \omega/c$. For a periodic grating with lattice parameter, a, this equation can be re-written as:

$$\frac{2\pi}{\lambda}\sin(\alpha) + m\frac{2\pi}{a} = k_{SP}$$

where m is an integer. The equation is visualized in the vector diagram in Figure 7.2.

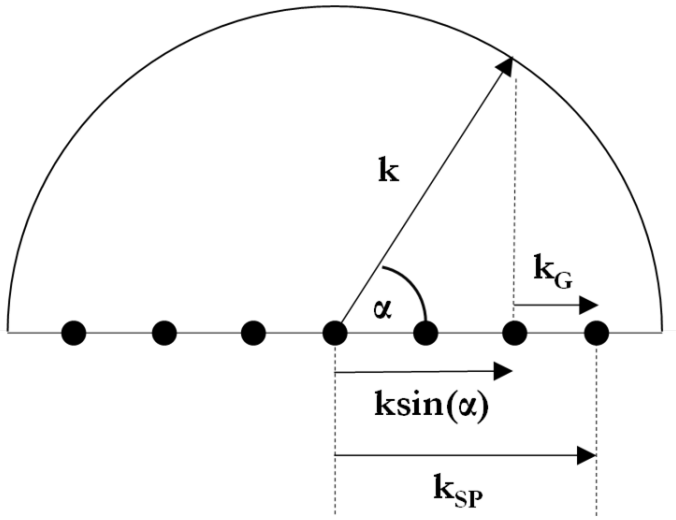


Figure 7.2: Vector diagram describing surface plasmon phase-matching condition. Adapted from [163]

Using the dispersion relation for surface plasmons calculated in Chapter 1, where ε_m and ε_d are the complex valued permittivities of the metal grating and dielectric interface material, this equation can again be re-written as:

$$\frac{2\pi}{\lambda}\sin(\alpha) + m\frac{2\pi}{a} = k\sqrt{\frac{\varepsilon_m \varepsilon_d}{\varepsilon_m + \varepsilon_d}}$$

Therefore, given the material optical constants and the incident wavelength of light, a grating can be designed and the approximate couping angles calculated. A common method to measure this coupling is via reflectometry. In this case, the reflectance of a particular wavelength of light off of a grating is measured as a function of incident angle. At the angles at which the light couples into the surface plasmon wave, there will be a dip in the reflection.

For metallic TiN thin films, the crossover wavelength is near 500-650nm and the surface plasmon wavelength is expected to be closer to 700-1100nm, thus the gratings should be designed for coupling within this wavelength regime. The measurement setup was able to measure reflection in angles greater than 20°. Therefore gratings with lattice parameter, a, near 1-1.5 μm were expected to couple incoming light with wavelengths near 700-100nm. These calculations were confirmed via Finite-Difference Time Domain (FDTD) simulations as will be discussed in the following section.

7.1.2 Finite-Difference Time Domain (FDTD) Simulations

2D FDTD simulations were completed to verify the expected resonance behavior. Lumerical FDTD Solutions software v. 8.15.568 was used. Diagrams of the simulation setup are shown in Figure 7.3. A "grating coupler 2D" structure group was used to create the metallic grating on the dielectric substrate. The grating geometry was specified by four main parameters: the total film thickness, the groove etch depth, the pitch (or period) and finally the width of the grating lines. The width of the grating was specified in terms of the duty cycle which can be defined as the width divided by the pitch.

The simulation region had perfectly matched layer (PML) boundary conditions in the y-directions consisting of 12 'steep-angle' layers. The width of the simulation region in the x-direction was set to the same length of the grating period with Bloch boundary conditions. The simulation time was set

to 600fs with an auto cut-off stopping the simulation sooner if the error fell below 1e-5. The built-in 'auto non-uniform' mesh setting was used. A single wavelength plane wave source was used to imitate the reflectance measurements. The source was injected along the negative y-axis at an angle θ from the normal, shown as 25° in the figure. The purple arrow denotes the direction of the wavevector propagation, k, and the blue arrows denote the electric field direction. In this example, the polarization angle is set to 0° in the figure with the electric field perpendicular to the grating, corresponding to transverse-magnetic (TM) or p-polarization [94, 164, 165]. A polarization angle of 90° was used to simulate s-polarization expected behavior. Two frequency domain profile monitors were used, the first beneath the grating to measure transmission and the second above the injected source to measure the reflectance from the structure.

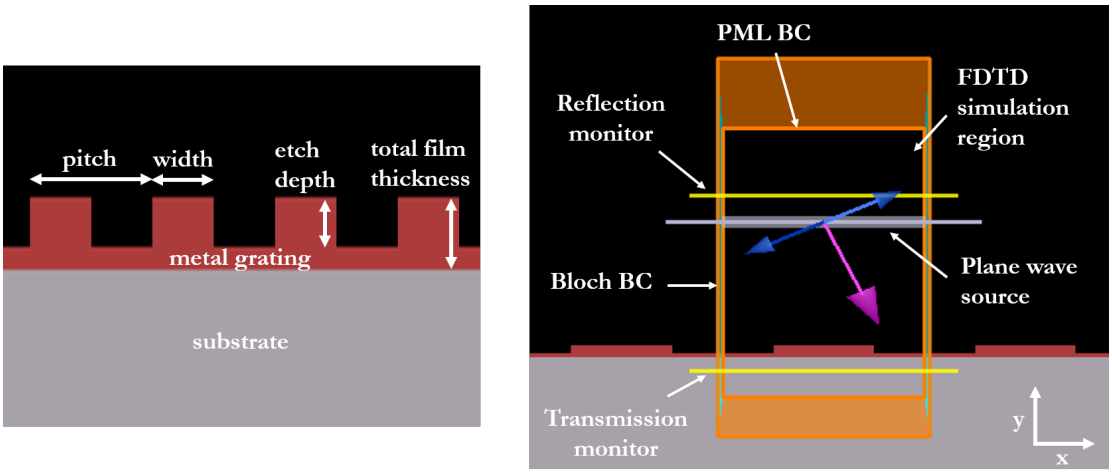


Figure 7.3: Setup of 2D FDTD simulations of TiN metallic surface plasmon grating coupler

Once the initial geometry was set-up, simulations were done to optimize the grating geometry to achieve the best coupling into the surface plasmon mode, defined as the maximum dip in the reflectance at the coupling angle. As described earlier, there are four main parameters which define the grating geometry: the pitch, linewidth, etch depth, and total film thickness. Throughout the simulations shown here, the pitch was fixed at 1.5μm to keep the expected resonance angle within the most

easily measurable range experimentally of 20-50°. Therefore, to optimize the coupling, the etch depth of the grating grooves was first varied to determine the optimal etch depth for a fixed film thickness of 90nm. The results are shown in Figure 7.4. For a film thickness of 90nm, the etch depth at which the resonance dip is deepest seems to be between 40-60nm. Note however that when the grooves are 60nm deep, the reflectance overall drops significantly outside of the resonance range. This is because half of the film is now only 30nm thick and a significant amount of light is transmitted rather than being reflected or coupled into the surface plasmon mode. Therefore, for a 90nm thick film, an etch depth of 40-50nm seems optimal. In addition, it seems that films with total thickness of less than 50nm are unlikely to be ideal for the metal grating geometry if maximum coupling is desired.

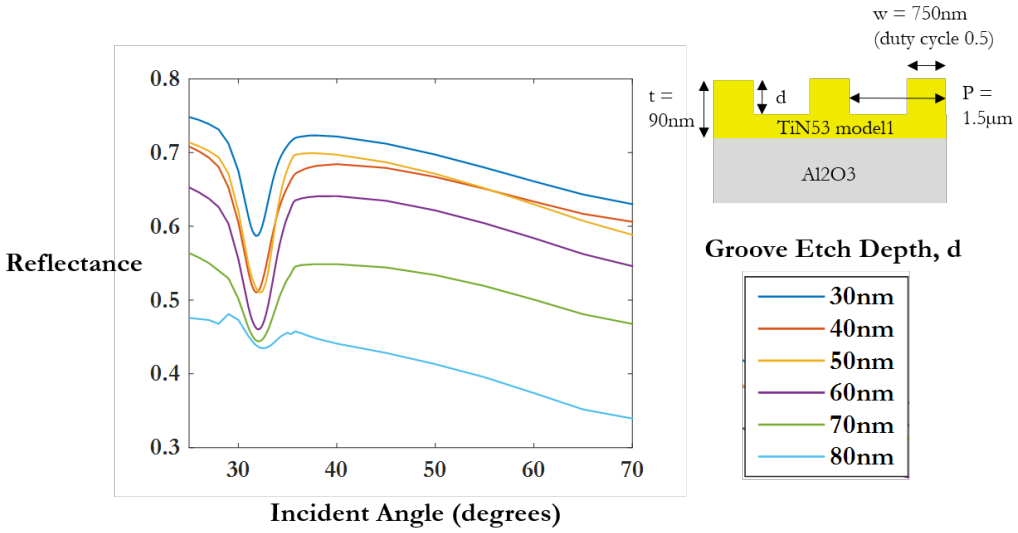


Figure 7.4: FDTD simulated reflectance dip for varied etched groove depths on a TiN metallic grating on sapphire

Next, the duty cycle of the film was varied while the pitch was again held constant at 1.5μm. Using the results of the previous simulations, a total film thickness, t = 90nm and an etch depth of d = 50nm were also fixed. The duty cycle was varied from 0.4 to 0.6, translating to linewidths, w, of 600nm to 900nm respectively. A selection of the results is shown in Figure 7.5. The resonance dip remained at

the same incident angle as the duty cycle varied, which agrees with the fact that the additional k-vector picked up due to the grating is determined by the equation $k_G = 2\pi m/a$. Therefore, as expected, the period of the lines rather than the linewidth determines the coupling angle. According to this figure, it is clear however that to optimize coupling efficiency, the fabricated grating structure should have a duty cycle as close to 0.5 as possible with the linewidth equal to half of the grating pitch. For both larger and smaller linewidths, the intensity of the coupling decreased dramatically.

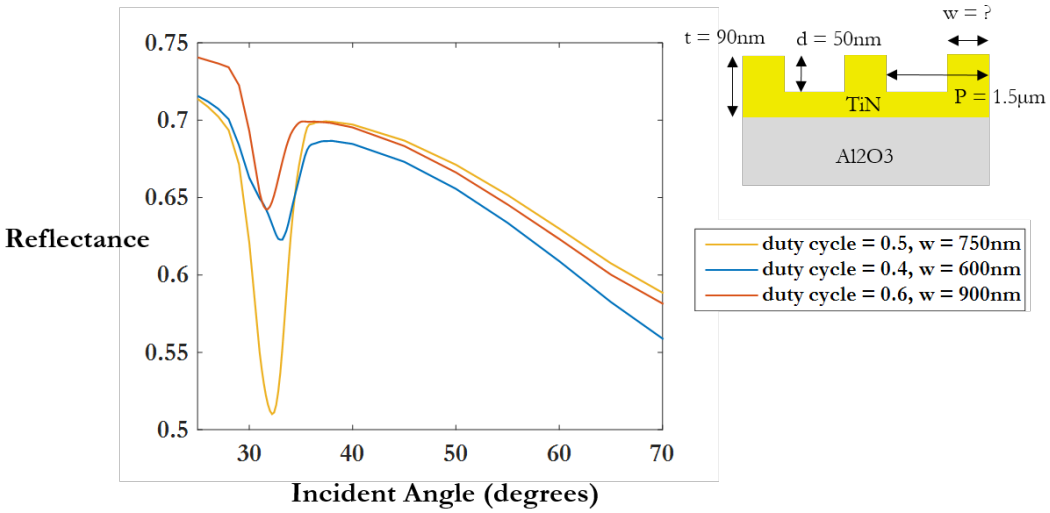


Figure 7.5: FDTD simulated reflectance dip for varied duty cycle on a TiN metallic grating on sapphire

Finally, it is important to point out that these first sets of simulations were done at a fixed incident wavelength of λ = 800nm; however, it is expected that the surface plasmon wavelengths can exist over a range of wavelengths. For this reason, the incident wavelength was next varied for a fixed geometry determined to be optimal based on previous simulations. The results are displayed in Figure 7.6 for a film thickness = 100nm, etch depth = 50nm, period = 1.5μm and duty cycle = 0.5. In this figure, the simulated measured absorption is also plotted as well as the transmission calculated according to R + T + A = 1. This figures shows wide tunability of the grating resonance for a single geometry by varying the incident wavelength without a significant loss in coupling efficiency. In fact, simulations showed the

dip continuing without significant change in intensity to 1300nm however angles below 20° were not accessible in our measurement geometry so at this time, these results have not been explored further.

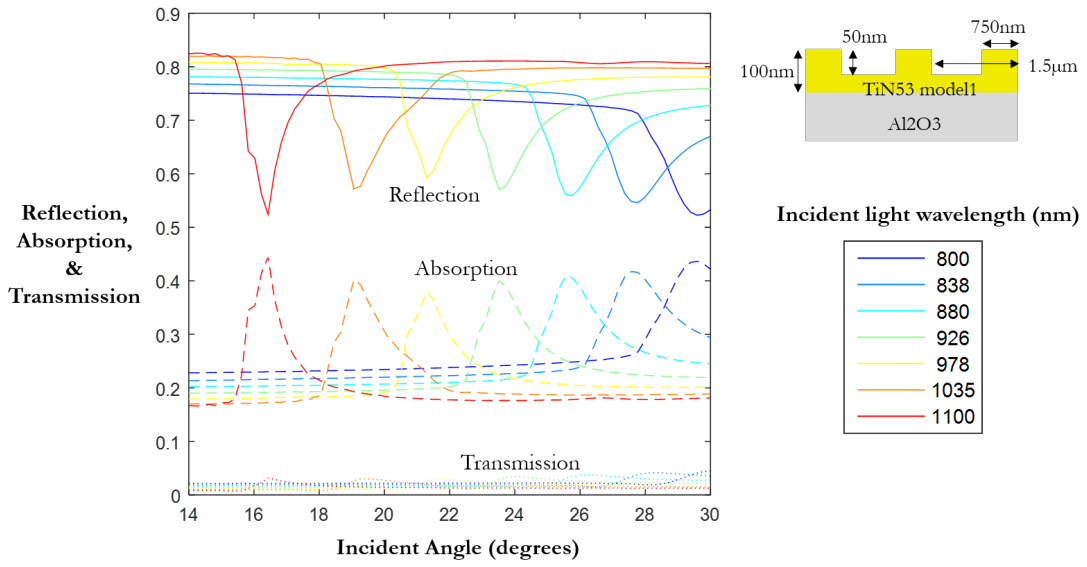


Figure 7.6: FDTD simulated reflectance dip for varied incident wavelengths on a TiN metallic grating on sapphire

It has been suggested that in addition to metallic gratings, dielectric gratings can also satisfy the phase-matching condition leading to surface plasmon coupling. Since these gratings were only intended as a proof of concept to show that the TiN is indeed metallic enough to support surface plasmon modes and since creating dielectric gratings requires fewer fabrication steps than metallic gratings, simulations were also performed over a range of dielectric grating parameters. The relative performance of dielectric gratings created on top of flat metallic TiN films was compared to the coupling into metallic gratings etched directly into the TiN films. It was determined that thicker dielectric gratings out-performed thin dielectric gratings in terms of both coupling strength and sharpness of the resonance width. Select results are shown in Figure 7.7.

Figure 7.7 simulates the predicted resonances of a dielectric grating with heights varying from 100

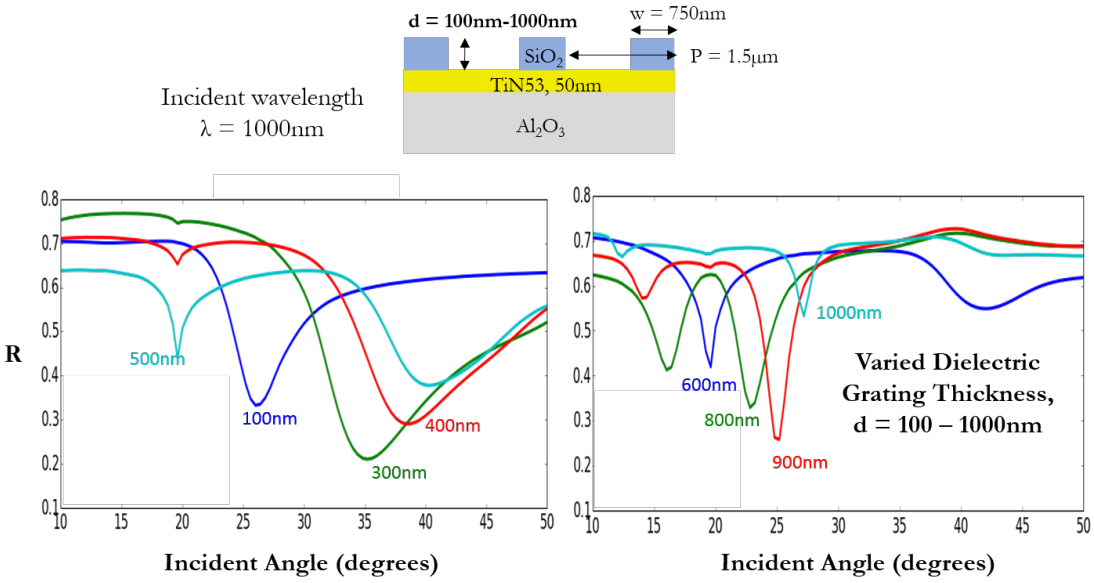


Figure 7.7: FDTD simulated reflectance dip for varied thickness dielectric grating on top of a thin TiN film on sapphire substrate. Simulations performed by and adapted plot from Mena Gadalla.

to 1000nm on top of a 50nm thick TiN film on sapphire substrate. The incident wavelength for all simulations was $\lambda = 1000$nm. The height range simulated was chosen to approximate the thicknesses available using HSQ-based electron beam resists. The optical constants for SiO_2were used to approximate the optical constant of these resists since after baking, exposure and development they are known to behave similarly. Interestingly, at shorter dielectric heights (100-400nm, left plot), the resonances are significantly deeper than the metallic gratings, but also quite broad. At thicknesses of 500nm and above, multiple peaks begin to appear with a peak near 18-25° coupling incident angle which has both a large coupling efficiency and a more narrow peak width. A narrow peak is desirable in simulations since in experimental situations, variations in structure dimensions lead to broadened peaks.

To verify that the coupling seen is due to a plasmonic effect rather than solely an effect of the dielectric grating, the simulations were repeated using the measured optical properties of three different TiN films of varying metallic character (Samples: TiN53 - metallic, TiN35 - moderately metallic, and

TiN40 - barely metallic). The dielectric grating had a height = 900nm and the TiN film in each case a thickness - 50nm. The results shown in Figure 7.8 verify that the coupling is clearly correlated with the metallic and therefore, plasmonic nature of the film with the resonance disappearing in the unoptimized TiN films (TiN35 and TiN40).

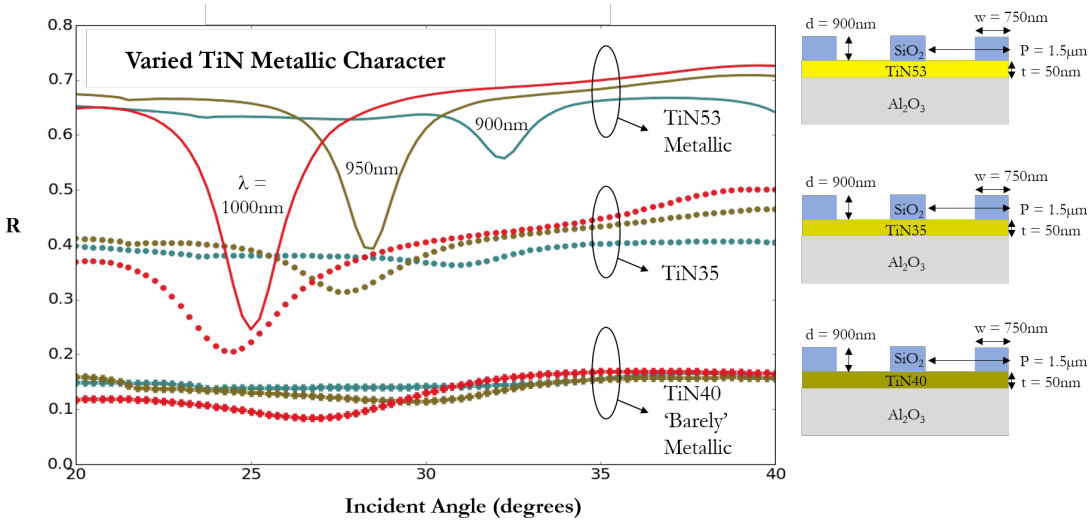


Figure 7.8: FDTD simulated reflectance dip for TiN films of varied metallic character. Simulations performed by and adapted plot from Mena Gadalla.

7.1.3 Experimental Results

FDTD simulations confirmed that optimized metallic TiN films are indeed metallic enough and have low enough losses that they should be able to support surface plasmons in the near-IR wavelength range. Therefore, experiments were next undertaken based on these designs to confirm this experimentally. Since the best overall coupling in the simulations was seen in the design shown in Figure 7.7 with a dielectric thickness of 900nm, this was the chosen design structure. The fabrication was relatively straight-forward and involved first, cleaning the sputtered TiN film sample in acetone, isopropyl alcohol, and a DI rinse and then dehydration bake, followed by electron beam spinning, exposure and development. A schematic of the chosen structure and the fabrication steps is drawn in Figure 7.9.

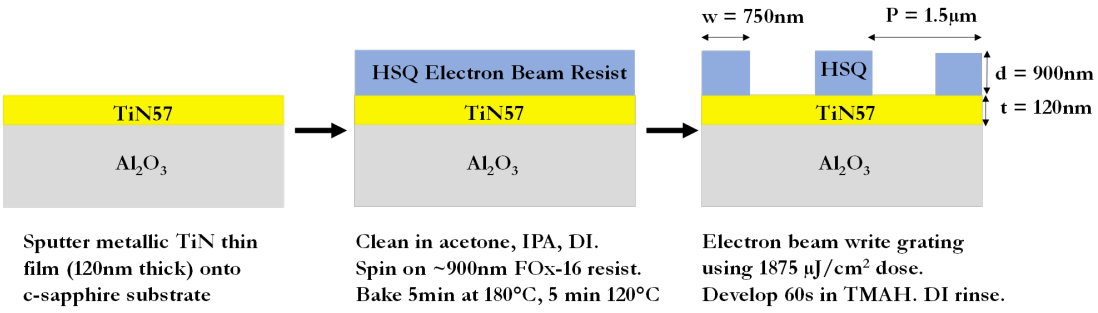


Figure 7.9: Schematic of fabricated plasmon grating coupler design including fabrication steps. The fabricated grating consisted of an 800-900nm thick dielectric grating (double layer FO_x resist) made via electron beam lithography on top of a 120nm thick TiN thin film sputtered onto c-plane sapphire substrate.

The challenge to this fabrication process was the desired thickness of the electron beam resist. Unfortunately, while the HSQ-based electron beam resist available (FOx-16 flowable oxide by Dow Corning) had a rated thickness of 450-950nm dependent upon recipe [166], the maximum thickness achieved experimentally with a single well-distributed layer after spinning was near 600nm, even spinning slowly at 1000rpm. Therefore several trials were done to spin on multiple layers of the resist to increase the thickness to near the desired 900nm. These layers were each spun at 3000rpm for 45 sec followed by a 5min 180°C bake and a 5 min 120°C bake. However it was found that even with baking, each layer only added about 10% additional thickness to the previous layer, so many layers would be necessary to reach 900nm.

Another way to solve this problem and reduce the number of layers needed is to increase the thickness of the resist so that it does not spread out as thinly during spinning. It was found that by first spinning a single layer as stated above and then by dropping on the FOx-16 resist and then waiting for a few seconds before starting the spinner, that some of the solvent would evaporate and a thickness between 800 and 900nm could be achieved with only a double layer. The film studied below was produced via this method. After spinning, the procedure included a 5min 180°C bake, then a 5 min 120°C bake, electron beam exposure at a dose of 1875 μC/cm², and development for 60sec in TMAH

followed by a DI water rinse.

The reflectance measurements were performed using the same J.A.Woollam ellipsometer described in Section 3.3. The gratings are designed to be resonant at the correct angles and wavelengths with p-polarized incident light. However, measurements were made with both s- and p-polarized incident light. The s-polarized measurements showed no reflection dips as expected (not shown). An enlarged grating has been drawn onto the sample in the schematic shown in Figure 7.10 to demonstrate the measurement geometry.

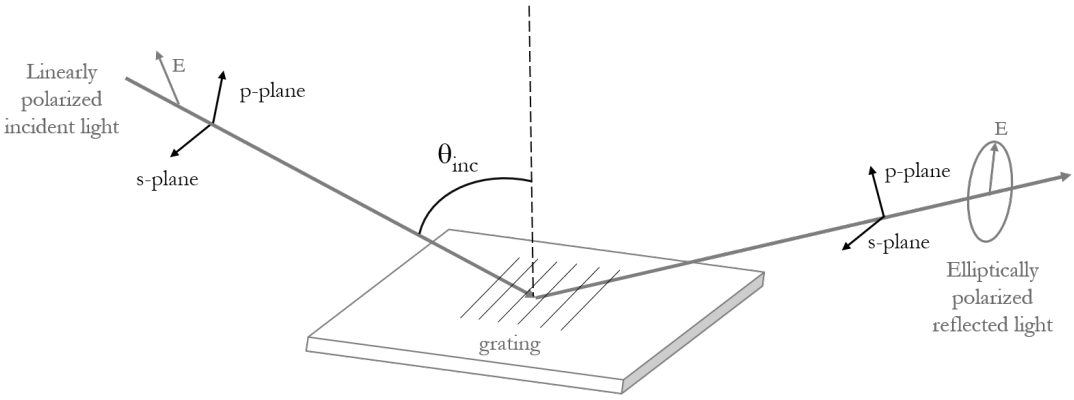


Figure 7.10: Grating coupler reflectance measurement geometry

When the grating was illuminated with p-polarized light, a significant resonance dip was observed for wavelengths greater than about 800nm, as expected. The experimental measurements as compared to the expected results via FDTD simulations are plotted in Figure 7.11 for selected wavelengths of 880, 900, and 920nm near where the observed resonances were strongest for this particular structure. While the gratings are clearly able to couple in light to surface plasmons at the TiN interface due to the deep reflectance dips, there are some issues to resolve. The spacing of the peaks in the experiment as compared to in the simulations is equivalent but the experimental peaks are shifted just over 2 degrees higher in coupling angle. SEM images were taken of the fabricated grating structure to determine the potential cause of the shift in the data. The micrographs are shown in Figure 7.12.

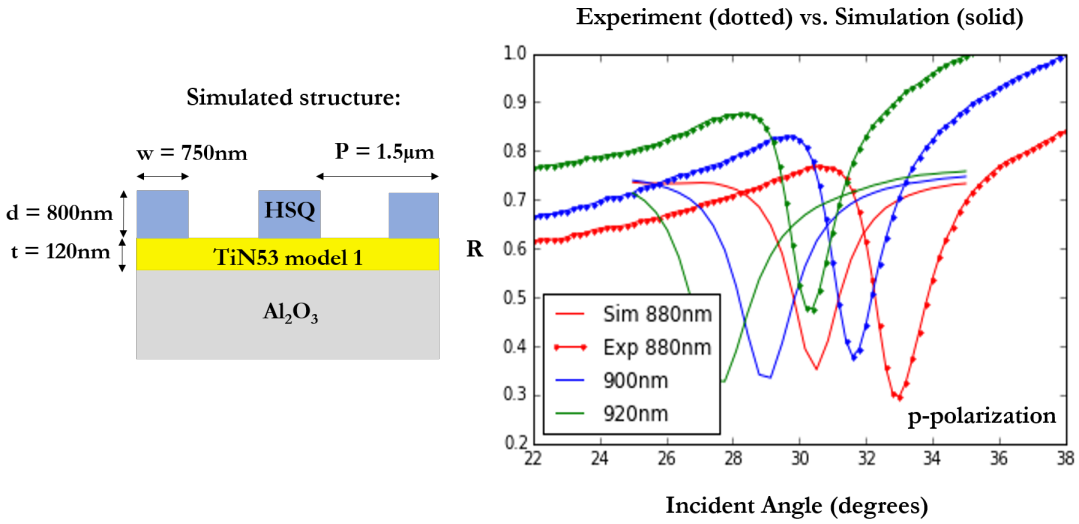


Figure 7.11: Measured experimental reflectance off of SiO_2 grating on TiN as a function of angle at 880, 900, 920nm compared to simulations. Incident radiation is p-polarized. Sample: TiN57EB3

As shown in Figure 7.12(a) from a top-down view, the grating initially seemed to exhibit the expected geometry. The period was measured to be very close to 1.5μm and duty cycle close to 0.5. The height of the grating approximated by profilometry was measured to be between 800 and 900nm tall. The sample was next mounted on a tilt stage to examine the film from an angle (b & c). Figure 7.12(b) shows an SEM looking at the edge of the grating from the side at a grazing angle of about 10°. From this view, the height of the film on the edge was measured to be closer to 800-850nm. It is from this angle that the variation in dose caused by the proximity effect is also seen. Near the edge, the line clearly has a thinner width. In figure (c), I zoomed in on a spot near the center of the grating. From this tilted angle and high magnification it is easy to see that the center of the grating has been overexposed with some of the resist between the grating lines remaining even after development.

Based on the SEM images, several additional simulations were run to determine the effect of slight changes in the grating geometry on the expected reflectance dips. Even slight variations in the geometry cause significant shifts in the data as shown in Figure 7.13, thus it is not surprising that an approximate

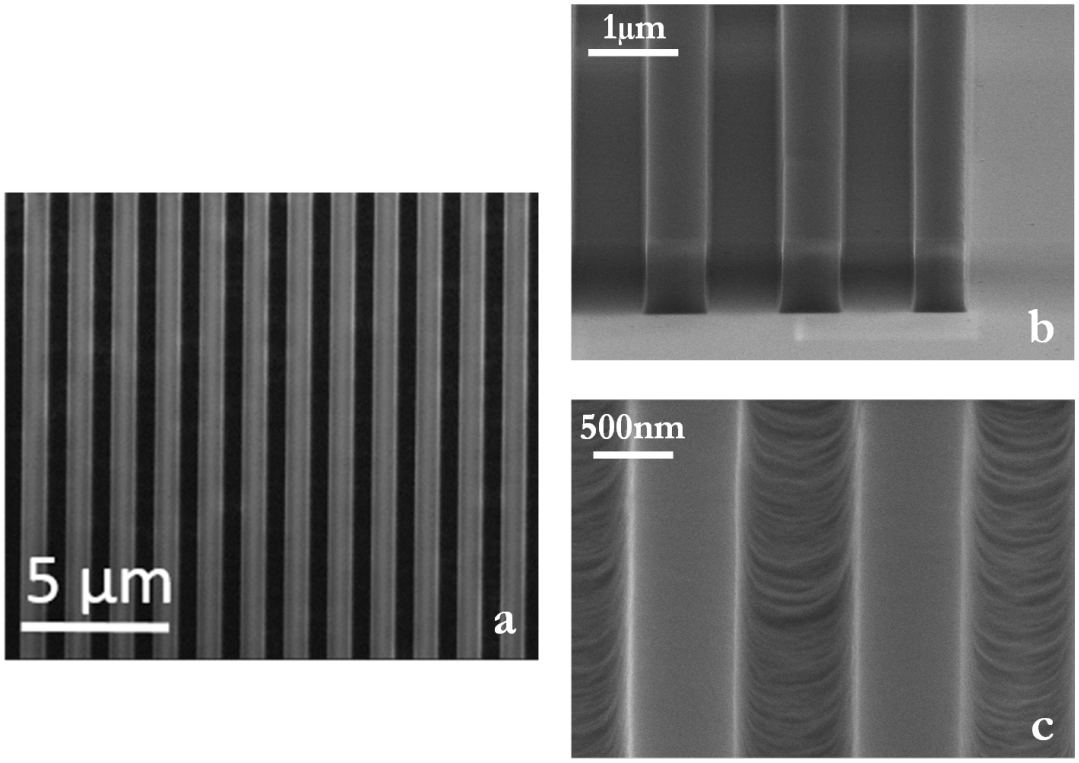


Figure 7.12: (a) Top-down SEM of fabricated grating seems to show expected geometry (b) Tilted SEM near edge shows proximity effect issues with varying thickness of grating lines (c) Overexposure due to proximity effect is confirmed at the center of the grating pattern

2° shift was at first observed between the experimental and simulated data. As shown in the figure, slight increases in the grating period, dielectric thickness, or duty cycle are all expected to cause the coupling angles to shift to increased values. Since the initial simulation used a dielectric thickness of 800nm, by increasing this the simulated data should shift closer to the experimental data. In addition, the experimental data exhibits a deeper dip for incident wavelength = 880nm (red) and shallower dip at 920nm (green). A similar trend is seen for duty cycles slightly increased to 0.51 or 0.52, fairly likely based on the overexposure.

The only feature of the original experimental data which could not be explained by the new simulations was the trend of increasing background reflectance for increasing incident angle since all simu-

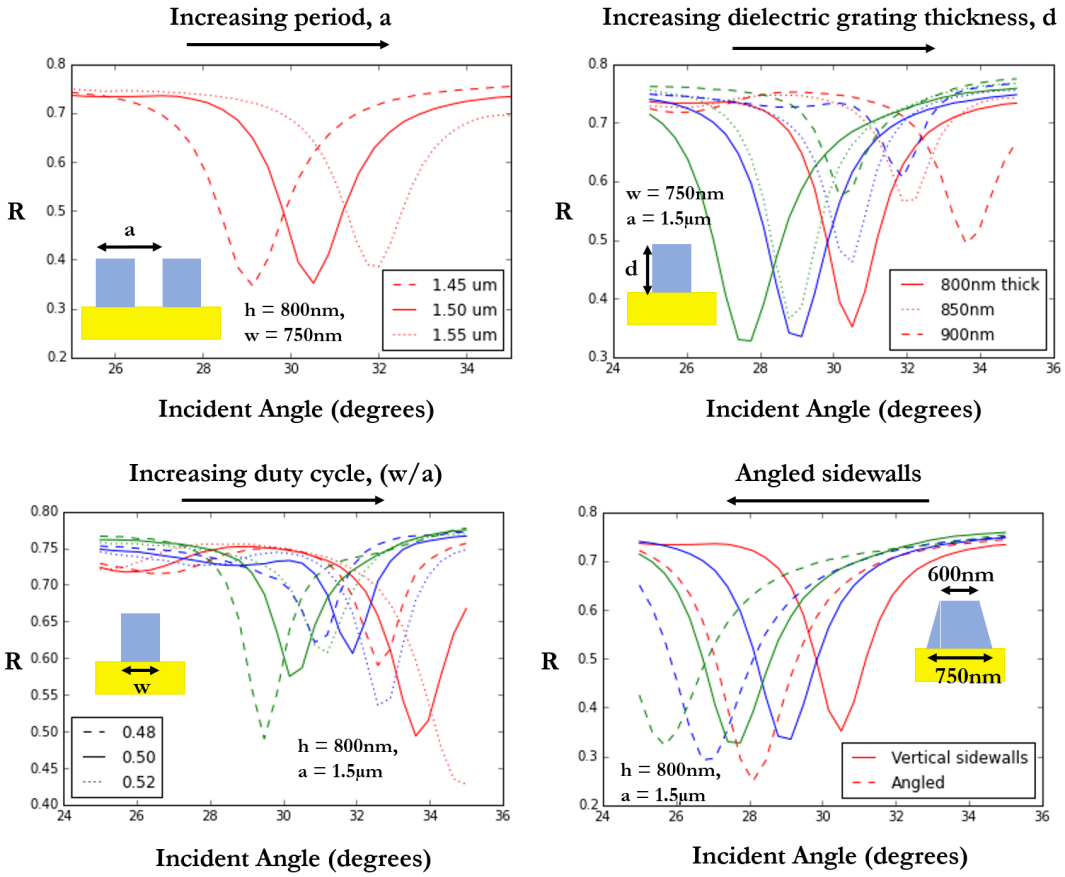


Figure 7.13: FDTD simulations showing effect of slight grating geometry variations on expected reflectance dips

lations showed relatively flat backgrounds. It was determined that there had been an error in the normalization in the additional measurements and therefore new experimental reflectance measurements were performed. The new experimental data and adjusted simulations are compared in Figure 7.14. The new experimental and simulated data shows good agreement. In conclusion, the proof of concept that these optimized TiN films were metallic enough and with low enough losses to indeed support surface plasmon modes was successful.

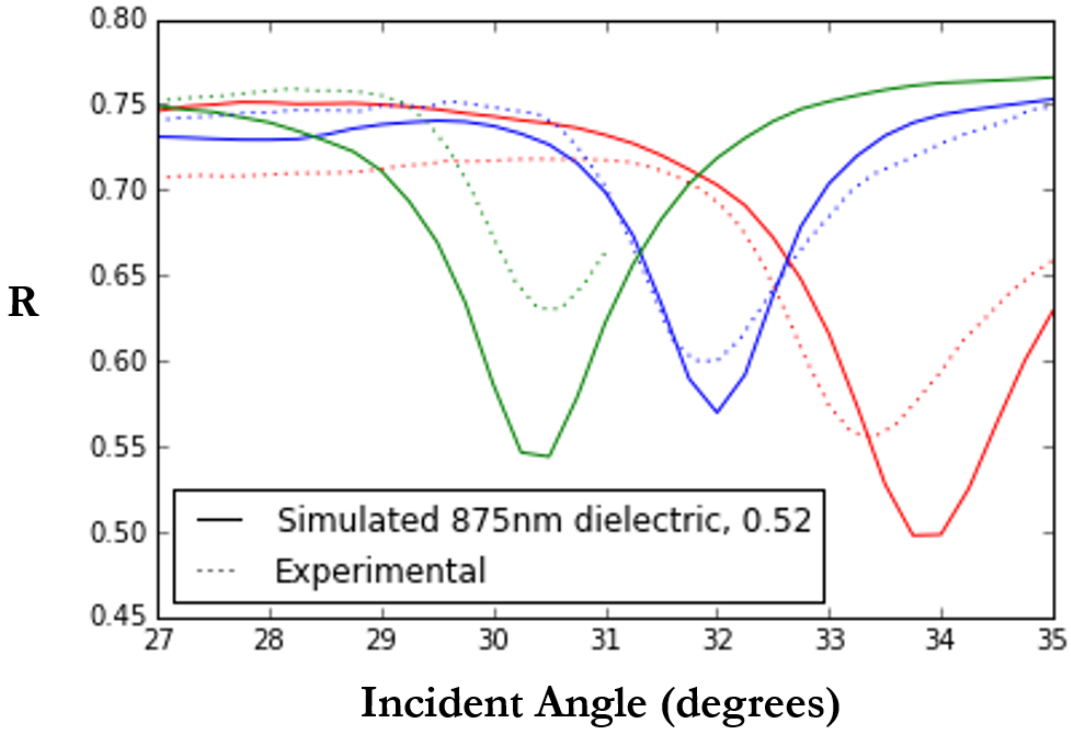


Figure 7.14: Measured experimental reflectance off of SiO_2 grating on TiN as a function of angle at 880, 900, 920nm compared to modified simulations. Incident radiation is p-polarized. Sample: TiN57EB3

7.2 Mid-infrared (Mid-IR) Nanoantennas (collaboration with University of Stuttgart)

In close collaboration with researchers at the University of Stuttgart, the feasibility of using TiN as a plasmonic material further out in the near to mid-IR wavelength regime was next explored since our initial measurement setup limited experiments to a maximum wavelength of about 1600nm though simulations had shown the potential of resonances longer than this. Plasmonic nanoantennas were fabricated via two methods: direct laser writing and laser interference lithography and the plasmonic resonances simulated as well as measured from about 3- 7μm. The fabrication methods will next be discussed briefly followed by a summary of the experimental results.

7.2.1 Fabrication Methods

Two methods were used to fabricate the mid-IR nanoantennas: direct laser writing (DLW) and laser interference lithography (LIL). In DLW, a two photon absorption process was used to write the nanoantenna pattern (Photonic Professional GT, Nanoscribe GmbH system). In the first set of experiments, Si substrates were used. They were cleaned in a quick 49% HF dip then sonicated in acetone, isopropyl alcohol and rinsed in DI water. Next, a 50nm layer of TiN was sputtered non-reactively onto the Si using the 20°C plus 100V bias recipe (Sample: TiN43 Si-2sp). Next, 5nm/100nm Cr/Au films were electron beam evaporated (Pfieffer Vacuum Model PLS-500) onto the TiN film to serve as an etch mask. Finally, the nanoscribe polymer resist (Nanoscribe IP-Dip) was dropcast onto the surface of the Au over the area in which the pattern was desired.

The nanoscribe laser was used to write an array of nanoantennas of varying dimension using a two-photon absorption process to expose the resist. After removal of the unexposed resist (15 min development in Microresist mr-dev 600), an Ar^+ ion beam etch (Technics Plasma Model R.I.B. - Etch 160) was used to transfer the pattern into the gold mask. The IBE has approximately a 50:1 selectivity

in terms of Au etch rate:TiN etch rate so the sample was purposefully slightly overetched to ensure that all excess gold and the Cr sticking layer was removed outside of the mask. Next chemical etching using a basic Piranha etch ($1NH_4OH : 2H_2O_2 : 5H_2O$ ratio by volume, at 75°C) was used to etch down into the TiN layer to the Si surface. After this an oxygen plasma (Diener electronic Plasma-Surface-technology) was used to remove any remaining resist. Finally, the gold was removed via a second Ar^+ IBE leaving only TiN nanoantennas remaining on the Si substrate. The process is outlined in Figure 7.15. The LIL process is similar however a different photoresist is used (ma-N 405) which has been optimized for the LIL exposure process. This photoresist is developed in AZ826. The mask layer is also thinner with 2nm/35nm Cr/Au, respectively. Measurements of the nanoantenna transmittance were made via a Bruker Vertex 80 spectrometer coupled to a Bruker Hyperion microscope. The sputtering process was completed at Harvard University and the nanoantenna fabrication and transmittance experiments were completed at the University of Stuttgart.

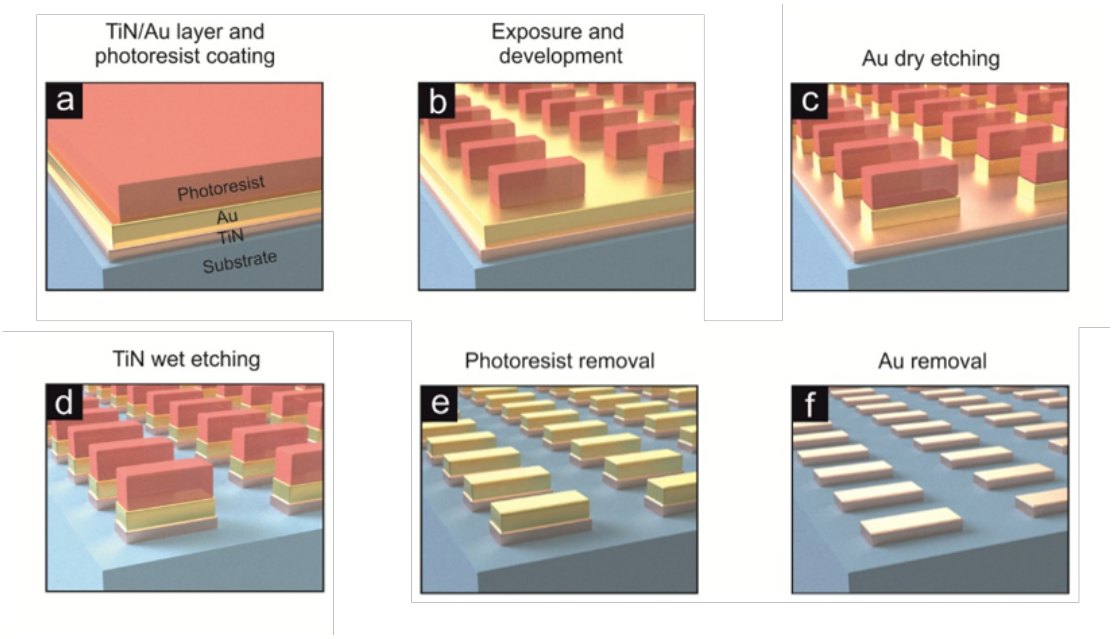


Figure 7.15: Fabrication steps for mid-infrared nanoantennas. Figure created by Shahin Bagheri. Adapted from [71]

7.2.2 Simulations & Experimental Results

TiN thin films from two sputtering runs were used in these experiments. The first was a moderately metallic film on Si substrate and the second a more optimized metallic film on sapphire substrate. The optical properties of both films were measured using a J.A.Woollam ellipsometer with an extended range from 300nm to 2.2μm. Models were made within this range by measuring psi and delta at varied angles of incidence from 45° to 65° in steps of 5° and then combining them with reflectance data measured in the mid-IR to extrapolate the optical properties into this regime. The final approximated optical properties for both films used are plotted in Figure 7.16.

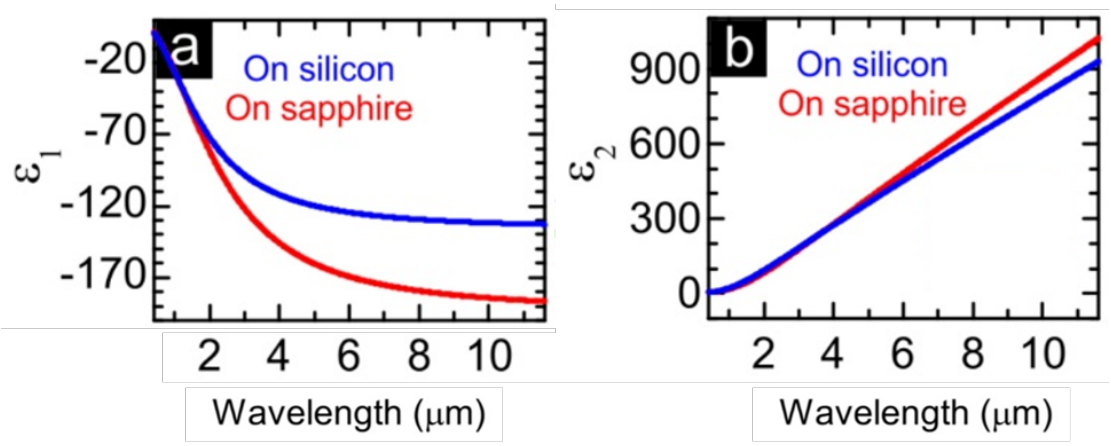


Figure 7.16: Optical properties of TiN thin films extrapolated into mid-infrared. Samples: TiN43 Si, TiN49 Saph. Adapted from figured created by Shahin Bagheri. Adapted from [71]

The extrapolated optical properties were used to simulate plasmonic nanoantenna resonances with antennas of varied lengths using a Fourier modal method numerical simulation approached as described in [167]. Figure 7.17(a) shows the simulated results for nanoantenna arrays on sapphire substrates with different periodicities, p, and antenna lengths, L, which determine the resonance wavelengths. Red: p = 1.5μm and L = 1.0μm, Green : p = 2.0μm and L = 1.5μm, and Blue: p = 2.0μm and L = 2.0μm. For these simulations, the polarization of the electric field is parallel to the long axis of

the antenna as depicted in the schematic. Subfigures (b) and (c) demonstrate the agreement between experiment and simulation of one such fabricated nanoantenna array with p = 1.5μm and L = 0.83μm. The width of the antennas is 200nm.

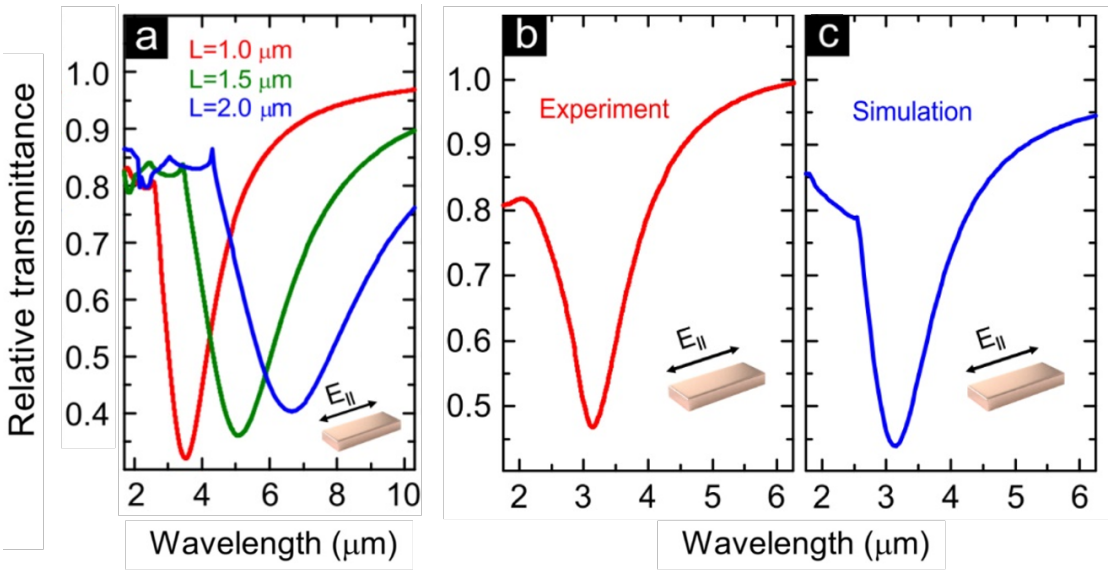


Figure 7.17: Simulated and experimental results of TiN nanoantenna relative transmittance on sapphire substrate. Sample: TiN49 Saph. Adapted from figures created by Shahin Bagheri. Adapted from [71]

While the resonance was not quite as strong on the Si substrates due to the lesser plasmonic quality of the material, a broader resonance was still clearly visible and tunable over a wide range of IR wavelengths by fabricating arrays of various geometries with lengths ranging from 200 - 1400nm even with this 'moderately' metallic material. The widths and heights of the antennas are 250nm and 50nm, respectively. The results of the experimental measurements and simulations agree fairly well as shown in Figure 7.18. Top-down SEMs of the corresponding nanoantenna arrays are also shown. The resonance positions are plotted versus the antenna lengths demonstrating a highly linear relationship as shown in figure (c). The quality of this response as compared to the response measured on the more highly optimized films confirms the important of the careful control of the TiN material quality for plasmonic applications. This experiment also confirms however the wide tunability of this material.

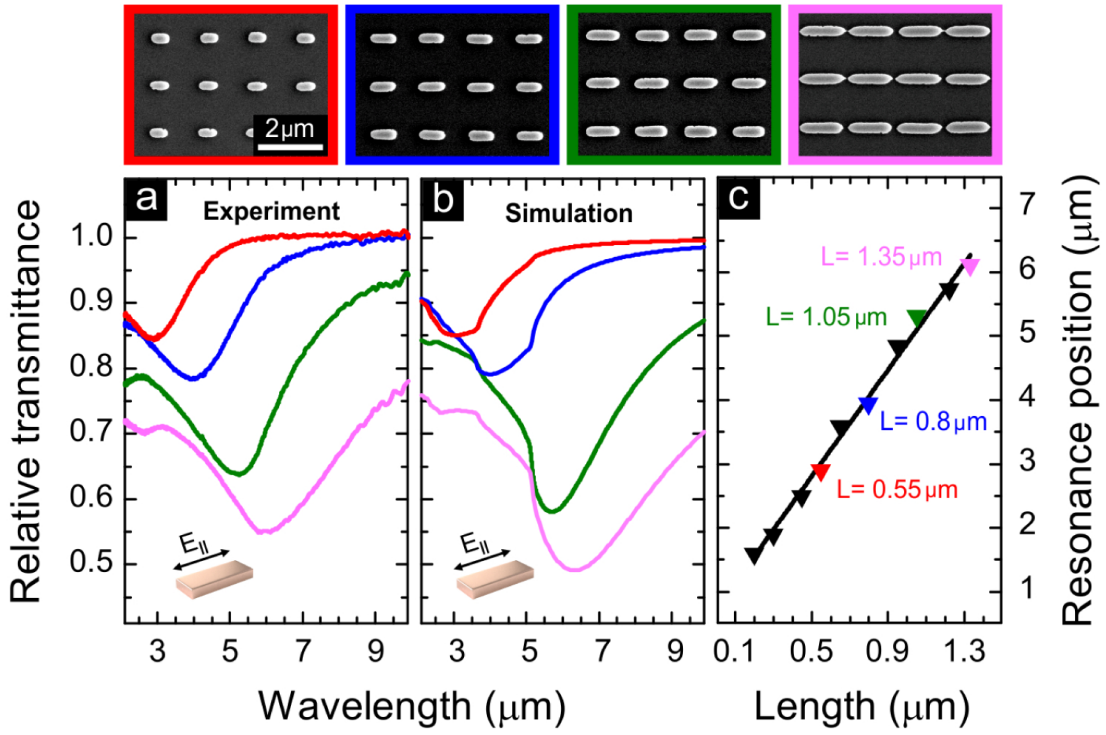


Figure 7.18: Experimental results of tunable TiN nanoantennas fabricated by direct laser writing (DLW) on Si substrate. Figure created by Shahin Bagheri. Sample: TiN43 Si-2sp. From [71]

Finally, it was stated at the beginning of this section that nanoantennas with IR plasmonic resonances were fabricated via two methods: DLW and LIL. To this point, the nanoantennas discussed have all been fabricated via DLW which allows for writing of arrays with several different dimensions on one sample and shows the possible tunability of these nanoarrays. However, there is significant interest in larger scale fabrication of nanoscale devices and LIL is one potential method via which nanoantennas can be patterned over a large scale quickly. An example of creating TiN nanoantennas via this method is demonstrated in Figure 7.19. Subfigure (a) shows an example of a TiN nanoantenna array patterned onto a sapphire substrate next to a coin for reference. The entire pattern is created after only a few seconds of laser exposures. (b) Shows a top-down SEM of the TiN nanoantenna array fabricated via LIL on a Si substrate with the corresponding transmittance resonance plotted in (c).

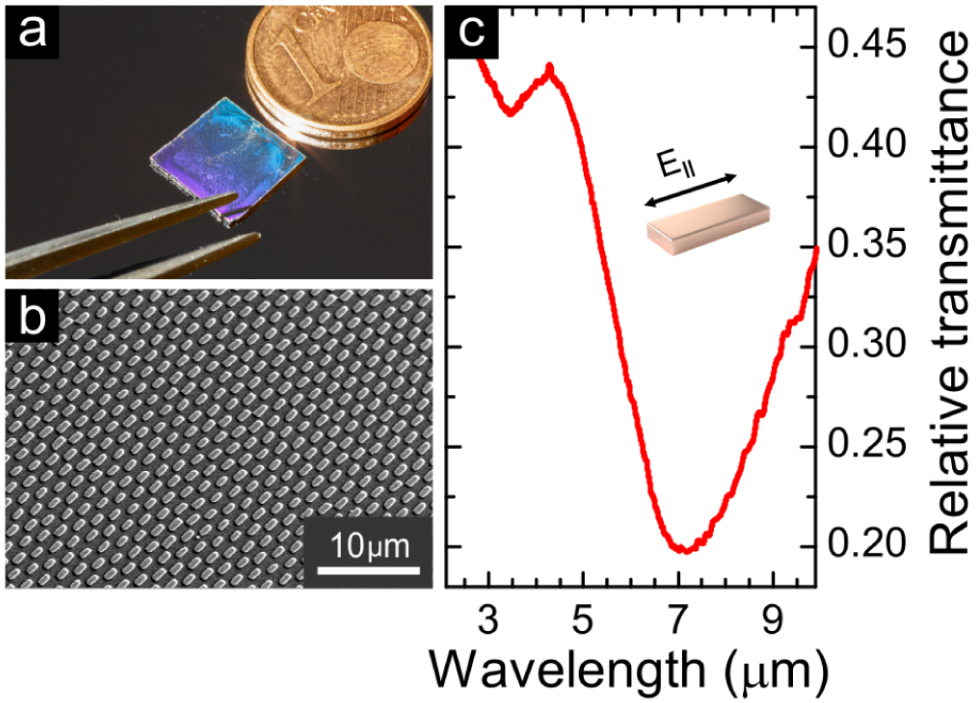


Figure 7.19: Experimental results of large-area TiN nanoantennas fabricated by laser interference lithography (LIL). Figure created by Shahin Bagheri. Sample: TiN43 Si-2sp From [71]

This set of experiments is important because it shows that large scale fabrication of TiN nanostructures is plausible and extends the range over which TiN has been shown to serve as an alternative plasmonic material. This extension into the mid-IR range is potentially quite exciting due to the recent surge in interest in thermophotovoltaics, thermal emission and perfect absorption [2, 47, 168]. Many of the applications within this regime require robust materials due to the intense focusing of light leading to elevated temperature, therefore using a refractory material such as TiN which can withstand higher temperatures than more commonly used plasmonic materials could have significant impact within this field.

7.3 Photothermal Drug Therapy using TiN Pyramidal Arrays (collaboration with Eric Mazur Research Group)

Drug delivery and drug therapy are current important research topics with significant interest in localized, targeted therapy of unhealthy cells rather than treatment which can damage both healthy and unhealthy cells equally. Significant recent research has focused on targeted therapy using metallic plasmonic nanoparticles. It has been found that by irradiating metallic nanoparticles with high intensity laser beams that surface plasmon excitation of the particles creates large electric fields and local heating which can local destroy tumors or open up holes in the cell membranes [169–173]. Unfortunately, this process can kill healthy cells and can also break up the nanoparticles into small nanometer fragments leading to a potential toxicity problem [174]. Rather than inserting nanoparticles into the body, another option is to collect the unhealthy cells from the patient, treat them, and then reintroduce the healthy cells back into the patient. Preliminary experiments were performed to explore the potential to

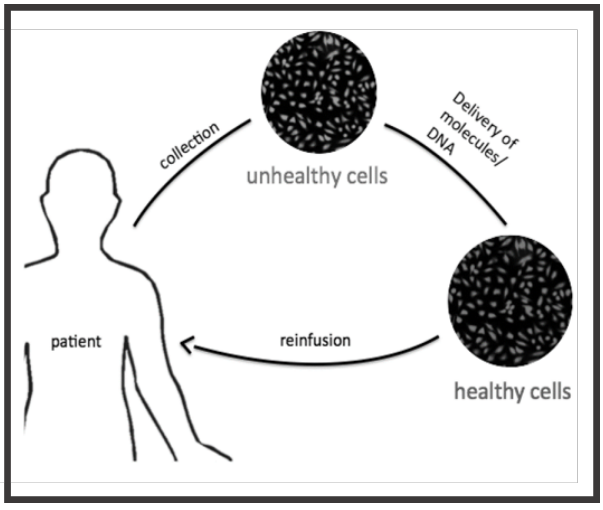


Figure 7.20: Unhealthy cells are collected from the patient, treated, and the new, healthy cells are re-infused back into the patient. Diagram from Nabiha Saklayen and Alexander Raun, Eric Mazur Research Group.

treat cells using this method with TiN micropyramidal substrates as the plasmonic material in collab-

oration with the Eric Mazur Research Group at Harvard University. The initial efforts are discussed in this section.

7.3.1 Introduction and Motivation

One of the ways which unhealthy cells can be treated is by cell transfection, or the delivery of genetic material such as DNA or RNA in a controlled way into mammalian cells. There are many different proposed methods to do this, all with different advantages and disadvantages. Some of the most desirable attributes are high-throughput, efficiency and cell viability. In short, it is desirable that many cells can be treated quickly and remain viable after treatment, therefore able to be reinfused into the patient.

One of the hurdles to overcome when delivering these macromolecules to cells is finding a way to transfer the information through the cell membrane which is impermeable to large objects such as DNA. A recent proposed method which is gaining traction and has been proven to be fast and also efficient is via microcavitation, by using high intensity light pulses to create bubbles which permeate cell membranes for large-scale drug delivery into mammalian cells [173]. Recently, gold substrates with arrays of plasmonic micropyramids have been used to achieve high-poration efficiency and cell viability with low toxicity [175]. While little gold residue is left after poration using the pyramid array, the pyramid tips show some damage due to the strong electric field enhancement and heating effects. Since TiN is known to have a higher heating efficiency than gold as well as also being nontoxic [176] and already currently used in biomedical implants [177–179] and ongoing studies of the use of TiN nanoparticles for photothermal medical therapy [46], this study focused on first replicating the nanopyramid poration experiments with TiN pyramids rather than gold pyramids.

A schematic of the proposed experimental drug delivery setup using a TiN micropyramid array is depicted in Figure 7.21. The pyramidal array is fabricated on a transparent substrate to allow for illumination from the backside. The enhanced field produces local heating near the tops of the pyramids

which produce bubbles at the tips of the pyramids coinciding with their contact points with the cells. These bubbles porate the cell membrane to allow permeation.

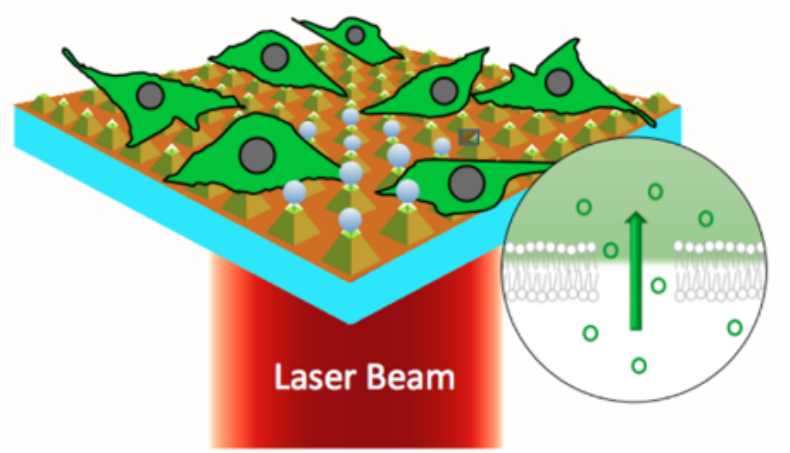


Figure 7.21: Arrays of TiN plasmonic nanopyramids are fabricated on transparent cover slips. A laser illuminates the pyramids from beneath. The enhanced plasmonic field at the tips of the nanopyramids create bubbles which porate the unhealthy cells allowing drug delivery. Image provided by Nabiha Saklayen and Alexander Raun.

Human cells are on the order of 10-30μm. Each pyramid in the array has a length of approx. 2μm dependent upon the fabrication design. Therefore, one cell will spread across many pyramids. For a size reference comparison between the cells and the pyramidal array, an SEM image is shown in Figure 7.22 (left).

7.3.2 Fabrication Methods

The pyramid array is fabricated via a template-stripping process as described in [175]. Photolithography is used to create an inverted square mask array on a Si wafer. The wafer is then anisotropically wet-etched in KOH to reveal the inverted pyramidal array. A thin 30-50nm layer of gold is evaporated onto the inverted Si pyramidal array. The sample is then coated in Norland NOA61 UV-curable epoxy

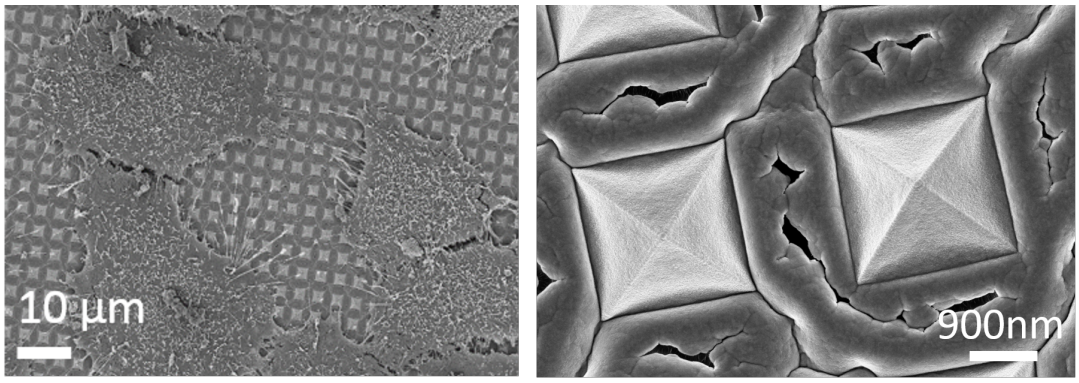


Figure 7.22: SEM of biological cells on TiN plasmonic nanopyramid array and zoom in of pyramids prior to irradiation. Images provided by Alexander Raun.

and secured with a glass coverslip. The coverslip/epoxy/gold layers are template-stripped from the Si substrate and flipped over to reveal the gold thin film atop epoxy nanopyramid array.

Ideally, in a final design, there would not be a gold layer present in this sample, however TiN sticks to Si and cannot be easily template stripped via the same method. Therefore, solely as a preliminary effort, TiN films 50nm in thickness were first sputtered directly onto an epoxy array (no gold), however there was significant damage to the pyramids upon laser irradiation via this method and the cells were not successfully permeated, therefore, next the TiN thin film was sputtered directly onto the gold pyramidal array, using the gold as a buffer layer. An SEM of the resulting structure is shown in Figure 7.22 (right). While the TiN sputtered onto the pyramids looks structurally sound, there were large cracks in the TiN film in the regions surrounding the pyramids, likely caused by stress in the film. In future experiments, the fabrication method will be improved to reduce these imperfections. Regardless of the structural defects, this array allowed for successful permeation of the cell membranes using TiN with high viability as will be shown in the following section.

7.3.3 Preliminary Experimental Results

After the cells are laser-activated on the TiN micro-pyramid plasmonic substrate, whether the cell membranes have been permeated and also whether the cells are still alive after the process is tested by introducing two different dyes. Calcein green is a cell impermeable dye which can only be uptaken into the cells if the membranes have been permeated during the cavitation process. The permeated cells will fluoresce in green. An example image of cells taken on a TiN plasmonic substrate after activation is shown in Figure 7.23 (left). For this therapy to work, the cells must be able to survive the permeation process, therefore not only the permeability but also the cell viability after activation is also important. The cell viability is measured using a different dye, Calcein AM. The viability after activation on the same TiN plasmonic substrate is shown in the right-hand side of the figure. In this experiment, a 1064nm 4ns pulsed laser was used with a repetition rate of 50Hz and fluence on the order of 10-20mJ/cm^2 to to activate the substrates and permeate the cell membranes.

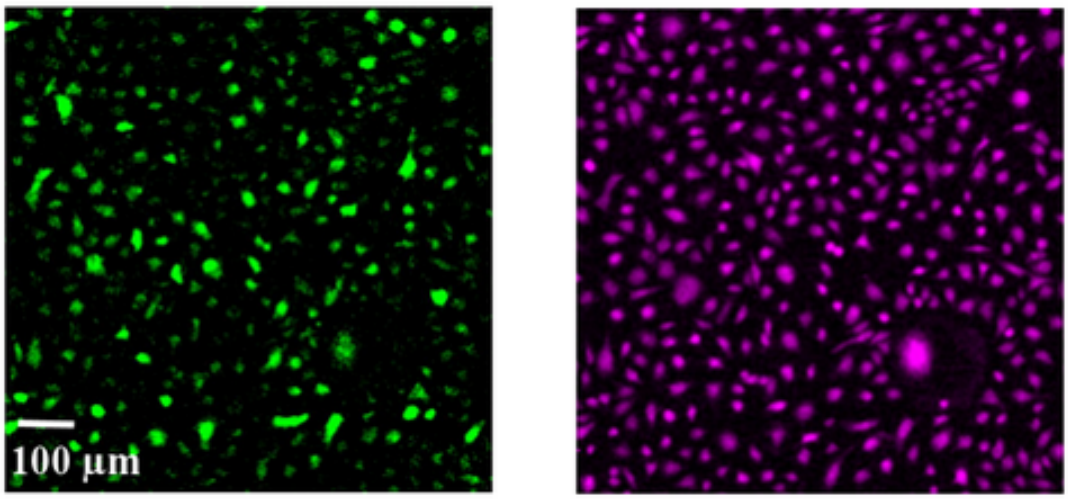


Figure 7.23: Optical image of different colored dyes showing successful cell poration and viability. Data provided by Alexander Raun and Nabiha Saklayen.

While this work is still quite preliminary, there are several important implications. First, is the con-

firmed potential that TiN can serve as an alternative plasmonic material for biomedical applications with low toxicity proven by the high viability of the cells measured after the experiment. More generally, this set of experiments has demonstrated the ability to deposit TiN on a wide variety of substrates including flexible substrates using the techniques developed within this thesis. While the plasmonic quality of this material is not as high, for example, as that of epitaxial grown TiN on MgO, even without optimization of the sputtering recipe TiN of plasmonic quality was still able to be sputtered even onto an epoxy polymer substrate. With previous methods for growing plasmonic TiN requiring temperatures >600°C, the use of epoxy as a substrate would have seemed impossible. Therefore, above and beyond the interesting potential photothermal medical applications for which TiN shows significant potential, the ability to sputter plasmonic quality TiN at room temperature allows for possibilities previous unconsidered including flexible substrates such as shown here. An example is shown in Figure 7.24 in which part of the template stripped epoxy substrate has curled up, yet the TiN pyramids have remained intact.

Acknowledgements

The work within this chapter was completed with the help of many people whom I would like to specifically acknowledge. A visiting Research for Undergraduates (REU) student, Mono Livingston, spent a summer working on etching TiN to create metallic gratings. In addition, Harvard S.M student in applied optimization, Mena Gadalla, spent a semester studying not only the FDTD simulations of the dielectric gratings on TiN, but also bowtie nanoantennas as well as TiN nanopatches for phase control which may be the subject of future work. The mid-IR studies shown in Section 7.2 were performed in collaboration with the University of Stuttgart and would not have been possible without Professor Harald Giessen and Ph.D. student Shahin Bagheri as well as many other members of the 4th Physics Institute. Shahin and I worked closely during my two week visit to fabricate the near to mid-IR nanoantennas and he performed many of the measurements and analysis presented after the

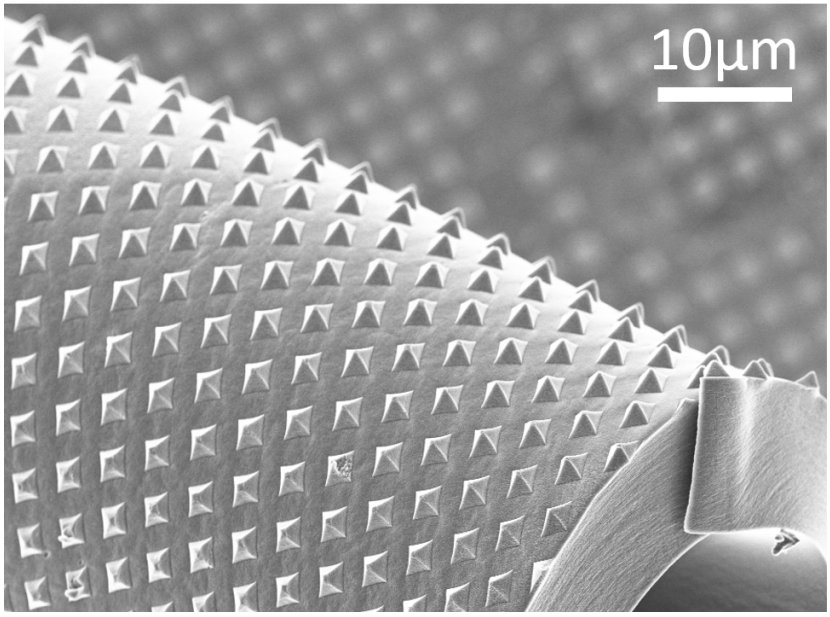


Figure 7.24: SEM of TiN plasmonic pyramid array sputtered at room temperature onto flexible polymer epoxy substrate. Image provided by Alexander Raun.

conclusion of my visit. Finally, I thank Harvard Ph.D. student Nabiha Saklayen and undergraduate Alexander Raun for their interest in exploring TiN for potential photothermal drug delivery applications. While I have provided them with TiN thin films as well as advice, this work has been mainly performed by them and is included briefly here mainly to highlight the wide ranging potential of this optimized plasmonic TiN.

8

Conclusions

Recently, interest in applying materials research within the field of plasmonics to pursue materials which are tailored specifically to a particular plasmonic operation and operating wavelength has surged. This has resulted on the investigation of the potential compatibility of a wide array of materials with plasmonic device design. One of the suggested materials, titanium nitride, has been shown to exhibit a wide array of optical properties depending on the methods and particular conditions under which the film is deposited. The method of deposition chosen in this study was magnetron sputtering. A careful study was presented in this thesis discussing the ways in which the optical, electrical, and structural properties of these films are related and how they can be controlled through variation of the sputtering deposition conditions.

Large variations in the optical behavior in the sputtered films were seen based on the chemical com-

position and bonding. For oxynitride films with large oxygen content (greater than approx. 25-30 atomic%) the films were significantly less conductive and some even exhibited optical properties suggesting dielectric behavior. As the amount of incorporated oxygen was lowered, how the nitrogen was bound within the films played a more important role than the absolute Ti:N:O ratio. Films with more N bound to Ti exhibited more negative real parts of the permittivity (more metallic optical behavior) than those with more N bound in oxynitride form. Finally, 'more crystalline' films did seem to exhibit lower optical losses than highly nanocrystalline films. Films with lower oxygen content (less than approx. 10-15%) were in generally fairly metallic. For films with similar oxygen incorporation, more crystalline films (such as epitaxially grown or those with larger crystal grains) were in general more metallic than noncrystalline films; however, even epitaxially grown films were seen to be less metallic than polycrystalline films when the polycrystalline films had less incorporated oxygen. In summary, the chemical composition, chemical bonding, and film crystallinity were all seen to have effects on the resulting optical behavior of TiN and TiO_xN_y sputtered films.

The metallic character can be controlled by careful optimization of the sputtering deposition conditions. In general it was found that to have a metallic film, either the TiN needed to be sputtered at elevated substrate deposition temperature or with an applied substrate bias. This is due to the effects on the oxygen incorporation as well as crystallinity. By sputtering at elevated substrate temperatures, the amount of oxygen present in the films is reduced and larger crystalline grains are observed. The metallic character increases gradually as the temperature increases. In addition, applying a negative substrate bias while sputtering (approx. 80-100V) significantly reduces the atomic % oxygen incorporated during film growth. Using an applied bias also allows sputtering of metallic TiN films at room temperature which allows for deposition on a number of substrates which were previously inaccessible and confirms the potential CMOS compatibility of this material. Films sputtered with an applied bias in general are less ordered with more nanocrystalline grain structure however as compared to films sputtered with larger deposition temperatures, so there may be some tradeoff. Of the (100) MgO, c-

plane sapphire, and (100) silicon substrates which were tested, the most crystalline growth achieved was highly textured heteroepitaxial growth on an MgO substrate via reactive sputtering due to the close lattice match between the TiN and MgO lattices. However, with the addition of an applied substrate bias, highly metallic films were also routinely sputtered onto sapphire and MgO substrates but with smaller grains and higher losses.

The high plasmonic quality of the optimized TiN films were confirmed via fabrication and measurement of the plasmonic response of several benchmark structures, namely: surface plasmon grating couplers, nanoantennas resonant in the mid-infrared, and nanopyramids for photothermal drug delivery. Owing to advantages of the the robustness, chemical stability, biocompatibility and CMOS-compatibility of TiN as well as the controllable nature of its optical nature, there is significant potential for this material to greatly increase the visibility of plasmonic devices in everyday technology.

A

Extended list of TiN samples and deposition conditions

This Appendix includes a listing of the full deposition conditions for the sputtered TiN, TiO_xN_y and ITO samples. The first column of each table describes the same name or number as referred to within the thesis. For TiN, which was sputtered both reactively and non-reactively, the next column indicates which was used (reactively (R) when Ti Target was used, or non-reactively (NR) when TiN target was used.) Next, the magnetron gun sputtering deposition power (PWR) is specified in Watts and as either RF or DC. The base pressure of the chamber is specified prior to flowing in any gases and sputtering in Torr. All TiN samples were sputtered at an overall deposition pressure held constant at 4mT and

all ITO at 3mT. Starting with sample TiN21, all TiN depositions were performed in chamber SP-2 (6 target AJA load-locked sputtering chamber described in detail in Chapter 2). The first samples, TiN1-20, with the exception of TiN3 and TiN7 were instead sputtered in chamber SP-3 (a 3 target AJA sputtering chamber, without load lock). Al ITO samples were sputtered in the SP3 chamber with the exceptions of ITO7 and ITO8 which were sputtered in the SP-2 load-locked chamber. The Ar, N_2, and O_2 columns refer to the sputtering gas flows rates in sccm and the substrate deposition temperature is specified next with RT = room temperature and other values specified in °C. Applied substrate bias values were applied using an RF source and were measured in volts. Time column shows the total length of sputtering in minutes. A second value indicates the length of time a capping layer was sputtered on top of the TiN film. The final column lists the substrates onto which TiN was simultaneously deposited during that run with PR = photoresist on silicon substrate, Si = (100) p-silicon, Ge = germanium, g = glass slide, SiO_2 = SiO_2 on Si substrate, MgO = (100) MgO, Saph = (0001) sapphire, GaN = gallium nitride, Mazur = pyramid array, and finally a G or Giessen = for collaboration with Giessen Group. MgO substrates were bought in 10 x 10mm squares in packages of 5-10. The notation (new) indicates that the first of a new shipment of these substrates were used. Pre-sputtering of the targets was done prior to deposition for all round starting with TiN13.

#	Reac	PWR	Base	Ar	N_2	Temp.	Time	Subs
1	NR	150 RF	2.9e-7	15	-	RT	20	Si,Ge,g,PR
2	NR	120 RF	2.9e-7	15	-	RT	35	Si,Ge,g,PR
3	R	150 RF	4e-7	12	18	RT	45	Si,Ge,g,PR
4	NR	150 RF	8.4e-7	15	-	350	25	Si,Ge,g,PR
5	R	300 DC	2.7e-7	2	8	RT	-	Si,Ge,g,PR
6	R	300 DC	2.7e-7	4	6	RT	-	Si,Ge,g,PR
7	R	250 DC	2.5e-6	15	3	RT	20	Si,Ge,g,PR
8	R	250 DC	2e-7	4	6	RT	25	SiO_2,Ge,g,PR
9	R	250 DC	4e-7	4	6	50	-	SiO2,Ge,g,PR
10	R	250 DC	3.6e-7	4	6	RT	60	SiO_2,Si,g,PR
11	R	250 DC	4.8e-7*RT	4	6	400	25	SiO_2,g
12	R	250 DC	1.8e-6	4	6	500	30	SiO_2,Si,g,Ge
13	R	200 DC	3.2e-7*RT	10	5	600	25	SiO_2,Si,g,Ge
14	R	200 DC	3.1e-7	10	5	RT	31.5	SiO_2,Si,g,PR
15	R	200 DC	8.5e-7	4	6	600	25	SiO_2,Si,g
16	R	250 DC	1.1e-7	10	5	50	25	SiO_2,Si,g
17	R	250 DC	5.7e-7	12	4	RT	17	Si,Ge,g
18	R	200 DC	1.3e-6	4	6	600	75	Si,Ge
19	R	200 DC	1.3e-6	4	6	600	12	Si,Ge,Saph
20	R	200 DC	9.2e-7	4	6	600	76	Si,Ge,Saph
21	R	200 DC	2.5e-6	8	12	600	60	Si,Saph
22	R	200 DC	9.8e-7	8	12	600	60	Si,Saph, MgO
23	R	200 DC	2.4e-7	12	8	600	60	Si,Saph, MgO
24	NR	150 RF	4.9e-7	40	-	600	45	Si,Saph
25	R	200 DC	1.4e-6	12	4	600	60	Si,Saph, MgO
26	R	200 DC	5.2e-7	12	8	600	47	Si,Saph, MgO
27	NR	150 RF	5.6e-7	40	-	600	60	Si,Saph, MgO
28	NR	150 RF	2e-7	40	-	RT	60	Si,Saph, MgO
29	R	200 DC	2.7e-7	12	4	600	60	Si,Saph, MgO(new)
30	R	200 DC	2e.2-7	12	8	600	60	Si,Saph, MgO
31	R	200 DC	2e-7	12	8	RT	53	Si,Saph, MgO
32	NR	150 RF	5e-8	40	-	RT	55	Si,Saph, MgO
33	R	200 DC	3.2e-7	12	8	600	120	Si,Saph, MgO
34	NR	150 RF	3.0e-7	40	-	600	110	Si,Saph, MgO(new)

Table A.1: List of Extended TiN & TiO_xN_y Deposition Conditions (No Bias, TiN1 - 34)

#	Reac	PWR	Base	Ar	N_2	Bias	Time	Subs
35	R	250 DC	3e-8	12	8	100	45/5SiN_x	Si,Saph, MgO,SiN_x
36	NR	150 RF	7e-8	40	-	108	45/5	Si,Saph, MgO
37	NR	150 RF	7.8e-8	40	-	108	45/0	Si,Saph, MgO
38	NR	150 RF	1.0e-7	40	-	150	45/2	Si,Saph, MgO
39	R	250 DC	4.8e-8	12	8	128	75/0	Si,Saph, MgO
40	R	250 DC	6.9e-8	12	4	128	75	Si,Saph, MgO(new)
41	R	250 DC	7e-8	8	12	18%/126	75	Si,Saph, MgO
42	NR	150 RF	7e-8	40	-	18%/90	90	Mazur, SiO_2
43	NR	150 RF	5e-8	40	-	18%/108	100/2	Si(G),Saph, MgO
44	R	250 DC	4.9e-8	12	4	18%/126	35?	Si,Saph, MgO
45	NR	150 RF	3.0e-7	40	-	18%/83**	60	Si(noHF),Saph, MgO
46	NR	150 RF	5.4e-8	40	-	18%/99	60	Si,Saph
47	NR	150 RF	5.5e-8	40	-	14%/79	60	Si,Saph
48	NR	150 RF	4.8e-8	40	-	22%/112	60	Si,Saph
49	NR	150 RF	4.8e-8	40	-	18%/94	100	Si,Saph, Saph(G)
50	NR	150 RF	3.9e-8	40	-	18%/95	50	Mazur
51	NR	150 RF	5.6e-8	40	-	18%/84	25	Saph w/Cr
52	NR	150 RF	5e-8	40	-	8%/83	32	Saph w/Cr
53	NR	150 RF	3.8e-8	40	-	18%/83	168	MgO, Saph, Saph/Cr
54	NR	150 RF	2.6e-8	40	-	18%/83	16	Saph/Cr
55	NR	150 RF	2.2e-7	40	-	18%/83**	90	Saph, MgO
56	NR	150 RF	3.7e-8	40	-	18%/80	59.5	Saph, Si, Au(Mazur)
57	NR	150 RF	2.4e-8	40	-	79-109	191.6	Saph(large), MgO
58	NR	150 RF	2.8e-8	40	-	18%/75-87	142	Saph(large),MgO
59	NR	150 RF	3.3e-8	40	-	93-104	77	Saph(Giessen)
60	NR	150 RF	3.8e-8	40	-	18%/87	75/13SiO_2	Si,Saph,SiO_2
61	NR	150 RF	2.6e-7	40	-	18%/82-101	51	MgO(G), Saph(G)
62	NR	150 RF	2e-7	40	-	15%/90-102	42.5	MgO(G), Saph(G)
63	NR	150 RF	4.5e-8	40	-	15%/97	165	Saph 2" wafer.MgO

Table A.2: TiN List of Extended Deposition Conditions (With Bias, TiN35 - 63). **All samples with bias were deposited at room temperature, with the exception of TiN45 and TiN55 which each had a substrate temperature of 200°C in addition to the applied bias.

#	PWR	Base	Ar	O_2	Temp.	Time	Subs
ITO1	60 RF	3e-6	15	-	200	30(130nm ellips)	g,Ge,Si
ITO2	60 RF	8e-7	12	-	RT	30(85-90nm)	g,Ge,Si
ITO3	60 RF	1e-6	15	-	RT	30(83nm)	g,Ge,Si
ITO4	60 RF	7.7e-7	12	-	RT	30	g,Ge,Si
ITO5	60 RF	e-7	12	-	RT	aborted	g,GaN,Si
ITO6	60 RF	1.7e-6	12	-	RT	10.5	g,GaN,Si
ITO7	60 RF	1.6e-7	12	-	RT	9.25	g,Si
ITO8	60 RF	1.6e-7	12	-	RT	9.25	g,Si,GaN
ITO9	60 RF	8.9e-7	12	-	RT	18.5(50nm)	Si,g,GaN
ITO10	60 RF	7e-7	15	-	RT	9.25	g,Si,GaN

Table A.3: List of Extended ITO Deposition Conditions

B

Detailed Standard Operating Procedure for AJA International ATC-2200-V Sputtering Chamber for Metallic TiN

This appendix describes the standard operating procedures (SOP) in detail for using the AJA International ATC 2200-V load-locked turbo pumped sputtering system at Harvard's CNS, specifically to sputter titanium nitride thin films suitable for plasmonic applications on various substrates. In general, for the substrates to be of plasmonic quality, we have found that they either need to be deposited at high temperature (> 600°C) or with an additional applied bias substrate (-80-100V).

General Sputtering Procedure

1. Load empty substrate holder.
2. Pre-sputter Ti and TiN targets into empty chamber.
3. While waiting for 10-30min pre-sputtering to finish, clean substrates.
4. Unload substrate holder now coated with Ti/TiN.
5. Mount, then load substrates into chamber.
6. If depositing at elevated temperature, ramp up temperature.
7. Ramp up target to full power. If applying bias, turn on 20 sec before ramp is finished.
8. Open shutter and sputter desired films.
9. When done, close shutter and turn off bias (if applicable).
10. If depositing at elevated temperature, let samples cool under vacuum (until under 50-100°C)
11. Unload substrates.

Now, I will describe the procedure in full detail including subtleties which I have found to be important or useful with our chamber and particularly for TiN thin films, but first here are the conditions I would recommend to try first for highly metallic TiN films. You may then adjust conditions as necessary.

B.1 Recommended starting parameters for highly metallic TiN films

B.1.1 High-temperature, highly crystalline on MgO

To sputter the most crystalline, lowest loss metallic films, use (100) MgO as a highly lattice-matched substrate. Sputter at elevated temperatures (>600°C) and allow to cool under vacuum before venting the chamber. Expect rates of approximately 0.5-0.55nm/min (but calibrate this as rates will change).

High Temperature Suggested Starting Deposition Conditions
Reactive sputtering with Ti target
Power: 200W, DC
Deposition Pressure: 4mT
Base Pressure: <5e-8 Torr
Gas flow rates: 12 sccm Ar, 8 sccm N_2 Note: Rough starting point only
Temperature: 600°C and literature predicts higher temperatures may even be better
No substrate bias necessary

B.1.2 Room temperature plus substrate bias, highly metallic on varied substrates

To sputter highly metallic films both at room temperature and onto a wider range of substrates, an additional bias is applied to the substrate during deposition. Suggested starting deposition conditions are shown below. These have been shown to work relatively well on a wide array of substrates (c-sapphire, silicon, epoxy, glass, etc.).

Room Temperature + Bias Suggested Starting Deposition Conditions
Non-reactive sputtering with TiN target
Power: 150W, RF
Deposition Pressure: 4mT
Base Pressure: <5e-8 Torr
Gas flow rates: 40 sccm Ar
Temperature: 20°C
Substrate Bias: -80 to -100V

B.2 Loading the substrate holder into the chamber

1. When arriving at the sputtering chamber, first check that the sample holder has two screws without clips across from each other as depicted in Figure B.1 (a). Mount the required number of sample clips on the empty sample holder in the 4 remaining spots.

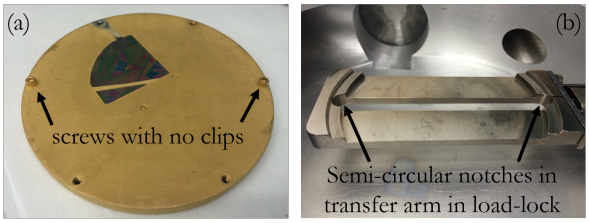


Figure B.1: (a) Empty sample holder with two screws for seeding into arm. (b) Empty transfer arm in load-lock chamber

2. Insert the sample holder up-side down onto the arm in the load lock as shown in Figure B.2. The two screws without clips on them should fit securely into the semi-circular notches on the transfer arm shown in Figure B.1(b). On the back-side of the sample holder one of these screws should line up with one of the three notches. This notch should point towards the main chamber as shown by the white arrow in Figure B.2. This is so that when transferring the holder onto the propeller you are able to align it easily though the chamber port window.



Figure B.2: Back of the sample holder sitting in the load lock. The opening shown screws into a propeller to allow the samples to hang inverted above the magnetron sources.

3. Put the lid on the load lock and flip the switch to pump down the chamber. Wait approx. 3-4 min until the load lock pressure is in the 10^{-7} mbar range. During this time, verify that the BLT is at the transfer height of 34 or adjust using the motor control. See Figure B.3.

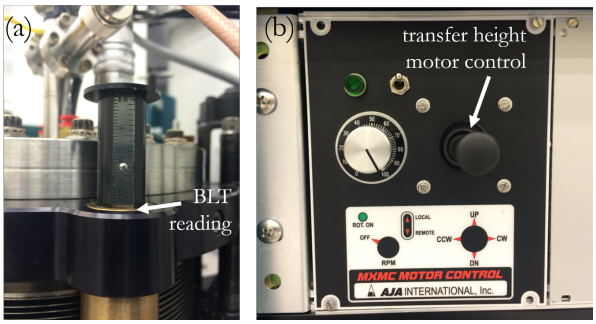


Figure B.3: (a) Transfer height as depicted on BLT. (b) Motor control to adjust transfer height

4. After the load lock has reached 10^{-7} mbar range, open the valve to the main chamber (FigureB.4(a)) by spinning the silver knob/black wheel until it is full open. You will hear a click and the knob will stop turning.

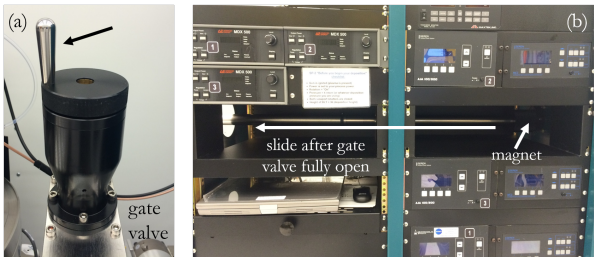


Figure B.4: (a) Gate valve. (b) Transfer arm with white arrow pointing to black magnet

5. Slide the black magnet on the load lock arm towards the chamber to transfer the sample holder from the load lock into the main chamber. See Figure B.4(b). If the magnet feels like it is stuck, try spinning it on the pole and then continue transferring. You may also need to spin it at the end to get the magnet to stay all of the way at the end of the arm and align properly.

6. Use the flashlight to look through the chamber port window of the main chamber. You should see the sample holder sitting on the transfer arm directly underneath the propeller. Move the propeller adjustment knob left/right to spin the propeller so that the 3 arms align with the 3 holes in the substrate holder and then lower the propeller into the holder until there is only 1-2mm separation. The propeller should look like it is continuously lowering down and should smoothly disappear into the grooves. If it seems to stop when you get to the holder, DO NOT KEEP LOWERING as the propeller arms and grooves on the back of the sample holder are misaligned and you could bend the propeller or transfer arm. Sometimes you can fix a slight misalignment by again spinning the black magnet gently on the transfer arm. If this does not work, raise the propeller, try to realign and lower again until the propeller goes in smoothly.

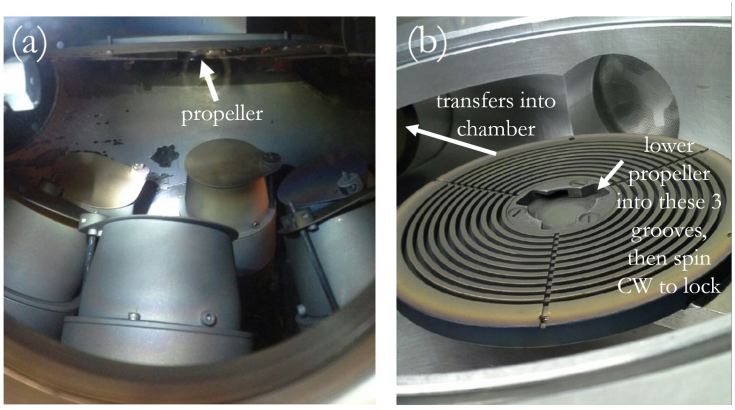


Figure B.5: (a) Confocal 6-target sputtering chamber setup. The substrate hangs upside-down inside the chamber on a rotating stage at the position dictated by the white arrow. (b) After gate valve is opened, the sample holder can e transferred into the chamber. The propeller is then lowered down into the grooves shown and the thumbwheel spun clock-wise to lock.

7. Once the propeller is fully within the sample holder and there is only 1-2mm separation, spin the thumbwheel at the top of the chamber clockwise to lock the sample holder into the propeller. See Figure B.6(a). The wheel should spin easily and about 1/4 turn. If it does not turn smoothly, you have either lowered the propeller too much or not enough. Use the flashlight to look through the

window again and adjust the height.

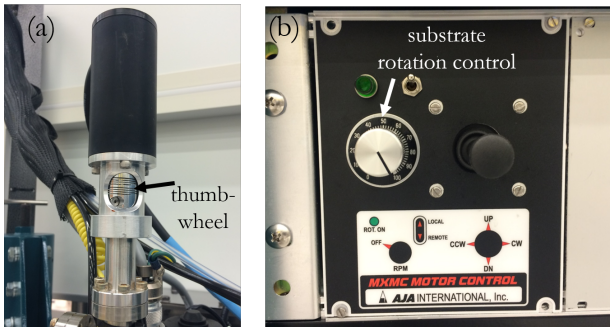


Figure B.6: (a) Thumbwheel to lock and unlock substrate holder from propeller. (b) Substrate rotation control knob.

8. Raise the propeller/sample holder up to the deposition height (BLT = 36)

9. Remove the transfer rod fully from the chamber and close the valve between the main chamber and load lock. Turn on substrate rotation (Figure B.6(b)) and close the shutter over the chamber viewport so that the window does not get covered during deposition.

10. At this point, if you have not already done so, log-in to interlock. (if no one is before you, you can save a few minutes and do the steps above before logging in)

B.3 Target pre-sputtering and deposition

Next, you should pre-sputter the targets to remove any oxides from their surface. By sputtering Ti briefly with the target shutter closed, the hope is that some of the remaining oxygen in the chamber is deposited inside the chimney and therefore not on the substrate holder. However, this cannot be done for long as it will cause buildup and flakes in the chimney. Therefore, after a few minutes of sputtering with the shutter closed, you should open the shutter and sputter into the chamber. This will also coat the inside of the chamber and the substrate holder with a thin layer of Ti/TiN. This pre-sputtering should be sufficient to get oxygen impurity concentration in the final TiN films down

to <10 atomic%. I am not sure if it is possible to reduce the oxygen content much lower than this. This is a shared chamber which is also used for oxides and has a minimum pressure of 1e-8 Torr. In general, for the highest quality TiN deposition, ultra-high vacuum would be desired and a chamber dedicated solely to nitride deposition.

You should always pre-sputter the target/s which you intend to use for your deposition, however sometimes I would also do a quick layer of gold since it is non-reactive and sputters so quickly just to try to stop anything from being ejected from the substrate holder/chamber and being incorporated into my film. Sometimes I would sputter Ti for longer to try and lower the chamber pressure if it was particularly high (e.g. 6e-7 to 1e-6 Torr). If depositing at elevated temperature, I would sputter a relatively thick coating of TiN onto the empty sample holder before mounting the samples. This is to prevent previous films sputtered into the chamber from melting when the substrate is heated and re-depositing onto the back of the substrate (I did see this happen with gold a couple times). If you need to pre-sputter without removing the holder from vacuum afterwards, there is a shutter onto which the quartz crystal monitor is mounted which can be used to shutter the substrates from the pre-sputter deposition. Ask the CNS staff for additional training on using this.

B.3.1 Target pre-sputtering and substrate cleaning

1. Prior to pre-sputtering, note the main chamber pressure. Turn off the ion gauge. Check that the sample is at deposition height (BLT = 36), the chamber view-port shutter is closed and rotation is on.

2. Turn on the Ar and set the flow rate to 40sccm.

3. Click "pressure" and set to 25mTorr if sputtering from an RF source (TiN will always be in RF, Ti could be in DC or RF) or set to 4mTorr if a DC source.

4. Once the pressure is stabilized, set the ramp time first and then the desired power %. For RF targets

(Check the gun name on the laptop e.g. RF2, RF3,...) first set the ramp time to 0 seconds and ignite at 10-20% power. Click the "on" button and the plasma indicator should turn purple. At this point, reduce the chamber pressure to 4mTorr. Then, ramp over 1 Watt/sec to final deposition power (usually 50%.). For example, for TiN, ignite at 10% (or 30W). Desired sputtering power is 50% (150W), so after ignition, set ramp time to 120 seconds first and then set deposition power to 50%. REMEMBER TO ALWAYS SET THE TIME FIRST BEFORE THE POWER. As soon as you click out of the power box the ramping will start and going directly from 30W to 150W on a ceramic target could crack the TiN and you will no longer be able to sputter. Slow ramp-up and ramp-down is very important for non-metal, RF targets. For DC targets (e.g. usually Au, Ag, Ti, etc), you can ramp right up to 50% power over 30 seconds at 4mTorr.

5. After the power has ramped up to 50%, pre-sputter with the chimney closed for about 2-5minutes (too long can cause flake buildup). After this, open the shutter by clicking the large green circle by the gun in use and sputter for an additional 10-30 minutes.

6. While the targets are pre-sputtering is a good time to clean your substrates if you have not already done so. For TiN, the best substrates we found were (100) MgO and c-plane sapphire. For MgO, the substrates came individually wrapped and are sensitive to moisture so I would not open them until in the cleanroom and then just do a few minutes sonication in isopropyl alcohol (IPA) and N_2 dry. For c-plane sapphire substrates which I had to cut into smaller pieces, I would sonicate them for approximately 10 minutes in acetone followed by 10 minutes in isopropyl alcohol (squirting IPA on them during transfer as to not allow the acetone to dry). Then N_2 dry. I also tried baking some substrates on the hot plate near 120 °C for a few minutes after N_2 dry to remove further moisture but did not notice a significant result in film quality. I have read however that baking substrates for an hour at high temperature while under vacuum can potentially allow them to outgas and produce higher quality films. This may be worth looking into if sputtering at high temperature.

7. When done pre-sputtering, close the shutter by again clicking the large circular button and then ramp down for RF targets by 1 W/s (e.g. TiN, 120sec to 10% power) and for DC targets over 30 sec to 0% power. When the ramp down has finished, click off for the plasma.

8. Click "open" for the pressure and turn off the Ar gas flow.

9. After a few seconds, turn back on the ion gauge and wait for the pressure in the main chamber to drop below the load lock pressure.

10. Turn off rotation. Open valve between load lock and main chamber and slide in transfer rod all of the way.

11. Rotate the substrate holder so that the two empty screws line up with the semi-circular grooves in the load lock arm. Begin lowering down the substrate holder towards the load lock arm. As the substrate holder approaches the arm, verify that the screws line up with the grooves and slowly lower until the screws are fully within the grooves and the gap between the propeller/substrate holder has almost closed.

12. Turn the thumbwheel counter clockwise (approx. 1/4 turn) to release the substrate holder from the propeller. It should spin smoothly. If not try raising or lowering the propeller slightly.

13. Raise the propeller up to the transfer height (BLT = 34).

14. Pull out the transfer arm from the chamber, close the valve to the load lock completely and then flip the switch to vent the load lock vacuum pump.

B.3.2 Deposition

1. Mount the clean substrates on the sample holder using the provided clips. Make sure to leave the 2 additional screws across from each other without any clips so that the holder will be level on the

transfer arm. The substrates will hang up-side down within the chamber and the holder will rotate so check them to make sure they are tight.

2. Follow steps in the sections above again to load the samples, set proper chamber conditions, and then ramp up the target to full power (with the shutter closed).

3. Once at 50% power, you do not need to pre-sputter again since you have already done it. Using the pre-determined rate, calculate the length of time needed to reach the desired thickness and then open the shutter to deposit. Note the forward and reflected power as well as the DC voltage, deposition pressure, and gas flow. Note the values in the interlock system.

4. When the deposition has finished, close the shutter and then ramp down slowly as described earlier, as to not crack the target.

5. Follow steps 8 to 14 (section B.3.1) to shut off gas, pump down, unload chamber and vent load lock to remove samples.

C

Standard Operating Procedure for Measuring TiN Spectroscopic Ellipsometry Data

This appendix describes the basic operating procedures for using the WVASE Spectroscopic Ellipsometer at Harvard's CNS and the associated data analysis software from J.A. Woollam Co. Inc. Included are suggested starting SE data measurement parameters for titanium nitride thin films.

C.1 General Spectroscopic Ellipsometry Procedure

General Spectroscopic Ellipsometry Procedure
1. Turn on lamp. Wait approx. 1 hour for lamp to warm-up and stabilize before using the system.
2. Load the calibration sample and align.
3. Calibrate the hardware.
4. Mount TiN sample and repeat alignment procedure.
5. Set-up measurement parameters as listed below.
6. Take spectroscopic ellipsometry (SE) data.
7. Create a model for the sample as described in Chapter 3 to extract the thickness and optical constants.

C.2 Set-up Measurement Parameters

The following is a list of suggested starting SE measurement parameters for metallic TiN using a J.A. Woollam WVASE32 vertical angle spectroscopic ellipsometer.

1. Range: 300-1700nm in 5-10nm steps
2. Angles: 50°, 60°, 70° (based on advice from Woollam)
3. Revs per Measurement: 15-20 is generally enough for highly reflective samples such as TiN and will make the scan go much more quickly. At shorter wavelengths, you may need a larger number however, so also turn on dynamic averaging and set it to 100. The system will only use these extra revs if a low signal is auto-detected. The RPM will need to be set much higher (could be 100-200) for non-reflective samples.
4. Save the file during the scan: recommended every 3-5 minutes. This setting doesn't seem to slow down scan much if at all and once the data is recorded, you can then open another instance of the

software and begin working on the modeling while the scan is still completing.

5. The skip wavelength range from 1300-1400nm box should be checked if using the standard optical fiber. Checking this box will cause no data to be taken within this range. If you do not check this box and see spikes in your data, you are likely using the standard optical fiber which has transmission dips within this range.

6. Isotropic measurement: This setting is generally okay for metallic TiN. (You should verify that the Autoretarder and depolarization are off, or the measurements will take much longer. These settings may be needed however for higher oxynitride content films or other anisotropic films.)

References

[1] Na Liu, Martin Mesch, Thomas Weiss, Mario Hentschel, and Harald Giessen. Infrared perfect absorber and its application as plasmonic sensor. *Nano letters*, 10(7):2342–2348, 2010.

[2] Marcus Diem, Thomas Koschny, and Costas M Soukoulis. Wide-angle perfect absorber/thermal emitter in the terahertz regime. *Physical Review B*, 79(3):033101, 2009.

[3] Gunnar Dolling, Martin Wegener, Costas M Soukoulis, and Stefan Linden. Negative-index metamaterial at 780 nm wavelength. *Optics letters*, 32(1):53–55, 2007.

[4] Costas M Soukoulis, Stefan Linden, and Martin Wegener. Negative refractive index at optical wavelengths. *Science*, 315(5808):47–49, 2007.

[5] Jon A Schuller, Edward S Barnard, Wenshan Cai, Young Chul Jun, Justin S White, and Mark L Brongersma. Plasmonics for extreme light concentration and manipulation. *Nature materials*, 9(3):193–204, 2010.

[6] Francesco Aieta, Patrice Genevet, Mikhail A Kats, Nanfang Yu, Romain Blanchard, Zeno Gaburro, and Federico Capasso. Aberration-free ultrathin flat lenses and axicons at telecom wavelengths based on plasmonic metasurfaces. *Nano letters*, 12(9):4932–4936, 2012.

[7] Yanxia Cui, Yingran He, Yi Jin, Fei Ding, Liu Yang, Yuqian Ye, Shoumin Zhong, Yinyue Lin, and Sailing He. Plasmonic and metamaterial structures as electromagnetic absorbers. *Laser & Photonics Reviews*, 8(4):495–520, 2014.

[8] Urcan Guler, Alexandra Boltasseva, and Vladimir M Shalaev. Refractory plasmonics. *Science*, 2014.

[9] Alexandra Boltasseva and Harry A Atwater. Low-loss plasmonic metamaterials. *Science*, 2011.

[10] Min Hu, Jingyi Chen, Zhi-Yuan Li, Leslie Au, Gregory V Hartland, Xingde Li, Manuel Marquez, and Younan Xia. Gold nanostructures: engineering their plasmonic properties for biomedical applications. *Chemical Society Reviews*, 35(11):1084–1094, 2006.

[11] Jin Zhong Zhang. Biomedical applications of shape-controlled plasmonic nanostructures: a case study of hollow gold nanospheres for photothermal ablation therapy of cancer. *The Journal of Physical Chemistry Letters*, 1(4):686–695, 2010.

[12] Urcan Guler, Sergey Suslov, Alexander V Kildishev, Alexandra Boltasseva, and Vladimir M Shalaev. Colloidal plasmonic titanium nitride nanoparticles: Properties and applications. *Nanophotonics*, 4(1):269–276, 2015.

[13] Rashid Zia, Jon A Schuller, Anu Chandran, and Mark L Brongersma. Plasmonics: the next chip-scale technology. *Materials today*, 9(7):20–27, 2006.

[14] Zubin Jacob and Vladimir Shalaev. Plasmonics goes quantum. 2011.

[15] Nathaniel Kinsey, Marcello Ferrera, Gururaj V Naik, VE Babicheva, Vladimir M Shalaev, and Alexandra Boltasseva. Experimental demonstration of titanium nitride plasmonic interconnects. *Optics express*, 22(10):12238–12247, 2014.

[16] Katherine A Willets and Richard P Van Duyne. Localized surface plasmon resonance spectroscopy and sensing. *Annu. Rev. Phys. Chem.*, 58:267–297, 2007.

[17] Jeffrey N Anker, W Paige Hall, Olga Lyandres, Nilam C Shah, Jing Zhao, and Richard P Van Duyne. Biosensing with plasmonic nanosensors. *Nature materials*, 7(6):442–453, 2008.

[18] Stefan Alexander Maier. *Plasmonics: fundamentals and applications*. Springer Science & Business Media, 2007.

[19] W Andrew Murray and William L Barnes. Plasmonic materials. *Advanced materials*, 19(22):3771–3782, 2007.

[20] C. Kittel. *Introduction to Solid State Physics*. Wiley, 2004.

[21] N.W. Ashcroft and N.D. Mermin. *Solid State Physics*. Cengage Learning, 2011.

[22] Richard P Feynman, Robert B Leighton, and Matthew Sands. *The Feynman Lectures on Physics*. Basic books, 2013.

[23] Paul R West, Satoshi Ishii, Gururaj V Naik, Naresh K Emani, Vladimir M Shalaev, and Alexandra Boltasseva. Searching for better plasmonic materials. *Laser & Photonics Reviews*, 4(6):795–808, 2010.

[24] Edward D Palik. *Handbook of optical constants of solids*, volume 3. Academic press, 1998.

[25] Dispersion relationship. Image released to public domain by author ScottTParker. Accessed from`https://commons.wikimedia.org/wiki/File:Dispersion_Relationship.png` on 25 April 2016.

[26] P. Patsalas and S. Logothetidis. Optical, electronic, and transport properties of nanocrystalline titanium nitride thin films. *Journal of Applied Physics*, 90(9), 2001.

[27] Pierre Berini. Figures of merit for surface plasmon waveguides. *Optics Express*, 14(26):13030–13042, 2006.

[28] Peter Offermans, Martijn C Schaafsma, Said RK Rodriguez, Yichen Zhang, Mercedes Crego-Calama, Sywert H Brongersma, and Jaime Gómez Rivas. Universal scaling of the figure of merit of plasmonic sensors. *Acs Nano*, 5(6):5151–5157, 2011.

[29] U Guler, Gururaj V Naik, Alexandra Boltasseva, Vladimir M Shalaev, and Alexander V Kildishev. Performance analysis of nitride alternative plasmonic materials for localized surface plasmon applications. *Applied Physics B*, 107(2):285–291, 2012.

[30] Andrea Alù, Mário G Silveirinha, Alessandro Salandrino, and Nader Engheta. Epsilon-near-zero metamaterials and electromagnetic sources: Tailoring the radiation phase pattern. *Physical Review B*, 75(15):155410, 2007.

[31] Ruben Maas, James Parsons, Nader Engheta, and Albert Polman. Experimental realization of an epsilon-near-zero metamaterial at visible wavelengths. *Nature Photonics*, 7(11):907–912, 2013.

[32] Sean Molesky, Christopher J Dewalt, and Zubin Jacob. High temperature epsilon-near-zero and epsilon-near-pole metamaterial emitters for thermophotovoltaics. *Optics express*, 21(101):A96–A110, 2013.

[33] Y Ekinci, HH Solak, and JF Löffler. Plasmon resonances of aluminum nanoparticles and nanorods. *Journal of Applied Physics*, 104(8):083107, 2008.

[34] Mark W Knight, Lifei Liu, Yumin Wang, Lisa Brown, Shaunak Mukherjee, Nicholas S King, Henry O Everitt, Peter Nordlander, and Naomi J Halas. Aluminum plasmonic nanoantennas. *Nano letters*, 12(11):6000–6004, 2012.

[35] Mark W Knight, Nicholas S King, Lifei Liu, Henry O Everitt, Peter Nordlander, and Naomi J Halas. Aluminum for plasmonics. *ACS nano*, 8(1):834–840, 2013.

[36] N Kinsey, M Ferrera, VM Shalaev, and A Boltasseva. Examining nanophotonics for integrated hybrid systems: a review of plasmonic interconnects and modulators using traditional and alternative materials [invited]. *JOSA B*, 32(1):121–142, 2015.

[37] Gururaj V Naik, Vladimir M Shalaev, and Alexandra Boltasseva. Alternative plasmonic materials: beyond gold and silver. *Advanced Materials*, 25(24):3264–3294, 2013.

[38] Jennifer A Dionne and Harry A Atwater. Plasmonics: metal-worthy methods and materials in nanophotonics. *MRS Bulletin*, 37(08):717–724, 2012.

[39] Joshua T Guske, Jeff Brown, Alex Welsh, and Stefan Franzen. Infrared surface plasmon resonance of azo-ag-azo sandwich thin films. *Optics express*, 20(21):23215–23226, 2012.

[40] Martin G Blaber, Matthew D Arnold, and Michael J Ford. A review of the optical properties of alloys and intermetallics for plasmonics. *Journal of Physics: Condensed Matter*, 22(14):143201, 2010.

[41] Frank HL Koppens, Darrick E Chang, and F Javier Garcia de Abajo. Graphene plasmonics: a platform for strong light–matter interactions. *Nano letters*, 11(8):3370–3377, 2011.

[42] D Steinmüller-Nethl, R Kovacs, E Gornik, and P Rödhammer. Excitation of surface plasmons on titanium nitride films: determination of the dielectric function. *Thin Solid Films*, 237(1):277–281, 1994.

[43] NC Chen, WC Lien, CR Liu, YL Huang, YR Lin, C Chou, SY Chang, and CW Ho. Excitation of surface plasma wave at tin/air interface in the kretschmann geometry. *Journal of Applied Physics*, 109(4):043104–043104, 2011.

[44] Gururaj V Naik, Jongbum Kim, and Alexandra Boltasseva. Oxides and nitrides as alternative plasmonic materials in the optical range [invited]. *Optical Materials Express*, 1(6):1090–1099, 2011.

[45] Gururaj V Naik, Jeremy L Schroeder, Xingjie Ni, Alexander V Kildishev, Timothy D Sands, and Alexandra Boltasseva. Titanium nitride as a plasmonic material for visible and near-infrared wavelengths. *Optical Materials Express*, 2(4):478–489, 2012.

[46] Urcan Guler, Vladimir M Shalaev, and Alexandra Boltasseva. Nanoparticle plasmonics: going practical with transition metal nitrides. *Materials Today*, 18(4):227–237, 2015.

[47] Wei Li, Urcan Guler, Nathaniel Kinsey, Gururaj V Naik, Alexandra Boltasseva, Jianguo Guan, Vladimir M Shalaev, and Alexander V Kildishev. Refractory plasmonics with titanium nitride: broadband metamaterial absorber. *Advanced Materials*, 26(47):7959–7965, 2014.

[48] Panos Patsalas, Nikolaos Kalfagiannis, and Spyros Kassavetis. Optical properties and plasmonic performance of titanium nitride. *Materials*, 8(6):3128–3154, 2015.

[49] Gururaj V Naik, Bivas Saha, Jing Liu, Sammy M Saber, Eric A Stach, Joseph MK Irudayaraj, Timothy D Sands, Vladimir M Shalaev, and Alexandra Boltasseva. Epitaxial superlattices with titanium nitride as a plasmonic component for optical hyperbolic metamaterials. *Proceedings of the National Academy of Sciences*, 111(21):7546–7551, 2014.

[50] Urcan Guler, Alexander V Kildishev, Alexandra Boltasseva, and Vladimir M Shalaev. Plasmonics on the slope of enlightenment: the role of transition metal nitrides. *Faraday discussions*, 178:71–86, 2015.

[51] Paul Ehrlich. Über die binären systeme des titans mit den elementen stickstoff, kohlenstoff, bor und beryllium. *Zeitschrift für anorganische Chemie*, 259(1-4):1–41, 1949.

[52] Koichi Momma and Fujio Izumi. *VESTA3* for three-dimensional visualization of crystal, volumetric and morphology data. *Journal of Applied Crystallography*, 44(6):1272–1276, Dec 2011.

[53] William M Haynes. *CRC handbook of chemistry and physics*. CRC press, 92 edition, 2011.

[54] Peter W. Kelly. Advantages of titanium nitride coated gear tools. *Gear Technology*, pages 12–48, 1984.

[55] PW Kelly. Gear cutting with tin-coated tools. *American machinist*, 126(11):125–128, 1982.

[56] PW Hatto and DG Teer. Ion plating with an arc source. *Vacuum*, 36(1):67–69, 1986.

[57] RL Hatschek. Coatings-revolution in hss tools. *American Machinist*, 127(3):129–144, 1983.

[58] LE Toth. Transition metal nitrides and carbides. *Refractory Materials Series, Academic Press, New York and London*, (7):91, 1971.

[59] P. Schwarzkopf and R. Kieffer. *Refractory hard metals: borides, carbides, nitrides, and silicides; the basic constituents of cemented hard metals and their use as high-temperature materials*. Macmillan, 1953.

[60] M. I. Aivazov and I. A. Domashnev. Influence of porosity on the conductivity of hot-pressed titanium-nitride specimens. *Soviet Powder Metallurgy and Metal Ceramics*, 7(9):708–710.

[61] BO Johansson, J-E Sundgren, JE Greene, A Rockett, and SA Barnett. Growth and properties of single crystal tin films deposited by reactive magnetron sputtering. *Journal of Vacuum Science & Technology A*, 3(2):303–307, 1985.

[62] C Agte and K Moers. Methoden zur reindarstellung hochschmelzender carbide, nitride und boride und beschreibung einiger ihrer eigenschaften. *Zeitschrift für anorganische und allgemeine Chemie*, 198(1):233–275, 1931.

[63] W Sinke, GPA Frijlink, and FW Saris. Oxygen in titanium nitride diffusion barriers. *Applied Physics Letters*, 47(5):471–473, 1985.

[64] Nikhil K Ponon, Daniel JR Appleby, Erhan Arac, PJ King, Srinivas Ganti, Kelvin SK Kwa, and Anthony O'Neill. Effect of deposition conditions and post deposition anneal on reactively sputtered titanium nitride thin films. *Thin Solid Films*, 578:31–37, 2015.

[65] Hermann Von Seefeld, Nathan W Cheung, Martti Maenpaa, and Marc-A Nicolet. Investigation of titanium—nitride layers for solar-cell contacts. *Electron Devices, IEEE Transactions on*, 27(4):873–876, 1980.

[66] NW Cheung, H Von Seefeld, M-A Nicolet, F Ho, and P Iles. Thermal stability of titanium nitride for shallow junction solar cell contacts. *Journal of Applied Physics*, 52(6):4297–4299, 1981.

[67] A Armigliato, G Celotti, A Garulli, S Guerri, P Ostoja, R Rosa, and G Martinelli. Characterization of titanium nitride films deposited onto silicon. *Thin Solid Films*, 92(4):341–346, 1982.

[68] Li-Jian Meng and MP Dos Santos. Characterization of titanium nitride films prepared by dc reactive magnetron sputtering at different nitrogen pressures. *Surface and Coatings Technology*, 90(1):64–70, 1997.

[69] Emanuel I Cooper, Rekha Rajaram, Makonnen Payne, and Steven Lippy. Selective high-throughput tin etching methods. In *Solid State Phenomena*, volume 195, pages 143–145. Trans Tech Publ, 2012.

[70] Andrew J Dowling, Muralidhar K Ghantasala, ED Doyle, and Erol C Harvey. Selective wet-etching of filtered-arc-deposited tin films on cr sacrificial layers. In *Microelectronics, MEMS, and Nanotechnology*, pages 213–220. International Society for Optics and Photonics, 2004.

[71] Shahin Bagheri, Christine M. Zgrabik, Timo Gissibl, Andreas Tittl, Florian Sterl, Ramon Walter, Stefano De Zuani, Audrey Berrier, Thomas Stauden, Gunther Richter, Evelyn L. Hu, and Harald Giessen. Large-area fabrication of tin nanoantenna arrays for refractory plasmonics in the mid-infrared by femtosecond direct laser writing and interference lithography. *Opt. Mater. Express*, 5(11):2625–2633, Nov 2015.

[72] J Tonotani, T Iwamoto, F Sato, K Hattori, S Ohmi, H Iwai, et al. Dry etching characteristics of tin film using ar/chf3, ar/cl-2, and ar/bcl3 gas chemistries in an inductively coupled plasma. *Journal of Vacuum Science & Technology B*, 21(5):2163–2168, 2003.

[73] Martin Sandberg, Michael R Vissers, Jeffrey S Kline, Martin Weides, Jiansong Gao, David S Wisbey, and David P Pappas. Etch induced microwave losses in titanium nitride superconducting resonators. *Applied Physics Letters*, 100(26):262605, 2012.

[74] Chang-Il Kim et al. Dry etching characteristics of tin thin films in bcl 3-based plasma. *Transactions on Electrical and Electronic Materials*, 12(3):106–109, 2011.

[75] Young-Hee Joo, Jong-Chang Woo, and Chang-Il Kim. Dry etching characteristics of tin thin films in cf 4/bcl 3/n 2 plasma. *Thin Solid Films*, 520(6):2339–2342, 2012.

[76] Hyungjoo Shin, Weiye Zhu, Lei Liu, Shyam Sridhar, Vincent M Donnelly, Demetre J Economou, Chet Lenox, and Tom Lii. Selective etching of tin over tan and vice versa in chlorine-containing plasmas. *Journal of Vacuum Science & Technology A*, 31(3):031305, 2013.

[77] Bruno Lee Sang, Marie-Josée Gour, Maxime Darnon, Serge Ecoffey, Abdelatif Jaouad, Benattou Sadani, Dominique Drouin, and Abdelkader Souifi. Selective dry etching of tin nanostructures over sio2 nanotrenches using a cl2/ar/n2 inductively coupled plasma. *Journal of Vacuum Science & Technology B*, 34(2):02M102, 2016.

[78] V Ern and AC Switendick. Electronic band structure of tic, tin, and tio. *Physical Review*, 137(6A):A1927, 1965.

[79] DS Stone, KB Yoder, and WD Sproul. Hardness and elastic modulus of tin based on continuous indentation technique and new correlation. *Journal of Vacuum Science & Technology A*, 9(4):2543–2547, 1991.

[80] Hugh O Pierson. *Handbook of Refractory Carbides & Nitrides: Properties, Characteristics, Processing and Apps.* William Andrew, 1996.

[81] K.-H. Habig. Chemical vapor deposition and physical vapor deposition coatings: Properties, tribological behavior, and applications. *Journal of Vacuum Science & Technology A*, 4(6), 1986.

[82] P. Schwarzkopf and R. Kieffer. *Refractory hard metals: borides, carbides, nitrides, and silicides; the basic constituents of cemented hard metals and their use as high-temperature materials*. Macmillan, 1953.

[83] S.R. Kurtz and R.G. Gordon. Chemical vapor deposition of titanium nitride at low temperatures. *Thin Solid Films*, 140(2):277 – 290, 1986.

[84] E. Pascual, M.C. Polo, J. Esteve, and E. Bertran. Surface reflectivity of tin thin films measured by spectral ellipsometry. *Surface Science*, 251:200 – 203, 1991.

[85] Seyedmohammed Shayestehaminzadeh. *Growth of Functional Thin Films by HiPIMS: Fundamentals, Challenges, and Applications*. PhD thesis, University of Iceland, 2015.

[86] Sputtering. Image by Jesse Viviano was released to the public domain. Accessed from `https://en.wikipedia.org/wiki/Sputter_deposition` on 1 Feb. 2016.

[87] SK Ghandi. Vlsi fabrication principles: Silicon and gallium arsenide. interscience series, 1983.

[88] Milton Ohring. *The Materials Science of Thin Films*. Academic Press, 1992.

[89] Circular planar magnetron target. Image by Axelfusillo was released to the public domain. Original image accessed from `https://commons.wikimedia.org/wiki/File:12_Circular_Planar_Magnetron_Target.png` and modified on 1 Feb. 2016.

[90] Kurt J. Lesker Company. Seminar on physical vapor deposition (pvd) technologies and techniques. 2015.

[91] Niels Marquardt. Introduction to the principles of vacuum physics, 1999.

[92] John A. Thornton. The microstructure of sputter-deposited coatings. *Journal of Vacuum Science & Technology A*, 4(6), 1986.

[93] Andre Anders. A structure zone diagram including plasma based deposition and ion etching. *LBNL Paper LBNL-2768E.*, 2010.

[94] *Guide to Using WVASE 32: Spectroscopic Ellipsometry Data Acquisition and Analysis Software*. J. A. Woollam Company, Incorporated, 2008.

[95] H.G. Tompkins and W.A. McGahan. *Spectroscopic Ellipsometry and Reflectometry: A User's Guide*. Wiley, 1999.

[96] Electromagnetic wave. Image by P.wormer is licensed under CC BY-SA 3.0 license. Accessed from https://commons.wikimedia.org/wiki/File:Electromagnetic_wave.png on 10 March 2016.

[97] Polarisation state. Image by Cepheiden is licensed under CC BY-SA 3.0 license. Accessed from https://en.wikipedia.org/wiki/Polarization on 10 March 2016.

[98] Polarizer. Image by Mikhail Ryazanov was released to the public domain. Accessed from https://en.wikipedia.org/wiki/Polarizer on 10 March 2016.

[99] A. Yariv and P. Yeh. *Photonics: Optical Electronics in Modern Communications*. The Oxford series in electrical and computer engineering. Oxford University Press, 2007.

[100] N White, AL Campbell, JT Grant, R Pachter, K Eyink, R Jakubiak, G Martinez, and CV Ramana. Surface/interface analysis and optical properties of rf sputter-deposited nanocrystalline titanium nitride thin films. *Applied Surface Science*, 292:74–85, 2014.

[101] J Rivory, JM Behaghel, S Berthier, and J Lafait. Optical properties of substoichiometric tin x. *Thin Solid Films*, 78(2):161–165, 1981.

[102] S Tripura Sundari, R Ramaseshan, Feby Jose, S Dash, and AK Tyagi. Investigation of temperature dependent dielectric constant of a sputtered tin thin film by spectroscopic ellipsometry. *Journal of Applied Physics*, 115(3):033516, 2014.

[103] William H Press, Saul A Teukolsky, William T Vetterling, and Brian P Flannery. Numerical recipies in c, 1988.

[104] Stefan Franzen. Surface plasmon polaritons and screened plasma absorption in indium tin oxide compared to silver and gold. *The Journal of Physical Chemistry C*, 112(15):6027–6032, 2008.

[105] AK Kulkarni, Kirk H Schulz, TS Lim, and M Khan. Dependence of the sheet resistance of indium-tin-oxide thin films on grain size and grain orientation determined from x-ray diffraction techniques. *Thin solid films*, 345(2):273–277, 1999.

[106] S Laux, N Kaiser, A Zöller, R Götzelmann, H Lauth, and H Bernitzki. Room-temperature deposition of indium tin oxide thin films with plasma ion-assisted evaporation. *Thin Solid Films*, 335(1):1–5, 1998.

[107] Kim Sok Won, Kang Manil, Kim Inkoo, Chu Minwoo, and Ryu Ji-Wook. Optical properties of sputtered indium tin oxide thin films. *Journal of Korean Physical Society*, 59:3280, 2011.

[108] Shi Qiang Li, Peijun Guo, Lingxiao Zhang, Wei Zhou, Teri W Odom, Tamar Seideman, John B Ketterson, and Robert PH Chang. Infrared plasmonics with indium–tin-oxide nanorod arrays. *ACS nano*, 5(11):9161–9170, 2011.

[109] Yu Wang, Antonio Capretti, and Luca Dal Negro. Wide tuning of the optical and structural properties of alternative plasmonic materials. *Optical Materials Express*, 5(11):2415–2430, 2015.

[110] Feiliang Chen, Shao-Wei Wang, Liming Yu, Xiaoshuang Chen, and Wei Lu. Control of optical properties of tin x o y films and application for high performance solar selective absorbing coatings. *Optical Materials Express*, 4(9):1833–1847, 2014.

[111] A Rizzo, MA Signore, L Tapfer, E Piscopiello, A Cappello, E Bemporad, and M Sebastiani. Graded selective coatings based on zirconium and titanium oxynitride. *Journal of Physics D: Applied Physics*, 42(11):115406, 2009.

[112] Chiew Keat Lim, Hui Huang, Chee Lap Chow, Pei Yun Tan, Xiaofeng Chen, Man Siu Tse, and Ooi Kiang Tan. Enhanced charge transport properties of dye-sensitized solar cells using tin x o y nanostructure composite photoanode. *The Journal of Physical Chemistry C*, 116(37):19659–19664, 2012.

[113] Michael EA Warwick, Geoffrey Hyett, Ian Ridley, Fathima R Laffir, Celia Olivero, Patrick Chapon, and Russell Binions. Synthesis and energy modelling studies of titanium oxy-nitride films as energy efficient glazing. *Solar Energy Materials and Solar Cells*, 118:149–156, 2013.

[114] Radhouane Bel Hadj Tahar, Takayuki Ban, Yutaka Ohya, and Yasutaka Takahashi. Tin doped indium oxide thin films: Electrical properties. *Journal of Applied Physics*, 83(5):2631–2645, 1998.

[115] R.A Synowicki. Spectroscopic ellipsometry characterization of indium tin oxide film microstructure and optical constants. *Thin Solid Films*, 313–314:394 – 397, 1998.

[116] Zhaolin Lu, Wangshi Zhao, and Kaifeng Shi. Ultracompact electroabsorption modulators based on tunable epsilon-near-zero-slot waveguides. *Photonics Journal, IEEE*, 4(3):735–740, 2012.

[117] Daniel Traviss, Roman Bruck, Ben Mills, Martina Abb, and Otto L Muskens. Ultrafast plasmonics using transparent conductive oxide hybrids in the epsilon-near-zero regime. *Applied Physics Letters*, 102(12):121112, 2013.

[118] Junghyun Park, Ju-Hyung Kang, Xiaoge Liu, and Mark L Brongersma. Electrically tunable epsilon-near-zero (enz) metafilm absorbers. *Scientific reports*, 5, 2015.

[119] A Mumtaz and WH Class. Color of titanium nitride prepared by reactive dc magnetron sputtering. *Journal of Vacuum Science & Technology*, 20(3):345–348, 1982.

[120] AJ Perry, M Georgson, and CG Ribbing. The reflectance and color of titanium nitride. *Journal of Vacuum Science & Technology A*, 4(6):2674–2677, 1986.

[121] H.Z. Wu, T.C. Chou, A. Mishra, D.R. Anderson, J.K. Lampert, and S.C. Gujrathi. Characterization of titanium nitride thin films. *Thin Solid Films*, 191(1):55 – 67, 1990.

[122] S Niyomsoan, W Grant, DL Olson, and B Mishra. Variation of color in titanium and zirconium nitride decorative thin films. *Thin Solid Films*, 415(1):187–194, 2002.

[123] Jeremy Freixas, Etienne Eustache, Pascal Roussel, Charlene Brillard, Dominique Deresmes, Nicolas Nuns, Nathalie Rolland, Thierry Brousse, and Christophe Lethien. Sputtered titanium nitride: a bifunctional material for li-ion microbatteries. *Journal of The Electrochemical Society*, 162(4):A493–A500, 2015.

[124] Jagdish Narayan, P Tiwari, X Chen, J Singh, R Chowdhury, and T Zheleva. Epitaxial growth of tin films on (100) silicon substrates by laser physical vapor deposition. *Applied physics letters*, 61(11):1290–1292, 1992.

[125] Taeyoon Lee, H Seo, H Hwang, B Howe, S Kodambaka, JE Greene, and I Petrov. Fully strained low-temperature epitaxy of tin/mgo (001) layers using high-flux, low-energy ion irradiation during reactive magnetron sputter deposition. *Thin Solid Films*, 518(18):5169–5172, 2010.

[126] Hien Do, Yue-Han Wu, Van-Truong Dai, Chun-Yen Peng, Tzu-Chun Yen, and Li Chang. Structure and property of epitaxial titanium oxynitride grown on mgo (001) substrate by pulsed laser deposition. *Surface and Coatings Technology*, 214:91–96, 2013.

[127] Christine M. Zgrabik and Evelyn L. Hu. Optimization of sputtered titanium nitride as a tunable metal for plasmonic applications. *Opt. Mater. Express*, 5(12):2786–2797, Dec 2015.

[128] Nadia Saoula, Karim Henda, and Rafika Kesri. Influence of nitrogen content on the structural and mechanical properties of tin thin films. 2009.

[129] Shinobu Ohya, Ben Chiaro, Anthony Megrant, Charles Neill, Rami Barends, Yu Chen, Julian Kelly, David Low, Josh Mutus, Peter O'Malley, et al. Sputtered tin films for superconducting coplanar waveguide resonators. *arXiv preprint arXiv:1306.2966*, 2013.

[130] Adam Tarniowy, Ryszard Mania, and Mieczyslaw Rekas. The effect of thermal treatment on the structure, optical and electrical properties of amorphous titanium nitride thin films. *Thin Solid Films*, 311(1):93–100, 1997.

[131] Lishi Wen and Rongfang Huang. Low temperature deposition of titanium nitride. *J. Mater. Sci. Technol.*, 14:289–293, 1998.

[132] M. H. Kibel. *Surface Analysis Methods in Materials Science*, chapter X-Ray Photoelectron Spectroscopy, pages 175–201. Springer Berlin Heidelberg, Berlin, Heidelberg, 2003.

[133] Thermo Fisher Scientific. *Avantage Knowledge Base*, 2014.

[134] PH Mayrhofer, F Kunc, J Musil, and C Mitterer. A comparative study on reactive and non-reactive unbalanced magnetron sputter deposition of tin coatings. *Thin Solid Films*, 415(1):151–159, 2002.

[135] Mark C Biesinger, Leo WM Lau, Andrea R Gerson, and Roger St C Smart. Resolving surface chemical states in xps analysis of first row transition metals, oxides and hydroxides: Sc, ti, v, cu and zn. *Applied Surface Science*, 257(3):887–898, 2010.

[136] M Delfino, JA Fair, and D Hodul. X-ray photoemission spectra of reactively sputtered tin. *Journal of applied physics*, 71(12):6079–6085, 1992.

[137] Chang-Lin Liang, Guo-An Cheng, Rui-Ting Zheng, Hua-Ping Liu, Jie-Chi Li, Hua-Fang Zhang, Guo-Jia Ma, and Yan-Li Jiang. Composition and texture of tin thin films fabricated by ecr enhanced sputtering deposition. *Surface and Coatings Technology*, 201(9):5537–5540, 2007.

[138] Alastair P Hibbins, J Roy Sambles, and Christopher R Lawrence. Surface plasmon-polariton study of the optical dielectric function of titanium nitride. *journal of modern optics*, 45(10):2051–2062, 1998.

[139] Sadao Adachi and Mitsutoshi Takahashi. Optical properties of tin films deposited by direct current reactive sputtering. *Journal of Applied Physics*, 87(3):1264–1269, 2000.

[140] Ji Hoon Kang and Kwang Joo Kim. Structural, optical, and electronic properties of cubic tinx compounds. *Journal of applied physics*, 86(1):346–350, 1999.

[141] B Karlsson, RP Shimshock, BO Seraphin, and JC Haygarth. Optical properties of cvd-coated tin, zrn and hfn. *Physica Scripta*, 25(6A):775, 1982.

[142] C Ernsberger, J Nickerson, T Smith, AE Miller, and D Banks. Low temperature oxidation behavior of reactively sputtered tin by x-ray photoelectron spectroscopy and contact resistance measurements. *Journal of Vacuum Science & Technology A*, 4(6):2784–2788, 1986.

[143] P Prieto and RE Kirby. X-ray photoelectron spectroscopy study of the difference between reactively evaporated and direct sputter-deposited tin films and their oxidation properties. *Journal of Vacuum Science & Technology A*, 13(6):2819–2826, 1995.

[144] Naresh C Saha and Harland G Tompkins. Titanium nitride oxidation chemistry: An x-ray photoelectron spectroscopy study. *Journal of Applied Physics*, 72(7):3072–3079, 1992.

[145] Thermo Fisher Scientific. *Avantage Data Analysis & Spectrum Processing*, 2007.

[146] AR González-Elipe, G Munuera, JP Espinos, and JM Sanz. Compositional changes induced by 3.5 kev ar+ ion bombardment in ni-ti oxide systems: A comparative study. *Surface Science*, 220(2):368–380, 1989.

[147] E McCafferty and JP Wightman. An x-ray photoelectron spectroscopy sputter profile study of the native air-formed oxide film on titanium. *Applied Surface Science*, 143(1):92–100, 1999.

[148] RNS Sodhi, A Weninger, JE Davies, and K Sreenivas. X-ray photoelectron spectroscopic comparison of sputtered ti, ti6al4v, and passivated bulk metals for use in cell culture techniques. *Journal of Vacuum Science & Technology A*, 9(3):1329–1333, 1991.

[149] F.A. Baiocchi M.J. Vasile, A.B. Emerson. *J. Vac. Sci. Technol. A*, 8(1), 1990.

[150] TP Thorpe, AA Morrish, and SB Qadri. Effect of grain size on the oxidation kinetics of sputtered titanium nitride films. *Journal of Vacuum Science & Technology A*, 6(3):1727–1729, 1988.

[151] Jenny P Glusker and Kenneth N Trueblood. Crystal structure analysis: A primer (iucr texts on crystallography). 2010.

[152] Paul Scherrer. *Bestimmung der inneren Struktur und der Größe von Kolloidteilchen mittels Röntgenstrahlen*. Springer, 1912.

[153] J Il Langford and AJC Wilson. Scherrer after sixty years: a survey and some new results in the determination of crystallite size. *Journal of Applied Crystallography*, 11(2):102–113, 1978.

[154] Scott A Speakman. Estimating crystallite size using xrd, 2008.

[155] Alexander J Blake, Jacqueline M Cole, John SO Evans, Peter Main, Simon Parsons, and David J Watkin. *Crystal structure analysis: principles and practice*, volume 13. OUP Oxford, 2009.

[156] David B. Williams and C. Barry Carter. *Transmission Electron Microscopy: A Textbook for Materials Science*, chapter The Transmission Electron Microscope, pages 3–22. Springer US, Boston, MA, 2009.

[157] Rodrigo Andrade. Imagej, image processing and analysis in java: "fft measurements".

[158] Caroline A Schneider, Wayne S Rasband, Kevin W Eliceiri, et al. Nih image to imagej: 25 years of image analysis. *Nat methods*, 9(7):671–675, 2012.

[159] B. Fultz and J.M. Howe. *Transmission Electron Microscopy and Diffractometry of Materials*. Graduate Texts in Physics. Springer Berlin Heidelberg, 2012.

[160] David B. Williams and C. Barry Carter. *Transmission Electron Microscopy: A Textbook for Materials Science*, chapter Obtaining and Indexing Parallel-Beam Diffraction Patterns, pages 3–22. Springer US, Boston, MA, 2009.

[161] Wendy L Sarney. *Understanding transmission electron microscopy diffraction patterns obtained from infrared semiconductor materials*. Army Research Laboratory, 2003.

[162] David B. Williams and C. Barry Carter. *Transmission Electron Microscopy: A Textbook for Materials Science*, chapter Diffraction from Crystals, pages 3–22. Springer US, Boston, MA, 2009.

[163] M.C. Hutley. *Diffraction gratings*. Techniques of Physics Series. Academic Press, 1982.

[164] Alastair Paul Hibbins. *Grating coupling of surface plasmon polaritons at visible and microwave frequencies.* PhD thesis, University of Exeter, 2000.

[165] Areum Kim, Chikyu Choi, Young Hun Yu, and Won Ki Jung. Metallic reflection grating under surface plasmon resonance condition. *JOURNAL-KOREAN PHYSICAL SOCIETY*, 45:67–70, 2004.

[166] Dow Corning Corporation. Dow corning® fox-1x and fox-2x flowable oxides: Form no. 11-3503a-01, 2015.

[167] Thomas Weiss, Gérard Granet, Nikolay A Gippius, Sergei G Tikhodeev, and Harald Giessen. Matched coordinates and adaptive spatial resolution in the fourier modal method. *Optics express*, 17(10):8051–8061, 2009.

[168] Shanhui Fan. Photovoltaics: An alternative'sun'for solar cells. *Nature nanotechnology*, 9(2):92–93, 2014.

[169] Dakrong Pissuwan, Stella M Valenzuela, and Michael B Cortie. Therapeutic possibilities of plasmonically heated gold nanoparticles. *TRENDS in Biotechnology*, 24(2):62–67, 2006.

[170] Xiaohua Huang, Ivan H El-Sayed, Wei Qian, and Mostafa A El-Sayed. Cancer cell imaging and photothermal therapy in the near-infrared region by using gold nanorods. *Journal of the American Chemical Society*, 128(6):2115–2120, 2006.

[171] Surbhi Lal, Susan E Clare, and Naomi J Halas. Nanoshell-enabled photothermal cancer therapy: impending clinical impact. *Accounts of chemical research*, 41(12):1842–1851, 2008.

[172] B Devika Chithrani, Arezou A Ghazani, and Warren CW Chan. Determining the size and shape dependence of gold nanoparticle uptake into mammalian cells. *Nano letters*, 6(4):662–668, 2006.

[173] Yi-Chien Wu, Ting-Hsiang Wu, Daniel L Clemens, Bai-Yu Lee, Ximiao Wen, Marcus A Horwitz, Michael A Teitell, and Pei-Yu Chiou. Massively parallel delivery of large cargo into mammalian cells with light pulses. *Nature methods*, 12(5):439–444, 2015.

[174] Andre Nel, Tian Xia, Lutz Mädler, and Ning Li. Toxic potential of materials at the nanolevel. *Science*, 311(5761):622–627, 2006.

[175] Sébastien Courvoisier, Nabiha Saklayen, Marinus Huber, Jun Chen, Eric D Diebold, Luigi Bonacina, Jean-Pierre Wolf, and Eric Mazur. Plasmonic tipless pyramid arrays for cell poration. *Nano letters*, 15(7):4461–4466, 2015.

[176] Alexandra Boltasseva and Vladimir M. Shalaev. All that glitters need not be gold. *Science*, 347(6228):1308–1310, 2015.

[177] Melinda K Harman, Scott A Banks, and W Andrew Hodge. Wear analysis of a retrieved hip implant with titanium nitride coating. *The Journal of arthroplasty*, 12(8):938–945, 1997.

[178] Antonio Scarano, Maurizio Piattelli, Giuseppe Vrespa, Sergio Caputi, and Adriano Piattelli. Bacterial adhesion on titanium nitride-coated and uncoated implants: an in vivo human study. *Journal of Oral Implantology*, 29(2):80–85, 2003.

[179] B Subramanian, CV Muraleedharan, R Ananthakumar, and M Jayachandran. A comparative study of titanium nitride (tin), titanium oxy nitride (tion) and titanium aluminum nitride (tialn), as surface coatings for bio implants. *Surface and Coatings Technology*, 205(21):5014–5020, 2011.